



Multiwavelength Observations of the TeV Binary

LS I +61 303

Andrew Whitson Smith

December 2007

*Submitted in accordance with the requirements for
the degree for Doctor in Philosophy.*

The University of Leeds
School of Physics & Astronomy

The candidate confirms that the work submitted is his own and that appropriate credit
has been given where reference has been made to the work of others.

This copy has been supplied on the understanding that it is copyright material
and that no quotation from the thesis may be published without proper acknowledgment

Abstract

This thesis describes the search for and eventual detection of very high energy gamma-ray emission from the galactic binary LS I +61 303 utilizing both the Fred Lawrence Whipple 10 meter atmospheric Cherenkov telescope as well as VERITAS, which is a newly constructed array of atmospheric Cherenkov telescopes; both sensitive in the TeV gamma-ray regime. Although the source was not detected with the Whipple 10 m telescope, flux upper limits were placed on its emission above >540 GeV. Observations of LS I +61 303 were conducted with the VERITAS array in the 2006/2007 observing season resulting in a detection of the source in > 310 GeV gamma-rays at a 7.23σ significance. Along with the detection in very high energy gamma-rays by VERITAS, contemporaneous observations of LS I +61 303 in the hard X-ray regime with the Rossi X-ray Timing Explorer and Swift satellites are described. All three sets of observations show LS I +61 303 to be a variable source in both energy regimes, with this variability associated with changes in the 26.496 day orbital cycle of the binary system. A search for correlation between emission in both the hard X-ray and energy regimes is carried out with no statistically viable correlation found. The two most basic models built to describe the system (i.e. microquasar vs binary pulsar) are described in detail and compared to the available observations. It is found that neither model satisfactorily describes the emission properties of the system as detailed in this work.



For my mother Paula: ER nurse, master gardener, and dog collector extraordinaire. You have provided unwavering support regardless of whatever idea happened to be rolling around in my head of what I want to do with my life that week. It is no small coincidence that your favorite of these was always astronomy. As a nurse you have spent a good deal of time caring for the well being of others and, as such, any sense that I have about how to treat other people decently and be a good person-I owe to you.



For my father Ray: Although spending most of his adult life serving his country as a fighter pilot in the United States Air Force, Ray Smith was truly a man of science at heart; instilling within me a profound respect for the ultimate power of quantitative analysis and logical deduction from a very young age. From the time that he showed me how to measure the height of the peaks of the Grand Teton mountains using only the relevant angle and distance, he started me on a journey. One which, if I'm lucky, I'll spend the rest of my life attempting to complete.

Acknowledgments

First and foremost, my brother Ian: fly-fisherman, firefighter, and father of the century- I never would have imagined this at age 8 when you were busy stuffing socks in my mouth, but you are without a doubt the strongest and bravest individual I've ever known. I've always sought your advice about my life and you've never been wrong. You're my hero bro.

Anna, thank you for putting up with my hypochondriac-ness and always being there for me. You've provided a great deal of support to me and the rest of my family, of which, I'm ecstatic that you're a part of.

Tom, Mitzi, Uncle Jim- thanks for everything over the last 20 odd years of me talking about doing this. I guess I finally got around to it in one way or another.

To the best group of friends I could ask for: Jenner- 15 years of friendship has meant alot to me and I appreciate all your support over the years. From teaching me how to kick-flip and take a fall, to banana bread in the 'stang over the Berkeley Hills, to a much fabled persimmon, to unlimited stay at the Whitson suite-thanks man. Paul: you're more than the best Britain has to offer- 40s of San Miguel, mole-men, fat birds, hand puppets, being grown up at "15"- I don't need three glasses of wine and a nightbus ticket to be your mate- you've become a very close and trusted friend quickly over the last few years when we lived with the nutjobs in Leeds and I always value your perspective and advice. Blake: espace tu face my man. From escorting me around Berkeley in my apron and blown out pupils, to letting me crash in Oxford and waking the Stuffy McStuffersons with drunken Dead covers-you've courageously gone out on a limb with your (extremely successful) life abroad and I admire you for it more than you know. Louis: my guitar, cooking, philosophy, and pretty much everything else mentor and friend- your skills as, well basically, just an amazing human being always humble me- and I'm proud to have you as a friend. Cavan: Very soon you might be lying slightly less when you tell women at bars that I am, in fact, a doctor and can prescribe them medicine. Thanks for always encouraging me and being a loyal friend. Johnny- thanks for looking out for Ian. By looking out for him, I mean harassing him when I can't be there to do it. You're a great guy and good friend.

Professionally, there are two people who I must acknowledge in their impact on my life. First of all, none of the last three years would have been remotely possible if it were not for the generosity, guidance, and kindness of my field advisor Trevor Weekes. From sending me all over the world to conferences to always bringing cheer into any group meeting at basecamp to providing me with timely and insightful comments on this work; you have done me a great service and I will never forget it. I can't honestly imagine working for a better person. Secondly, Stuart Bale- from

hiring a busboy as a research assistant, to urging me to go abroad for my postgraduate studies, and giving me honest advice about what its like to work in science- you have had a massive, positive effect on my professional life. You taught me to always be the biggest proponent of my own work and this has proved invaluable.

Thank you to my Leeds advisor Stella Bradbury for giving me extremely helpful advice and comments on my thesis, as well as always fighting for my interests while going toe to toe with the bureaucratic juggernaut that is the University of Leeds.

There are a few people within the VERITAS collaboration that have been absolutely crucial in helping me along the way as co-workers, and more importantly, good friends. Deirdre- thank you thank you thank you. You've always been so patient with all my questions. I have a confession- its was me that always put on Metallica at the Red Garter-I'm sorry. Pascal- thanks for the much-too-enjoyable bike crawls across Tucson and putting me up in NYC- I has fun looking at all the crazy people. Tizzle-Top Toner: thanks for the nights at Dunkin' Donuts- you're honestly the nicest person I know and I'm glad to be your buddy. Party Boy Ward- thanks for the trash talking and laughs. Stephan Cefegan- you are the smartest guy I know-thank you so much for the help over the last 3 years.

The Tucson crew that has bent over backwards to help me out and has shown me a great time- John Kildea: I owe you samosas, thanks for all the help. Mark Theiling- thank you so much for laughing at my jokes, you know how important this is to me. Ryan and Sarah- congratulations!- thank you for the fun nights out. Jeremy and Donna Perkins-thanks for putting up with me- Ive had a great time over the last year. Peter Cogan- you never got tired of answering my questions and you can drink your weight in Fat Tire. Ben Zitzer- the best poker player in the collaboration. Wytan Benbow- thanks for the job advice. The Leeds group: Richard White, Joachim Rose, Jeff Grube, Alex Syson- thanks for all your help in my first six months of this PhD. Especially you Richard for printing this whole thing out! Mary Kertzmann and Glenn Sembroski- I had a blast in Merida with you two. Special thanks to Jamie Holder for supporting my work and telling other people that I'm an alright guy, although I suspect you'd never *have the guts* to say that to my face. Pat Moriarty for all the grammatical and punctuation help with my publications and more importantly not pointing out that I just ordered a large plate of nothing but ham in Barcelona. Thanks to Gernot for all the help with the LSI analysis. Amy Furniss for keeping my spirits up during the last few weeks of writing and editing- time for a beer ay?

The Whipple basecamp staff: Jack (breaks the back of funk on the bass), Emmet, Danny, Cesar, Gene- thanks so much for the travel assistance (and the Jay-Z album), Dan Brocious, Karen Erdman-Myres, and Steve Criswell.

Nic Harcourt and Jason Bentley for keeping my feet tapping during long nights at the telescope. Django, Trey, Jerry, Sting- I don't think the guy in the office next door likes you nearly as much as I do.

Last but certainly not least Ken Gibbs- the man who was nice enough to let me share his office for six months. I can't believe you didn't bludgeon me to death with a copy of The Economist. Thanks for the advice and perspective.

Contents

List of figures	x
List of tables	xi
List of Abbreviations	xii
1 High Energy γ-Ray Astronomy	1
1.1 Experiments Past and Present	1
1.2 High Energy Gamma-Ray Sources	17
2 The Imaging Atmospheric Cherenkov Technique	29
2.1 High Energy Interactions In The Atmosphere	30
2.2 Cherenkov Radiation	32
2.3 Gamma-ray Initiated Extensive Air Showers	33
2.4 Cosmic-Ray Initiated Extensive Air Showers	36
2.5 Implementation of the Technique	40
2.6 Rejecting Cosmic Rays	41
2.7 Properties of The Technique: The Benefits of Stereo	44
2.8 Summary	48
3 Technique Implementation: The Whipple 10 m and VERITAS	49
3.1 The Fred Lawrence Whipple 10 m Telescope	49
3.2 The VERITAS Array	70
3.3 Summary	101
4 The Astrophysics of TeV Binaries	103
4.1 High Mass X-ray Binaries	103
4.2 PSR 1259-63	109
4.3 LS 5039	111
4.4 Cygnus X-3	113

4.5	LS I +61 303	114
4.6	Summary	134
5	Whipple 10 m Observations of Cygnus X-3 and LS I +61 303	135
5.1	Flux and Flux Upper Limit Calculations	135
5.2	Data Quality Selection and Analysis Parameters	138
5.3	Crab Nebula Data Set	139
5.4	Cygnus X-3 Observations	141
5.5	LS I +61 303 Observations	141
6	VERITAS Observations of LS I +61 303	147
6.1	Data Selection and Reduction	147
6.2	Crab Nebula Observations	153
6.3	LS I +61 303 Observations	156
6.4	Summary	165
7	X-ray Observations of LS I +61 303	167
7.1	RXTE Data Reduction and Analysis	167
7.2	Results	169
7.3	Re-Analysis of Archival RXTE Data	172
7.4	<i>Swift</i> Contemporaneous Observations with VERITAS	174
7.5	X-ray Behavior in Perspective	175
7.6	Comparison of X-ray and TeV Data	177
7.7	Total Dataset Comparison	178
7.8	Combined Spectra	184
8	Comparison to Emission Models	187
8.1	Microquasar Model	187
8.2	Binary Pulsar Model	191
8.3	Conclusion	194
9	Conclusions and Outlook	196
9.1	Overview	196
9.2	Unresolved Issues	199

List of Figures

1.1	Photos of some of the second generation atmospheric Cherenkov telescopes. . . .	5
1.2	The third generation IACTs.	6
1.3	Two of the more significant discoveries made by the H.E.S.S. collaboration. . . .	7
1.4	Two of the most significant recent observations taken by VERITAS.	9
1.5	GLAST: A pair-tracking telescope	11
1.6	A plot of the sources in the 3 rd EGRET catalog (Hartman et al., 1999).	12
1.7	Pictures of the Swift, INTEGRAL, and GLAST satellites.	13
1.8	The improved angular resolution of GLAST vs EGRET	14
1.9	The Milagro water Cherenkov detector.	16
1.10	Alternative high energy ground-based observatories: STACEE and the Tibet air- shower array.	17
1.11	Flux sensitivities of modern high energy gamma-ray observatories.	18
1.12	All currently known TeV sources.	19
1.13	The physical framework of an AGN.	20
1.14	Attenuation of TeV gamma-rays by the EBL.	22
1.15	TeV supernova remnants: MSH 15-52 and RXJ0852.0-4622.	23
1.16	Diffuse gamma-ray emission from the Cygnus region and galactic center.	25
2.1	A plot of the cross section as a function of incident photon energy for transmission through the atmosphere.	31
2.2	The Cherenkov emission process.	32
2.3	A schematic of the coherent Cherenkov wavefronts emitted by a particle traveling at a velocity $\beta c > c$	34
2.4	The light distribution from a typical extensive air shower.	36
2.5	The properties of air shower development for gamma rays and cosmic rays. . . .	37
2.6	Properties of the Cherenkov light from gamma-ray showers versus cosmic-ray showers.	39

2.7	The Hillas parameters.	42
2.8	Length and Width distributions for simulated gamma-ray and cosmic-ray showers.	43
2.9	Differences between the resulting Cherenkov signal between gamma-ray and cosmic-ray induced air showers.	43
2.10	The α parameter discriminant.	44
2.11	An illustration of how a stereo Cherenkov array can improve upon single telescope observations.	45
2.12	How local muons produce a problem for single telescope observations.	47
3.1	The Fred Lawrence Whipple 10m Gamma-Ray Reflector: a Davies-Cotton telescope.	50
3.2	A demonstration of the degradation of the mirrors used for the Whipple 10 m reflector.	51
3.3	The effects of the deformation and bias alignment on the mirrors of a Davies-Cotton telescope.	53
3.4	The current camera used on the Whipple 10 m.	54
3.5	Various Whipple 10m imaging camera configurations from 1982 to the present.	55
3.6	How a CFD works.	56
3.7	An example bias curve taken from the Whipple 10m in 2006.	57
3.8	A schematic representation of the Whipple 10m signal trigger.	58
3.9	The effects of varying levels of night-sky background on the pedestal distribution.	60
3.10	The levels of data calibration and cleaning in offline 10m analysis.	61
3.11	Various images from real Whipple 10 m data.	62
3.12	Distributions of discrimination paramaters from real Whipple 10 m data on the Crab Nebula.	63
3.13	The method for determining whether an ON/OFF pair contained a viable gamma-ray signal.	65
3.14	The distributions corresponding to the determination of $N_{ON}, N_{OFF}, N_{good}$, and N_{bad}	67
3.15	The effective area and peak energy response for the Whipple 10 m extracted from simulations.	68
3.16	Performance of the Whipple 10 m as demonstrated by observations on the Crab Nebula.	69
3.17	Photos of the VERITAS-4 array.	71
3.18	Various photos of a VERITAS telescope and its associated electronics.	72
3.19	Mirror reflectivity vs incident light wavelength for the VERITAS mirrors.	73

3.20	The 499 pixel VERITAS camera.	74
3.21	A graphical schematic of the VERITAS array trigger system.	76
3.22	The functionality of the DAT modules.	79
3.23	An example of a full array bias curve taken for the 3 telescope array.	80
3.24	A sample FADC trace from a pixel involved in a shower event.	82
3.25	An example of using the timing information provided by the FADCs	84
3.26	The effect of T_{Offset} correction to the arrival time of pulses over the camera.	86
3.27	The digital count distribution from a “single p.e.” laser run.	88
3.28	Demonstrating the computation and efficacy of the mean scaled parameters.	91
3.29	How independent shower images can be used to locate the exact shower core impact position.	92
3.30	A demonstration of how the images from all telescopes are combined to locate the angular position (on the camera) where the shower is assumed to have originated from.	93
3.31	A Θ^2 distribution for ~ 1.5 hours of Crab Nebula data taken with 2 telescopes.	94
3.32	Wobble Mode Observing.	95
3.33	A demonstration of how the Ring Background Model works.	97
3.34	An example of the lookup tables used for determining the primary gamma-ray energy via its reconstructed impact parameter and measured <i>size</i> parameter.	98
3.35	Examples of detector response versus primary energy for various zenith angles.	99
3.36	Simulated energy resolution of the VERITAS-2 array.	100
4.1	Classification of binary star systems.	104
4.2	The binary pulsar and microquasar models for TeV HMXBs	106
4.3	The accretion/ejection model and its associated spectral properties in both radio and X-ray.	108
4.4	The H.E.S.S. observations of PSR 1259-63 in 2004.	110
4.5	H.E.S.S. observations of LS 5039.	112
4.6	A schematic of the orbital geometry of LSI +61 303.	115
4.7	Analysis of 359 B band optical plates from Harvard College Observatory on LS I +61 303.	116
4.8	The results of several radio monitoring campaigns on LS I +61 303.	117
4.9	Radio maps of LS I +61 303.	119
4.10	The results of two ROSAT monitoring campaigns on LS I +61 303 in soft X-rays.	120
4.11	A comparison of the radio and soft X-ray emission from LS I +61 303.	121

4.12	The first full orbital X-ray monitoring campaign on LS I +61 303 performed by RXTE.	122
4.13	Background subtracted count rates and hardness ratio taken from the 2005 XMM-Newton long observation of LS I +61 303.	124
4.14	The Chandra X-ray image of LS I +61 303.	125
4.15	Archival X-ray observations of LS I +61 303.	126
4.16	The EGRET observations of LS I +61 303.	128
4.17	The MAGIC detection of LS I +61 303.	129
4.18	The predictions of the microquasar model of Bosch-Ramon et al. (2006b).	132
4.19	The spectrum produced by the binary pulsar model of Dubus (2006).	133
5.1	An example of the determination of the upper limits counts for a sample data set.	136
5.2	The estimation used for energy threshold vs elevation for Whipple 10 m data.	137
5.3	The results of the selected Crab Nebula observations from 2005-2007.	140
5.4	The results of the Cygnus X-3 observations taken in 2006.	142
5.5	Comparison of the RXTE ASM and Whipple TeV upper limits derived from 2006 Cygnus X-3 observations.	143
5.6	The results of the Whipple 10 m dataset on LS I +61 303 recorded in 2004-2007.	144
5.7	The results of Whipple 10 m observations of LS I +61 303.	146
6.1	FIR data used as a run quality discriminant.	149
6.2	The L3 rates used as a run quality discriminant.	149
6.3	Example effective area (right) and energy bias (left) plots from KASCADE simulations.	151
6.4	A graphical representation of the production of energy spectra.	152
6.5	VERITAS-2 Crab Nebula observations.	154
6.6	Differential energy spectrum for the Crab Nebula derived from VERITAS-2 observations.	155
6.7	The VERITAS Crab Nebula differential energy spectrum points plotted along with results from other experiments.	156
6.8	Properties of the VERITAS-2 LS I +61 303 dataset.	157
6.9	VERITAS-2 observations of LS I +61 303.	158
6.10	The TeV lightcurve from the 2006-7 LSI data plotted by orbital phase.	159
6.11	LS I +61 303 gamma-ray lightcurve binned by orbital phase.	159
6.12	Flux upper limits and detections from VERITAS observations of LS I +61 303.	160

6.13	Two dimensional significance maps generated by orbital phase for VERITAS observations of LS I +61 303.	161
6.14	The derived LS I +61 303 differential energy spectrum from VERITAS observations along with the Crab Nebula spectrum for comparison.	163
6.15	The VERITAS differential energy spectrum compared to that derived by MAGIC observations in 2005-2006.	164
6.16	Comparison of the differential energy spectrum from “low” and “high” flux states of LS I +61 303.	164
6.17	The differential energy spectrum derived from 10/27/06	165
7.1	The integrated spectrum from all 9 observations with RXTE fit with an absorbed powerlaw model.	168
7.2	RXTE monitoring of LS I +61 303 in 2006.	170
7.3	Spectral and flux values from RXTE observations taken in 2006.	171
7.4	Results of the re-analysis of archival RXTE data on LS I +61 303.	173
7.5	Swift X-ray observations in Fall 2006 binned by both MJD and orbital phase. . .	175
7.6	Combined Swift and RXTE observations of LS I +61 303.	176
7.7	“Aligned” spectral indices vs orbital phase of X-ray observations.	177
7.8	LS I +61 303 TeV and X-ray data points binned by MJD.	178
7.9	LS I +61 303 TeV and X-ray data points binned by orbital phase.	179
7.10	The ZDCF correlation test tested on simulated sinusoidal lightcurves.	181
7.11	The 2006 LS I +61 303 X-ray lightcurve tested for auto-correlation with the ZDCF.	182
7.12	The same as in figure 7.11 with the X-ray lightcurve altered for greater continuity.	182
7.13	The TeV lightcurve on which the ZDCF auto-correlation test was performed . . .	183
7.14	A ZDCF test performed on the lightcurve of 7.13 altered for continuity.	183
7.15	ZDCF cross-correlation test performed on the TeV and X-ray lightcurves.	184
7.16	The broadband spectra of LS I +61 303 during both “low” and “high” states. . .	186
8.1	The prediction of the TeV (left) and X-ray lightcurves (right) from Bosch-Ramon et al. (2006b) (red lines) compared to data presented in Chapter 7.	188
8.2	The spectral behavior predicted by the model of Bosch-Ramon et al. (2006b) for two separate regions of the orbital cycle.	189
8.3	Milli-arcsecond scale radio imaging of LS I +61 303 during various orbital phases.	192
8.4	The broadband spectra arising from the model of Dubus (2006) compared to the same observational data as in figure 8.2	193

9.1 The simulated response of the LAT instrument aboard GLAST to 55 hours of exposure on LS I +61 303.	201
--	-----

List of Tables

1.1	The various second generation Cherenkov experiments.	4
1.2	The confirmed source discoveries made by the second generation IACTs. Information from tevcat.uchicago.edu	4
2.1	A table showing the resultant properties of gamma-ray air showers of several different energies. Data taken from Weekes (2003).	35
3.1	<i>Supercuts 2000</i>	64
3.2	The properties of the Whipple 10 m and several versions of the VERITAS array. .	102
5.1	2004-2007 LS I +61 303 Observations	145
6.1	VEGAS Analysis Parameters	150
6.2	LS I +61 303 Phase Binned Results	162
7.1	RXTE October 2006 Results	171
7.2	Table 2: RXTE March 1996 Results	174

List of Abbreviations

ASM	All-Sky Monitor
AGN	Active Galactic Nuclei
CAT	Cherenkov Array at Themis
CGRO	Compton Gamma-Ray Observatory
EBL	Extragalactic Background Light
EGRET	Energetic Gamma-ray Experiment Telescope
FOV	Field of View
GLAST	Gamma-ray Large Area Space Telescope
HEASARC	High Energy Astrophysics Science Archive Research Center
HEGRA	High Energy Gamma-Ray Astronomy
H.E.S.S	High Energy Stereoscopic System
IACT	Imaging Atmospheric Cherenkov Technique
MAGIC	Major Atmospheric Gamma-ray Imaging Cherenkov
MJD	Modified Julian Date
NASA	National Aeronautics and Space Administration
NSB	Night Sky Background
PCA	Proportional Counter Array
PCU	Proportional Counter Unit
PMT	Photomultiplier
PSF	Point Spread Function
RXTE	Rossi X-ray Timing Experiment
VERITAS	Very Energetic Radiation Imaging Telescope Array System

Chapter 1

High Energy γ -Ray Astronomy

*A good idea will keep you awake during the morning,
but a great idea will keep you awake at night.*

Marilyn vos Savant

1.1 Experiments Past and Present

The field of gamma-ray astronomy ($\sim 100 \text{ MeV} \rightarrow 100 \text{ TeV}$) developed as a response to the study of ultra high energy cosmic rays. This class of particles consisting of electrons, protons, and heavier nuclei with energies $> 10^{18} \text{ eV}$ was first discovered by Nobel laureate Victor Hess in 1912 through a series of balloon experiments. The discovery of a cosmic flux of particles with energies much greater than anything conceivably created by then known astrophysical processes confounded and amazed physicists of that time (as well as ours!). These charged particles apparently arrive at the Earth with virtually no directional information due to galactic magnetic fields confusing their trajectories as they travel through the galaxy. It is primarily due to this lack of origin information that, to this date, there does not exist a comprehensive explanation for the origin of high energy cosmic rays.

Since cosmic rays carry no directional information, we are forced to look for signatures of their production that do carry directional information. Very high energy gamma-rays are an ideal candidate. Their production requires extremely violent and energetic astrophysical processes to take place, and it is not hard to imagine that some of these processes might also generate fluxes of high energy cosmic rays. The outcome of this hypothesis can be illustrated by promising the reader that after having said all of the above, the preceding discussion will be the only mention of the origin of high energy cosmic rays contained within this thesis! The connection between the two fields of high energy gamma-ray astronomy and cosmic ray genesis, although still possible,

has proved to date ultimately ambiguous and to this day there does not exist a comprehensive explanation for the origin of the highest energy cosmic rays. Fortunately however, the field of gamma-ray astronomy has proved to be exceedingly fruitful in and of itself and in the last 20 years it has changed the nature of our understanding of energetic processes in both galactic and extragalactic objects.

The first experiments designed to detect cosmic gamma-rays were NASA satellite experiments carried out in the 1960's. The Explorer 11 satellite (Clark et al., 1968) was launched in 1961 and was the first ever satellite launched for purely astronomical purposes. Through its ~ 140 hour data set, the Explorer 11 recorded an excess of ~ 140 gamma-ray events with energies near 100 MeV. Most of these events were attributed to gamma-rays produced by cosmic ray interactions in the Earth's limb. There remained only 30 excess events that could be attributed to the sky, therefore, only a flux upper limit was set by this experiment. Following on the heels Explorer 11, the OSO 3 (Kraushaar et al., 1965) detected a total of 621 sky events above 100 MeV with a clear excess towards the galactic center. This excess was confirmed by the subsequent OSO-5 satellite in 1968. There was now a known cosmic source, if only diffuse, of high energy gamma rays.

The first detection of a gamma-ray point source came from the SAS-2 spark chamber satellite launched by NASA in 1972. Owing to the newly used spark chamber technique of identifying pair-production by an incident gamma-ray, the SAS-2 was able to not only confirm the galactic center excess but establish the presence of four galactic gamma-ray point sources above 35 MeV: the Crab pulsar, the Vela pulsar, the X-ray binary Cygnus X-3 (controversial), and an unidentified source $\gamma 195+5$ (Fichtel, 1975; Hartman et al., 1979). Next came the launch of the COS-B satellite by the ESA in 1975. Sensitive in the range of 50 MeV to 5 GeV, COS-B added to the catalog of known gamma-ray sources by discovering 25 more galactic point sources (Swanenburg et al., 1981). Some of these sources reinforced the earlier SAS-2 detections, some had obvious counterparts, some did not and were labeled as unidentified sources. It should also be noted, in the interest of foreshadowing chapter 5, that Cygnus X-3 was auspiciously absent from the COS-B source list. In general, approximately half of the sources detected by the COS-B experiment were never confirmed and are now considered to be aberrations resulting from poor background subtraction.

The greatest leap forward in gamma-ray source detection came with the launch of the EGRET experiment aboard NASA's Compton Gamma-Ray Observatory (CGRO) in 1991. EGRET, sensitive in the range of 20 MeV to 30 GeV, added an astounding 271 point sources to the gamma-ray catalog. Both galactic and extragalactic in nature, the EGRET point sources (catalogued most completely in the 3rd EGRET catalog or 3EG (Hartman et al., 1999)) remain today as the most expansive collection of GeV gamma-ray sources in the sky, despite roughly 120 sources which are

no longer considered to be true point sources). The EGRET experiment, as well as its soon to be launched successor GLAST, will be covered in greater detail later in this chapter.

1.1.1 Discovery Experiments

While these developments were taking place in the realm of space-based gamma-ray observations, techniques for detecting higher energy gamma-rays (100 GeV→100 TeV) on the ground were developing as well. In 1948, P.M.S. Blackett (Blackett, 1948) predicted that a small ($\sim 0.01\%$) but measurable component of the light coming from the night-sky should be due to Cherenkov radiation from cosmic ray secondaries in the atmosphere. He brought this idea to the attention of John Jelley and Bill Galbraith at the Harwell Air Shower Array (see Weekes (2006)) for a brief review of the early history of this field). Subsequently, Galbraith and Jelley measured brief pulses of Cherenkov light coming from large cosmic rays showers and published the first observations using the “atmospheric Cherenkov technique” in 1953 (Galbraith and Jelley, 1953). Ironically these first detected cosmic ray showers turn out to be the principal source of noise for any ground based gamma-ray observatory! However, very high energy gamma rays behave much the same as these high energy cosmic rays after entering the Earth’s atmosphere and this detection can be considered the first step towards the ground-based detection of very high energy gamma-ray sources. Galbraith and Jelley followed up their initial detection with more extensive experiments performed at the Harwell Air Shower Array in which they advanced the initial understanding of the technique (Galbraith and Jelley, 1955; Jelley and Galbraith, 1955) and their work is considered to be the foundation of the field as much as the work of Dirac and Heisenberg could be considered the foundation of quantum mechanics.

1.1.2 1st Generation Experiments

Although there were many early experiments based upon the atmospheric Cherenkov technique, (see for example the work in Crimea (Chudakov et al., 1965), Dublin (Fruin et al., 1964), and the initial configuration of the Whipple 10 m telescope (Fazio et al., 1968)) these experiments typically only utilized a single photomultiplier detector and hence suffered from the lack of a mechanism to discriminate the incoming gamma-ray signals from the overwhelming background of cosmic ray signals.

1.1.3 2nd Generation Experiments

The idea of using an imaging camera to discriminate between gamma-ray and cosmic ray signals was initially proposed in 1977 by Weekes and Turver (Weekes and Turver, 1977) and this hurdle

Table 1.1: The various second generation Cherenkov experiments. Information taken Catanese and Weekes (1999)

Collaboration	Telescopes	Energy Threshold
<i>Sponsoring Countries</i>		
Whipple	1×10m	400 GeV
<i>UK-USA-Ireland</i>		
HEGRA	5×3m	500 GeV
<i>Spain-Germany-Armenia</i>		
CANGAROO I/II	1×3.8m/1×7m	500 GeV/400 GeV
<i>Japan-Australia</i>		
Durham Mk6	3×7m	250 GeV
<i>UK</i>		
CAT	1×3m	250 GeV
<i>France</i>		
7-Telescope Array	7×2m	500 GeV
<i>Japan</i>		

Table 1.2: The confirmed source discoveries made by the second generation IACTs. Information from tevcat.uchicago.edu

Source	Class	Discovery	Year
Crab Nebula	Pulsar Wind Nebula	Whipple	1989
Markarian 421	Active Galactic Nuclei	Whipple	1992
Markarian 501	Active Galactic Nuclei	Whipple	1996
1ES 2344+514	Active Galactic Nuclei	Whipple	1998
H1426+428	Active Galactic Nuclei	Whipple	2002
PKS 2155-304	Active Galactic Nuclei	Durham Mk6	2001
1ES 1959+650	Active Galactic Nuclei	7-Telescope Array	1999
M87	Active Galactic Nuclei	HEGRA	2003
TeV 2032	Unidentified	HEGRA	2002
Cas A	Supernova Remnant	HEGRA	2001

1.1. EXPERIMENTS PAST AND PRESENT

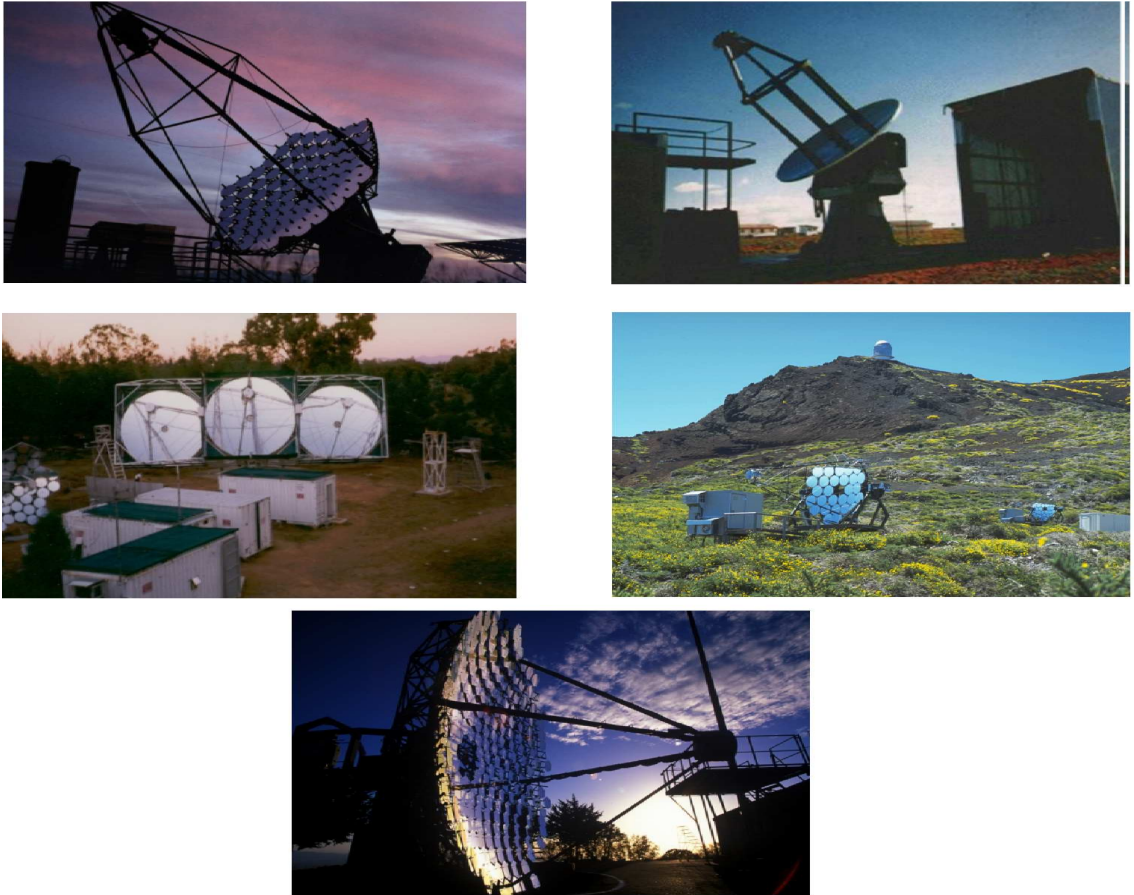


Figure 1.1: Photos of some of the second generation atmospheric Cherenkov telescopes. From left to right and top to bottom are shown *CAT*, *CANGAROO*, *Durham Mark 6*, *HEGRA*, and the Whipple 10m.

was finally overcome in 1989 (Weekes, 1989) at the Fred Lawrence Whipple 10 m gamma-ray observatory. This instrument had the ability to actually image the resulting Cherenkov light from the showers and, for the first time, allowed for sufficient gamma-ray/cosmic ray discrimination. The newly implemented analysis technique known as “Hillas Parametrization” (see Hillas (1985) and chapter 2) was crucial to the initial development of the field. The Crab Nebula was detected by the Whipple 10 m telescope in >700 GeV gamma-rays at the 9σ level over 80 hours of observations. This detection represented the first concrete proof of concept for this “second-generation” of imaging atmospheric Cherenkov telescopes (IACTs) and gave birth to a new branch of astronomy. The Whipple 10 m telescope (still in operation after a succession of upgrades) maintained its pre-eminence in the field during the 1990s with further initial detections of TeV sources including the first detected extragalactic sources: the blazars Markarian 421 (Punch et al., 1992), and Markarian 501 (Quinn et al., 1996). Other successful instruments which utilized the technique over this time



Figure 1.2: The third generation IACTs. Clockwise from top left are shown the MAGIC telescope in La Palma, the VERITAS experiment in Southern Arizona, the H.E.S.S. experiment based in Namibia, and the CANGAROO-III experiment in Australia.

period included the French *CAT*, the German-Spanish-Armenian *HEGRA* array, the Australian-Japanese *CANGAROO III* collaboration, and the University of Durham's (UK) Mark6 telescope in Australia. Out of these, and next to Whipple, the HEGRA collaboration was the most noteworthy of these experiments with its pioneering use of an array of five 3.4m imaging Cherenkov telescopes to improve both the angular and energy resolution of the technique. The properties of these second generation instruments as well as the various discoveries made by them are shown in tables 1.1 and 1.2.

1.1.4 3rd Generation Experiments

Building upon the success of both the Whipple and HEGRA experiments the development of the third generation of IACTs has resulted in an explosion of new source discoveries and pioneering technological advances.

H.E.S.S.

In 2004, a French-German led collaboration began operating the High Energy Stereoscopic System (H.E.S.S.) at the foot of the Gamsburg, Namibia (Bernlohr, 2003) ($23^{\circ}16'18''$ S latitude, $16^{\circ}30'00''$ E longitude, 1800 m asl). Shown in figure 1.2 (top left), H.E.S.S. is an array of four 12.5 m diameter telescopes which is sensitive in the range of ~ 100 GeV \rightarrow ~ 50 TeV. The princi-

1.1. EXPERIMENTS PAST AND PRESENT

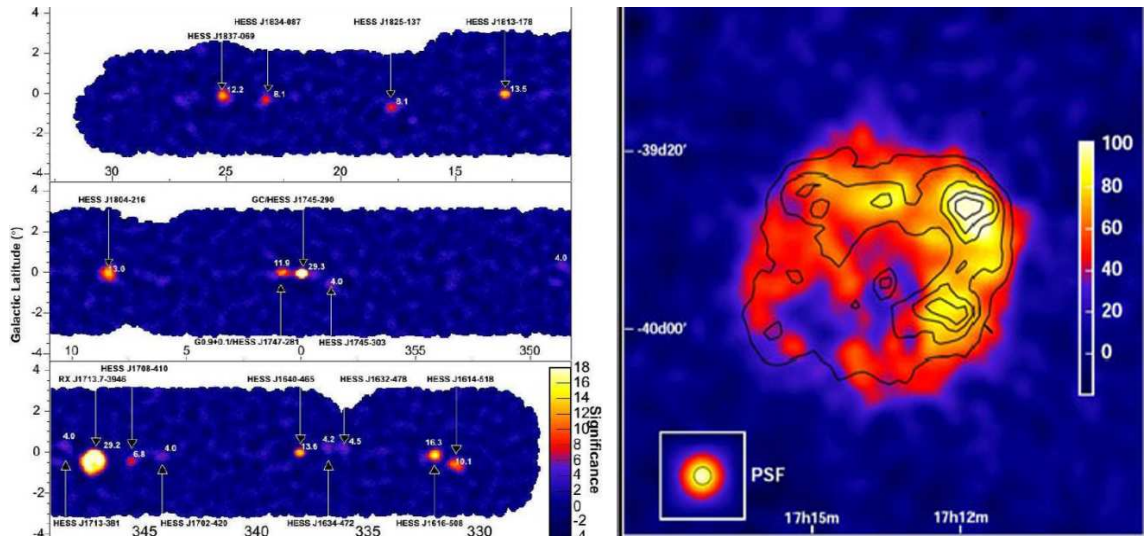


Figure 1.3: Two of the more significant discoveries made by the H.E.S.S. collaboration. On the left is shown the results of the survey of the inner galactic plane, revealing many new sources coincident with supernova remnant, pulsar wind nebula, and further unidentified counterparts. On the right is shown the results of the H.E.S.S. observations of the shell type supernova remnant RX J 1713.7-3946. Overlaid contours represent X-ray emission as observed by ASCA in the 1-3 keV range. (Left taken from Aharonian (2007f), right taken from Horns (2007))

pal advancement of the H.E.S.S. experiment has been its utilization of extremely large (5°) and finely pixelated ($960 \text{ pixels} \times 0.16^\circ$) imaging cameras on each of its telescopes. It is arguably because of this factor (as well as other factors such as site location and excellent planning) that the H.E.S.S. experiment is considered to be overwhelmingly successful. Since its inception in 2004, H.E.S.S. has published over 30 new source discoveries with a majority of these coming from their extremely detailed survey of the galactic plane (see figure 1.3). Again, due to their wide field of view and finely pixelated camera, H.E.S.S. has also made the first observations of extended gamma-ray sources which have yielded valuable morphological information on the arc minute scale (see figure 1.3). With an energy threshold of $\sim 250 \text{ GeV}$ for most observing angles, H.E.S.S. has the capability to detect a source flux on the order of 1% of the Crab Nebula flux (the standard candle of VHE gamma-ray astronomy) at the 5σ level in 25 hours. The H.E.S.S. collaboration is planning to upgrade the experiment to include a large 28 m telescope in the center of the existing square of four 12.5m telescopes (Vincent, 2005). With an extremely large mirror area and a 2048 pixel camera, this telescope's addition to the array (known as H.E.S.S. II) will allow the observational threshold of the array to be lowered to $\sim 50 \text{ GeV}$.

MAGIC

On the Canary island of La Palma, a Spanish-German led collaboration has built the **M**ajor **A**tmospheric **G**amma **I**maging **C**herenkov **T**elescope (MAGIC) which began full operations in 2005 (shown in figure 1.2, top right) (Cortina, 2005). As opposed to the array design of H.E.S.S. and VERITAS, MAGIC chose to further develop the single telescope design, utilizing a single 17 m reflector. Whereas the strengths of the array designs of H.E.S.S. and VERITAS lie in the use of multiple telescopes with proven technological components, the strength of MAGIC's single telescope design lies in their use of advanced cutting edge technologies. For instance, the PMTs in their $\sim 3.8^\circ$ field of view camera are coated with wavelength shifter in order to better match their sensitivity to the peak wavelength of the Cherenkov signal (see chapter 2 and Paneque et al., (2004)). The PMT signals are transmitted by fibre optic cable which reduces signal distortion and the analog signals are readout by 2 GSPS (Giga-Samples Per Second) FADC boards which allow for greater temporal resolution of the air shower development than traditional digitization systems (see section 3.2.5). MAGIC is also optimized for detecting VHE signals from gamma-ray bursts with its very fast mount positioner capable of slewing at an average of $3\text{-}4^\circ/\text{s}$. The main design goal of MAGIC was to lower the energy threshold for gamma-ray observations which, in principal, is accomplished by the large mirror area's (236 m^2) ability to collect more light from lower energy air showers. However, the effect of Cherenkov signals from local muons (see 2.7) limits this capability of MAGIC and, although their trigger threshold is at $\sim 50\text{ GeV}$, there has been little evidence that their analysis is yet capable of extracting a gamma-ray signal below 150 GeV (Albert et al., 2006a; ?). The MAGIC collaboration is attempting to improve their observational capacity by constructing a second 17 m telescope nearby in order to form an array. The 2 telescope array is expected to begin operations in 2009 and is expected to have an analysis threshold of $\sim 50\text{ GeV}$ (Baixeras et al., 2005). Some of the more notable source discoveries that MAGIC is responsible for include the detection of the blazar Markarian 180 (which was the first blazar detection to be triggered by an outburst in the optical regime (Albert et al., 2006c)); the (as of yet unconfirmed) detection of the most distant VHE blazar known, 3C 279 (Teshima et al., 2007); and the initial VHE detection of subject of this thesis, the galactic binary LS I +61 303 (?).

CANGAROO-III

Although not as sensitive as H.E.S.S., the CANGAROO-III (Enomoto et al., 2006) array contributes to the world-wide coverage capability of the third generation of IACTs. Located in Australia, this Japanese-Australian collaboration began operations in 2004 and has since improved upon the sensitivity of the earlier CANGAROO-I and II experiments. An array of four 10 m tele-

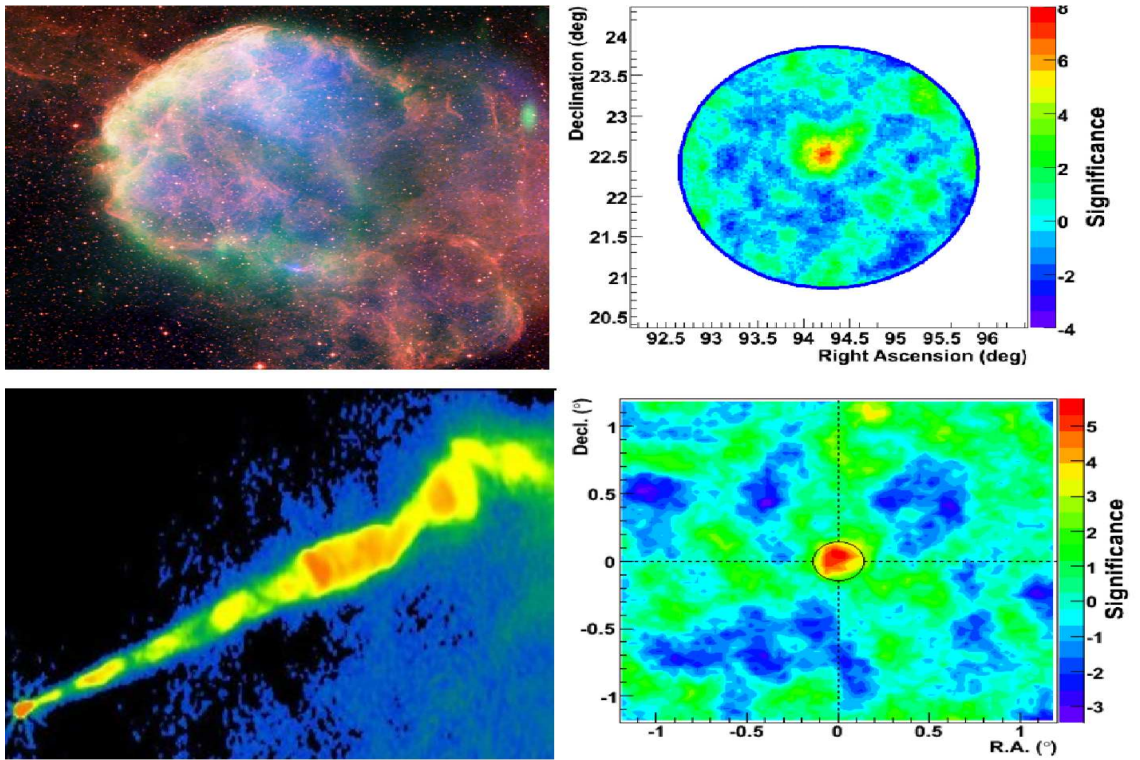


Figure 1.4: Two of the most significant recent observations taken by VERITAS. Top left shows the CHANDRA X-ray image of the supernova remnant IC 443 (Gaensler et al., 2006); top right shows the VERITAS 2-d sky map from observations taken on IC 443 revealing it to be an extended VHE gamma-ray source (Humesnky et al., 2007). The bottom left shows the VLA radio image of the active galaxy M87 (courtesy of NRAO/NSF); the bottom right is the associated VERITAS 2-D sky map from observations taken on the source (Colin et al., 2007).

scopes (shown in figure 1.2, bottom left), CANGAROO-III has primarily focused on confirming the existing source catalog of southern hemisphere H.E.S.S. sources as well as determining flux upper limits on candidate sources.

VERITAS

Located at the base of Mt. Hopkins in southern Arizona, the VERITAS IACT array (Maier et al. 2007a) (shown in figure 1.2, bottom right) is the most sensitive VHE gamma-ray observatory in the northern hemisphere and observations taken with the array are the primary focus of this thesis work. While a full technical and performance description of the array will be delayed until section 3.2, it is worth mentioning some of the key highlights of the project. The full array of four 12 m telescopes began full its full observational program in April 2007. Each telescope is equipped with 347 hexagonal mirrors which focus light from air showers onto a 499 pixel PMT camera. The

signals from these cameras are read out by a system of 500 MHz FADCs which have the ability to distinguish gamma-ray signals from cosmic-ray signals by recording small temporal differences in the shower development. The full array has a energy threshold of 200 GeV for observation angles above 55° elevation and similar flux sensitivity to that of the H.E.S.S. experiment described above. The preliminary array of two telescopes began observations in Spring 2006 with a third telescope available for observations taken between December 2006 and April 2007 (when the fourth telescope came on-line). It is in these 2 and 3 telescope array configurations that the data for this thesis were taken. Since stereo observations began in 2006, VERITAS has confirmed the VHE gamma-ray detections of the active galaxies M 87, and 1ES 1218+30.4 (Colin et al., 2007; Fortin et al., 2007); the supernova remnant IC 443 (Humesnky et al., 2007); and the TeV binary LS I +61 303 (Maier et al., 2007b). Over the next few years as the full VERITAS array is used at its full operational capacity, it will compliment the observations of H.E.S.S. and MAGIC with undoubtedly many new source discoveries and investigations.

1.1.5 Satellite Experiments

At a much lower energy band than that covered by the ground-based observatories, satellite-based gamma-ray observations have contributed a great deal to the field of high energy gamma-ray astronomy including an impressive number of source discoveries. Since gamma rays of energy below ~ 50 GeV will not create air showers large enough to be readily observable on the ground, satellite observatories must cover the lower energy range of gamma rays. Typically operating in the energy range of ~ 10 MeV to ~ 30 GeV, these detectors observe the incident gamma rays by direct detection. This is generally accomplished by using a layer of material (converting layer) which converts the incident gamma-ray into an e^-/e^+ pair (see section 2.1), followed by layers of tracking material which measure the paths of the e^-/e^+ pairs, and then finally a calorimeter material which detects the deposition energy of the pair. By detecting particles through these stacks of material, both the original trajectory and energy of the gamma ray can be reconstructed. To reject signals from cosmic rays, the layers are surrounded by an anti-coincidence detector which vetoes cosmic ray events in the detector that are ionizing enough to register at the anti-coincidence layer. Although there are other designs for gamma-ray satellite observatories, (see, for example COMPTEL (Schoenfelder et al., 1981)) this “pair-tracking” design is the most successful and is the basis for both the EGRET and GLAST satellites. Because these detectors utilize direct methods to observe the gamma-ray flux from sources, they have extremely good detection efficient as well as having very large fields of view. However, this comes at the price of having a very small effective area due to the fact that, unlike IACTs, the gamma ray has pass through the apparatus. Although



Figure 1.5: Left: The basic design of a pair-tracking telescope as it is explained in the text. Right: The GLAST satellite during environmental testing. It can be easily seen how the design on the left is integrated into the large section on the top (known as the *Large Area Telescope* or LAT). The locations of some of the *Gamma – Ray Burst Monitor* units are also shown- see section 1.1.5.

no data from any gamma-ray satellite will be reduced within this thesis, there will be numerous references to previous results (as they apply to ground-based observations) from the following list of gamma-ray experiment:

CGRO

In 1991, the Compton Gamma-Ray Observatory (CGRO) was launched from the space shuttle Atlantis. During its 9 year observational service, CGRO made unprecedented contributions to the understanding of astronomy in the energy range of 15 keV to 30 GeV. CGRO was home to four distinct detectors:

- *BATSE*: The Burst and Transient Source Experiment, designed primarily for the detection of gamma-ray bursts and solar flare activity, was sensitive in the range of 15 keV-110 MeV.
- *OSSE*: The Oriented Scintillation Spectroscopy Experiment provided detailed spectrographic measurements in 0.05-10 MeV range.
- *COMPTEL*: The Compton Telescope utilized an alternate method (to the pair-tracking design) of detecting gamma rays based on their ability to Compton-scatter electrons within a detector framework. This instrument provided a large field of view (~ 1 steradian) for observations in the 1-30 MeV range.
- *EGRET*: Along with BATSE, the Energetic Gamma-Ray Experiment Telescope was the

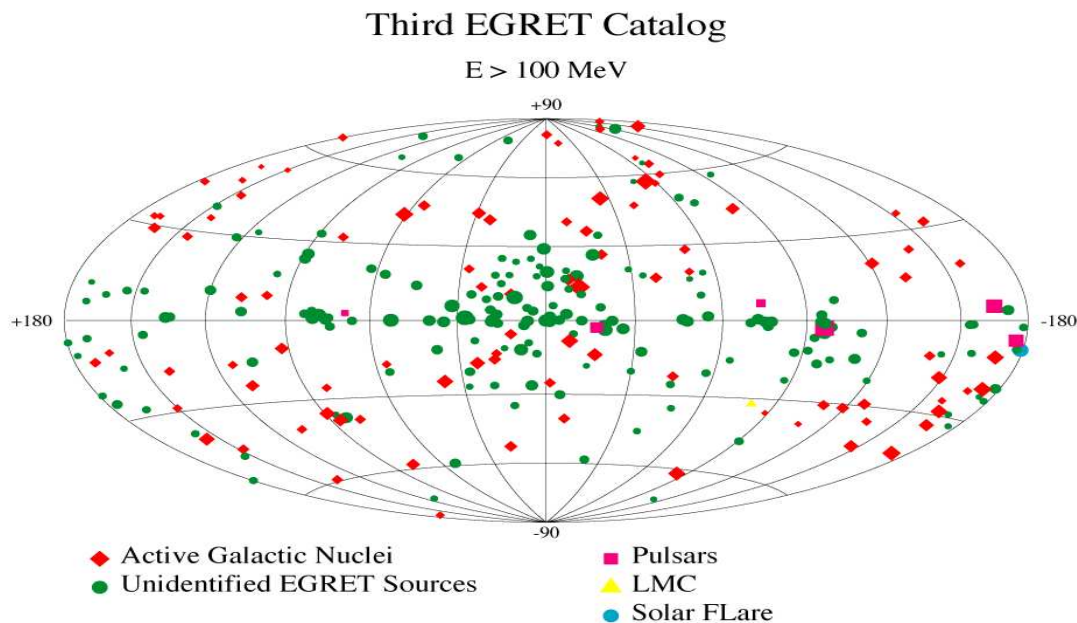


Figure 1.6: A plot of the sources in the 3rd EGRET catalog (Hartman et al., 1999).

most successful of all of the instruments aboard CGRO (Thompson et al., 1995). It provided, for the first time, sensitive measurements of the sky in the 20 MeV-30 GeV range. With angular resolution of $\sim 1^\circ$ - 4° and 9-12% energy resolution, EGRET expanded the catalog of known high energy gamma-ray point sources significantly. In the third compilation of all detected EGRET sources, (known as the 3rd EGRET Catalog (Hartman et al., 1999)) there are over 250 point sources included (see figure 1.6). Many of these are identified with active galactic nuclei, with many more sources remaining unidentified but believed to be of galactic origin.

INTEGRAL

Launched in 2002, the INTErnational Gamma-Ray Astrophysics Laboratory (INTEGRAL) (Winkler et al., 2003), followed in the footsteps of the CGRO mission's multiwavelength approach, focusing this time instead on the optical and X-ray counterparts to gamma-ray observations. Sensitive in the high energy range of 3 keV to 10 MeV, INTEGRAL (shown in figure 1.7, top left) is composed of four separate but complimentary detectors:

- *SPI*: The SPectrometer aboard INTEGRAL provides detailed spectrographic analysis in the range of 20 keV and 8 MeV.
- *IBIS*: The Imager aBoard the INTEGRAL Satellite provides highly resolved (up to 12 ar-

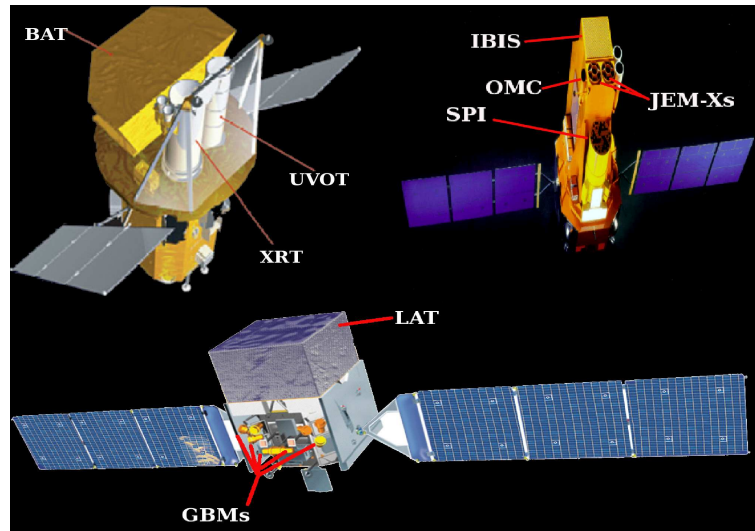


Figure 1.7: Illustrations of Swift (left) and INTEGRAL (right), and GLAST (bottom) along with their instrumental components as described in the text. Photos courtesy of NASA HEASARC (heasarc.gsfc.nasa.gov).

cm⁻¹) images of sources in the range of 15keV to 10 MeV.

- *JEM-X 1,2*: The Joint European Monitors of X-rays provide more resolved pointed X-ray observations in the range of 3-35 keV.
- *OMC*: The Optical Monitoring Camera provides the ability for optical observations within the high energy framework of the satellite.

SWIFT

Launched in 2004, and primarily designed as a multiwavelength gamma-ray burst detector, NASA's SWIFT satellite (shown in figure 1.7, top right) (Gehrels et al., 2004) is comprised of a UV/Optical Telescope (UVOT), a pointed X-Ray Telescope (XRT), and a (gamma-ray) Burst Alert Telescope (BAT). The BAT, sensitive in the range of 15-150 keV and having a field of view of 2 steradians, will detect a GRB within its field of view and alert the ground relay network on Earth. Within minutes after re-positioning the satellite, the XRT (by observing the X-ray afterglow) is able to refine the source position of the GRB within the BAT field of view. After several more minutes, the UVOT (by observing optical afterglows) is able to further refine the source position as well as provide redshift measurements. In this way, SWIFT provides accurate source localizations, light curves, and redshifts for over 100 GRBs per year, significantly advancing our understanding of these energetic phenomena (see section 1.2.8 for further detail).

GLAST

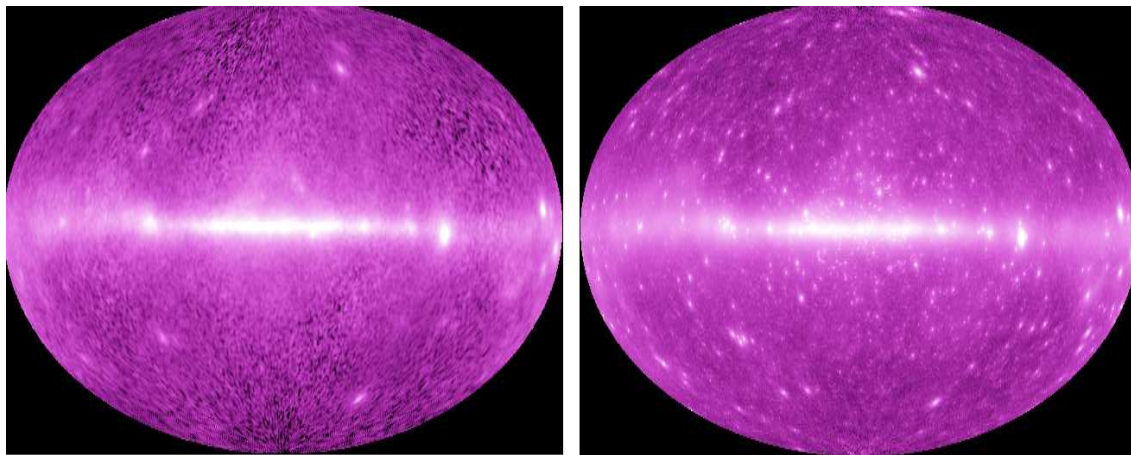


Figure 1.8: Results from simulated observations of gamma-ray sources above 100 MeV by EGRET (left) and GLAST (right). The improvement in angular resolution of sources is immediately obvious. Taken from the NASA GSFC (www.gsfc.nasa.gov).

Scheduled to be launched in early 2008, the Gamma-ray Large Area Space Telescope (GLAST) (Mattox et al., 1996) will significantly alter the current knowledge base of high energy gamma-ray astronomy. Designed as a successor to EGRET, GLAST is comprised of 2 instruments: a Large Area Telescope (LAT) and a series of Gamma-ray Burst Monitors (GBMs). GLAST will be sensitive in the range of 10 keV to 300 GeV overlapping with ground-based IACTs. The LAT will have a field of view of 2.5 steradians and provide observations in the range of 20 MeV and above, with a point source sensitivity of nearly 100 times that of EGRET at 100 MeV and positional accuracies down to 30 arcseconds for strong sources (see figure 1.8 for an example of the performance improvement of GLAST over EGRET). The GBM units are designed for (nearly) all-sky coverage for gamma-ray bursts. 8 GBMs provide a field of view of 3π steradians in the range of 10 keV to 30 MeV and are expected to detect ~ 200 GRBs per year (Omodei et al., 2006), doubling the rate of SWIFT. GLAST will resolve the issue of the nature of many of the EGRET unidentified objects as well as increasing the number of known high energy sources by at least an order of magnitude.

RXTE

Although the Rossi X-ray Timing Explorer (RXTE) is not a gamma-ray observatory, its demonstrated usefulness in performing multiwavelength monitoring campaigns along with gamma-ray instruments merits a description of it here. Data taken with RXTE is reduced and presented in this thesis in chapters 5 and 7. Launched by NASA in 1995, RXTE is sensitive to X-rays in the

range of 1.2-200 keV with peak sensitivity lying in the range of 2-60 keV (Swank, 1994). The observatory consists of three distinct instruments: the High Energy X-Ray Timing Experiment (HEXTE), the All Sky Monitor (ASM), and the Proportional Counting Array (PCA). The HEXTE instrument was designed as a high energy X-ray imaging device functioning in the range of 20-200 keV. However, in practice the HEXTE instrument has proven to be insensitive to anything but the strongest X-ray sources and data from this instrument is not presented in this thesis. The ASM instrument provides X-ray count observations of nearly 80% of the sky in the 1.2 to 10 keV band. The ASM functions mainly as a long term monitoring instrument for about 350 sources deemed to be of interest in the X-ray band. The ASM has only moderately accurate counting resolution, and is therefore typically only used as an alert device for objects which appear to be flaring.

The PCA consists of 5 individual units (PCUs), each sensitive in the range of 2-60 keV with a typical energy resolution of 18% (Jahoda, 2006). The PCUs detect X-rays by the photoelectric effect of the X-ray photons with the Xenon molecules. Each PCU consists of three layers of Xenon-filled detection layers, although in general for low energy, weak flux sources (such as the observations detailed in this thesis), only the top Xenon layer is used for analysis due to the energy requirements for a particle to interact with underlying layers. Since approximately the year 2000, the PCA has functioned with reduced sensitivity, utilizing typically only 2-3 of the PCUs for any given observation. Despite the reduced functionality of the PCUs, the PCA is still capable of detecting weak sources (several percent of the Crab Nebula X-ray flux) in kilo-second scale observations.

1.1.6 Alternative Ground-Based Gamma-Ray Observatories

Complementary to the methods described in the previous sections for detecting high energy gamma rays, there exist further classes of observatories that measure gamma rays on the ground via methods that are similar to IACTs but differing enough to be discussed separately.

Water Cherenkov Experiments

The Milagro experiment, located near Los Alamos, New Mexico (Sullivan et al., 2001) was a 5000 m² pool of water surrounded by 175 secondary tanks of water which together with the main pond structure, comprise an area of 40,000 m². Shown in figure 1.9, these pools of water were interlaced with layers of PMTs that are sensitive to the Cherenkov light emitted by secondary particles (originally created by the interaction of VHE gamma rays with the atmosphere) as they enter the water. Milagro had an energy threshold of ~ 250 GeV, although it was more sensitive at higher energies (approaching 20 TeV).

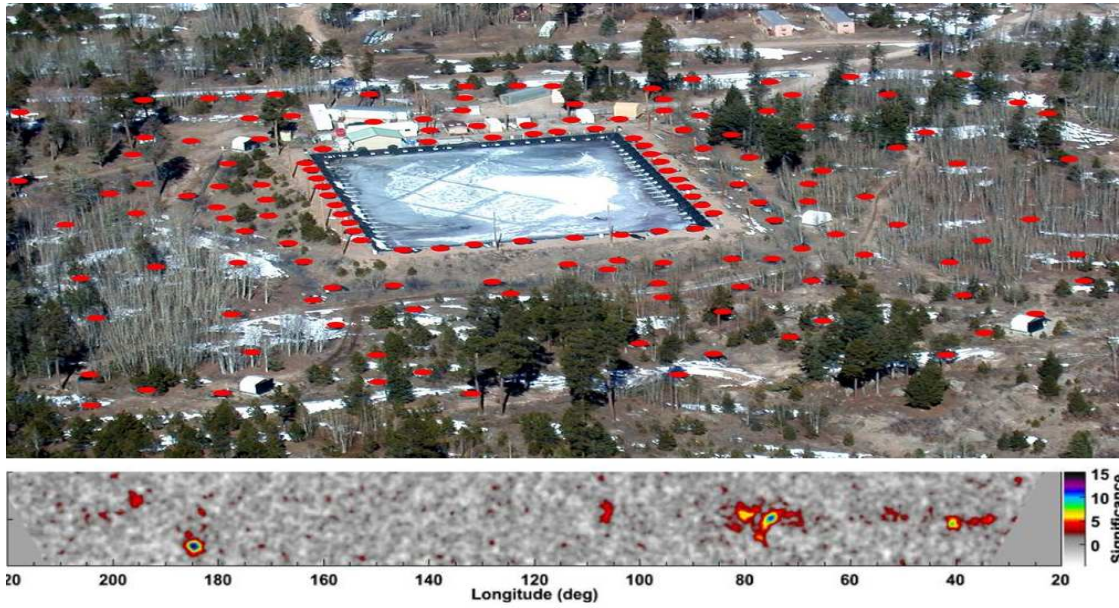


Figure 1.9: Top: The Milagro water Cherenkov detector (center) surrounded by its associated outriggers tanks (red dots). Below this is shown the Milagro view of the galactic plane at ~ 20 TeV.

Milagro observed the sky with a 2 steradian field of view, which, combined with a 100% duty cycle made it ideal for observing extremely extended, diffuse sources. Until recently, Milagro suffered from a lack of ability to discriminate between gamma-ray and cosmic ray secondaries (Catanese and Weekes, 1999). However, recent (2003) advances in their analysis have allowed Milagro to contribute significant results, including the detection of a tentative diffuse source within the highly congested Cygnus region (Abdo et al., 2007a; Konopelko et al., 2007). Milagro has now ceased operation but will be followed shortly by the HAWC experiment, a 300×300 m water pond to be built in Mexico (Sinnis, 2005).

Solar Furnace Experiments

In the spirit of recycling an already “green” venture, solar furnace experiments in general use large arrays of mirrors, at night, which were originally designed for solar energy experiments. These arrays of mirrors focus Cherenkov light from gamma-ray induced air showers onto a central secondary mirror which then routes light from each primary mirror onto a separate PMT. Although these experiments operate at a lower energy threshold than IACTs (due to very large mirror areas) their sensitivity was never competitive with IACTs due their general lack of efficient background rejection. Several experiments have been successfully constructed and operated in the 1990s and early 2000s (see STACEE (Williams et al., 2000), CELESTE (Giebels et al., 1998), Solar-2 (Zweerink et al., 1999), and GRAAL (Arqueros et al., 2001)), however, due to a lack of

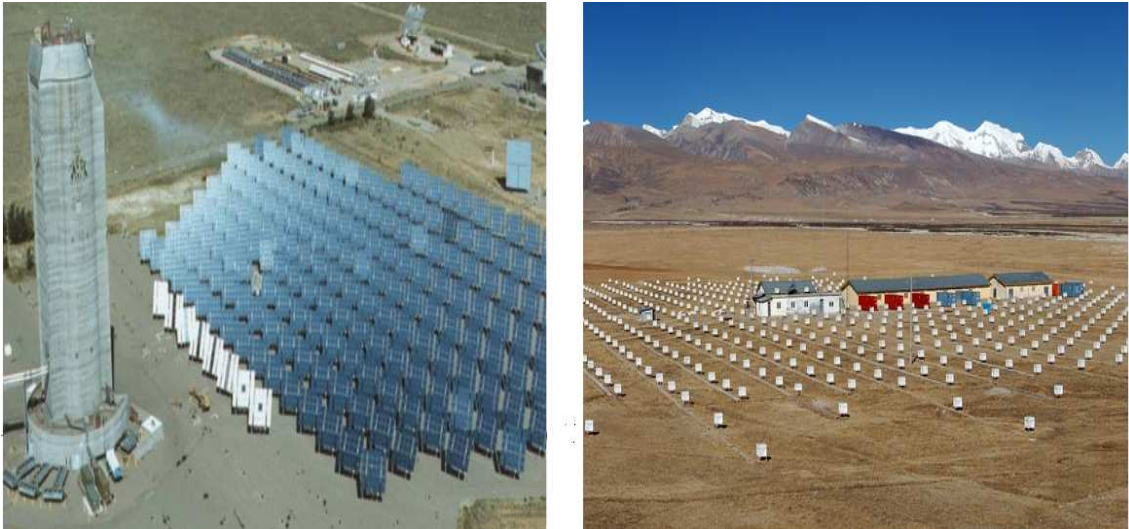


Figure 1.10: Left: The STACEE experiment consisting of solar furnace mirrors which focus Cherenkov light onto a central mirror atop the tower shown to the left. Right: The Tibet air shower array located at 4300m above sea level in Yangbajing (Tibet). The majority of the 697 scintillation detectors are shown.

significant science results from these experiments, this very clever idea has all but been abandoned for more efficient detection methods.

Air Shower Detector Arrays

Although Milagro could be placed into this category, most air shower particle detectors operate at an energy above 10 TeV and have sensitivities extending into the PeV regime. The technique uses a vast array (several hundred) of scintillation detectors connected to PMTs which detect the penetrating particle component of both high energy gamma ray and cosmic ray induced air showers. Detectors built upon this principle usually contribute more to the study of high energy cosmic rays than high energy gamma rays. However, results from these experiments (such as the Tibet Array in China (Amenomori et al., 2007), ARGO (Bacci et al., 2002), CASA-MIA (Borione et al., 1992), GRAPES-III (Gupta et al., 2005), AUGER (Abraham et al., 2004) have direct impact of our understanding of astronomy in the high energy regime.

1.2 High Energy Gamma-Ray Sources

Shown in figure 1.12 are the current (December 2007) known source positions for all of the known very high energy gamma ray sources to date. If this map had been produced merely five years ago, it would have shown only about 10 sources. The explosion in new sources primarily due to the

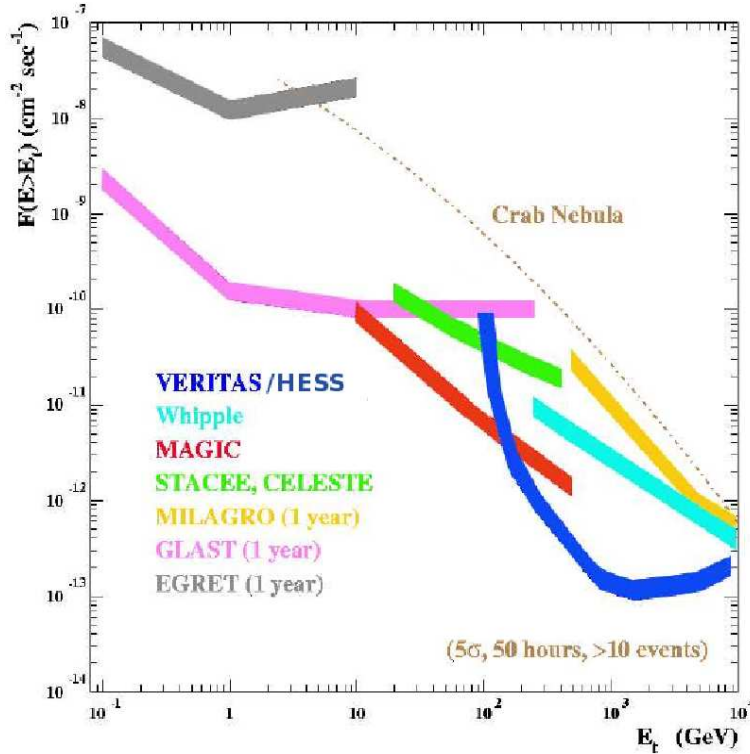


Figure 1.11: The simulated flux sensitivities of the instruments described in this chapter. The sensitivities are produced assuming a 50 hours observation integration, a minimum 5σ detection, with at least 10 excess events recorded. Taken from Cogan (2007).

H.E.S.S. and MAGIC experiments has been phenomenal and based upon their success along with the capabilities of the VERITAS array, VERITAS will no doubt add many new source discoveries in the coming years.

1.2.1 Active Galactic Nuclei

Although not the subject of this thesis, the study of active galactic nuclei (AGN) has proved to be a fruitful endeavor for modern gamma-ray astronomers. These objects are galaxies which contain a supermassive (10^6 - $10^9 M_{\odot}$) black hole (SMBH) at their center which acts as an enormously powerful accretion-powered engine producing vast amounts of radiated energy, outshining the rest of the host galaxy. As the SMBH pulls material into its center it will create an accretion disk around it. Through this accretion process, material with random orientation in angular momentum will eventually form a dusty torus-like structure around the SMBH. This torus will obscure light from the lateral view of the AGN (such as the strong UV and optical emissions from the disk), and thus, the center of AGN are typically only able to be viewed directly from $<30^{\circ}$ away from the direction orthogonal to the accretion disk. In addition to this, near to the SMBH, there will

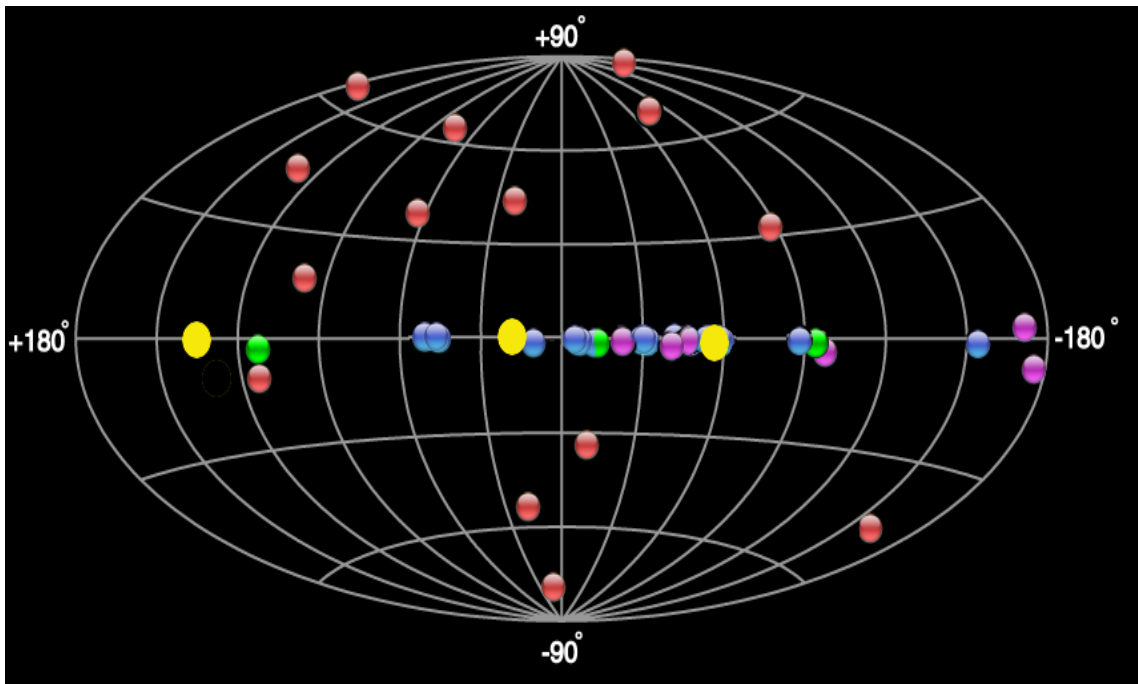


Figure 1.12: The locations (in galactic coordinates) of all currently detected TeV sources. Red dots represent AGN, purple are pulsar wind nebulae, green are shell type supernova remnants, yellow are TeV binaries, and blue dots represent unidentified sources. (Figure produced with TeVCat (tevcap.uchicago.edu)).

be clouds of gas moving at very high velocities around the center of mass, emitting broad optical lines (broad-line regions). Outside the torus and accretion disk are slower moving clouds of gas which emit narrower optical lines (narrow-line regions). Figure 1.13 shows a generalized model of an AGN.

AGN can be broken down into two main subclasses: radio-quiet and radio-loud. The radio-quiet variety are mostly composed of spiral galaxies which show no evidence for TeV gamma-ray emission, although are strong X-ray sources. In the radio-loud variety, the central SMBH creates an extremely powerful, helical magnetic field coming out of the accretion disk (see figure 1.13) (Koide et al., 2000). Charged particles are accelerated along the magnetic field lines and undergo synchrotron losses resulting in the emission from radio all the way up to X-ray. The radio losses are particularly great and typical radio output from the centers of radio-loud AGN can lie in the range of $10^{35} \rightarrow 10^{38} \text{W}$. It is these radio-loud AGN that are of interest to high energy gamma-ray astronomers, in particular the sub-class of AGN known as *Blazars*. Blazars are AGN that are oriented such that the radio loud jet is pointing directly along the line of sight to the Earth (Blandford and Rees, 1978). With the exception of the galaxy M87 (Aharonian et al., 2003;

1.2. HIGH ENERGY GAMMA-RAY SOURCES

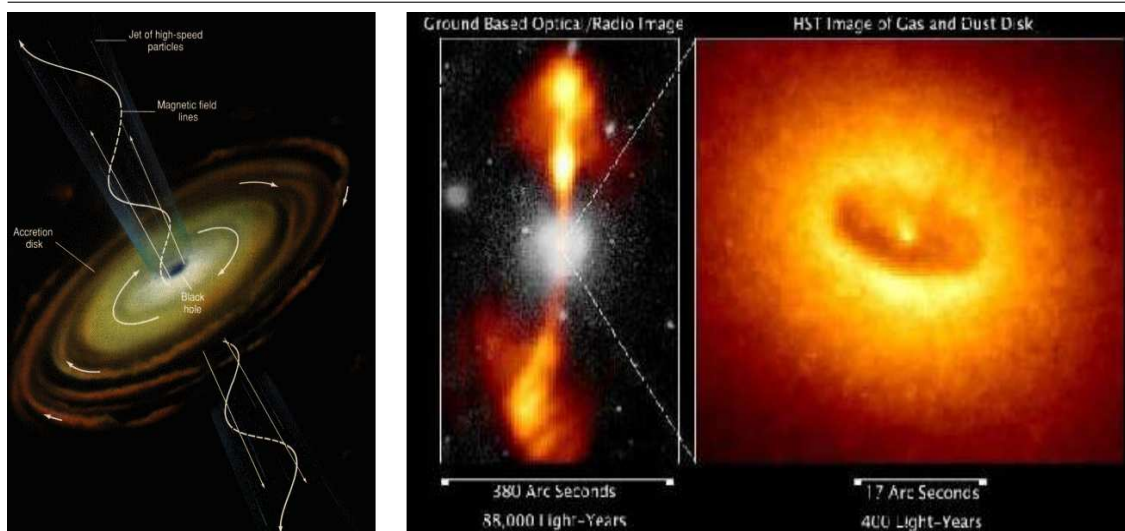


Figure 1.13: A schematic showing the general physical structure for AGN (left) along with a diagram showing the helical structure of magnetic field lines coming from the disk. Charged particles are accelerated around and along these field lines resulting the synchrotron radio and X-ray emission detected from these objects. Images taken from astronomyonline.org (left) and science.nasa.gov (right).

Beilecke et al., 2005; Colin et al., 2007) (which is essentially just a slightly off-axis blazar) all the detected extragalactic TeV sources have been blazars thus far. Blazars are most commonly characterized by their double peaked emission structure (Ghisellini, 1999) with the first peak occurring in the IR-UV range and the second peak occurring in the MeV-GeV range. Blazars come in two different types (although the distinction between the two types is at times vague), flat spectrum radio quasars (*FSRQs*) which are characterized by strong emission lines and BL Lacertae objects which have weak or no emission lines. The class of BL Lacertae objects can be classified further (Padovani and Giommi, 1995): those blazars with stronger X-ray than radio emission are *High Frequency Peaked BL LACS* or (HBLs), and those with the opposite emission properties are known as *Low Frequency Peaked BL LACS* or (LBLs). This differentiation turns out to be an important one for VHE gamma-ray astronomers as all currently discovered TeV blazars are HBLs including the blazars Markarian 421 and Markarian 501 which were the first extragalactic TeV emitters to be discovered by ground-based TeV observatories (Punch et al., 1992; Quinn et al., 1996).

The models for high energy emission from blazars are diverse. The leptonic models generally presuppose the existence of a population of electrons accelerated to relativistic energies by a first-order Fermi process within the jet (Maraschi et al., 1992). The electrons are then accelerated

around and along the helical magnetic field lines of the AGN, resulting in the synchrotron peak that is evident in the spectra of most blazars (first peak in IR-UV or even X-ray). The second, higher energy, peak is generated by these relativistic electrons up-scattering photons via the inverse Compton process (see section 2.1) to GeV-TeV energies. Where this population of seed photons comes from is the main difference between the two main leptonic models. Models such as that of Sikora and Madejski (2001) hypothesize that the synchrotron radiation of the electrons provides an adequate population of seed photons for up-scattering (*Synchrotron Self – Compton Models*). Contrary to this, the *External Inverse – Compton* models of emission generate the population of seed photons from the IR to soft X-ray emission from the accretion disk (Dermer et al., 1991), or from synchrotron photons reprocessed by the broad-line regions. Although these models can provide a reasonable fit to multiwavelength observations of AGN, extrapolations of the energy and magnetic field requirements of the AGN jet in leptonic models have raised questions about whether or not the observed AGNs could support such physical properties (Marscher, 1999).

In the hadronic class of AGN emission models, high energy protons are accelerated within the jet and interact with ambient matter (such as the broad-line regions (Dar and Laor, 1997) or intergalactic material (Pohl and Schlickeiser, 2000)). Proton interactions produce energetic neutral pions according to the following:

$$p + p \rightarrow \pi^0 + \text{other secondaries} \quad (1.1)$$

which then decay by :

$$\pi^0 \rightarrow 2\gamma \quad (1.2)$$

where the energy of the gamma-ray pair is dependent upon the energy of the neutral pion which in turn is dependent upon the energy of the incident protons. It is believed that within AGN jets, protons are accelerated to energies of over 10^{20} eV which, through the above interaction, can easily create TeV gamma-rays. In this hadronic interaction, the cross section for neutral pion production is roughly equal to that of charged pion production. Charged pions can then undergo decay as:

$$\pi^\pm \rightarrow \mu^\pm + \nu_\mu \quad (1.3)$$

$$\mu^\pm \rightarrow e^\pm + \nu_e + \nu_\mu \quad (1.4)$$

which implies that, if TeV gamma-rays are indeed being produced by this mechanism, then a given TeV source may even be a feasible target for neutrino telescopes (albeit at a very low flux). In fact, the neutrino detection experiment AMANDA-II (Barwick et al., 2002) has reported a neutrino directionally coincident with the TeV blazar 1ES 1959 (Zornoza et al., 2007) near a TeV flaring state in 2002, however, this detection was not statistically significant.

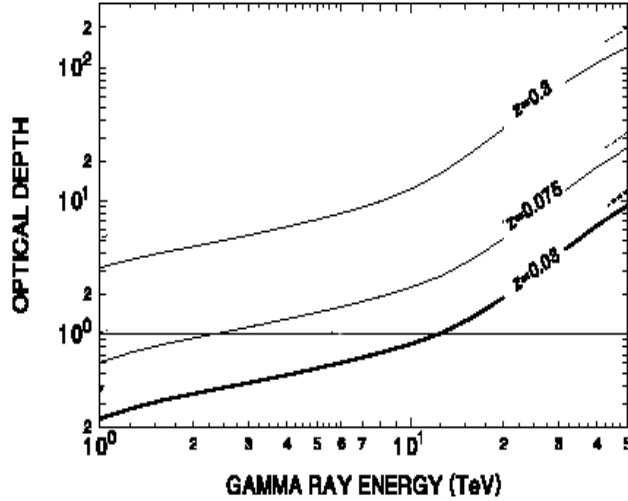


Figure 1.14: The attenuation of TeV gamma-rays of varying energy produced at redshifts of $z=0.2$ and 0.5 . Figure modified from Raue and Mazin (2008).

Regardless of which emission mechanism is at work in AGN, or how powerful a particular AGN is, there is a limitation of how far out TeV observatories can detect these sources. This is due to the presence of the extragalactic background light (EBL) which is composed of the relic 2.725 K black-body radiation from the Big Bang (CMB), and the optical and IR light produced by stars at different redshifts in all stages of stellar evolution. This EBL presents a pair-production target for photons traversing intergalactic space via the following interaction:

$$\gamma_{TeV} + \gamma_{target} \rightarrow e^+ e^- \quad (1.5)$$

For TeV gamma rays, this cross section peaks in the IR range (~ 0.5 eV) (Nikishov, 1962), therefore the IR component of the EBL presents an attenuating barrier to extragalactic TeV radiation in the range that is of interest to IACTs. Direct measurement of the density of the IR component of the EBL is not possible due to contamination by galactic IR radiation; therefore, in the case of measuring the spectra of distant AGN, the situation is somewhat of a “catch-22”. If the intrinsic spectra of AGN were known, the measured TeV spectra would provide a concrete measurement of the IR EBL. However, the intrinsic spectra of AGN are NOT known due to the lack of a direct measurement of the IR EBL and its associated attenuation power. Therefore, only models based on upper limits of integrated IR emission from galaxy counts can be used to reconstruct intrinsic source spectra of AGN (Dwek and Krennrich, 2005). However, the recent detection (and associated spectral measurements) of the distant blazar 1ES 10347-121 ($z=0.188$) by the H.E.S.S. collaboration (Tluczykont et al., 2005), indicates that the IR component of the EBL may be less than 50% of the commonly accepted value derived from galaxy counts. Shown in figure 1.14 is

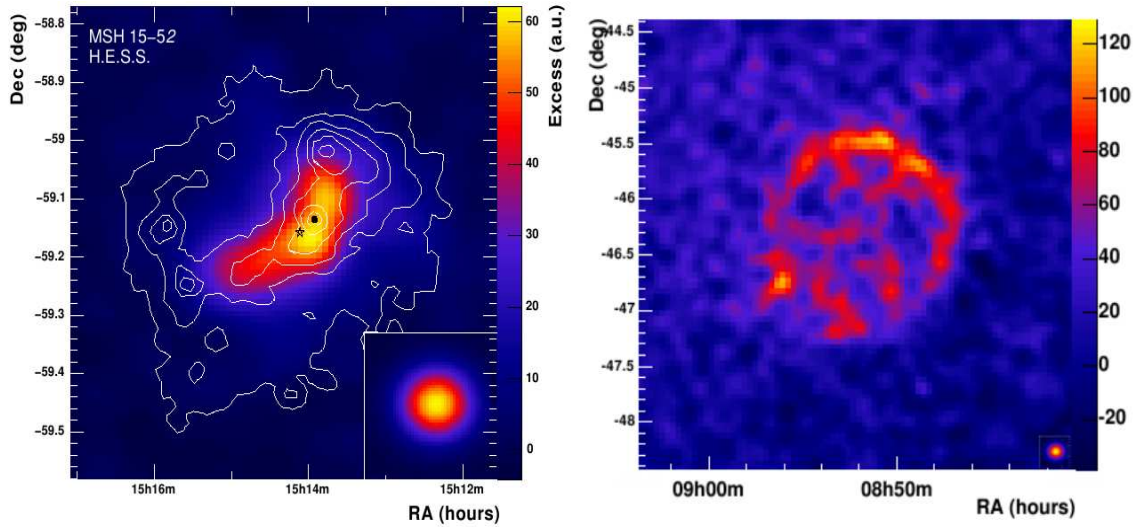


Figure 1.15: The H.E.S.S. 2-D sky maps of the plerion MSH 15-52 (left) (with ROSAT X-ray contours overlaid) and the shell type remnant RXJ0852.0-4622 (right). For comparison the size of the instrumental point spread function is shown in the bottom right corner. Taken from Aharonian et al. (2005b) and Aharonian et al. (2007).

a plot of the attenuation factor versus gamma-ray energy for two sources located at redshifts of 0.2 and 0.5. This model was taken from Raue and Mazin (2008) in which the authors construct a generic EBL model based on recent upper limits from the spectra of distant AGN. H.E.S.S. has also recently detected the blazar PG 1553+113 which may have a redshift up to $z=0.4$ (Aharonian et al., 2006a), although this distance measurement is not definite. The MAGIC experiment has also reported the detection of 3C 279 at a redshift of 0.52 (Teshima et al., 2007), which would constrain the EBL even further. It is evident that the use of TeV observations of AGN provides valuable insight into the determination of the EBL density, and consequently the history of star formation and extinction throughout the local universe.

1.2.2 Plerionic Supernova Remnants

The study of plerions in TeV gamma rays has proven extremely valuable for the latest generation of IACTs. A plerion can be classified as the remnant of a supernova which is comprised of an energetic pulsar surrounded by stellar material created in the supernova explosion. The fast rotation of the pulsar and its associated magnetic field will create a stream of particles (or pulsar wind) which will interact with surrounding media resulting in non-thermal emission. For this reason, plerionic remnants are also commonly known as “pulsar wind nebulae”. It is believed that the TeV emission in plerions is a result of the pulsar wind electrons (or protons) inverse-Compton

scattering local seed photons. The Crab Nebula is the most famous of all TeV plerions and has been reliably detected by all IACT experiments. However, the latest generation of IACTs have successfully detected several new plerionic supernova remnants, an example of which is the remnant MSH 15-52 ((Aharonian et al., 2005b)) detected by the H.E.S.S. group in 2005 (figure 1.15 left).

1.2.3 Shell Type Supernova Remnants

Unlike plerions, shell-type supernova remnants are generally very large, extended nebulae which are powered not by active pulsars at the center of the nebula, but rather by the shocks from the original supernova traveling through the interstellar medium. Although the mechanism for production of TeV gamma-rays within shell-type remnants is still not clearly known, it is believed that electrons will undergo first order Fermi acceleration at shock fronts and subsequently inverse-Compton scatter ambient seed photons to TeV energies resulting in the gamma-rays observed by IACTs. This is a natural solution since the energy spectra of TeV gamma rays coming from shell type supernova remnants is consistent with a powerlaw and first order Fermi acceleration results in a population of electrons with energies described by a power law distribution:

$$\frac{dN}{dE} \propto E^{-\alpha} (\alpha > 2) \quad (1.6)$$

An alternate model would suppose that instead of electrons, the shock acceleration may power a population of protons which then interact with interstellar matter to create gamma rays via hadronic interactions (similar to the one proposed for TeV emission from AGN). If this is indeed the case, then shell type supernova remnants would represent an ideal candidate for high energy cosmic ray production sites. Currently, spectral analyses of detected shell type supernova remnants by IACTs are not able to conclusively rule out either the hadronic or the leptonic models (Lemoine-Goumard et al., 2005).

1.2.4 High Mass X-ray Binaries

Since TeV emission from a high mass X-ray binary (namely LS I +61 303) is the focus of this work, a detailed description of the properties of X-ray binary systems will be delayed until chapter 4. In brief, high mass X-ray binaries (HMXBs) are composed of a pairing of a massive main sequence star (O or B) with a compact object (neutron star or black hole). HMXBs are singled out for their periodic outbursts in the X-ray band which usually have some correspondence to the orbital parameters of the system. There are two flavors of HMXBs: binary pulsars and microquasars. Binary pulsars are the pairing of a pulsar in orbit around the main sequence star. In this model,

1.2. HIGH ENERGY GAMMA-RAY SOURCES

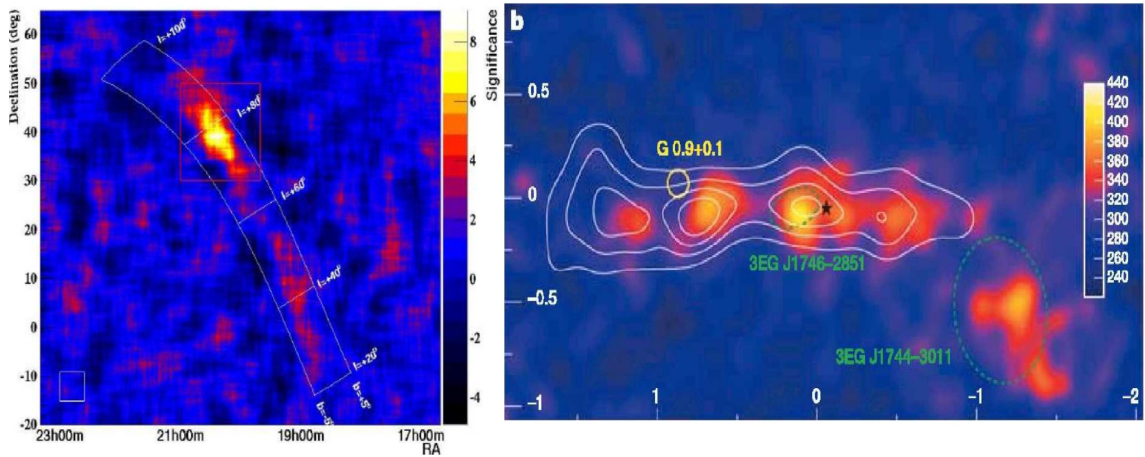


Figure 1.16: The Milagro diffuse emission from the Cygnus region (left) and the H.E.S.S. galactic center diffuse emission in galactic latitude and longitude (right). The H.E.S.S. map shows the emission after subtraction of the signals from SgrA* and a local supernova remnant G0.9+0.1. Also shown (in green contours) are the locations of several EGRET unidentified sources. Maps taken from Abdo et al. (2007a) and Aharonian et al. (2006b).

high energy emission results from interactions between the pulsar wind and the dense equatorial wind of the massive main sequence star. The microquasar scenario for HMXBs supposes that the system is composed of either a neutron star or black hole which accretes matter via either Roche lobe overflow or stellar wind loss. This loss of material from the main sequence star is then fed onto an accretion disk around the compact object. Changes in the accretion rate can cause the formation of a radio loud jet. In this scenario, TeV emission is generated by high energy electrons in the jet up-scattering stellar UV photons. The H.E.S.S. detection of the binary pulsar PSR 1259-63 (Aharonian et al., 2005c) stands as the first concrete detection of a TeV binary system by an IACT. This was followed quickly by the detection of the (assumed) microquasar LS 5039 (Aharonian et al., 2005d). These detections (as well as other TeV binary detections) will be discussed in greater detail in chapter 4.

1.2.5 The Galactic Center

The region (first claimed to be a detected TeV source by the CANGAROO-III collaboration (Tsuchiya et al., 2004)) near the supermassive ($\sim 10^6 M_{\odot}$) black hole SgrA* has been detected by both the Whipple (Kosack et al., 2004) and H.E.S.S. (Aharonian et al., 2004b) experiments at a significance of $3.7\sigma (>2 \text{ TeV})$ and $>10\sigma (>165 \text{ GeV})$ respectively. The exact nature of the emission mechanism is unclear, however, it has been postulated that the TeV emission may result

from either curvature radiation (Aharonian et al., 2004b) or from shock acceleration of particles as stellar material is accreted onto the SMBH.

1.2.6 Galactic Diffuse Emission

Following up on the satellite observations of extensive diffuse gamma-ray emission throughout the galaxy, ground-based experiments have made observations in the TeV range searching for evidence of regions of diffuse emission in various parts of the galaxy. The Cygnus region (reported by EGRET to be the brightest gamma-ray region in the Northern Sky (Hartman et al., 1999)) is particularly active with diffuse emission detected by the Milagro (Abdo et al., 2007b) experiment. Milagro detected a signal in this region, over a 5° extension, of a 2 Crab flux above 3 TeV at a significance of 9.1σ . The TeV emission is thought to be possibly associated with OB star rich regions which are potential particle acceleration sites. The galactic center ridge has also been detected as a hot spot of diffuse TeV emission by the H.E.S.S. collaboration (Aharonian et al., 2006b). In their survey of the galactic plane, the detected diffuse emission traces the known positions of CO emission from molecular clouds which are believed to be possible sites of cosmic ray interaction.

1.2.7 Unidentified Sources

In their survey of the galactic plane, the H.E.S.S. group detected more than 15 TeV point sources which have no counterparts at other wavelengths and are not readily identified with any star or stellar structure. The most heavily studied of these so called “dark accelerators” is TeV J2032+4130. The source, which has been detected by both HEGRA (Aharonian et al., 2002) and Whipple (Konopelko et al., 2007), appears to be very strange in behavior with no two detections in agreement over the exact location or basic morphology (one or two sources in the field of view). Although this source has been possibly associated with the nearby microquasar Cygnus X-3 as well as the star forming region Cygnus OB2 (a region of dense O and B stars thought to possibly emit TeV gamma-rays through stellar wind interactions), the exact nature of this source is yet to be determined. It is possible (through increased observations in radio and X-ray) that the unidentified TeV sources along the galactic plane will be eventually associated with “normal” TeV accelerators such as microquasars or other known galactic sources. However, it is also possible that their presence indicates a new class of unknown accelerators.

1.2.8 Possible TeV Sources

Although currently undetected by any IACT, there are several classes of objects which may emit TeV gamma-rays.

Gamma-Ray Bursts

Gamma-ray bursts (GRBs) are the most powerful explosions detected by any scientific instrument. These brief, powerful flashes of gamma-rays will (for a few seconds or minutes) outshine their host galaxy significantly. Although first detected by the military in the 1960s, gamma-ray bursts were not extensively studied until the 1990s by the BATSE satellite. The interest in GRBs exploded in 1997 when the Beppo-SAX (Costa et al., 1997) satellite instrument, for the first time (due to more accurate source reconstruction), conclusively proved (through connections with optical afterglow studies) that these extreme explosions were originating from cosmological distances. Although these events are readily detected at MeV energies by satellites, there has yet to be a detection of a GRB in the TeV regime. Modern IACTs are linked to a Global Coordinate Network (GCN) which receives GRB alerts from satellites such as SWIFT (and soon to be GLAST) so that IACTs can perform TeV observations within a short time span after the GRB is detected at MeV energies. Several papers detail upper limits on TeV GRB observations (Horan et al., 2007; Bastieri et al., 2007) and it is generally expected that with the increased sensitivity to GRB observations that GLAST will provide, IACT arrays are soon to move into the realm of regular GRB observations.

Dark Matter

The most promising (particle) candidate for a solution to the dark matter problem is provided by the supersymmetric extension of the standard model of particle physics. Supersymmetry offers an elegant solution to the “hierarchy problem” in particle physics (i.e. why is the Planck scale so much larger than the weak scale?) by hypothesizing an entirely new class of (as of yet undiscovered) particles. One of these particles is known as the “neutralino”(or χ^0) and certain models predict both a mass and cosmological abundance that would fit in well with the requirements for the dark matter problem. The χ^0 has the peculiar property of being its own antiparticle, thus, when it comes into contact with another neutralino, it mutually annihilates. This annihilation is of particular interest to gamma-ray astronomy as one of the channels for annihilation involves the process:

$$\chi^0 + \chi^0 \rightarrow \gamma\gamma/Z\gamma \quad (1.7)$$

where Z represents a Z boson. Both of these processes result in a gamma-ray signal with the exact rest mass energy of the χ^0 . Since some (out of literally thousands) of the supersymmetric

models involved do predict a χ^0 mass in the range above 100 GeV, this line signal could be observed by IACTs (see Bergstrom et al. (1998) for a review of the detectability of neutralino annihilations). Although the channel above would result in a “line” emission signal which would be a very obvious excess in the energy spectrum of a dark matter target, the cross section for this process is very low. More likely is the process of “cascade” emission from neutralino annihilations where the χ^0 self-annihilates into a quark/anti-quark final state:

$$\chi^0 + \chi^0 \rightarrow \bar{q} + q \quad (1.8)$$

These quarks pair would then decay into neutral pions which can in turn decay into TeV gamma rays. Since the gamma rays resulting from this process have a range of energies, the signal from such an annihilation process would be a small excess “bump” below the χ^0 mass in the TeV energy spectra of a dark matter target. This excess would be extremely hard to distinguish from the overall energy spectra, however, it is still a viable option for detecting the neutralino.

Although the vast majority of supersymmetric models are grossly underconstrained, the place to look for these χ^0 annihilations would naturally be at the center of mass of large structures. Therefore, the center of our own galaxy, the center of other galaxies, and the center of galactic clusters all make reasonable targets for dark matter annihilation observations. Currently however, no definitive detections have been made although upper limits have been placed on χ^0 annihilation within the galactic center by HESS and within the globular cluster M15 by Whipple observations (Horns et al., 2007; LeBohec et al., 2003). Although a relatively long shot, the indirect detection of dark matter would be a considerable milestone in physics and, as such, it is one of the top priorities for observations with VERITAS.

Starburst Galaxies

These galaxies are very dense galaxies which are believed to be undergoing very high rates of massive star formation and consequently, very high rates of supernova explosions. This has led to the belief that these galaxies may be viable sources of TeV gamma rays due to the large volume of energetic supernovae. Although a tentative detection of the starburst galaxy NGC 253 was reported by the CANGAROO collaboration (Itoh et al., 2003), it was later withdrawn when the H.E.S.S. collaboration (operating at a much higher sensitivity) observed NGC 253 and did not detect it (Aharonian et al., 2005e). However, upper limits from the HESS result as well as several Whipple upper limits on starburst galaxies (Nagai, 2004) still do not rule out the possibility of starburst galaxies being detectable targets for the current generation of IACTS.

Chapter 2

The Imaging Atmospheric Cherenkov Technique

It will most likely impress future science historians to consider the rapid development of the field of ground-based gamma-ray astronomy: from its outset it has been a science dominated by extremely clever people using very subtle facets of nature to gain what they seek. Although this could most likely be said of any branch of physical science, the advances made by other high-end fields of physics have been, in their principle philosophy, relatively simple. Particle physicists smash things together and look at the results; if they want to advance things along, they smash heavier things together at higher energies. Mainstream astronomers collect light: to advance they need bigger telescopes with bigger collection areas. Ground-based gamma-ray astronomy has required an altogether more elegant approach to a seemingly intractable problem: how do you observe high energy gamma rays from the ground when the atmosphere is almost totally opaque to high energy gamma rays?

It is known from the early experiments of Galbraith, Jelly, and Porter (Galbraith and Jelley, 1953) that high energy particles will create particle cascades as they enter the atmosphere. More specifically, high energy particles and photons initiate a chain reaction of particle production and scattering when they come into contact with the medium of the atmosphere. This chain reaction, or “Extensive Air Shower”, will produce a visible signal of what has happened. This visible signal comes in the form of extremely brief pulses of near-UV light produced by a process known as the Cherenkov effect. By observing these brief pulses of light, ground-based instruments can not only detect gamma rays, but they can also reconstruct (to a high degree of accuracy) the energy and trajectory of the gamma ray.

Although this may seem straight forward on the face of it, there is actually an amazing real-

ization possible: By observing a nanosecond timescale pulse of light from over 10 km away in the atmosphere, we are able to observe radiation that was created (in the case of AGN) hundreds of millions of years ago. After all this time, at the very last moment of their existence, they create an amazing fireworks display of light and energy that is almost completely absorbed in the tapestry of the night-sky background. This chapter will serve as a comprehensive explanation of how we can observe this fireworks display to conduct a postmortem reconstruction of the gamma ray's life: what it was like and where it came from. In short, how we learn from the last 10^{-9} seconds about the previous 10^{15} seconds that came before it.

2.1 High Energy Interactions In The Atmosphere

It is useful, before proceeding any further, to give a brief review of the electromagnetic processes that take place as high energy particles and radiation enter the Earth's atmosphere. There are six important processes to consider, three relating to photon energy loss and three to charged particles. They all play a significant role in the development of our chief target of interest: extensive air-showers.

Pair Production: The fundamental vertex of Richard Feynman's theory of quantum electrodynamics joins a single photon with an electron-positron pair. While this vertex in some form or another is used in almost all basic QED diagrams, by itself the process of vacuum pair production is not allowed by momentum conservation. For a free photon to pair produce into an electron-positron pair, it must be in the presence of an electric field. In our case (the atmosphere) the electric field is provided by the presence of an atomic nucleus. The incident photon must have a minimum energy of 1.02 MeV (twice the electron rest mass) in order for this process to take place. In our atmosphere, the cross section for pair production dominates at photon energies > 10 MeV (see figure 2.1), therefore it is the dominant process that we are concerned with in analyzing high energy gamma rays as they enter the atmosphere.

Compton Scattering: While the inverse of this process is important for most TeV gamma-ray production mechanisms believed to take place in astrophysical objects, its original form is more important as the gamma ray interacts with the atmosphere. This process occurs when an incident gamma ray interacts with a loosely bound atomic electron. The incident gamma ray will donate some of its energy to the electron, freeing it from its orbit. The gamma ray energy is lowered by this process as well as having an altered trajectory. This process is dominant for photon energies of $0.1 \text{ MeV} \lesssim E_\gamma \lesssim 10 \text{ MeV}$. Below this energy, the photoelectric process (in which the incident gamma ray is completely absorbed by the atom as it kicks out a higher shell electron) dominates.

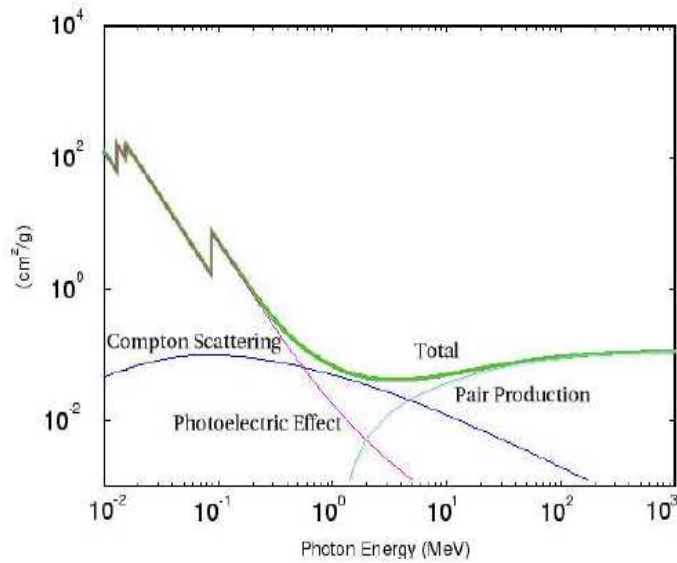


Figure 2.1: A plot of the cross section as a function of incident photon energy for transmission through the atmosphere. As can be seen, pair production dominates at higher energies, while photoelectric absorption dominates at lower energies. Taken from Gammell (2004).

However, since the energy at which this process dominates is lower than the region at which ground based gamma-ray telescopes operate, it is not considered relevant for our description of gamma-ray initiated air showers.

Bremsstrahlung: German for “braking radiation”, bremsstrahlung refers to the electromagnetic process which occurs when a charged particle encounters an electric field. The most useful example to give is that of an electron travelling in the vicinity of an atomic nucleus or electron shell; the electron will emit radiation as its path is altered by the electric field. The wavelength of the emission is determined by the energy of the incident electron and the strength of the electric field it encounters and extends into the gamma-ray regime for the charged components of extensive air showers described in this chapter. Bremsstrahlung is also the dominant electromagnetic loss mechanism for higher energy charged particles as they enter the atmosphere.

Coulomb Scattering: Charged particles in the atmosphere can also undergo Coulomb scattering, which is the process by which incoming charged particles will lose kinetic energy by interacting with nuclei and giving them a kinetic “kick”. This loss mechanism dominates below the energy range where incoming electrons have enough kinetic energy for bremsstrahlung processes, and above the energy limit for ionization.

Ionization: The end stage energy loss process for a charged particle is that of ionization. Incident electrons will remove outer shell atomic electrons. This process is highly energy consuming;

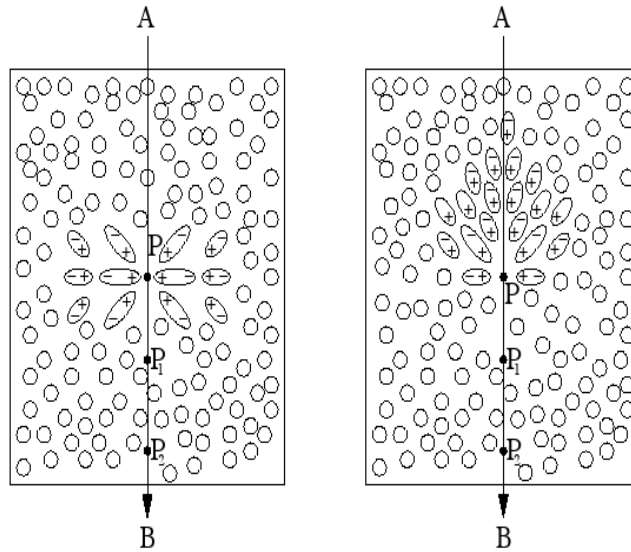


Figure 2.2: How a particle with $v > c$ will generate a coherent electromagnetic wave as described in the text. Figure taken from Horan (2001).

therefore, once the majority of an air shower contains particles whose ionization losses dominate, then the air shower is considered to have run its course and the number of active particles in the air shower starts to drop dramatically.

2.2 Cherenkov Radiation

The process responsible for the ability to monitor the development of the air shower in the atmosphere is known as the Cherenkov effect. This effect was first studied in a series of experiments by Pavel Alekseyevich Cherenkov in 1934 (Cherenkov, 1934) in which he bombarded liquids with β -particles and observed the resulting blueish light being emitted. This effect was described in 1937 by Frank and Tamm (Frank and Tamm, 1937) who explained the radiation by the presence of superluminal particles travelling through a dielectric medium. Although relativity forbids massive particles from travelling faster than light in a vacuum, light will travel slower through a medium:

$$v_{light} = c \longrightarrow v_{light} = c/n \quad (2.1)$$

Where n is the refractive index of the medium in question. Frank and Tamm observed that if a charged particle travels through that same medium with a velocity greater than the local speed of light in the medium, it will radiate light due to the effects of its polarization on the medium in which it travels.

Consider a dielectric gaseous medium with refractive index n . As a charged particle travels through this medium it will polarize the surrounding molecules to keep charges aligned (see figure 2.2). As the particle moves past, the molecules will relax and return to their previous state. Since the polarizing and relaxing effect is symmetric about the travelling particle, no coherent radiation is produced. However, if the charged particle is travelling faster than the local speed of light in the material, the particle will be moving faster than the electromagnetic field that it creates. This will form an asymmetry pointing in the particle's direction (again, see figure 2.2) When the particle leaves the area, the asymmetric polarization will relax resulting in an electromagnetic wavefront being produced. This wavefront is known as Cherenkov radiation.

The properties of the radiation are quite easily derived from geometrical considerations. Shown in figure 2.3, a particle is moving superluminally at velocity βc . Starting at the left side of the figure, it emits a Cherenkov wavefront at an angle θ with respect to the direction of motion. After a time t , the particle has traveled a distance βct while the wavefront has traveled a distance $\frac{ct}{n}$. From this we can derive that the Cherenkov angle is:

$$\cos\theta = \frac{1}{\beta n} \quad (2.2)$$

For a minimal condition, we can set $\theta = 0$ which can give us the minimum particle energy that will result in Cherenkov radiation for a given refractive index:

$$E_{threshold} = \frac{m_p c^2}{\sqrt{1 - \frac{1}{n^2}}} \quad (2.3)$$

It is important to note that since the radiation comes from the surrounding medium and not from an alteration of the motion of the particle, this emission angle will stay constant through the particle's trajectory in the same density of atmosphere. This will be an important consideration when taking into account the effect of local muons on extensive air shower observations. For the air showers described in this chapter, the spectrum of Cherenkov light produced by the particle populations under consideration peaks in the UV band. This feature can be capitalized upon by tailoring the detection equipment to be more sensitive to UV wavelengths (see section 2.5).

2.3 Gamma-ray Initiated Extensive Air Showers

As was stated in the introduction to this chapter, extensive air showers initiated by gamma-ray primaries will behave much the same as those initiated by cosmic ray primaries. However, there are a few very important differences between the development of the two classes of air showers.

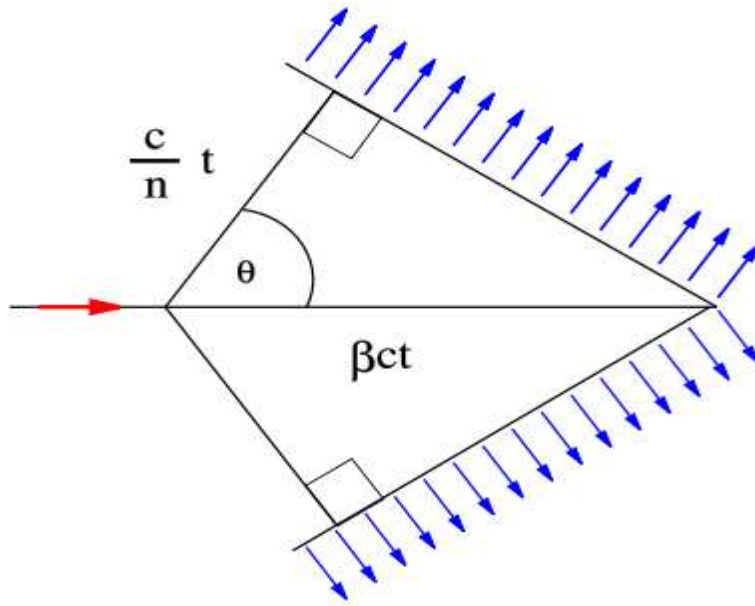


Figure 2.3: A schematic of the coherent Cherenkov wavefronts emitted by a particle traveling at a velocity $\beta c > c$ as described in the text.

These differences turn out to be critical to our ability to discriminate the Cherenkov light coming from cosmic ray air showers and those from gamma-ray primaries. However, before examining these differences, it is useful to understand what happens when a very high energy gamma ray enters the Earth's atmosphere.

Since the photons of interest have energies >100 GeV, our principal process of concern is pair production. Pair production has a radiation length of 37.7 g cm^{-2} (compared to the total atmospheric depth of $\sim 1000 \text{ g cm}^{-2}$) resulting in the primary interaction altitude of ~ 20 km above sea level. Since pair production is the relevant energy loss process for primary particle with $E > 50$ MeV, when the very high energy gamma-ray produces an electron-positron pair each of these particles will satisfy the minimum energy criteria for Cherenkov emission (21 MeV per particle via equation 2.3). Both the free electron and positron will Bremsstrahlung scatter creating another 2 free gamma rays. Each of these gamma rays will now continue on to pair produce again forming more electron-positron pairs which will then re-radiate gamma rays via Bremsstrahlung. Due to the angular spread in the trajectories of the secondary particles described above, the shower is now developing laterally as well as longitudinally (see figures 2.4, 2.5) and all of the electron-positron pairs produced thus far have radiated Cherenkov radiation which will form a distinctive pattern of light travelling towards the ground. This process of exponential shower development will continue until the average energy of the charged leptons involved reaches a critical value of 84.2 MeV. It is at this energy that the electrons involved in the shower will start to lose energy predominantly

Table 2.1: A table showing the resultant properties of gamma-ray air showers of several different energies. Data taken from Weekes (2003).

E_γ	Max Height(km)	N_{max}	N_{sea}	$N_{elevation}$	ρ_{sea}	$\rho_{elevation}$
100 GeV	10.3	130	0.04	1.4	4.6	7.6
1 TeV	8.4	1100	3	60	74	130
10 TeV	6.8	10,000	130	1700	1100	1700

to ionization as opposed to radiative processes. This point is known as the “shower maximum” and represents a limit to the lateral development (and thus a quantifiable characterization of the resulting Cherenkov light from the shower). Other particles closer to the original primary trajectory will still contribute to the shower development, but their numbers decrease rapidly resulting in the shape shown in figure 2.4.

What Cherenkov emission properties can be extracted from this? Shown in Table 2.1 are some examples of the resultant particle and photon density coming from gamma-ray showers of different primary energy. In this table, “Max height” represents the height in the atmosphere at which shower maximum is achieved, N_{max} represents the number of electrons produced at shower maximum, N_{sea} and $N_{elevation}$ represent the number of surviving particles at sea level and mountain elevation (2.3 km) respectively, ρ_{sea} and $\rho_{elevation}$ represent the Cherenkov photon density in γ/m^{-2} at sea level and mountain elevation respectively. As is expected, higher energy gamma rays produce showers with more particles and photons than lower energy showers. Also, it is obvious from Table 2.1 that placing gamma-ray observatories at higher altitudes is beneficial to collecting more photons, since more are available at those altitudes. However, there is a physical limit (~ 3 km) to how high an IACT should be placed in the atmosphere due to the fact that the light created by the showers will not create as large of an observable pool on the ground at very high altitudes (see below).

Most ($\sim 90\%$) of the Cherenkov light from an extensive air shower falls within a pool of light centered around the shower axis of radius 120m. Since the lower sections of the air shower will be in a denser region of the atmosphere, the Cherenkov angle will be greater and thus the light distribution will be biased towards the edge of the light pool (see figure 2.4). Although all parts of the air shower will contribute Cherenkov light, only 25% of the light is from the region of the shower between the primary interaction site and 10km elevation. 50% of the light comes from a 4 km long cylindrical volume from 10 km to about 6 km (containing the shower maximum), with the remaining 25% coming from emission below about 6 km which is more sporadically produced as the light produced at higher altitudes due to low statistics of the particles that have survived

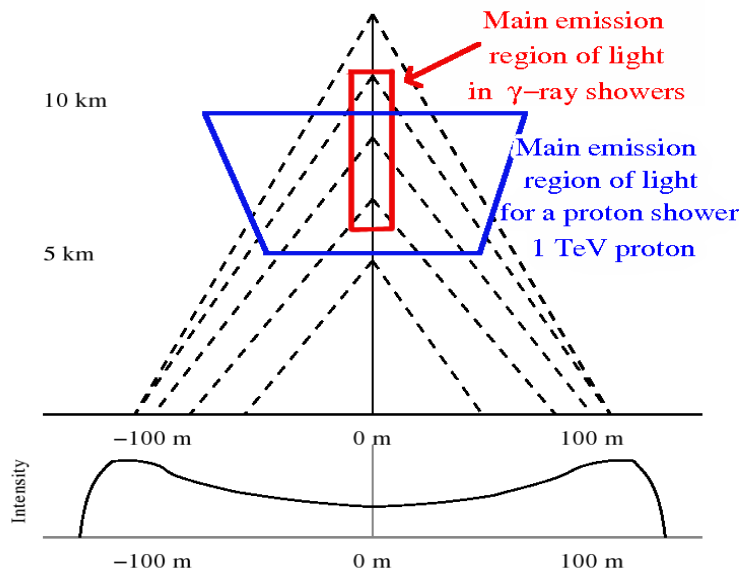


Figure 2.4: The light distribution from a typical extensive air shower. The regions where the majority of detected light from gamma-ray and hadronic showers come from are shown in red and blue, respectively. The bottom shows the light intensity distribution on the ground from an air shower, note that the edges of the light pool are enhanced due to the Cherenkov angle becoming larger with increasing atmospheric index (n) during later stages of the shower. Figure modified from Kosack (2005).

to this altitude (Weekes, 2003). The cylindrical region of diameter ~ 10 m containing 50% of the light turns out to be the most important region for our purposes since it will primarily determine many of the important properties of the image formed of the shower in gamma-ray telescopes. More specifically, the distribution of the light emitting regions is slightly different for a hadron initiated air showers, which is the key to the ability to distinguish these showers from the desired gamma-ray showers.

2.4 Cosmic-Ray Initiated Extensive Air Showers

The term *Cosmic ray* refers to any charged particle coming from space (both leptons and hadrons). However, since air showers initiated by cosmic electrons result in very small Cherenkov signals and therefore only pose a serious problem at energies below 50 GeV (below the sensitivity of the ground-based telescopes described in this work), we will not consider their signal to be a significant part of our background noise. Furthermore, although the Cherenkov emission from incoming heavier ions (such as iron) will create Cherenkov signals, their contribution is small

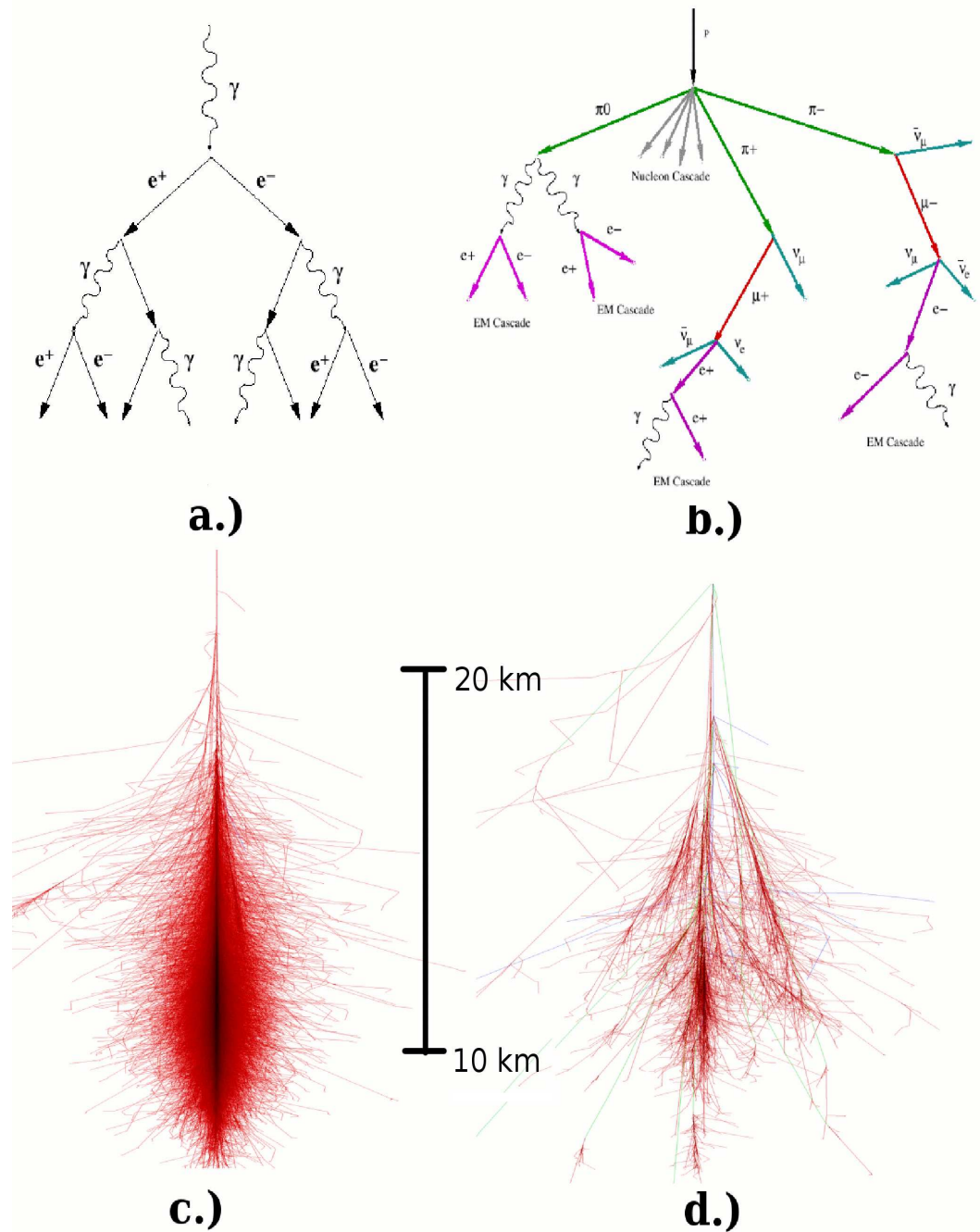


Figure 2.5: Various figures showing the properties of air shower development for gamma rays and cosmic rays. a.),b.) show the various physical processes at play as described in the text for a gamma-ray shower and cosmic ray shower, respectively. c.),d.) are the result of Coriska simulated particle tracks (*red = photon, e^- , e^+ ; green = μ^+ , μ^- , μ^0 ; blue = hadrons*) for a 100 GeV gamma-ray air shower and 100 GeV cosmic ray air shower respectively. Note that the gamma-ray shower is much more cohesive and laterally confined. a.) taken from Kosack (2005),b.) taken from Jelley (1958), c.),d.) taken from the CORSIKA website (Schmidt, 2007).

enough to ignore. Therefore, the principal source of background for ground-based gamma-ray observatories is hydrogen and (to a lesser extent) helium ions. The contribution from these ions is especially problematic due to two factors. The first is that, due to galactic magnetic fields twisting their trajectory, their flux is isotropic and homogeneous. If this was not the case then we could, in theory, compensate for the cosmic-ray contribution from a set part of the sky in offline analysis. Secondly, for a field of view of 2.2° (the f.o.v. of the Whipple 10 m telescope) their flux is roughly 10^3 times the flux of the strongest known source of high energy gamma rays, the Crab Nebula (Weekes, 2003). This poses a serious problem for our ability to distinguish and discover high energy gamma-ray sources against this seemingly overwhelming background. Luckily, the characteristics of cosmic-ray induced air showers that are recognizable in the resultant Cherenkov emission are sufficiently different from those present in gamma-ray shower. These differences allow the reliable identification of gamma-ray air showers on a statistical basis.

The primary interaction process for free protons in the atmosphere is spallation with other protons (located in atmospheric nuclei) which passes along about 1/3 of the primary energy into pions with the remaining energy deposited into secondary nucleonic particles. Depending on the charge of the pions produced, several different processes can occur at this point. Neutral pions (π^0) will quickly decay into two high energy gamma rays which then take part in the electromagnetic chain reactions as described in the previous section for gamma-ray primaries. Charged pions (π^+/π^-) will decay into muons (μ^+/μ^-) and muon neutrinos. These charged muons can either decay into electrons and neutrinos/anti-neutrinos, or can traverse the length of the atmosphere if they are sufficiently energetic. During this process, it is crucial to recognize that all of these primary and secondary particles will be emitting Cherenkov radiation creating a similar light pool on the ground to gamma-ray showers. Fortunately, since the secondaries involved in cosmic-ray air showers will be of much higher mass (>100 MeV), their trajectories will have much more transverse momentum imparted to them (see figure 2.5). This means that cosmic-ray air showers will have a much greater angular extent than gamma-ray air showers. Therefore, the Cherenkov light emitted by particles in these showers will also have a much greater angular spread. Also, due to the air shower involving particles that may traverse the atmosphere to ground level, the resultant temporal structure will be different than that of a purely electromagnetic air shower, since penetrating “local” particles will produce light arriving before the light produced from secondary products. This results in a double peaked structure for the light arriving from hadronic air showers (see figure 2.6).

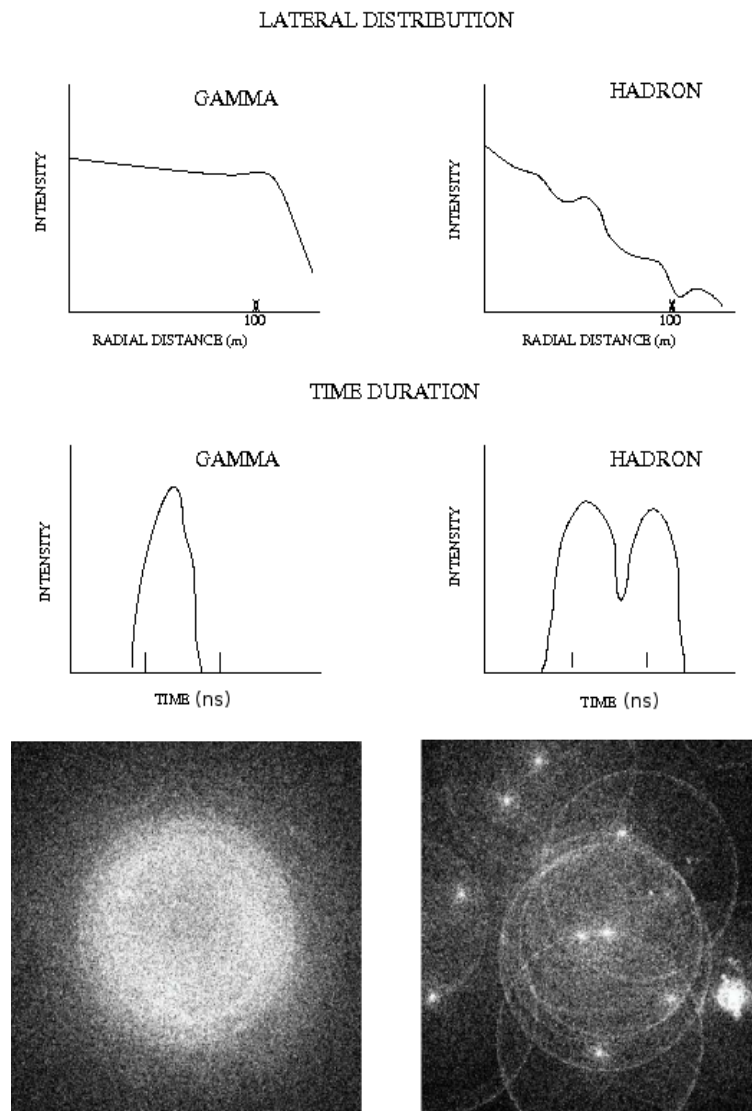


Figure 2.6: Here are shown some properties of the Cherenkov light from gamma-ray showers versus cosmic-ray showers. As can be seen, the light pool formed on the ground is much more erratic for hadronic showers (top row). Also, because of the presence of penetrating air shower particles in hadronic showers, the temporal distribution of light on the ground shows a significantly different structure than gamma-ray air showers (middle row). The bottom row shows the Cherenkov photon distribution on the ground from a 100 GeV gamma-ray shower (left) and a 100 GeV proton shower (right). Figures adapted from Weekes (2003) and Cogan (2007)

2.5 Implementation of the Technique

As was described in the previous section, the main factor that initially limited the development of this field is that there exists a nearly overwhelming background due to cosmic-ray air showers. However, this background is small when compared to the contribution of the light coming from the night-sky background. Over a field of view which would encompass the strongest known high energy gamma-ray source (the Crab nebula), the night-sky background produces over 10^6 more photons than the Cherenkov signal from the Crab Nebula. This would seem an insurmountable source of background. However, by taking advantage of two key features of Cherenkov emission, progress towards effective noise reduction is possible.

First, since Cherenkov pulses occur over a very short time frame (corresponding to the lifetime of the parent airshower, or 5-10 ns), by choosing a short integration time of around 25 ns, as well as a field of view comparable to the angular extent of the Cherenkov pulse ($\sim 1^\circ$) a usable data window is recovered. Over this time frame and angular extent a 1 TeV gamma-ray air shower produces about 100 photons/m⁻² within the light pool, whereas the night-sky background will only produce about 1-2 photons/m⁻² over this integration time, which is more than manageable (Weekes, 2003). Secondly, the Cherenkov light produced by air showers peaks in a very specific electromagnetic wavelength band (350-500 nm or UV-blue wavelengths), so by catering observations to have higher sensitivity in this waveband, it is possible to reduce the noise contribution coming from the night-sky background outside of this band.

Since all that is required is to merely sample part of the light pool and not contain it, it is possible to use a telescope with a large enough mirror area to collect sufficient light just placed “somewhere” within the light pool. The next step is to focus the light onto a photomultiplier device (PMT) with peak sensitivity in the 350-500 nm range. These PMTs are attached to counting electronics fast enough to read out data streams on a several nanosecond timescale. This is the fundamental design of an atmospheric Cherenkov telescope that has not been radically changed since the initial experiments by Galbraith and Jelley.

A given air shower will produce a Cherenkov photon flux at the camera of $C(\lambda)$:

$$C(\lambda) = kE(\lambda)T(\lambda) \quad (2.4)$$

Where k is a constant encompassing factors such as detector geometry and mirror structure, $E(\lambda)$ is the spectrum of Cherenkov light emitted, and $T(\lambda)$ represents the transmission of the atmosphere limited by factors such as ozone absorption, Rayleigh, and Mie scattering. The total number of photons S detected by the camera over a wavelength range ($\lambda_1 \rightarrow \lambda_2$) is then:

$$S = \int_{\lambda_1}^{\lambda_2} C(\lambda)\eta(\lambda)A\Omega d\lambda \quad (2.5)$$

where $\eta(\lambda)$ represents the quantum efficiency of the PMTs as a function of wavelength, A is the mirror collection area, and Ω is the solid angle subtended by the camera. Similarly, the total number of photons from the night-sky B is then:

$$B = \int_{\lambda_1}^{\lambda_2} B(\lambda)\eta(\lambda)A\Omega\tau d\lambda \quad (2.6)$$

where $B(\lambda)$ is the spectrum of night-sky background photons. This results in a signal to noise ratio of

$$S/N = S/\sqrt{B} = \int_{\lambda_1}^{\lambda_2} C(\lambda)\sqrt{\frac{\Omega A \eta(\lambda)}{\tau B(\lambda)}} d\lambda \quad (2.7)$$

The minimum energy at which a Cherenkov pulse is detectable above the night-sky background is proportional to the inverse of this ratio:

$$E_{threshold} \propto \frac{1}{C(\lambda)} \sqrt{\frac{\tau B(\lambda)}{\Omega A \eta(\lambda)}} \quad (2.8)$$

Therefore, by maximizing the mirror area A and quantum efficiency $\eta(\lambda)$ while minimizing the integration time τ , the energy threshold will be minimized while simultaneously maximizing the signal-to-noise ratio.

It has been shown that by custom tailoring our observations to detect Cherenkov emission from extensive air showers it is possible to conquer a major source of difficulty in detecting gamma-rays from the ground, i.e. the noise presented by the night-sky background. This, unfortunately, also tailors our observations to include light from cosmic-ray air showers which are much more numerous than gamma-ray showers. To overcome this second obstacle it is helpful to understand what the resulting Cherenkov light from an air shower looks like in the camera plane of the telescope.

2.6 Rejecting Cosmic Rays

In the previous section, it was shown that all that is necessary to detect Cherenkov pulses against the background is a large mirror area which focuses light onto a UV sensitive PMTs attached to fast pulse counting electronics. Today in practice telescopes that accomplish this are typically composed of a tessellated array of mirrors of diameter somewhere between 10-15 m and the PMTs are in the form of a camera composed of many (hundreds of) PMT pixels (see sections 3.1.3, 3.2.3). What does a Cherenkov signal look like to such a telescope? Shown in figure 2.9 are (somewhat idealized) examples of the resultant Cherenkov images formed on a camera plane placed within the

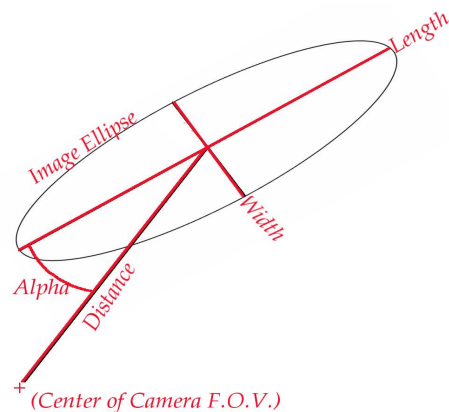


Figure 2.7: Here is shown the graphical definitions of the most commonly used geometric Hillas parameters. The use of these parameters is key in discriminating hadronic air showers from gamma-ray air showers.

light pool of both a gamma-ray air shower and one initiated by a cosmic ray. It is easily seen from this figure (and implied from previous sections) that the gamma-ray images are much more well organized than cosmic ray showers. The first success in codifying these differences was made by Michael Hillas in 1985 (Hillas, 1985). In that work, he developed geometric parameters describing the light distribution of the Cherenkov image, effectively approximating it to an ellipse. Although there were initially more parameters used in the initial formulation of the rejection technique by Hillas (and since then workers in the field have used variations upon these parameters), the most commonly used “*Hillas Parameters*” are the following (shown in figure 2.7). Given a shower image which triggers n pixels, each with camera coordinates x, y and having a PMT signal p the following can be defined:

- *Size*- The 0th order moment, or the total integrated charge of all the pixels taking part in the image.
- *Distance*- The distance on the camera between the center of the field of view and the image centroid (first moment of the image), equivalently $\sqrt{x_c^2 + y_c^2}$. Where (x_c, y_c) are the coordinates of the image centroid.
- *Width*- A second order moment of the image, visualized by referring to the width of the ellipse which parametrizes the image.
- *Length*- A second order moment of the image, visualized by referring to the length of the ellipse which parametrizes the image.

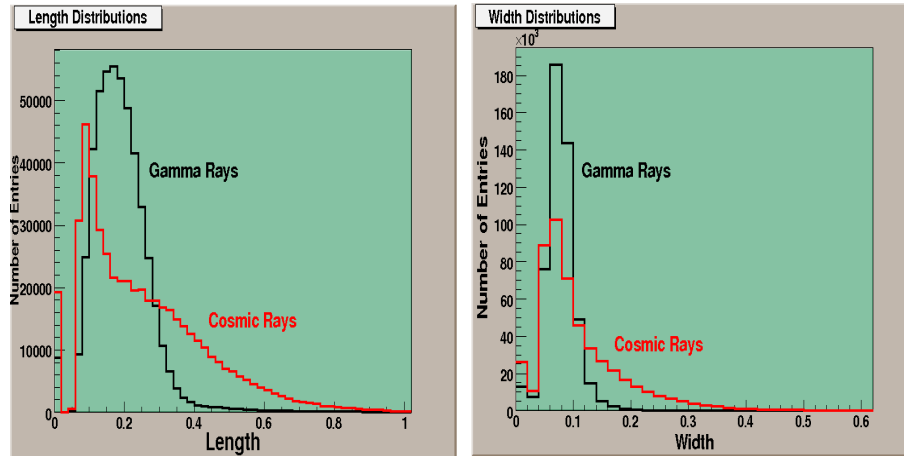


Figure 2.8: Here are shown *length* and *width* histograms for 500,000 Monte Carlo simulated gamma-ray and cosmic-ray showers. The physics is evident in the distributions: gamma-ray showers are much more compact and organized (i.e. tighter distributions). Placing cuts on these values helps to isolate the gamma-ray showers.

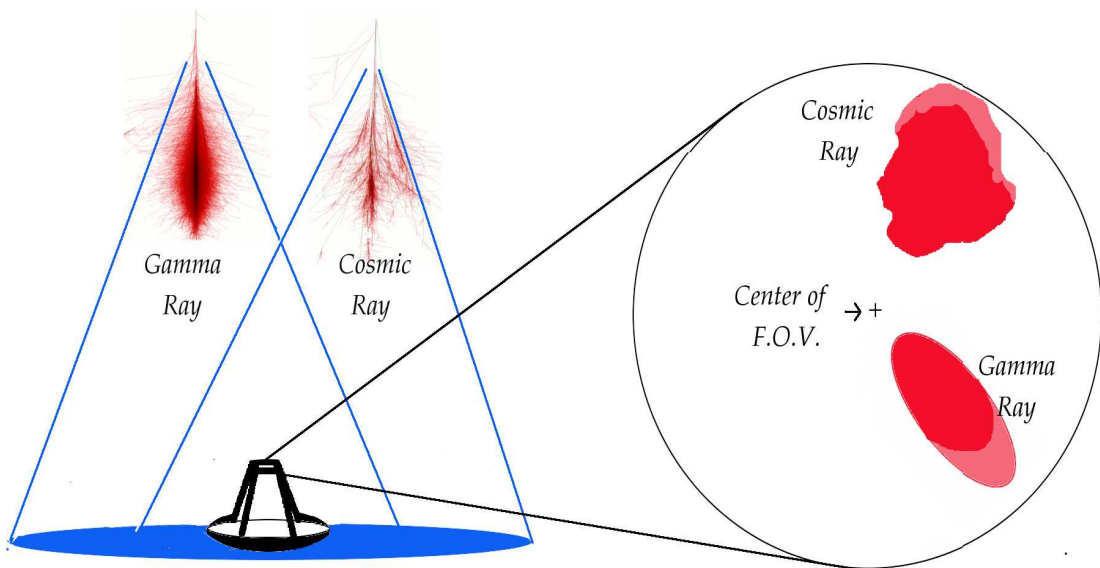


Figure 2.9: Here are shown the differences between gamma-ray and cosmic-ray induced air showers and the geometric differences that result when the Cherenkov light from these showers is collected in a telescope. The gamma-ray shower, due to its greater temporal and spatial cohesion, results in a much more compact and ellipsoid form on the focal plane of the camera. The development of the cosmic-ray shower is more erratic and is demonstrated in the irregular morphology of the Cherenkov light on the camera plane.

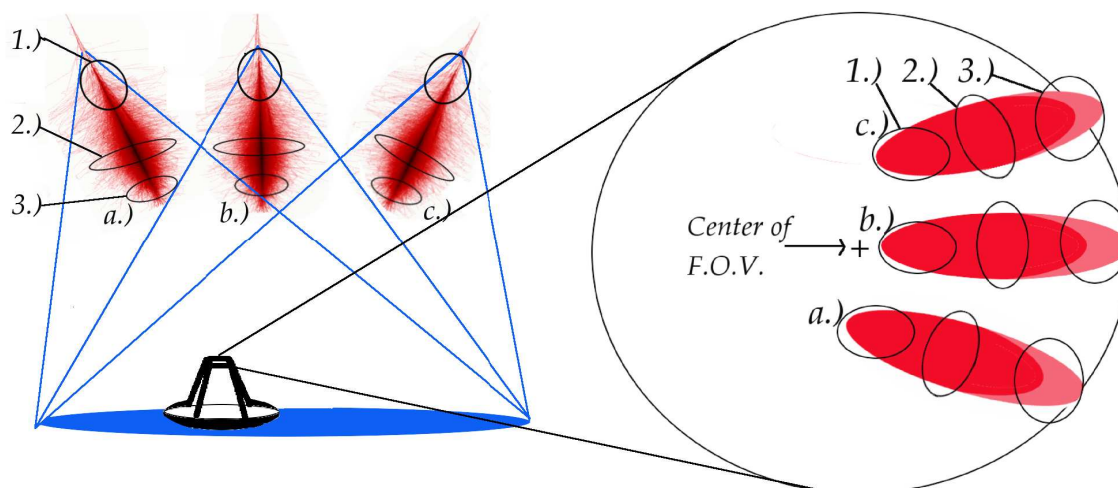


Figure 2.10: A demonstration of the logic behind the α parameter discriminant. Shows that originate from primaries not along the line of sight to the observing target will result in images which do not “point” towards the center of the camera. Also shown are rings representing where corresponding regions of light from the showers fall in the images.

- *Alpha*- The angle between the longer image axis and a line connecting the image centroid and the center of the field of view.

The *length* and *width* parameters will have significantly different distributions for gamma-ray and cosmic-ray air showers and are therefore used as selection criteria in order to eliminate as many hadronic showers as possible. Shown in figure 2.8 are some examples of Monte Carlo simulated distributions for *length* and *width*. The *distance* and *alpha* parameters are used to reject hadronic images that can pass the other two cuts successfully. The *alpha* cut is especially powerful as it only allows images which have good alignment with where they are “expected to be”, in other words, there may be images which pass all other cuts but are not from showers that originate from the direction in the sky that we are observing. This is demonstrated in figure 2.10. When a stereo array is used, this α parameter is modified slightly to a similar parameter more useful for stereo events (θ^2) which will be discussed in section 3.2.10.

2.7 Properties of The Technique: The Benefits of Stereo

There are several technical considerations involved with the technique described above which should be mentioned before proceeding further. The main purpose of mentioning these consider-

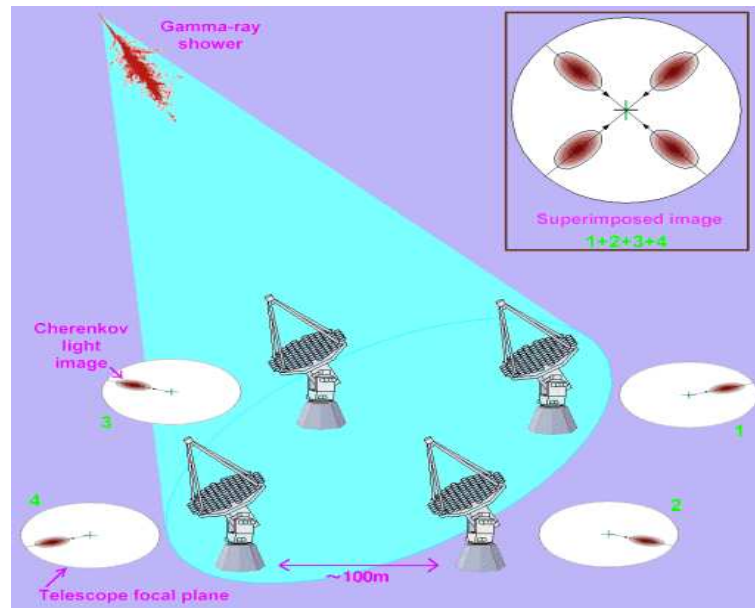


Figure 2.11: An illustration of how a stereo Cherenkov array can improve upon single telescope observations. Instead of having one image axis to reconstruct (which leaves a lot of ambiguity), there are multiple image axes. When these images are superimposed upon the same camera plane, they can more accurately indicate the original shower axis which in turn improves factors such as energy and angular resolution. Figure taken from <http://icrhp9.icrr.u-tokyo.ac.jp>.

ations is to demonstrate why the use of multiple telescopes to form a stereo array is so beneficial.

- Angular Resolution:** This refers to the ability of a telescope to resolve the original direction of the shower primary on the sky. Gamma rays do not deviate in trajectory from their source along their path through space. Furthermore, the development of electromagnetic air showers is tightly bunched laterally. This means that the more accurately that the angle of incidence and impact parameter of the shower core (or the distance at which an extrapolation of the shower's longitudinal axis would meet the ground) are reconstructed, the better we can reconstruct where the primary came from. To aid in this reconstruction, actual recorded shower images are compared to results of Monte Carlo simulated shower images for different shower parameters which give us an measurement of the arrival direction of the shower primary. The use of this technique results in an angular resolution of $\sim 0.1^\circ$ for single telescope observations, however, this measurement can be made more precise, to within $\sim 0.05^\circ$ for stereo observations of air showers from different angles (see next section).

- Energy Resolution:** Another very important property of an imaging Cherenkov telescope is

its ability to determine what energy the gamma-ray primary had, or its *energy resolution*. The more energetic a shower is, the more light it will produce and the brighter it will appear at the camera. This parameter is measured for real data by, again, comparison to the results of Monte Carlo simulations. Its determination will be more precise as more light is collected from the shower. Again, this is improved upon by going to a multiple telescope array which can sample the shower at different regions of the light pool formed on the ground. In addition, the stereo array's ability to determine the shower core position helps in determining the energy of the shower by eliminating the degeneracy over whether a shower might have been bright (and energetic) or the shower core was merely closer to the detector. Typical energy resolutions for single telescope observations (i.e. the Whipple 10m) are of the order of 30% (Mohanty et al., 1998) compared to around 10-15% for a stereo array.

- **Effective Collection Area:** The collection area which determines a telescope's ability to detect air showers is not equivalent to the actual mirror area, but is more of a function of the placement of the telescope within the light pool of diameter ~ 120 m. Therefore, for a 10 m reflector, the collection area is of the order of $\sim 10^5$ m² instead of $\sim 10^2$ m². This collection area will vary depending upon the energy of the shower in question (more energetic showers generate more light which allow easier detection) as well as the elevation of the observations since at lower elevation a gamma-ray air shower will generate a larger light pool on the ground than one at a smaller zenith angle solely due to geometric effects. Multiple telescopes combining their effective areas can generate a larger effective area (depending on the trigger configuration) for the array as a unit, ($\sim 10^6$ m²) for several 10 m scale telescopes placed at distances from each other comparable to the shower light pool scale.
- **Energy Threshold:** Technically, the energy threshold of a Cherenkov telescope is defined as the energy at which the differential rate of reconstructed gamma-ray showers (gamma rays per minute per unit energy) is a maximum. This is a markedly higher value than the telescope trigger threshold which is the energy at which the number of gamma-ray events which trigger the telescope peaks. This threshold, although dependent on factors such as elevation and image cleaning methods, has been traditionally limited for single telescopes by the presence of local muons. As mentioned in the previous section, hadronic cascades in the atmosphere produce energetic muons as byproducts. These particles are weakly interacting (both qualitatively and technically!) and often survive to the ground level. Along the way, due to their high velocity, they will produce Cherenkov radiation. However, since they are single isolated particles and their Cherenkov angle is not altered significantly dur-

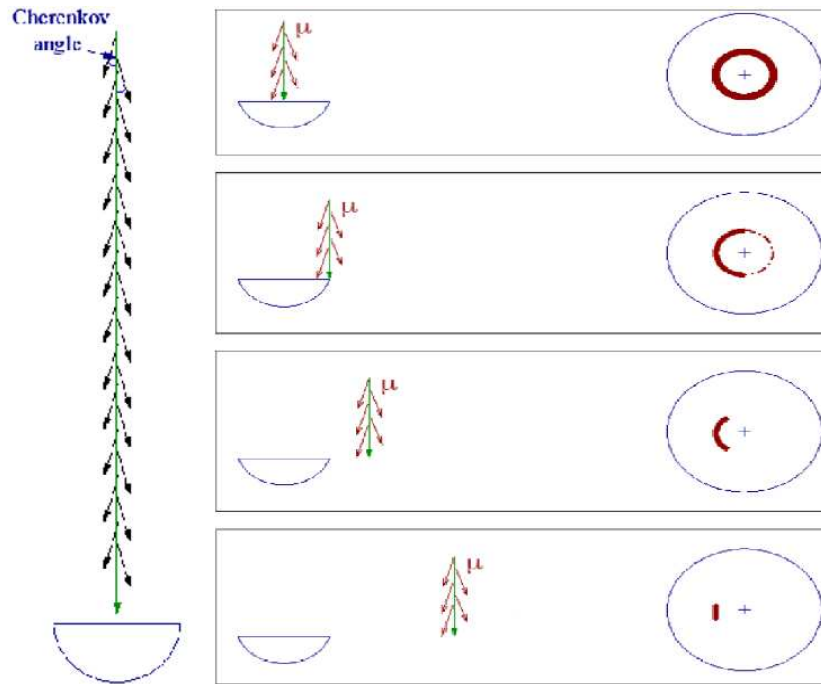


Figure 2.12: Local muons are a problem for single telescope observations due to their ability to mimic low energy gamma-ray showers (see text). The left shows the resulting signal from a muon traveling directly in line with the optic axis of the telescope. On the right is shown how images from these showers appear as the muon arrives further off-axis. Figures adapted from Horan (2001).

ing their trajectory, the resultant image on the ground will be a ring of light instead of an ellipse (see figure 2.12). These concentric rings will appear more similarly to *broken* ring segments the further the muon trajectory is off from the optic axis from the camera. For very far off-axis muon showers, the resulting image will trigger just a few tubes in a row and this mimics low energy gamma-ray showers. For a single telescope, these muon triggers will pass all available cleaning and cutting methods and present an effective wall for single telescope gamma-ray identification at around 200 GeV. However, by going to a stereo array, the muon shower that looks like a gamma ray in one telescope might look like more like the characteristic muon arc in another nearby telescope. The combination of these two images will NOT pass the gamma-ray identification scheme and the muon shower will be rejected. This (along with more accurate shower reconstruction) allows stereo arrays to lower energy thresholds to around 100 GeV.

2.8 Summary

This chapter has covered the basic ingredients necessary to understand the technique of ground based high-energy gamma-ray astronomy, that is, the atmospheric Cherenkov technique. It has covered the fundamental physical processes at play in atmospheric air showers as well as the physics behind Cherenkov emission and how they take place in both gamma-ray and cosmic-ray initiated air showers. After demonstrating the differences between how these types of showers behave, an explanation of how these differences are manipulated in order to identify gamma-rays was given using the setup of modern imaging atmospheric Cherenkov telescopes. After further examining how these telescopes take advantage of the physics of both cosmic-ray and gamma-ray initiated air showers, a short section on the generalized properties of these telescopes was given which identified their important functional characteristics (energy resolution, angular resolution, etc). This also illuminated why it is so advantageous to move towards a stereo array setup instead of single telescope observations. The next chapter will build upon the technique provided in this chapter to explain in more detail the inner workings of both the Whipple 10m telescope and the VERITAS stereo array.

Chapter 3

Technique Implementation: The Whipple 10 m and VERITAS

In the previous chapter, the methods and efficacy of the imaging Cherenkov technique were discussed for a generalized situation, i.e., a large mirror collection area, a pixelated camera composed of UV sensitive photomultiplier tubes, and fast pulse counting electronics. In this chapter, the physical plant of two specific observatories will be examined: the Fred Lawrence Whipple 10 m Telescope and its multiple telescope successor, the VERITAS array. The technologies involved in both of these experiments are very similar; however, there are some key advancements made by the VERITAS design which are an improvement over the Whipple telescope. These advancements involve some cutting edge technological improvements and the understanding of how and why these improvements are made is brought into focus by first examining the functionality of the Whipple 10 m. After a technical description of both of these telescopes, an examination of the observational methods employed at each are outlined.

3.1 The Fred Lawrence Whipple 10 m Telescope

Located on Mt. Hopkins in southern Arizona at 2,300 m above sea level, the Whipple 10 m telescope was constructed in 1968 and was the pioneering instrument in high energy gamma-ray astronomy, detecting the first galactic and extragalactic sources of very high energy gamma rays (Weekes, 1989; Punch et al., 1992). Although no longer the premier telescope, the Whipple 10m is the fifth most sensitive TeV telescope in the world, surpassed only by the latest generation of IACT arrays (VERITAS, HESS, MAGIC, and CANGAROO-III). It still plays an extremely active role in the field, taking part in a multiwavelength AGN monitoring campaign which provides triggering on gamma-ray outbursts from AGN that may have not been otherwise targeted by the

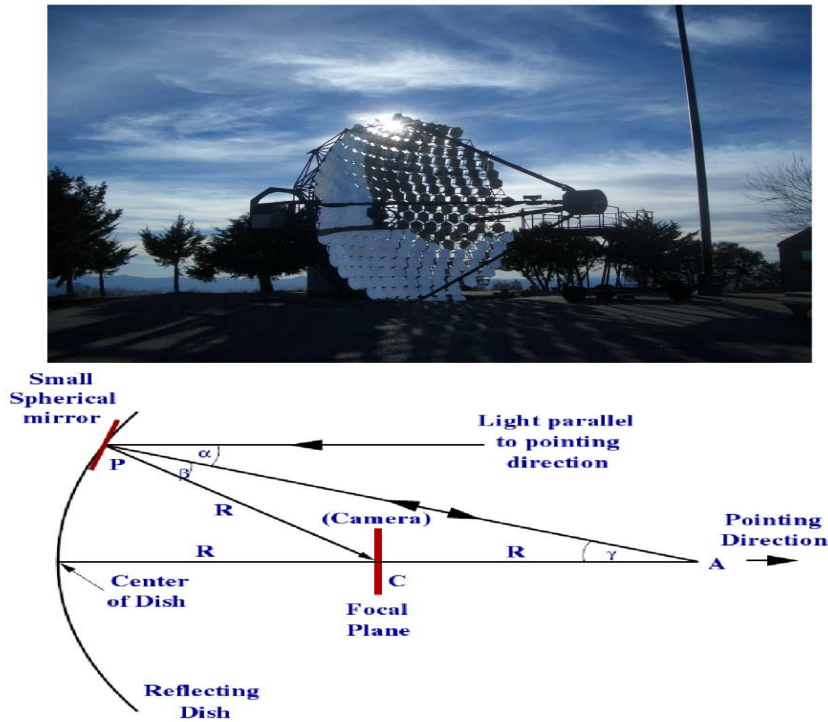


Figure 3.1: Top: The Fred Lawrence Whipple 10m Gamma-Ray Reflector. Bottom: The Davies-Cotton telescope design. The dish has a focal radius of R and is populated with many individual spherical mirrors of focal radius $2R$. The triangle PAC is isosceles and light coming from infinity is focused onto the focal plane where the camera is located. $\alpha = \beta$, therefore the law of reflection is satisfied. Figure taken from Kildea (2007).

newest instruments, as well as searching for TeV counterparts to gamma-ray bursts.

3.1.1 Optical Support Structure and Positioner

Shown in figure 3.1, the telescope follows the design proposed by Davies and Cotton (Davies and Cotton, 1957) in which a single reflector design is replaced by a tessellated structure of smaller mirrors, each of these mirrors having twice the focal length as the entire optical structure. From a logistical perspective, the design has the advantage of being much cheaper to build, and more resistant to damage (replacing several small inexpensive mirrors instead of one large expensive mirror). From a performance perspective, the Davies-Cotton design has a superior off-axis performance when compared to parabolic mirrors (Carter-Lewis, 1990); however, the Davies-Cotton design does introduce a dispersion into the arrival times of photons (a wave front will be distorted by ~ 6 ns). For the purposes of gamma-ray astronomy, the precise optical properties of the reflector are not as important as in optical astronomy and the Davies-Cotton design provides a more

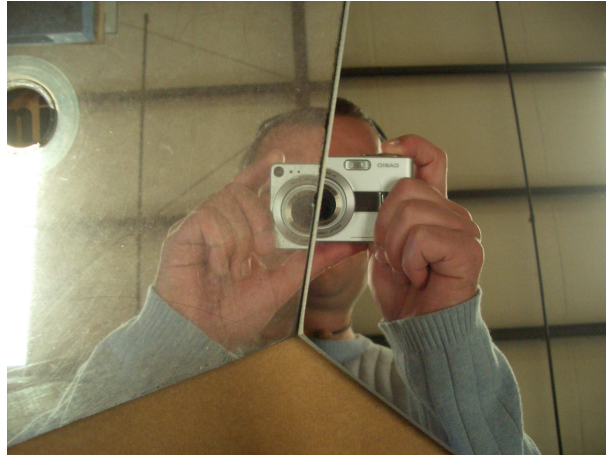


Figure 3.2: A demonstration of the degradation of the mirrors used for the Whipple 10 m reflector. On the left is a mirror taken from the a telescope after several years of exposure. On the right is a freshly re-coated mirror.

than satisfactory platform for the requirements of the Cherenkov technique.

In the case of the Whipple 10 m, the Davies-Cotton mirror implementation is provided by an optical support structure (OSS) composed of a 10 m diameter spherical, bowl-like lattice of welded tubular steel having a radius of curvature of 7.3 m. This OSS provides support for 248 hexagonal shaped, spherical mirror facets; each with a focal length of 14.6 m. In total, these mirrors comprise a total area of 75 m². Four quadrapod arms are attached at the sides which hold the camera housing out at a distance of 7.3 m. This entire structure is moved by an altitude-over-azimuth positioner which provides pointing to an accuracy of $<0.1^\circ$ at a slew speed of up to 1° per second. Since the mirrors and camera will undoubtedly produce a great deal of strain on the structure of both the OSS and quadrapod arms (predominantly from OSS flexure), this will affect the absolute pointing accuracy of the positioner. To account for the ill effects of flexure on the pointing, a series of corrections must be applied to the positioner software to negate these effects. Known as “T-point corrections”, they are measured by pointing the telescope at a bright star whose position is well known and recording (with a co-mounted CCD camera) the image that the star makes upon the focal plane of the camera. The pointing is then corrected until the star image is coincident with the desired focal point. This process is repeated for a number of stars at different elevations and azimuths until the pointing of the telescope is nominal for the entire range of telescope positioning.

3.1.2 Mirrors

The 248 mirrors on the Whipple 10 m are all 61 cm hexagonal mirrors with a radius of curvature of 14.6 m. These glass hexagonal mirror segments are anodized and front coated with aluminum to give a peak reflectivity of $\sim 90\%$ at wavelengths around 310 nm (UV) which is the range of the spectrum at which the Cherenkov signal peaks. Since the telescope mirrors are constantly exposed to the elements, the surfaces of the mirror naturally undergo degradation reducing their reflectivity to $\sim 60\%$ (Badran and Weekes, 2004) over a several year time period. To combat this effect, the mirrors are periodically washed (usually monthly) to remove build up of dirt and other degrading effects (see figure 3.2). Also, each mirror is periodically removed (ever 3-4 years) and stripped, re-coated and re-anodized at the in-house mirror coating facility at the Fred Lawrence Whipple Observatory.

There are two processes involved in aligning the mirrors, both of which apply to the Whipple 10 m and all 4 VERITAS telescopes. During the course of this work, the author was heavily involved in the alignment and subsequent bias alignment (see below) of all 4 VERITAS telescopes, becoming the most experienced VERITAS team member in the procedures of aligning the telescopes at Fred Lawrence Whipple basecamp. The first order alignment process was to set up a small beam laser exactly at the $2f$ point of the telescope at stow and shining it on the center of each individual mirror facet. The mounting screws for each mirror were then adjusted so that the return laser beam is pointed directly back along its original axis. This process is repeated for all 248 mirrors. In this way the light from the entire mirror surface is brought into focus while the telescope is at stow position ($EL=0^\circ$, $AZ=0^\circ$) which would be sufficient if all observations were taken at these coordinates or the telescope structure was perfectly rigid. However, since the OSS is a real structure, being stressed by both the weight of the mirrors and the focus box (and the arms that support it), it will undergo a flexure and deformation effect as the telescope is brought to elevation. The effect of the stress is shown in figure 3.3. To correct for this stress on the optics of the telescope, a second order alignment (or “bias” alignment) was performed on the mirrors so that the telescope will be optimally aligned when pointing at an elevation of 65° . This process began by attaching small moveable lasers to each mirror facet so that the laser spot fell near the focal point of the camera. The telescope is then moved to 65° elevation (the average elevation for most observations) and the movement of the laser spot on the focus box is recorded. In this way the movement of each individual mirror facet is accounted for as the telescope OSS is deformed. These measurements were then used to determine how much each mirror needs to be “de-aligned” at stow position so that it will come into proper alignment position at 65° elevation (See Toner (2007) for a complete description of this process as it is applied to the VERITAS telescopes). Af-

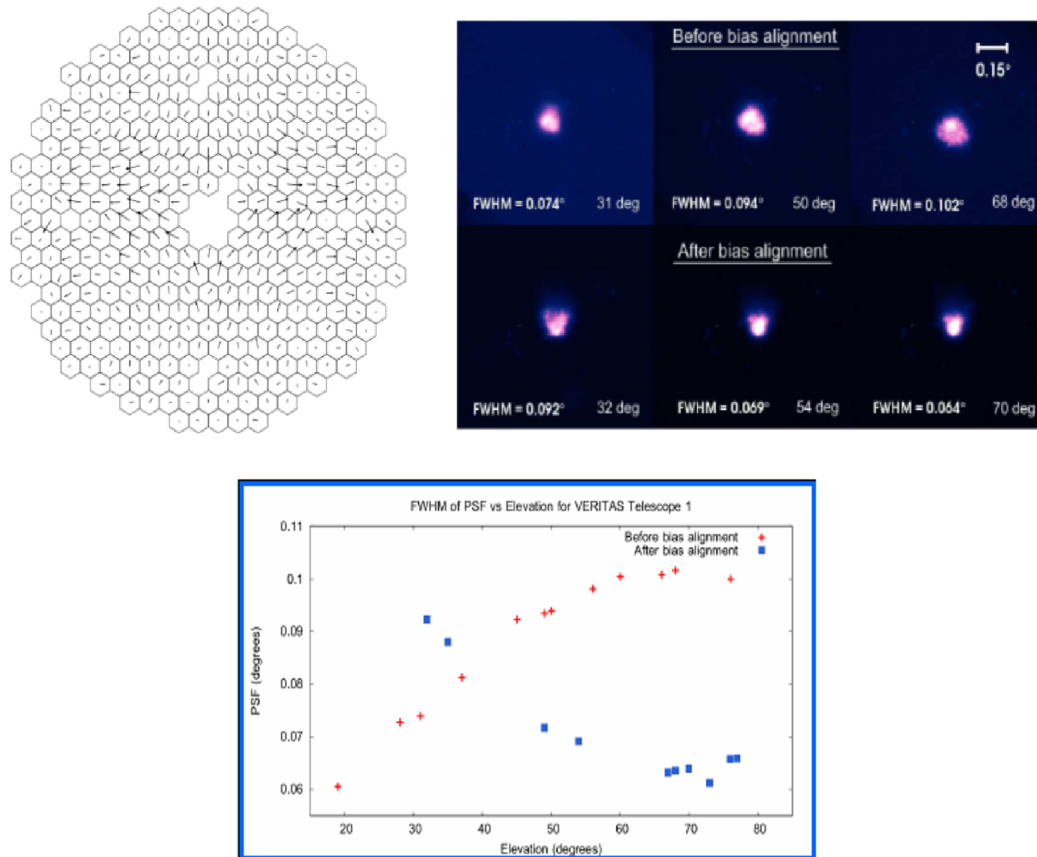


Figure 3.3: The effects of the deformation and bias alignment on the mirrors of a Davies-Cotton telescope. On the left is shown the mirror layout for a VERITAS telescope and associated motions of its mirrors (shown by arrows) as the telescope is moved to 60° elevation. The bottom and right figures show the effect that bias alignment has upon the PSF of the telescope taken at varying elevations. Figures taken from Toner et al. (2007)

ter both standard and bias alignment is carried out, the Whipple 10 m point spread function (PSF) is 0.12°. The VERITAS PSF, which is comparable to the size of an individual photomultiplier tube on the camera, is discussed later in this chapter.

3.1.3 The Camera

The PMT camera on the Whipple 10 m has gone through many alterations over its >30 year lifetime. In fact, prior to 1982, the camera was not actually a camera, but rather just a single PMT detector. Since then, the camera has gone through many variations with different combinations of small versus large pixels and combinations of both. These different camera configurations have resulted in differing fields of view as well as resolving abilities. A summary of the different camera

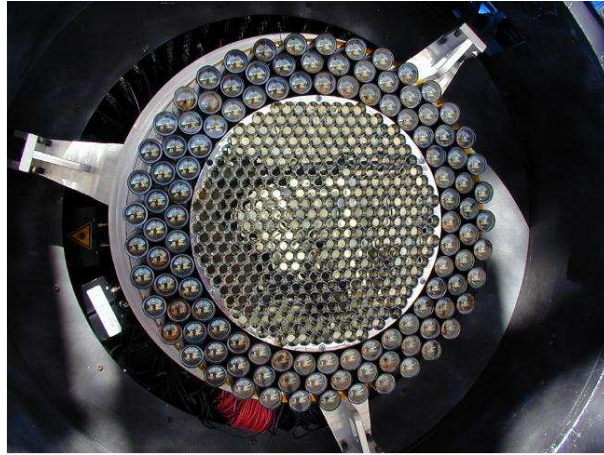


Figure 3.4: The current camera used on the Whipple 10 m. Both the surfaces of the PMTs as well as the lightcones can be seen. The outer ring of large PMTs are from a former camera configuration and are not currently in use.

configurations is shown in figure 3.5. This chapter will focus on the current camera configuration which has been in place since 2003. This consists of 379 0.12° diameter PMTs arranged in a circular pattern resulting in a total field of view of 2.2° . These PMTs have a quartz glass front entry window which maximizes their sensitivity to UV light. The light collecting ability of the camera is augmented by the installation of “light cones” which are structures (coated with the same reflective material as the mirrors) which fit over the PMTs and “funnel” light onto the PMTs which would normally fall in the inter-PMT space, increasing light collection efficiency.

3.1.4 Data Acquisition

Each PMT is attached to a channel of a bank of 10x voltage amplifiers inside the electronics room of the observatory (see figure 3.8). The output signal from the amplifiers is split into three components: 1 DC output and 2 AC outputs. The DC output is fed directly into a current monitoring system which allows the observer to monitor the camera and shut down individual PMTs if they are being flooded by light caused by bright stars. This monitoring process is important as not only can the PMTs be damaged by excess bright light, but the contribution of a star in the field of view will cause those affected pixels to trigger excessively. If this triggering effect is spread across enough pixels, this will show up as an excess of small scale events in the observation run and will bias the data taking.

As for the two AC components, one of these is fed directly (via a 120 ns delay cable) into a “charge analog to digital converter” (QADC) which will digitize the signal from the PMT based

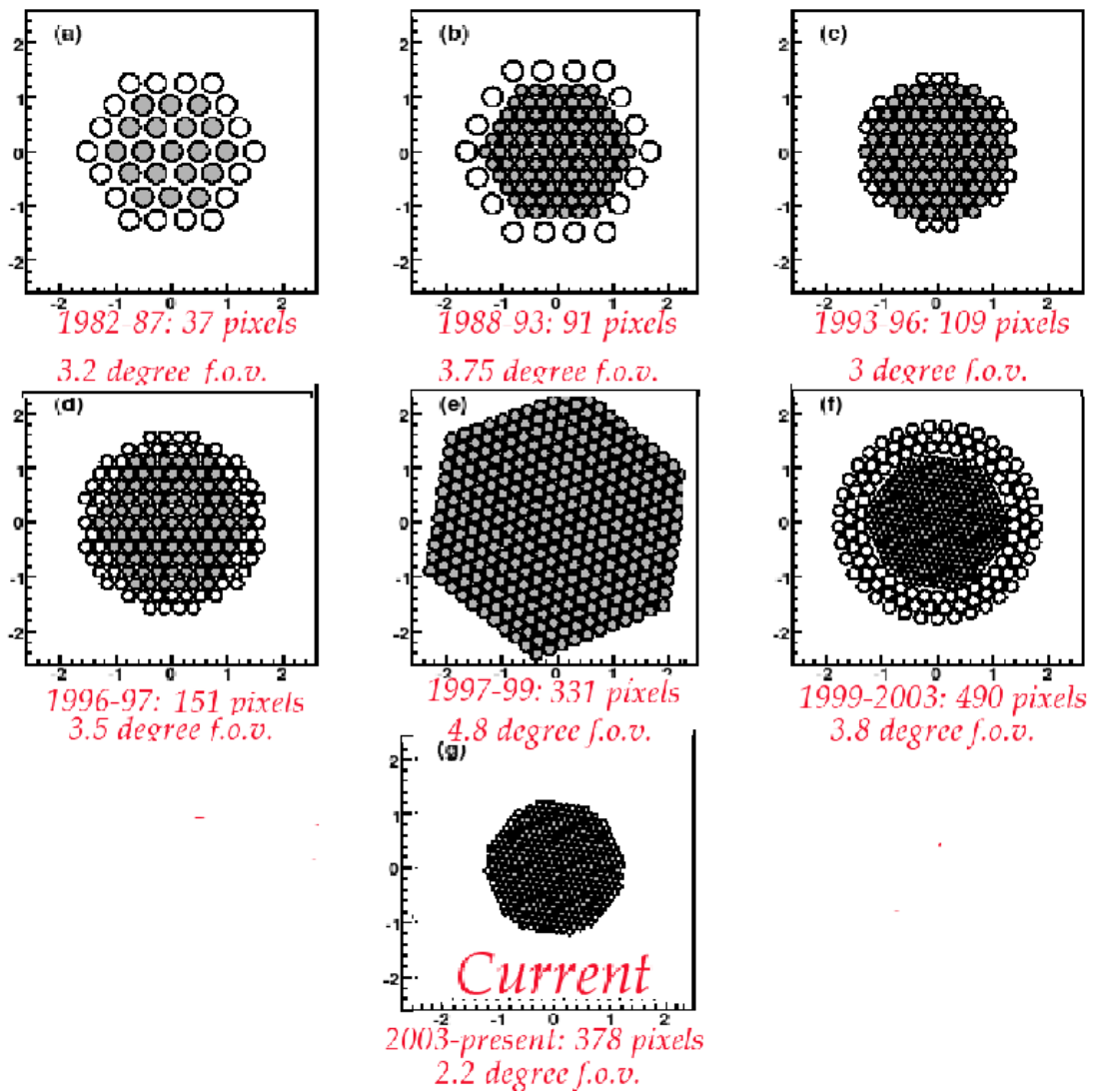


Figure 3.5: Various Whipple 10m imaging camera configurations from 1982 to the present. Figures and numbers taken from Kildea (2007).

on its integrated charge. However, we are still lacking a mechanism by which we decide whether or not the signal from the camera should be read out at all or contains only noise. This is accomplished by the second AC feed which is sent into a two level trigger system. The first level of the trigger consists of a rack of “constant fraction discriminator” modules (or CFDs) which determine if the signal from each individual PMT is large enough to constitute a trigger at the pixel level. In the first trigger level, the use of CFDs is necessary in order to eliminate the problem of “time-walk” in classical discriminators which arise when triggering is required at a certain voltage threshold. Signals with equal rise time but varying pulse maxima will cross a given threshold at different times which eliminates the discriminator’s ability to trigger accurately in time, which can

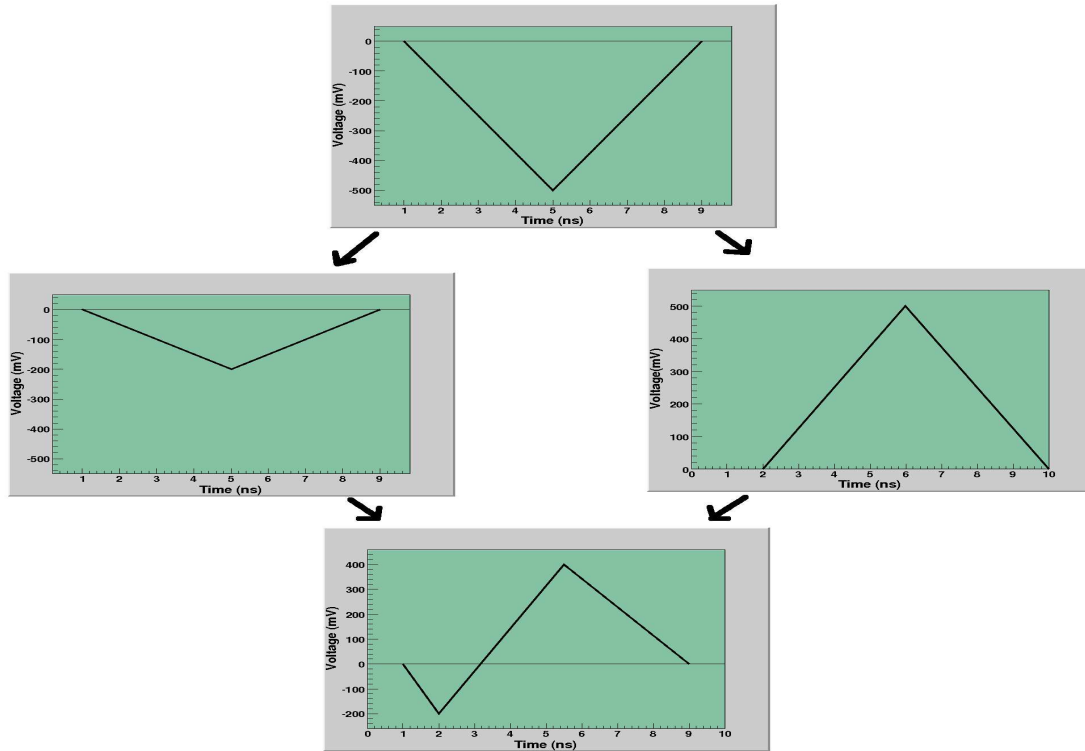


Figure 3.6: How a CFD works: the original signal pulse is divided into two parts. The first is attenuated by a constant fraction and the second is inverted and delayed by a set amount. These two projections are then summed and the zero crossing point is found. It is this point in time that the CFD is to trigger on.

effect the appearance of images consisting of many adjacent pixels triggering closely together in time. The CFDs function by duplicating the input signal; attenuating one copy and inverting and delaying the other copy. These two copies are then added together to get a zero crossing time at which the CFD should generate an output pulse which is independent of pulse maxima and only dependent upon signal rise time. This output pulse is produced only if the CFD measures that the input pulse crossed some programmable threshold. The threshold used is one of the more important parameters that can be set for a given telescope; if the threshold is too low, the CFDs will trigger nearly constantly on sky noise, while if the threshold is too high the telescope will not trigger on small showers raising the detection threshold of the instrument. This threshold is set yearly by observers as a check of system sensitivity as PMT and mirror degradation will necessitate lowering the CFD threshold. The process of checking this threshold is known as taking a “bias curve” and is accomplished by observing the trigger rate vary as a function of CFD threshold while the telescope is observing empty sky. For an example of a bias curve that the author took in 2006 with the Whipple 10m see figure 3.7.

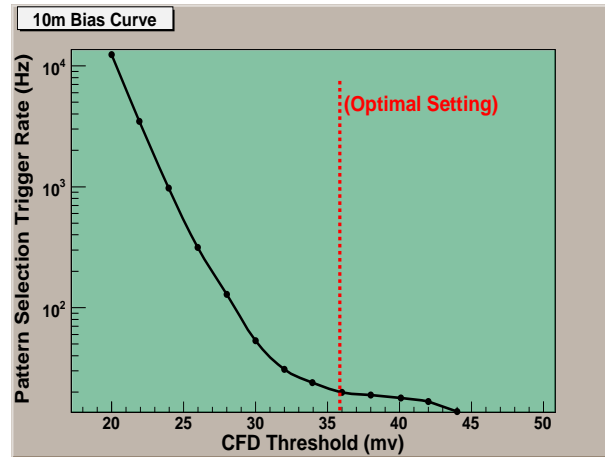


Figure 3.7: An example bias curve taken from the Whipple 10m in 2006. Here is shown how the rates of the pattern selection trigger will grow exponentially large when the CFD threshold is lowered and random night-sky background fluctuations begin to cause overwhelming triggers. The goal of taking a bias curve is to determine a threshold which will give reasonable pattern selection trigger rates. This optimal point, shown in the figure is determine by at what CFD threshold value the curve levels out.

The CFD modules produce two separate triggers. First, each PMT output is sent through an individual CFD channel to determine if it, by itself, passed the criteria for firing. If so then that channel is fired at the zero crossing point determined by the CFD. The signals from all of the fired pixels are then passed to a “pattern selection trigger” or PST. The PST (Bradbury et al., 1999) begins by dividing the camera into 61 overlapping sections of 19 adjacent pixels via a custom built signal-splitter. The output from the sections of the signal splitter is then summed up in a pattern selection trigger (PST) module to determine whether n pixels (for the current Whipple configuration $n=3$) satisfied the CFD trigger level. If this is the case then the pattern of fired pixels is then fed into a custom-built memory chip to see if the combination of fired pixels ($\sim 2^{19}$ possible in a 19 pixel sector) matches any of the PST’s pre-programmed patterns for adjacent pixels. If a pattern is matched, then the PST produces a trigger.

The CFDs also pass the signals from all of the CFD channels to a “multiplicity trigger” to determine if the camera event had a minimum of n number of pixels triggering which passed a preset threshold. A positive flag from both the multiplicity trigger and the pattern selection trigger is necessary for an overall trigger to be declared.

If a trigger is registered by both the PST and the multiplicity then the image of fired pixels is registered in a list processor. The positive trigger will also tell the QADC system to digitize the original event that was passed to it by the delayed AC signal directly from the amplifiers (see

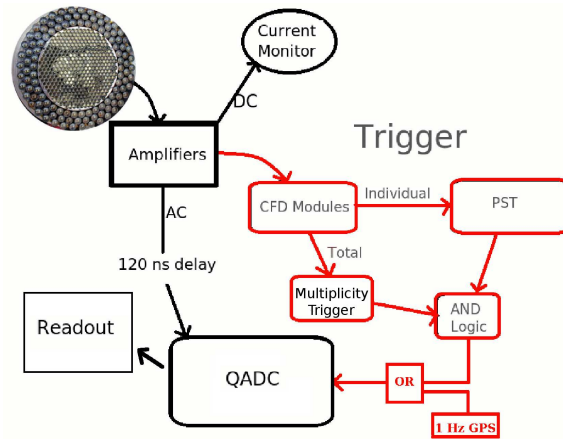


Figure 3.8: A schematic representation of the Whipple 10m signal trigger. See text for details.

figure 3.8). If this is the case, the QADC system will digitize a buffer of ~ 20 ns containing the event, converting the analog signal into an amount of digital counts (1 photoelectron from a PMT will produce roughly 3.3 digital counts at the QADC level). This long buffer time is allowed to compensate lag times in photons hitting the camera from differing radii on the mirror surface as well as intrinsic lag times from the electronic components and cables. A 1 Hz signal from a GPS module is fed into the QADC system to force it to read out once per second. The signal from this GPS trigger is assumed to be night-sky noise (free from gamma-ray signals) and is used as a gauge of the night-sky background in offline analysis (see next section). Regardless of whether the readout comes from an actual signal or GPS forced triggering, the output from the QADC modules is then GPS time-stamped and read out to the data acquisition computer via the programme known as “GRANITE”. The average event rate recorded to disc is on the order of 20-30 Hz.

3.1.5 Data Cleaning and Parametrization

Ultimately, the analysis parameters described in the previous chapter will be used to discriminate between gamma-ray and cosmic-ray air showers; however, there are still a few important steps left in order to optimize our ability to undertake the parametrization process. These involve levels of offline data cleaning of the digital data stream which will attempt to eliminate as much noise as possible from the recorded shower images (see figure 3.10).

- **Pedestal Injection:** In order to eliminate current biases (due to night-sky background) in each tube, the data stream from each PMT is AC coupled. However, if there are positive voltage fluctuations (while looking for a negative voltage signal) from the night-sky background, these will not be digitized in the QADCs and will thus introduce a bias in the

data stream. We do not know *a priori* the qualities of night-sky fluctuations (how large, where in the camera, when etc...). To cope with this, an offset “bias current” (assumed to be much larger than any night-sky fluctuations) of ~ 20 digital counts is injected into the data readout at the QADC level. In this way any positive fluctuations will be digitized and recorded. At the backend we can extract what the fluctuations were by examining the artificial triggers created by the 1 Hz GPS unit described in the previous section. As was mentioned, these artificial triggers force recording of night-sky background noise in each channel. By analyzing only these artificial events (or *pedestals*) over the course of the observation it is possible to determine how the presence of the night-sky background presents itself within various PMTs by observing the digital counts (d.c.) resulting from the pedestal events (i.e. $d.c._{NSB} = d.c._{recorded} - d.c._{injected\ current}$). More important however, is measuring how this pedestal rate varies over the course of an observation. The standard deviation of the pedestal rate (or *pedvar*) for each tube is a direct measure of how noisy that pixel was during the observation. The pedvar for each channel in an observation is calculated and then the median of those pedvars is calculated. Any channel which displays a pedvar of around 1.5 times above or below the median pedvar for the camera is considered to be noisy or malfunctioning (whether due to intrinsic functioning or the presence of outside noise). These pixels are discarded from the data analysis chain and are not allowed to participate in image reconstruction of Cherenkov events.

- **Gain Correction:** Though much care is taken to make sure that a uniform high voltage is supplied to the PMTs, small differences will remain in each PMT’s response to the same signal due to unavoidable manufacturing differences and PMT aging. Similar to the process of flat-fielding a CCD detector in optical astronomy, a process known as taking a “nitrogen run” is used in order to determine the relative gains of each PMT. This process involves a short (1-2 minutes) data run being taken at stow position while the camera is illuminated by a nitrogen arc lamp placed behind a diffusing screen at the center of the telescope OSS. This lamp produces short bursts of light (\sim at 1 kHz) which give a uniform coverage over all of the camera PMTs. This short run is then analyzed in order to determine the relative gains of each PMT within the camera.
- **Image Cleaning:** We know that the PST modules will only allow events to be recorded if the pixels satisfy some requirements about total charge and proximity to other active pixels; however, due to the integration time involved the pixels taking part in the recording of the shower image will most likely not be the only pixels with signal in the image. These rep-

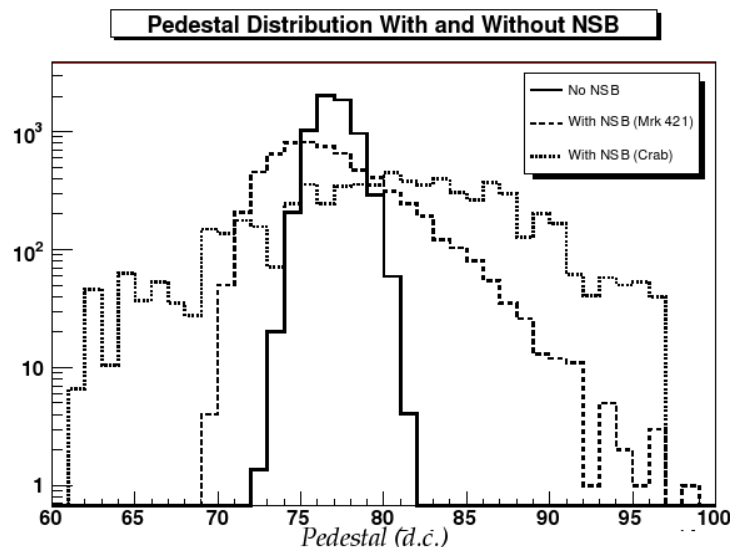


Figure 3.9: The effects of varying levels of night-sky background on the pedestal distribution. This distribution is taken from VERITAS data, however, the principle is identical for 10m data. The narrower distribution corresponds to data taken with the camera cover on, the Mrk 421 data is taken in a relatively dark star field whereas the Crab Nebula data is taken in a bright star field. These varying levels of background light correspond well to wider distributions in the pedestals. Taken from Cogan (2007).

resent a source of noise when trying to isolate and parametrize shower images. To remove them, the offline analysis isolates the pixels contributing to the actual image by demanding that “picture” tubes have a threshold d.c. count of 4.25 times the pedvar for that tube. The edges of the image are determined by locating “boundary” tubes which must satisfy the criteria of being adjacent to a picture tube and have a digital count of 2.25 times the pedvar for that tube (see figure 3.10). All tubes that do not satisfy either the picture or boundary conditions are set to zero light content in the analysis chain.

Although there are slight differences in how images from different observing modes are calibrated (see next section), these three methods are the basic procedures followed for every data run taken. After the images have undergone these cleaning processes, they are ready to be parametrized. Each image is fitted with an ellipse and analyzed in terms of its distribution of light within that ellipse (see Reynolds (1993) for a complete description of this process). An example of parametrization of the shower moments was explained in the last chapter in terms of defining each image in terms of its *size*, *length*, *width*, and *alpha* parameters which were shown to be an effective method for

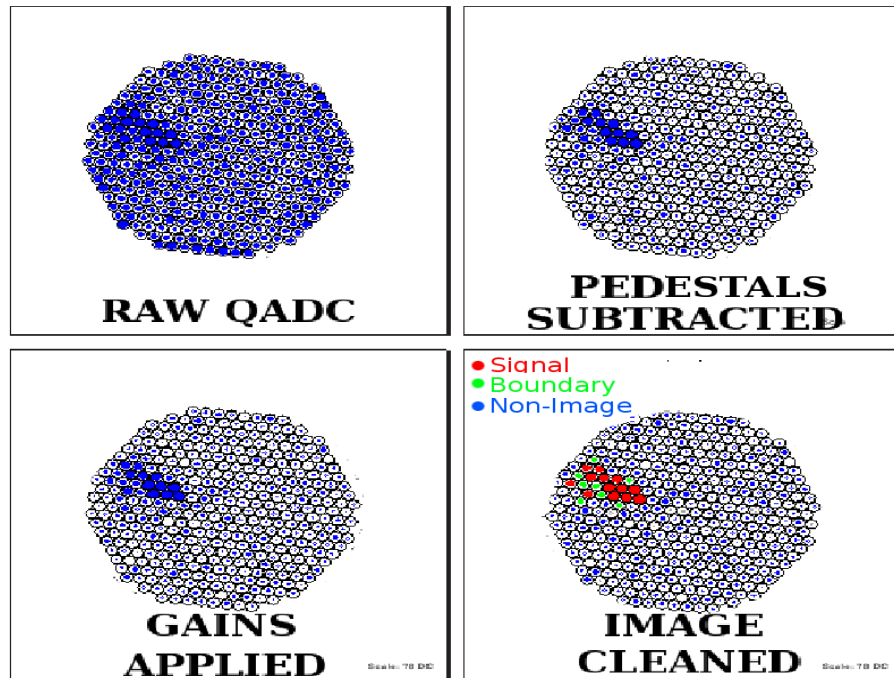


Figure 3.10: The levels of data calibration and cleaning in offline 10m analysis. Procedures described in text. Figures modified from Horan (2001).

initial discrimination of gamma-ray and hadron images. The actual set of discriminating factors used in practice are as follows:

- **Length** A second order moment of the shower image (corresponds to the longitudinal development of the shower).
- **Width** A second order moment of the shower image (corresponds to the lateral development of the shower).
- **Alpha** The angle between the primary shower image axis and a line connecting the center of the field of view to the image centroid (corresponds to the difference between the shower primary trajectory and the telescope pointing).
- **Distance** The distance between the center of the field of view and the image centroid.
- **Size** The integrated digital charge of all the pixels contributing to the shower image (used in later analysis to estimate the energy of the shower primary).
- **Max1, Max2** The charge in digital counts of the brightest (and second brightest) pixels taking part in the image (gamma-ray images, being more compact, will deposit a greater fraction of their total light into the brightest pixels within the shower).

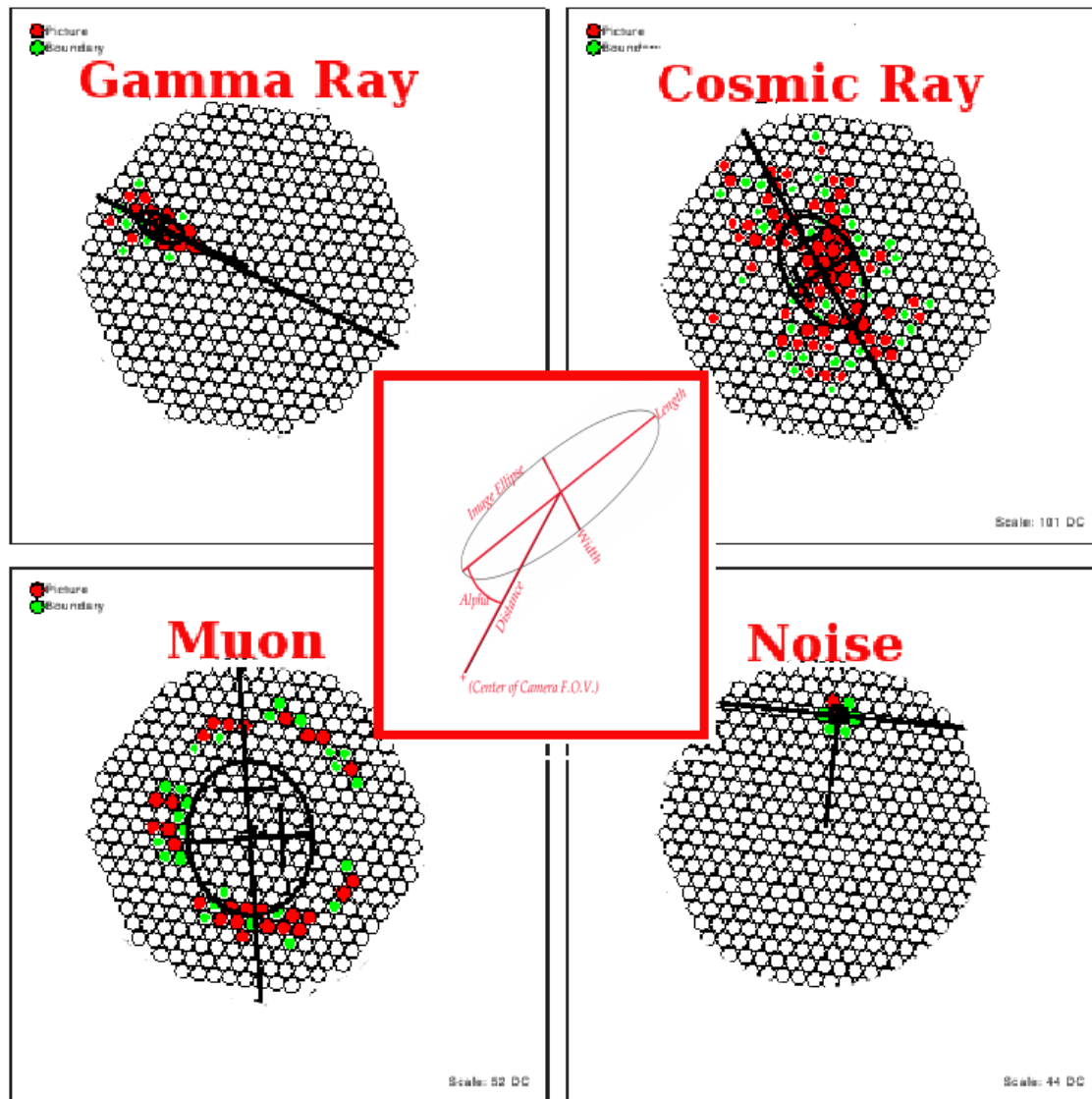


Figure 3.11: Various images from real 10m data showing the parametrization of a gamma-ray image (upper left), a cosmic-ray image (upper right), a muon ring (lower left), and night-sky background noise (lower right). Figures modified from Horan (2001).

- **Length/Size** This parameter is useful for removing muon images as the light from these showers will have a roughly constant value of light per unit length.

The values of these parameters are set by optimizing them on observations of the Crab Nebula since this target is assumed to have a constant flux and is strong enough to serve as a calibration tool. The values of these parameters, or “cuts”, have taken on many different values over the years of the Whipple 10 m mostly due to changes in camera configuration and other physical parameters of the system. The current set of cuts known as *Supercuts 2000* have been in use (since the year 2000) and constitute the most effective set of broad application cuts for the Whipple 10 m. It is

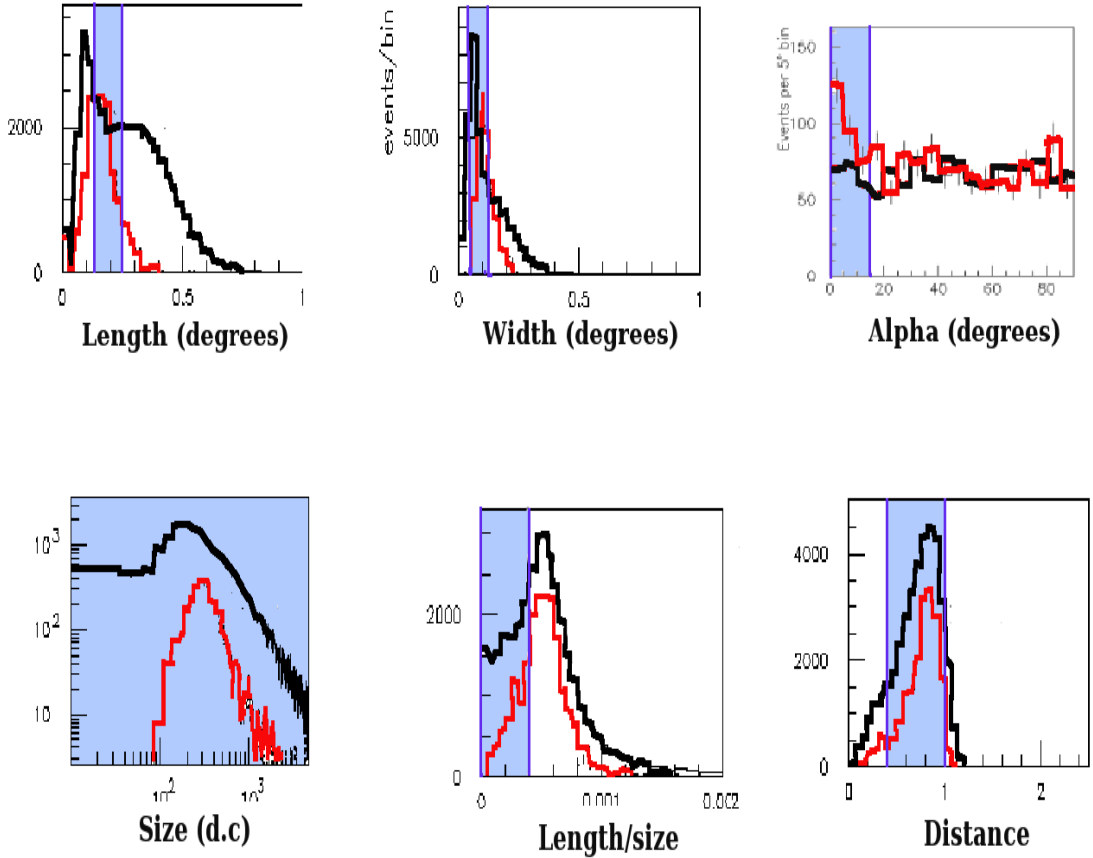


Figure 3.12: Here are parameter distributions from real ON/OFF Whipple 10 m data that was taken by the author on the Crab Nebula in 2006. The ON source data (data set containing the gamma-ray signal) is shown by a red line while the OFF source data (cosmic-ray data) is shown by black lines. The regions which are allowed by *Supercuts 2000* are shown by blue shading.

estimated that although these cuts result in the discarding of $\sim 50\%$ of incident gamma-ray images, they also discard $\sim 99\%$ of cosmic ray events. Although *Supercuts 2000* is not optimized for weak sources (Which would present a slightly different set of image parameters than strong sources), it remains the default set of cuts for discovery mode on the Whipple 10 m and these are the cuts used for the 10m data presented in this thesis. These cuts are shown in Table 3.1 as well as graphically in figure 3.12.

3.1.6 Observing Modes

Ground-based gamma-ray observatories are, in general, low duty cycle facilities. This is because they are limited by only being able to observe on clear, moonless nights. Compounding this (due to summer monsoon storms in Southern Arizona), the Whipple 10 m (and VERITAS) is only

Table 3.1: *Supercuts 2000* The cut parameters used for Whipple 10 m data analysis for this thesis. Variants of these cuts will be used for VERITAS data analysis.

	Length(°)	Width(°)	Distance(°)	$\frac{Length}{Size}$	Alpha(°)	Max1,2(d.c)
Lower Cut	0.13	0.05	0.4	0.0	0	30
Upper Cut	0.25	0.12	1.0	0.0004	15	∞

operable from approximately September to the end of June. Assuming the most favorable weather conditions possible, this only amounts to ~ 800 hours of live sky time available each observing season. There have recently been modifications of the hardware used for ground based gamma-ray experiments to allow for partial moon observing (see (Cortina, 2005) for a description of the MAGIC telescope on La Palma, Canary Islands); however, the current Whipple 10m camera was not designed for such observations and has to make optimal use of the observing time it has available every year. For each data run taken, the observers at the Whipple 10 m must judge for themselves what the condition of the sky is like (cloud cover, humidity, seeing, etc...) and whether or not any useful data can be extracted from it. The evaluation of this condition is graded by a letter scale from A+ (ideal) to C-(non-observable). Although this grading system has been notorious for inconsistency and subjectiveness due to its human grading, it is still a useful first criteria for judging the validity of data.

PAIRS (or ON/OFF) Mode:

During optimal weather conditions (A \rightarrow B), the preferred method of observation for established sources with the Whipple 10 m is known as “Pairs” mode, also referred to as “ON/OFF” mode, since the process involves taking both an ON source and an OFF source data run. A 28 minute data run is taken with the telescope pointed directly on source (ON run), a 2 minute break is taken during which the telescope is slewed to the exact position on the sky where it was when the ON run started (30 minutes behind in Right Ascension). Another 28 minute data run is then taken (OFF run) following the exact same path across the sky that the ON run took, except this time it is assumed that the telescope is tracking completely gamma-ray dark sky (background). In this way a direct measurement can be made of the background for the pointed observation. Although this method is time consuming (58 minutes of data taking for 28 minutes of pointed on-source observation), its ability to determine the character of the background makes it a necessity when looking for previously undetected sources or when attempting to determine spectral information about a source. Due to the possibility of the night-sky background showing significantly different levels of light during the ON and OFF runs, a data calibration procedure known as “Software Padding” (Cawley, 1993) is needed in order to remove a possible bias. The pedvar for each tube is measured

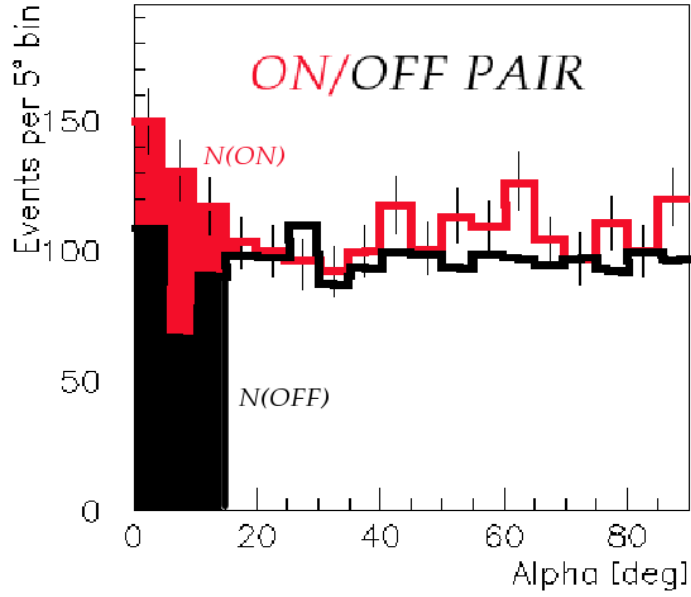


Figure 3.13: The method for determining whether an ON/OFF pair contained a viable gamma-ray signal. This is real Whipple 10 m data taken by the author on the Crab Nebula in 2007. The number of events passing the α cut, N_{ON} (red) taken from the ON run is compared to the number of events passing the α cut in the OFF run (N_{OFF}). Both distributions have passed all other selection cuts.

for both the ON and OFF run. Gaussian noise is then added to tubes which are darker (could be either ON or OFF) until the pedvars for both runs are equal. After software padding is carried out on the ON/OFF pair, the calculation of a possible signal and its significance can proceed. The number of events in each run that passed the α cut ($\alpha \leq 15^\circ$) are compared to determine whether there was an excess of showers in the ON run which originated from the pointing direction (see figure 3.13).

The calculation of the corresponding gamma-ray rate (R_γ) and significance (σ_γ) over an observation time ($\Delta t = \text{length of ON run}$) is given by (Horan, 2001):

$$R_\gamma \pm \Delta R_\gamma = \frac{N_{ON} - N_{OFF}}{\Delta t} \pm \frac{\sqrt{N_{ON} + N_{OFF}}}{\Delta t} \quad (3.1)$$

$$\sigma_\gamma = \sqrt{2} \left[ON * \ln \left(\frac{2(ON)}{ON + OFF} \right) + OFF * \ln \left(\frac{2(OFF)}{ON + OFF} \right) \right]^{1/2} \quad (3.2)$$

When the sky conditions are not good enough to get consistent results, or when an already known source is being monitored for flaring, the PAIRS mode is not considered an optimal use of the observing time and thus a different observing mode is employed, known as “tracking mode”.

Tracking Mode The mode of observation for already known sources to search for excess ac-

tivity is known as “tracking”. If a source is detected in this mode then it is customary for more precise observations to be carried out in ON/OFF mode. Tracking mode can be used in all weather conditions as it does not incorporate an ideally matched off-source control run requiring stable night-sky conditions. In this mode the source of interest is tracked directly at the center of field of view for a period of 28 minutes. Although this is an efficient observing mode as far as time consumption is concerned, its lack of *in situ* determination of the background rate is a cause for uncertainty in its measurements and therefore the tracking mode is not considered appropriate for new source detection or source spectral determination. To determine the background level for each tracking run, indirect methods must be employed. As was stated in the previous section, the cut parameters used for gamma/hadron discrimination include a cut on the *alpha* parameter which is a gauge of how well the image is consistent with an image coming directly from observational direction. It is assumed that images which have a parametrized *alpha* angle of $>15^\circ$ are not air showers originating from the target and most likely not gamma-ray images at all. Therefore, one can assume that all recorded images having an *alpha* parameter $>15^\circ$ are due to cosmic-rays and constitute our background for tracking runs.

The method employed to determine the significance and gamma-ray rate of each tracking observation is the following: the ON source region is taken to be all the events that pass the *alpha* cut of $\leq 15^\circ$ (N_{ON}) whereas events having a parameter of $20^\circ \leq \alpha \leq 65^\circ$ (N_{OFF}) constitute the OFF region for tracking observations (the truncation of events falling near the edge of the camera will result in a larger population of events with *alpha* $\geq 65^\circ$ and therefore this region is not considered stable for background determination). Since the ON and OFF regions are much different in size (in terms of *alpha* parameter space) for tracking observations, the raw number of events in the OFF region will always be much larger than that in the ON region, therefore, we must normalize the OFF counts to give a more reasonable depiction of the events in the background region. This is accomplished by determination of a number called the “tracking ratio” ρ . ρ is determined by analyzing a large set of OFF runs (in the PAIRS mode sense) from a single season and accumulating the following statistic:

$$\rho \pm \Delta\rho = \frac{N_{good}}{N_{bad}} \pm \sqrt{\frac{N_{good}}{N_{bad}^2} + \frac{N_{good}^2}{N_{bad}^3}} \quad (3.3)$$

Where N_{good} is the number of events from the accumulated OFF runs that pass the $\alpha \leq 15^\circ$ cut and N_{bad} are the events with $20^\circ \leq \alpha \leq 65^\circ$. In this way we have a mechanism that normalizes the OFF region to the ON region in tracking runs (ρ is usually ~ 0.3). This results in an ability to judge how many source gamma-ray events (N_γ) there were in a given tracking run by:

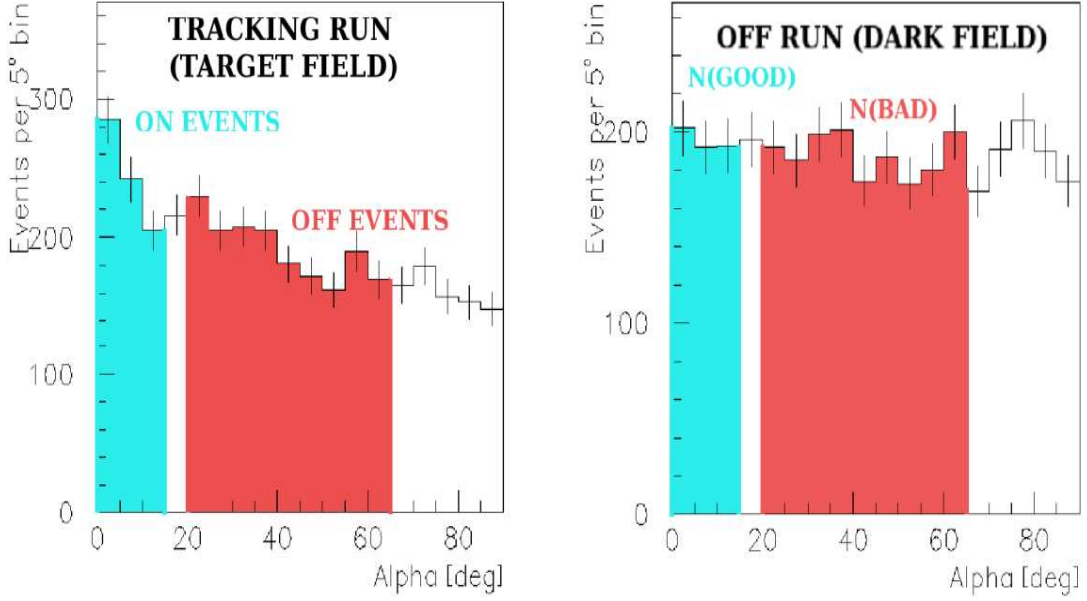


Figure 3.14: The distributions corresponding to the determination of N_{ON} , N_{OFF} , N_{good} , and N_{bad} .

$$N_{\gamma} = N_{ON} - \rho N_{OFF} \quad (3.4)$$

The associated gamma-ray rate and significance for a tracking run of length Δt is then calculated by (de la Calle Perez, 2002):

$$R_{\gamma} \pm \Delta R_{\gamma} = \frac{N_{\gamma}}{\Delta t} \pm \frac{\sqrt{N_{ON} + \rho^2 N_{OFF} + (\Delta \rho)^2 N_{OFF}^2}}{\Delta t} \quad (3.5)$$

$$\sigma_{\gamma} = \sqrt{2} \left[ON * \ln \left(\frac{1 + \rho}{\rho} \frac{(ON)}{ON + OFF} \right) + OFF * \ln \left((1 + \rho) \frac{2(OFF)}{ON + OFF} \right) \right]^{1/2} \quad (3.6)$$

Since the Whipple 10 m is now (2007) primarily used for monitoring known AGN sources for flaring activity, the *tracking* mode is currently the most used observation mode. However, the data from the Whipple 10 m that is presented in this thesis are all taken in *Pairs* mode since the goal was to attempt to detect several galactic microquasars. The additional analysis and data selection criteria that are used for that analysis will be presented in chapter 5.

3.1.7 Whipple 10 m Performance

Due to the lack of a method of directly calibrating and measuring the sensitivity of ground-based gamma-ray telescopes, one must instead rely on the use of Monte Carlo air shower simulations. These simulations accurately trace the projected path of millions of air showers particles (both gamma ray and cosmic ray) along with their associated Cherenkov light. The path of this light is

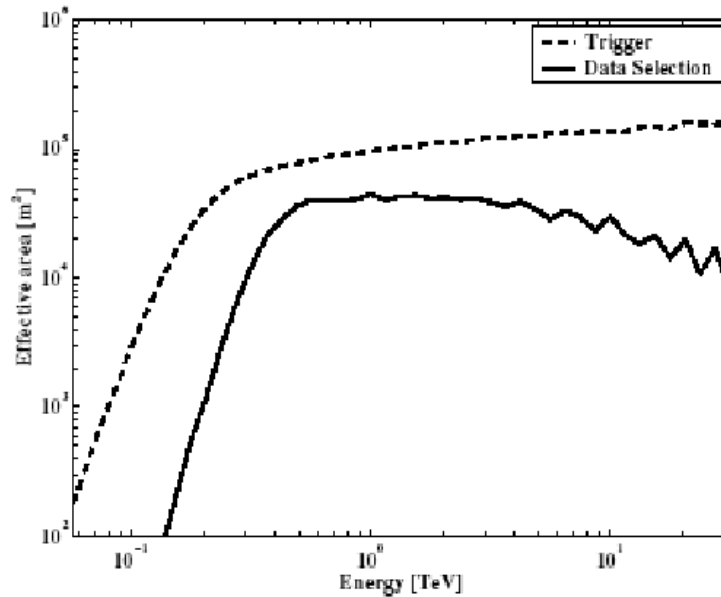


Figure 3.15: The effective area and peak energy response for the Whipple 10 m extracted from simulations. The effective collection area peaks at around $4 \times 10^4 \text{ m}^2$ for gamma-ray primaries of energy around 350 GeV, which is defined as the energy threshold of the telescope. Figure taken from Fegan (2004).

then ray traced through the telescope optics. Estimations of the detector response are then fed into software to see how a simulated detector would respond to the simulated light. In this way, one can simulate a source with a given spectrum and see what the resulting population of gamma-ray air showers would look like when compared to the simulated background. Through this method, characteristics of the detector such as at what energy the detector is most sensitive, its sensitivity range, and the effective collection area of the detector are determined. Some of these properties for the Whipple 10 m are shown in figure 3.15, and table 3.2. The recorded data are then compared to these simulations and spectra can be extracted. Because no spectral information from the Whipple 10 m will be used in this thesis, a full explanation of the process of spectral reconstruction will be delayed until section 6.1.3 where the process will be described as it applies to the VERITAS array.

As was mentioned previously, the Crab Nebula was the first VHE gamma-ray source detected by Whipple and still remains today as a standard candle for gamma-ray astronomy. Shown in figure 3.16 are the results of 18.43 hours of pointed observations (with an equivalent 18.43 hours of OFF data) taken on the Crab Nebula during the 2005-7 observing seasons with the Whipple 10 m. As can be seen the source is readily detectable by the Whipple 10 m with an average rate of 2-3 gamma rays per minute, shown by the straight line fit to the overall lightcurve. Shown also

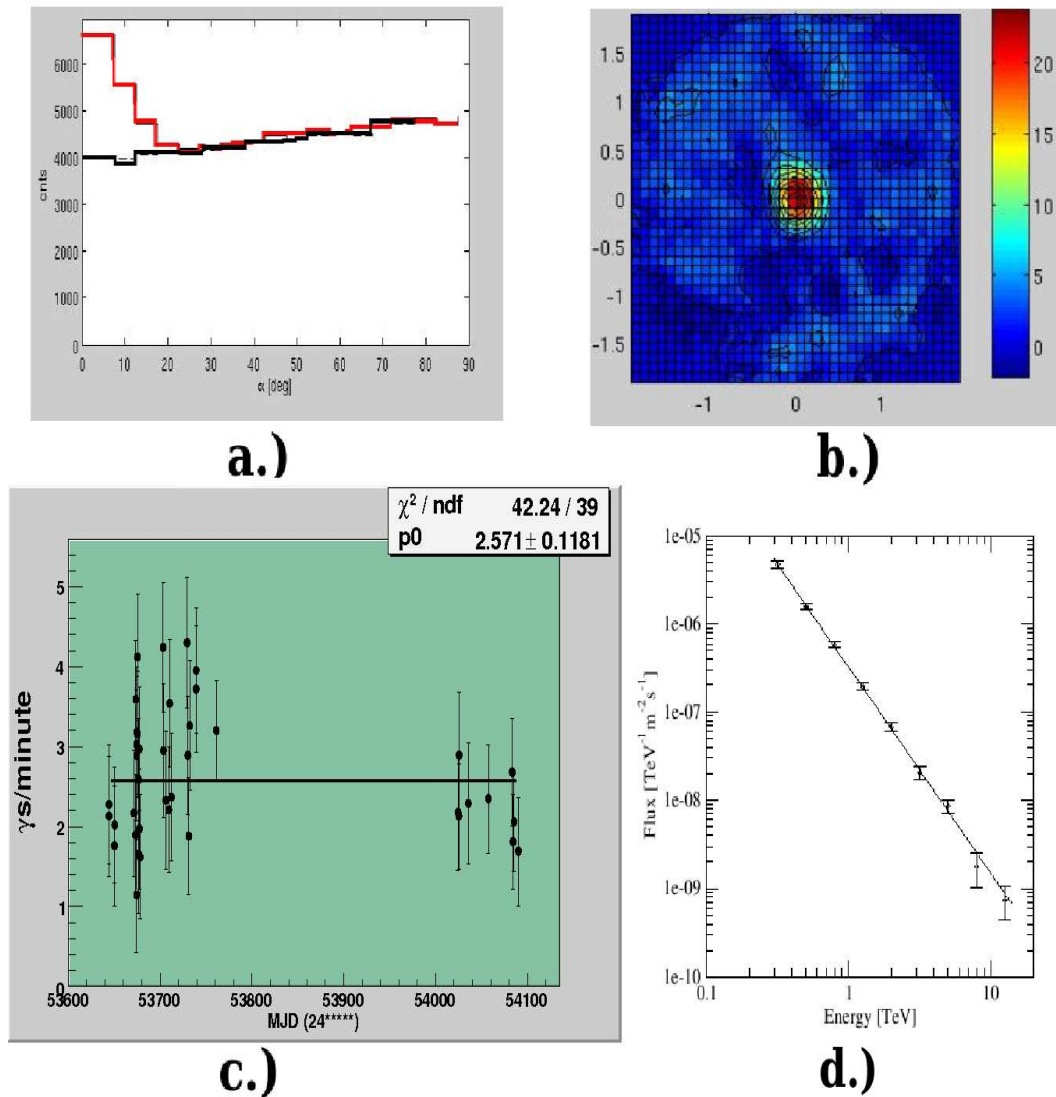


Figure 3.16: Performance of the Whipple 10 m as demonstrated by observations on the Crab Nebula. a.) The alpha plot resulting from 36 hours of PAIR observations (18 hours of ON/OFF each) on the Crab, a clear excess of the ON counts (red) at low alpha values is shown. b.) The 2-dimensional sky map produced from this data set showing a point-like source of VHE gamma rays. The color scales here represents varying degrees of significance. The total data represents a detection of 31.61σ at a rate of 2.6 gamma rays per minute. c.) The run by run light curve for the dataset, well fit by a constant rate hypothesis. d.) The differential energy spectrum extracted from a different Crab Nebula data set take in 2001 (figure taken from Schroedter (2004)). This spectrum is in good agreement with the results of the results from HEGRA, CAT, MAGIC.

is an extracted differential energy spectrum of the Crab Nebula from data taken in 2001. This energy spectrum is in good agreement with similarly produced spectra reported by other ground-based Cherenkov experiments which were developed subsequent to the Whipple 10 m, such as HEGRA (Aharonian et al., 2004c), CAT (Masterson et al., 2001), MAGIC (Albert et al., 2007), and H.E.S.S. (Aharonian et al., 2006c). The agreement of this extracted spectrum with other established experiments is one of the benchmarks for satisfactory performance of any ground-based Cherenkov experiment. It should be noted that since the Whipple 10 m telescope was, in fact, the first experiment to measure such a spectrum (Hillas et al., 1998), its results were for many years used as THE proficiency benchmark for detecting VHE gamma-ray sources. As will be shown in the next section, the VERITAS array has built upon the results and methods of the Whipple 10 m with new technological advances that improve all the performance aspects that have been described in this section.

3.2 The VERITAS Array

Located at the base of the mountain upon which the Whipple 10 m is perched, the VERITAS array represents the extension of the Whipple 10m into a third generation of ground-based TeV observatories. At 1270 m above sea level, the array is slightly lower than the Whipple 10 m; however, this is compensated for by the apparent increase in duty cycle over the Whipple site as well as a slightly darker aspect. The VERITAS array is composed of four ($f=1.0$) 12 m diameter telescopes separated by various distances (see figure 3.17), each telescope being nearly identical in physical design (with the exception of the f -ratio) to that of the Whipple 10 m (i.e. Davies-Cotton design, OSS composed of welded tubular steel, quadrapod arms supporting camera etc.). However, everything about the VERITAS telescopes is scaled to a larger size as will be shown in the following sections. In addition to the use of the stereoscopic imaging technique, there are several technological advantages that each VERITAS telescope has over the 10 m. These advantages include improved optical quality, faster signal processing, advanced data acquisition as well as a host of less obvious advantages. The first VERITAS telescope (T1) came on-line and began taking observations as a stand alone instrument in early 2005 (Holder et al., 2006). This was joined by the second telescope (T2) for observations in March 2006 and the experiment operated as a two telescope array until the addition of the third telescope (T3) in December of that year. The final telescope of the array (T4) was added to the system and full 4-telescope array observations began in April 2007. The data for this thesis was taken with both the 2-telescope array system (V2), and (to a lesser extent) the 3-telescope array (V3). In this section, the physical

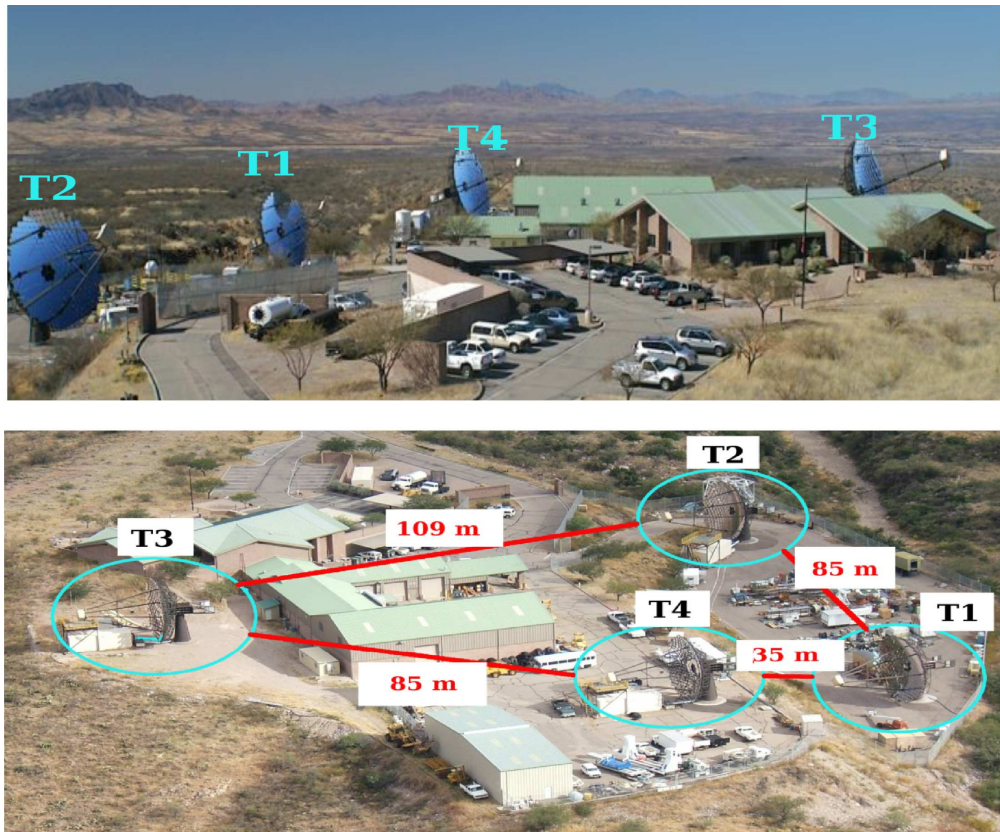


Figure 3.17: A side view (top) and an aerial view (bottom) showing the VERITAS-4 array. The distances between the telescopes shown in the bottom figure were not originally planned (originally an equal spacing of 85 m between all telescopes were planned) but site constraints necessitated this configuration. All simulations show that this distance configuration has little impact on the overall performance of the array. Photos courtesy of Steve Criswell.

and data acquisition properties of the FULL array (V4) will be described. This will be followed by a description of the data taking modes of the array and their associated analysis procedures.

3.2.1 Optical Support Structure and Positioner

Similar in design but not in scale to the Whipple 10 m, each of the four $f=1.0$ telescopes is of the Davies-Cotton design, consisting of a bowl-like dish of welded tubular steel 12 meters in diameter which supports the mirrors. Four quadrupod arms are attached at the edges which hold the camera housing out at a distance of 12 m. The weight of the arms, camera, and mirrors is balanced by several tons of counterweight attached to the back of the OSS. Each of the telescopes is positioned by an altitude-over-azimuth drive built by the Rotating Precision Mechanisms corporation. Each

3.2. THE VERITAS ARRAY

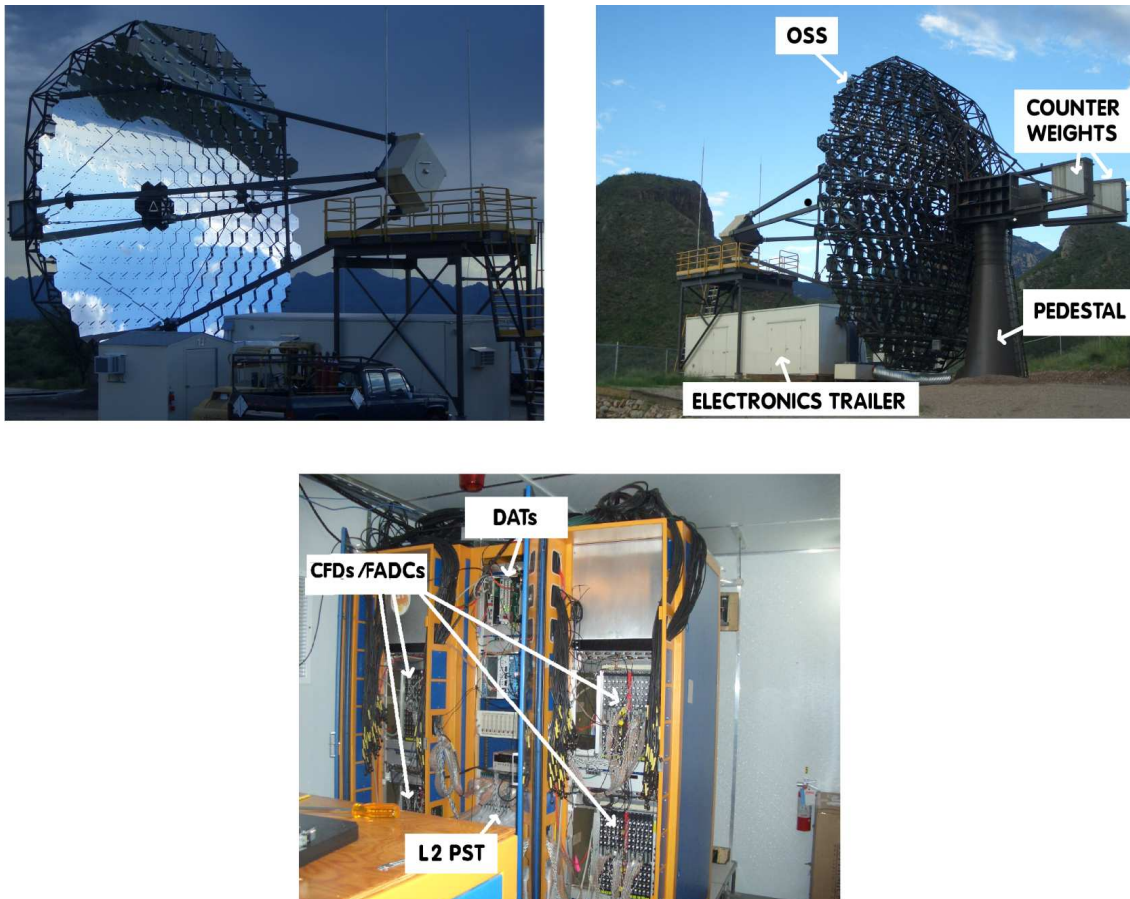


Figure 3.18: Top left: a view of a VERITAS telescope, in this case T4, on a not so ideal observing day. Top Right: A picture of telescope 3 showing the OSS, pedestal, and electronics trailer as described in the text. Bottom: a picture of the inside of the electronics trailer showing the location of the various trigger components as described in the text.

of these positioners has a pointing accuracy of $\leq 0.005^\circ$. Its maximum attainable slew speed is of the order of $1^\circ/\text{s}$, however, due to the size of the telescopes and their accompanying safety concerns, the telescopes are moved at a maximum of $0.5^\circ/\text{s}$. Similar to the 10 m, each VERITAS telescope OSS and quadrapod arms undergoes a degree of flexure as the telescope is moved in elevation. The process of “T-point corrections” (see section 3.1.1) is applied here also to minimize any pointing discrepancies that arise due to flexure and intrinsic pointing inaccuracies of the mechanical equipment.

3.2.2 Mirrors

The inside surface of the OSS is populated with a tessellated structure of 350 hexagonal mirrors comprising a total mirror area of 110 m^2 . Each mirror is 61 cm in diameter and 11.5 mm thick

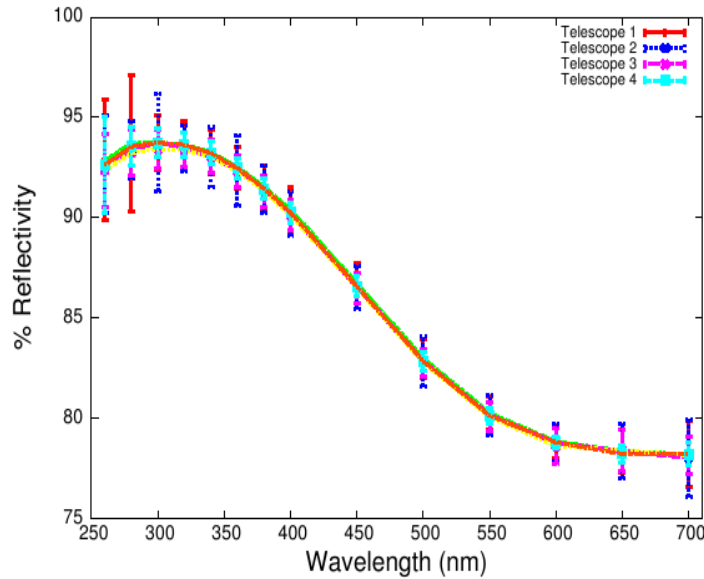


Figure 3.19: Mirror reflectivity vs incident light wavelength for the VERITAS mirrors. This result easily satisfies the design specifications stated in the text. Figure taken from Roache et al. (2007).

with a radius of curvature of 24m (Roache et al., 2007). The glass facets are produced by DOTI optics corporation (Roundrock, Texas) and are then shipped to the Fred Lawrence Whipple base camp for coating and anodizing. Similar to the 10 m mirrors, the VERITAS mirror facets are cleaned, front-aluminized, and anodized in the in-house mirror facility. The mirrors have a design specification of 90% reflectivity at 320 nm and $\geq 85\%$ for wavelengths between 280 nm and 450 nm. As can be seen in figure 3.19, these design specifications are easily met by all mirrors placed on the 4 telescopes. After all levels of coating and cleaning are applied, the mirrors are found to produce a spot size at the focal point of 6mm. Since the mirrors are exposed to the elements, care must be taken to minimize the damage that the elements caused to the reflectivity. To counteract this, all four telescopes are washed with a gentle detergent and water each month. Recent tests (Roache et al., 2007) show that the VERITAS mirrors lose $\sim 3\%$ reflectivity at 320 nm per year; therefore, a cycle of removing the mirrors and recoating them every four years began at the start of full V4 array operations in 2007.

Similarly to the Whipple 10m, the mirrors are aligned and then bias aligned using the procedure described in section 3.1.2. After all levels of alignment are completed, each VERITAS telescope has a PSF of 0.06° at 65° elevation, which is much less than the angular size of the camera PMTs described in the next section. This superior PSF allows for more accurate pixelation of the shower image, one of many improvements over the 10 m design.

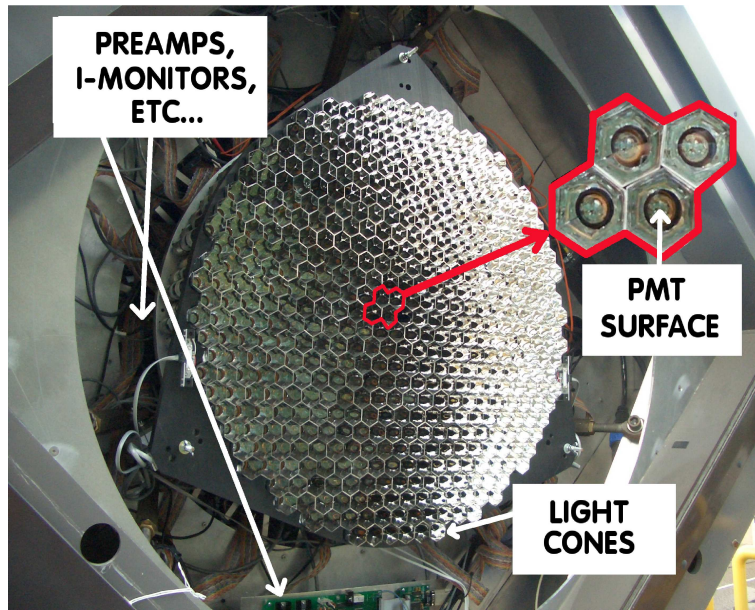


Figure 3.20: The 499 pixel VERITAS camera. Shown also is the location of the in-camera electronics such as the preamps, current monitor, and environmental sensors. The inset shows a close-up view of the camera face in which can be seen both the PMT fronts as well as the structure of the lightcones.

3.2.3 Camera

Each VERITAS telescope camera is comprised of a tightly packed array of 499 Photonis XP 2970/02 PMTs, each with an average gain of 2×10^5 . These PMTs have an angular spacing of 0.15° giving a total field of view of 3.5° for each camera. The PMTs were chosen based on their high sensitivity to UV light and their good quantum efficiency (20-25% for wavelengths between 300-400 nm). The camera face is also fitted with a set of highly reflective light cones designed to focus light that would normally be lost to the inter-PMT spacing (see figure 3.20). As well as the actual camera electronics, there are several other pieces of equipment located within the camera housing that support and augment the functioning of the camera. Control boards that regulate high voltage power are located behind the camera and maintain an accurate voltage to each individual PMT. These boards, powered by crates located in the electronics trailer next to the telescope, are automatically programmed to reduce voltage to individual PMTs that read high currents due to bright stars. Also, the high voltage boards are programmed to shut down voltages to the entire camera if a large percentage of PMTs register an abnormally high current. This safety mechanism is designed to insure that that PMTs do not get damaged by headlights from passing cars, or the spotlights from occasionally passing helicopters. The information that the high voltage crates act

upon is delivered via current monitor boards also located in the camera housing. These boards provide fast (10Hz) and accurate ($\sim 0.5\mu\text{A}$) readout of the anode currents produced by individual PMTs as they are exposed to the night-sky.

In order to provide the highest sensitivity to individual photoelectrons, each PMT is connected to a pre-amplification system also located within the camera housing. This preamplification system provides a gain factor of 6.6 to the output of each PMT enabling the entire camera system to produce a “triggerable” signal from 4.5 photoelectrons.

An improvement in technology over the Whipple 10 m is the VERITAS telescopes’ ability to artificially stimulate the camera readout with pulses that mimic the ones actually produced by light falling on the camera surface. This process, known as “charge injection” (Kieda, 2003) is accomplished via the use of several boards located within the camera housing. Pulses from these boards are sent directly into the base of the PMTs simulating real currents produced by the camera. This process is an extremely valuable tool for providing system calibration and diagnostic information for the most basic properties of the telescopes (looking for channel cross talk and dead channels etc.), to advanced properties of the system such as testing the topological pattern trigger functionality (see next section).

When the wiring necessary to power and control all the PMTs, current monitor boards, high voltage boards, and charge injection systems is taken into account, the camera housing is actually a quite crowded environment. The heat dissipated from all this equipment into a tightly packed space is an important consideration especially when taken in conjunction with temperatures in southern Arizona which can reach appreciable highs at night of $\sim 100^\circ\text{F}$. To deal with this concern, fan systems and temperature sensors are also located within the camera housing to provide a cooling and monitoring mechanism in case the system reaches an inoperable temperature.

3.2.4 VERITAS Trigger System

As in the 10 m, the signal from each PMT is amplified (in this case by the on-board pre-amplifiers located in the PMT base) and duplicated. One copy gets sent directly to a Flash Analog to Digital Converter device (known as FADCs, these are a vast technological improvement over the QADCs of the 10 m due to their finer temporal sampling- see section 3.2.5) in which it is temporarily stored awaiting a decision from the trigger system on whether or not to read out the pixel information. The other copy is passed to the trigger system, and if the event passes all levels of the trigger then a signal is sent to the FADC crates to read out the digitization of the original PMT signal. This process happens in all 4 telescopes within a timescale of 100 ns. If a trigger is broadcast, then all the triggered telescopes read out their individual digitizations and then combine them in what is

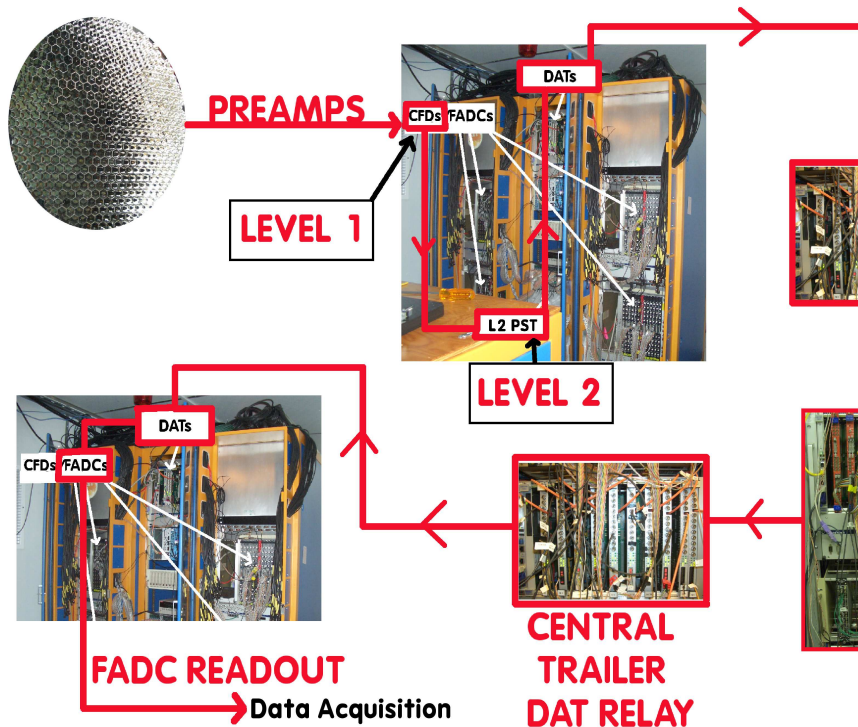


Figure 3.21: A graphical schematic of the VERITAS array trigger system as described in the text known as the “event builder” system.

There are three levels of the trigger system. This system is, in some ways, quite similar to that of the Whipple 10 m and when this is the case the reader will be referred to previous sections for explanations of details. In other ways, however, the trigger system for VERITAS represents a marked advance in both technology and engineering over the Whipple 10m. The trigger for VERITAS consists of three levels (L1,L2,L3) that could be described respectively as a trigger at the individual PMT level, a trigger at the “camera as a whole” level, and then finally a trigger at the “array as a whole” level.

- Level 1 Trigger: CFD** After amplification by the on-board preamplifiers in the camera housing, the signal from each PMT is carried via coaxial cable (Kieda, 2003) and gets duplicated with one copy passed directly to a Flash Analog Digital Converter rack (FADC- see section 3.2.5) in which it is temporarily stored awaiting decision from the trigger system on whether or not to read out the pixel information. The other copy is sent to the trigger system starting with passage through a CFD trigger which decides (based on a pre-programmed threshold) whether the PMT contained enough signal for a trigger as well as the optimal point in time to trigger on (zero crossing determinant or ZCD- see section 3.1.4). A new feature of VERITAS’ CFDs (as compared to those used in the Whipple 10m) is the implementation of a

noise reduction mechanism called a Rate Feedback Loop (RFB loop) (Vassiliev et al, 2003). When the PMTs are exposed to the night-sky background, they will produce small variations in current due to light fluctuations. These fluctuations can produce a slightly degraded calculation of the zero crossing point of the pulse (timing jitter). This can be countered by introducing a small offset in the current to the CFDs (similar to a pedestal), however, this will raise the threshold above which the CFD is capable of detecting pulses. The RFB loop addition to the CFDs remedies this by adding a DC offset to the zero crossing calculation which is proportional to the rate at which the ZCD part of the CFD is being triggered. In this way, as the PMT is exposed to more chaotic background light, the CFD “notices” this and provides an offset to the ZCD sector in order to reduce the error in determining the trigger time. The implementation of this RFB loop results in a $\sim 10\%$ reduction in timing jitter of the ZCD. Overall, VERITAS CFDs are capable of resolving coincident signals in adjacent PMTs down to ~ 4 ns (Vassiliev et al, 2003).

The determination of the CFD threshold is again made by taking “bias curves” which demonstrate the optimal voltage for eliminating as many false night-sky background triggers as possible (see figure 3.23). For the data taken for this thesis, the CFD threshold was determined to be optimal at 50mV, corresponding to 15.9 photoelectrons.

- ***Level 2 Trigger: Pattern Selection Trigger***

Similar to the Whipple 10 m, a topological pattern trigger is implemented to determine, based upon the CFD output, whether or not a pixel pattern compatible with an air shower has been presented. The motivation for the use of this pattern trigger is that noise will in general only trigger one or two adjacent pixels within the camera. By setting up a mechanism by which the trigger system can look for patterns of at least 3 or 4 adjacent triggered pixels, the noise background can be reduced and the threshold of the telescope can be lowered. This is implemented by feeding the outputs of the CFDs into a custom-built signal splitter which routes the pixel signals into overlapping patches of 19 pixels. Since showers that only trigger the outer ring of pixels will be poorly reconstructed (due to truncation of the image), only 463/499 pixels are included in the routing scheme, although the CFD outputs from these excess 36 pixels are still recorded in case a trigger decision is made which will then read these 36 signals out along with the rest of the camera. Each of the 19 PST modules looks at overlapping patches of 19 pixels. The PST module is programmed with a lookup capability for patterns of 3 or 4 adjacent triggered pixels. If the CFD outputs provide a signal that matches any of these patterns, then an L2 trigger is produced and delivered to the L3 trigger

level.

As in the determination of CFD threshold, the choice of whether to trigger on 3 or 4 adjacent pixels is made by calibrating the system response with both of these settings during “bias curve” observations. The differing PST configurations will result in differing night-sky background trigger rates, as shown in figure 3.23. For the data taken in this thesis, the optimal L2 trigger configuration was taken to be a 3-adjacent pixel criterion based on studies of the VERITAS array trigger (Weinstein, 2007).

- ***Level 3 Trigger: Array Trigger***

As events in each telescope pass their respective L2 triggers, the trigger signals are passed from each individual telescope to a central control trailer which combines them to look for “array as a whole” triggers. If an event triggers a preset number of telescopes out of the array within a programmable time window (usually ~ 100 ns), then an L3 trigger is produced and each telescope taking part in the trigger is then told to read out their stored FADC buffer containing that event which is then sent to the “event builder” for further processing. Since the L2 triggers from all 4 telescopes (~ 1 kHz per telescope) must be sent to a central L3 trigger for a decision within a 100 ns time window, a novel approach to data transfer was necessary in order to transfer very fast asynchronous signals (L2 triggers) between the telescopes and L3 and back again.

The solution to this was provided by the construction and commissioning (by the University of Leeds) of the Digital Asynchronous Transmission (DAT) modules in which the author was heavily involved in the first year of this thesis research. These modules provide precise, low jitter signal transfer of the L2 triggers to the L3 system and the L3 triggers back to the telescopes. Traditional signal cable between the telescopes (such as coaxial copper cables) have the disadvantage of susceptibility to lightning strikes, signal attenuation, and the signal dispersion within these cables would lead to an increased timing jitter within the trigger. Therefore an optical fibre link solution was preferred. However, the lasers that would be feasible to use in this situation have a safety feature that forces them to shut off if no data is transmitted (i.e. if they do not switch state) every microsecond or so. Since the L2 triggers are sporadic in nature, this is not acceptable. The DAT modules provide a solution to this problem by transmitting logic encoded optical signals from a transmitting module (TX) over a fibre optic line to be decoded at the receiving module (RX). The TX module combines the L2 triggers with a 25 MHz clock in XOR logic and the result of this combination is then sent over a fibre-optic line via a pulsed laser signal. Since a 25 MHz clock is used, some

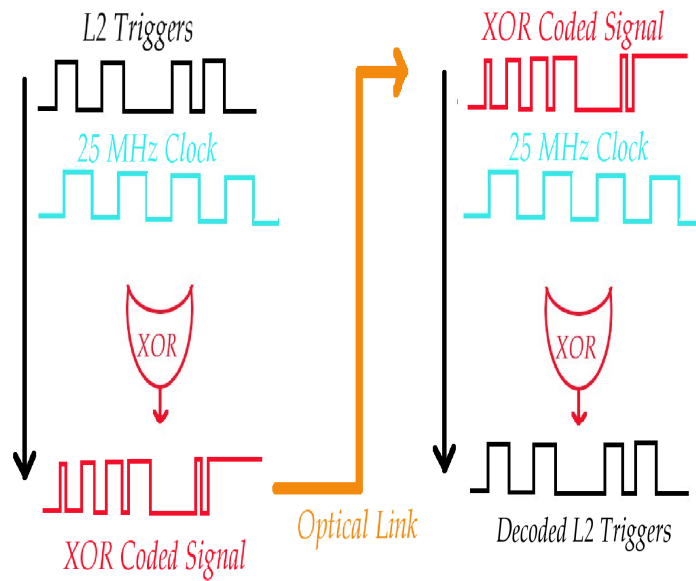


Figure 3.22: The functionality of the DAT modules. The L2 signals are matched with a 25 MHz clock in XOR logic and the result is passed to an optical uplink for transference to the RX module. At the RX module, the signal is again matched to the same 25 MHz clock in identical XOR logic which decodes the original signal and provides the L2 triggers to the L3 system.

signal will be sent by the laser units at least every 40 ns and the lasers will not shut off. At the RX end, the optical signal is received and matched again in XOR logic to a copy of the original 25 MHz clock and the signal is read out. In this way, the original L2 pulse shape is transmitted (see figure 3.21). The communication between the telescopes and L3 requires 8 pairs of DAT modules in total since, for each telescope, one TX/RX pair is required to transmit the L2 signals to L3 and another is needed to relay the L3 signals back to the telescope.

Several iterations of the design of this system were required to provide a final working solution. During the first iteration of the DATs in which the author was involved, the logic encoding of both the outgoing and incoming signal was provided by surface mounted logic chips. Although a cost effective solution, the author (along with Richard White of the University of Leeds) found that (due to the fundamental performance capabilities of the surface mounted chips) this design resulted in a single channel jitter of up to 8 ns and a cross channel skew of 10 ns. Since the overall timing resolution necessary for the VERITAS

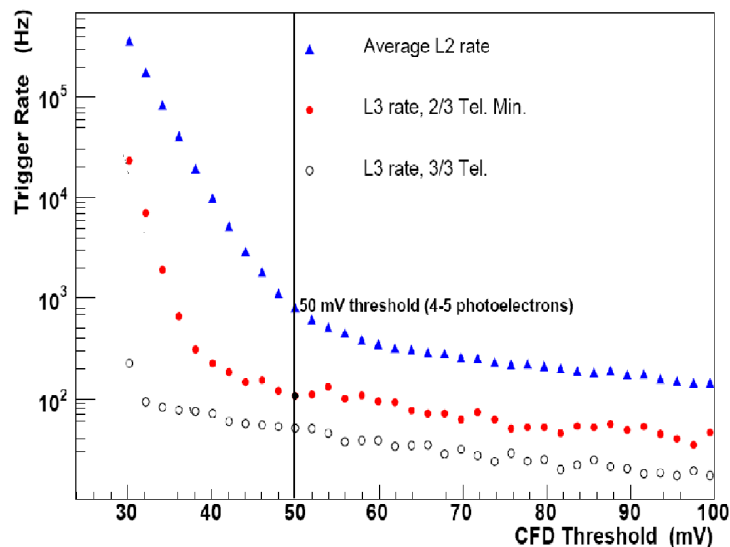


Figure 3.23: An example of a full array bias curve taken for the 3 telescope array. Here is shown the trigger rate as a function of CFD threshold for different configurations of the L3 system. From these observations it was determined that the optimal threshold/configuration for V3 was a CFD threshold of 50 mV and a 2/3 telescope L3 trigger requirement. Figure adapted from Weinstein et al. (2007).

trigger is on the order of 6 ns, this timing jitter was deemed unacceptable. Along with Richard White and Joachim Rose, the author decided that a Field Programmable Gate Array (FPGA) chip design to perform the required logic operations at a much faster rate was to be installed on the DAT boards. The author was involved in the design, implementation, and testing of this new design within the existing framework of the DATs. The installation of these chips to replace the surface mounted logic chips resulted in a marked improvement in timing resolution of the DAT boards of <1-2 ns jitter per channel which is well within operational constraints for the trigger system. There was a final iteration of the DAT design necessary to compensate for varying fibre optic cable lengths between channels, described in White (2007), however, the general framework which was designed by the author, Richard White, and Joachim Rose remains in operation today in the full 4 telescope VERITAS array.

The L3 trigger system can be configured to trigger on any combination of four telescopes (individually, 2/4,3/4,4/4). This choice, together with the choice of CFD threshold for individual pixels, combined with the choice of 3 or 4 adjacent pixel triggers within the PST, will result in a different trigger rate that must be optimized to minimize night-sky background

noise while keeping as many low energy showers as possible. This optimization is, again, achieved via the taking of “bias curve” observations. An example of the optimization for the three telescope array is shown in figure 3.23. The L3 system will produce triggers if signals that satisfy its telescope requirements arrive within a preset time coincidence window (25-100 ns). This large coincidence window will allow for slight variations in arrival times of L2 triggers from individual telescopes. To further reduce the time spread of signal coincidence, delays between signal inputs from telescopes must be applied to compensate for time spread between shower wave fronts hitting telescopes at different distances. These delays, known as “shower delays” are applied as function of observation azimuth and elevation in the L3 system and updated every 10 seconds. It should be noted that the implementation of the L3 array trigger virtually eliminates all triggers from local muons since these events typically only show up in one telescope. The background noise due to muons is one of the most restrictive setbacks for single telescope observations and its elimination via stereo observations is a great leap forward for the technique.

If a shower successfully passes the final L3 trigger requirement, a signal is sent back to each telescope to read the shower out from the FADC buffers. The exploitation of FADCs (as opposed to QADCs), as pioneered by HEGRA and used by MAGIC, represent one of the technological advances used in VERITAS which has the potential to greatly increase the sensitivity of ground based Cherenkov telescopes by allowing for greater temporal resolution of the shower arrival time. Their implementation and functionality are covered in more detail in the next section.

3.2.5 VERITAS FADC System

After an event flag is produced by all three levels of the trigger system described above, the L3 system will send a command to each telescope which took place in the array trigger to instruct it to read out its buffered FADC memory. The FADC’s used on VERITAS represent a significant step forward in the ability to resolve the shower development on a nanosecond time scale. As opposed to the ADC system implemented on the Whipple 10 m which only stores the integrated charge within a time window of 25 nanoseconds (QADCs), the VERITAS FADC system possesses the ability to measure the voltage in each pixel on timescales of 2 ns. Since gamma-ray airshowers will have a much more compact temporal development than cosmic ray showers, this timing information can be exploited to increase gamma-hadron separation within the offline analysis (Holder et al., 2006). Although this use of the FADCs was not (and at time of writing still is not) implemented within the standard data analysis framework of VERITAS, it is useful to explore what capabilities the use of FADCs have for future observations with VERITAS.

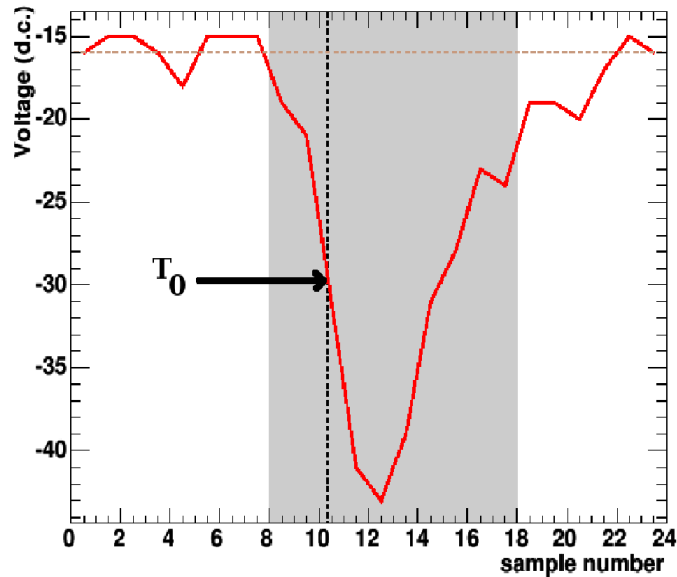


Figure 3.24: A sample FADC trace from a pixel involved in a shower event. The parameter T_0 is defined as the point at which the charge deposited reaches 50% of its maximum. Figure adapted from Holder et al. (2006).

The signals from each PMT are read out by 500 MSPS (Mega Samples per Second) FADC units with a memory depth of $32 \mu\text{s}$ and an 8 bit dynamic range corresponding to 0-255 digital counts (Buckley, 1999). The FADCs have the ability to function in both a High and Low gain mode (gain of 7.25 and 1.21 respectively), which implies that if the signal exceeds the dynamic range of the FADC channel than a delayed copy of the signal in a different gain mode is digitized instead. This results in an effective dynamic range of 1200 counts (Cogan, 2007). These FADC units digitize the shower by accessing its signal in the memory buffer over a range of 24 samples which corresponds to 48 ns (2 ns/FADC sample). Since the shower's signal in each PMT only lasts for a segment of this sample range (see figure 3.24), a FADC sample window must be chosen a priori which will capture the charge deposited within the 24 samples. Typically this window is set to 7-10 samples which catches the deposition of charge within a pixel. There are however, several calibration considerations that must be taken into account in order for this entire procedure to work.

First of all, since the FADCs will only read out if they receive a trigger flag from the L3 system, and forming a trigger decision (due to propagation of the signal through the trigger electronics) can take several μs , a mechanism must be adopted to insure that the FADCs read-out the correct part of their memory corresponding to the shower event. This is accomplished by the calculation of a "lookback time" for the FADCs by taking a special laser run (similar to the nitrogen runs on

the 10 m) whereby each telescope is triggered by a fast pulse nitrogen dye laser which diffuses its light evenly onto each camera face at a wavelength of 400 nm. The global lookback time for each telescope can be adjusted until the FADCs accurately sample the event provided by the laser run. The arrival of the signal in each FADC channel can vary by up to several nanoseconds due to the individual high voltage configurations of each PMT. The camera must be flat-fielded in this respect to remove these channel-to-channel delays. The camera is uniformly illuminated by a diffused source of 4 ns pulse width 400 nm nitrogen laser light. The arrival time of the pulse is measured at the FADC level by determining the time at which the FADC pulse attains half of its maximum value, T_0 (see figure 3.24). The mean value of T_0 is calculated for each channel over the laser run as well as for the entire camera. The differences in each individual pixel T_0 versus that of the camera as a whole can be subtracted off by utilizing a digital delay mechanism within the FADC board which can provide delays of up to 6 ns. Through this relative timing calibration, the channel-to-channel response delay time can be reduced to 0.85 ns (Holder et al., 2006). In addition to the FADC channel-to-channel uncertainty, the four VME crates used to house the FADCs will have a crate-to-crate jitter of 2 ns, which is corrected for by sending a separate copy of the L2 trigger to one FADC channel in each crate. The crates then use this channel as a trigger with which to synchronize on an event by event basis. At this level of data sampling, the FADCs are only functioning as a newer version of the Whipple 10m telescope QADCs. However, it is possible to extract much more information from the FADCs by calibrating and parametrizing the temporal development of the signal within the FADC. In order to properly utilize all of the timing information provided by the FADCs, the integration window must be accurately constrained so that as much of the pulse and as little of the non-pulse as possible is integrated within the 24 sample FADC range (signal-to-noise). The “Two-Pass Method”(Holder et al., 2006) is an example of how such timing information may be obtained and exploited.

The method consists of first setting a fixed FADC window of 20 ns and measuring the arrival time of the pulse as a function of PMT position along the long axis of the shower. The gradient of a linear fit to this function is known as $TGradX$. The value of $TGradX$ is then used to refine the start position of a shorter integration window of the FADC. This start position will vary as function of each pixel’s position within the shower image. Using this method, the integration window can be collapsed to as little as 10 ns which provides excellent resolution of the charge deposited in each pixel. Standard image cleaning and parametrization then takes place on the newly resolved images with preliminary improvements of charge resolution of the shower image at the 10% level (Holder et al., 2006).

There are also other techniques which utilize the capabilities of the FADCs, described in de-

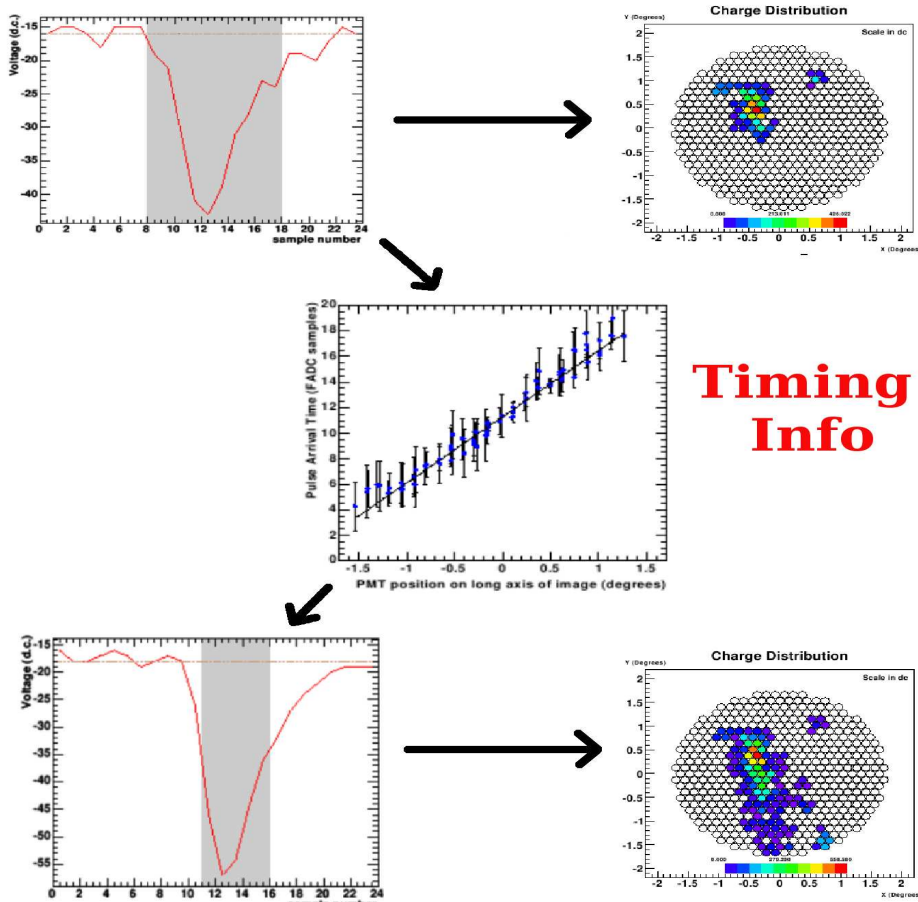


Figure 3.25: An example of using the timing information provided by the FADCs. On the top row is the integration window (20 ns) that results in the shower image seen to its right. Moving downward, a measure of the time of the pulse arrival as a function of pixel location along the long shower axis is measured. $TGrad_x$, or the gradient of the linear fit to this plot is used to determine the relative timing of each pixel involved in the shower. Individual (pixel by pixel) integration windows are then calculated in order to lower the FADC integration window which then results in an enhanced shower image (bottom row) due to a greater number of pixels passing the cleaning threshold. Figures modified from Holder et al. (2006) and Cogan (2007)

tail in Cogan (2007), mainly based upon enhanced parametrization of the FADC trace. For all the analysis performed in this thesis, however, only the standard method of a set FADC integration window with no timing information was utilized. In the future, the FADC system will be implemented in a greater capacity for observations with the full 4 telescope VERITAS array.

3.2.6 VERITAS Data Acquisition

There are functionally two levels of data acquisition for VERITAS. As one might imagine these consist of acquisition of data at the telescope level and acquisition at the array level. At the telescope level, the VME computer system responsible for most of the above trigger and readout operations (known as DACQ) oversees such things as the setting of FADC lookback times and CFD thresholds. When a trigger is enabled to readout the FADC buffers, DACQ will take the FADC readout along with the trigger time (GPS timestamped to within $1\mu\text{s}$) and event number stored in each FADC crate. The data is stored in the DACQ buffer until it is readout by the individual telescopes' "event builder" computer. The event builder performs basic data quality control by looking for incomplete or fragmented events and reads this information out in a coherent form to the observer. Once all fragments of the event are compiled from the FADCs, the event is transferred to the array level data acquisition system, or "data harvester".

The data harvester combines events from all telescopes with information from the L3 trigger system as well as another GPS timestamp for the array event as a whole. All this information is then stored in a custom designed binary data format, VERITAS Bank Format (VBF). Special compression schemes are utilized in order to bring down the size of each observational data run since, all told, a 30 minute data run of events from 4 telescopes will occupy 5 GB (after compression!). For comparison, a 30 minute telescope run from the Whipple 10m (after compression) is 3 MB in size. The primary reason for the large explosion in data size is the extra data (per event) provided by the FADCs.

3.2.7 VERITAS Data Calibration, Cleaning and Parametrization

The data calibration procedures are similar to the Whipple 10m in that steps are taken to ensure uniform camera response as well as the optimal rejection of background noise. Although many of these procedures are analogous to those performed on Whipple 10 m data, the hardware setup for VERITAS is sufficiently different that many of these calibration procedures require extra consideration.

- **Pedestals:** As was mentioned earlier in this chapter, since night-sky fluctuations present the most harassing background in the absence of Cherenkov light, a method must be em-

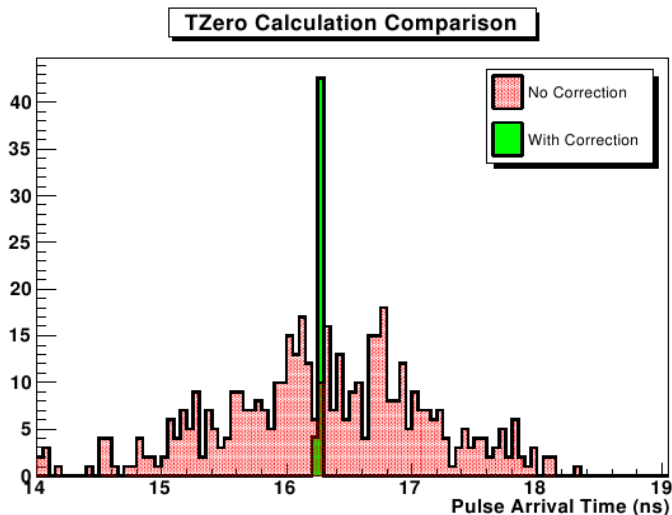


Figure 3.26: The effect of T_{Offset} correction to the arrival time of pulses over the camera. The red distribution shows the average arrival time of pulses per channel from a laser run. The green distribution shows the same quantity after T_{Offset} corrections. Figure courtesy of Peter Cogan.

ployed in order to pad the data against positive fluctuations from this background. This is accomplished through the use of pedestal injection which is described for the Whipple 10 m system in section 3.1.5. Similarly, pedestal events are artificially triggered at a rate of 1-3 Hz within the VERITAS trigger system. There are several differences between the pedestal calibration for VERITAS as opposed to the Whipple 10 m however. Firstly, in order to more accurately parametrize changing night-sky conditions due to rotation of the field of view, the pedvar corrected charge per pixel is calculated every three minutes during the data run. Additionally, extra care is needed to properly set what window the FADCs will integrate the pedestal events over. To ensure an accurate statistical measurement of the NSB, a few different FADC window sizes (2-10 samples) are chosen. In addition to this, the start time of the sample within the trace is chosen at random on a trace-by-trace basis (Cogan, 2006). The pedestal measurement is then averaged over all start times and integration windows per channel to give the most reliable measurement of the pedestal statistics possible.

- **T_{Offset} Calibration:** As was mentioned in the previous section, when illuminated by laser light falling simultaneously on every pixel, each pixel will have a slightly different value of T_0 , or the time at which the pulse within the FADC for that pixel reaches its 50% mark. This is mainly due to slightly different high voltage settings of the pixels. In order to correct for this discrepancy the calculation of the T_{Offset} value for each channel must be calculated which is simply the average difference between the signal arrival time in an individual pixel

and that average for the camera as a whole. The offsets are calculated on a pixel by pixel basis and corrections applied to the pulse timing for each channel. The effect of the T_{Offset} corrections can be seen in figure 3.26.

- **Gain Calibration:** The process of equalizing the gains from each PMT proceeds similarly to that of the 10 m. In the case of VERITAS, each telescope is linked up to a 337 nm nitrogen laser light source (kept at a central location) by quartz fibers. Opal diffusers placed 4 m in front of the camera illuminate the cameras evenly (down to 1% spread) with 4 ns pulses of laser light at 400 nm (Hanna et al., 2007). 5 minute long “laser runs” are taken every night in order to provide gain calibrations for each PMT for each camera. The PMT gains are adjusted so that each telescope camera provides a uniform response to the laser pulses. Additionally, the gain values per PMT are taken into account to accurately calibrate the charge deposited in each PMT during offline analysis.

- **Digital Counts/Photo-electron Calibration:**

Although not part of the online/nightly calibration techniques like pedestal injection or PMT gain measurement, it is important to clearly resolve the fundamental response parameters of the telescopes. Typically, this implies measuring how the cameras respond to signals that will only produce single (instead of multiple) photoelectrons within the PMT. This is important when attempting to characterize simulations of the detector’s response to air showers. There are several ways of making the single photoelectron (single p.e.) measurement. The most direct method involves placing a thin metal screen in front of the camera. This screen is completely opaque except for 499 identical tiny holes drilled at the exact location of the PMT fronts. This screen is illuminated with the nitrogen laser used for gain calibration and the intensity of the laser light is adjusted until the signal from single photoelectrons being produced at the photocathodes of the PMTs are clearly visible in the data stream. This is judged by acquiring a histogram of the digital charge integrated from the FADCs during these special “single P.E. runs”. There will be a peak in the distribution arising from pedestal events (i.e. no photoelectrons), however, any subsequent peaks will be due to single/multiple photoelectron events. An example of such a histogram is shown in figure 3.27. From measurements performed with this method, it is estimated that the $dc/p.e.$ is 5.3 ± 0.53 for VERITAS cameras (Holder et al., 2005).

An alternate method for measuring this $dc/p.e.$ ratio is via muon rings detected in data runs. As was described in section 2.7, Cherenkov light from local muons will create rings of light with a fixed amount of light per unit arc length. Additionally, the light observed by

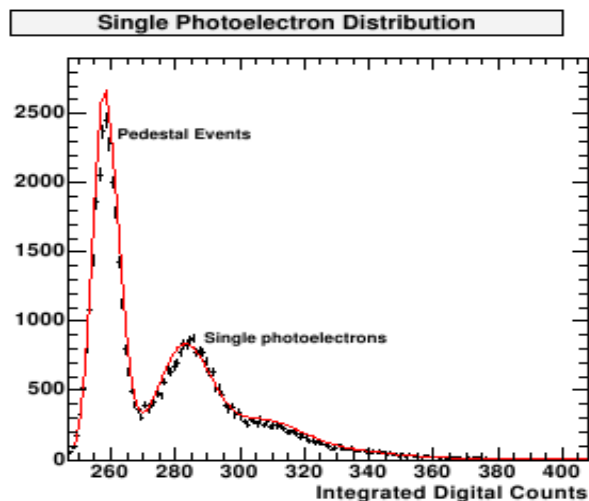


Figure 3.27: The digital count distribution from a “single p.e.” laser run. Here, the peak corresponding to pedestal events is readily identified as well as the peak corresponding to single p.e. events. The 2 p.e. event peak is just barely visible to the right. After taking into account the gain factors of the system, the dc/p.e. ratio was found to be 5.3. Figure taken from Holder et al. (2005).

a telescope from a muon event only depends on the impact parameter (distance of impact away from the camera) of that muon and will always be the same for muons of the same energy. The reliability of muon showers allows one to use them in calibrating the cameras. By picking out the muon events from a real observation data set, it is possible to accurately predict what energy muon created it and what its trajectory parameters were. Then, by comparing how many digital counts the muon created within the detector to Monte Carlo simulations of how many photoelectrons the same muon should have produced, one can extract a dc/p.e. ratio. This procedure was carried out for the first VERITAS telescope and is described in Humensky et al. (2005). The dc/p.e. ratio extracted via this method was 5.52 ± 0.49 which is in good agreement with the method using the special laser runs described above. It should be noted that the process of absolute calibration was carried out for the current Whipple 10 m configuration resulting in a calculate dc/p.e. ratio of 2.5 and is described in detail in Schroedter (2004).

- **Image Cleaning and Parametrization**

The processes involved in cleaning events at the camera level are essentially identical to those described for the Whipple 10 m and can be found in section 3.1.5. These are the subtraction of the injected pedestals, application of the gain corrections as determined by the laser calibration run, and finally the image cleaning based on the *image/boundary* thresholds

(based on pedvar calculations). For the VERITAS data, the *image/boundary* parameters are slightly different, namely, any pixel containing a $>5\sigma$ difference above its pedvar is considered to be an image pixel and any pixel neighbouring an image pixel with a $>2.5\sigma$ difference above its pedvar is considered to be a neighbour pixel. Runs taken in ON/OFF mode by VERITAS are also subject to software padding described in section 3.1.6.

The basic image parametrization applied to single telescope events at VERITAS is again, very similar to the Whipple 10 m method, namely, the fitting of an ellipse to the shower images and the application of parameters (Hillas, 1985) to quantify the geometry of that ellipse. However, the methods used for utilizing the results of that parametrization are slightly different for VERITAS as compared to the 10 m and are representative of the advantages (and difficulties) of going from single telescope observations to stereoscopic array observations.

3.2.8 VERITAS Individual Telescope: “Quality Cuts”

The set of cuts known as “Quality Cuts” is used in VERITAS in order to reject events (on a camera-by-camera basis) mainly due to night-sky background noise or improperly formed events within the camera. The more involved cuts which attempt to reject cosmic-ray images come with the utilization of “Image Shape Cuts” which are described in the next section. Quality Cuts reject small noisy events by setting the following cuts: *size* cut (usually 300-400 d.c.) per event in order to weed out weak NSB events; a cut on the number of pixels involved in the event (*NTubes*) which is set at ≥ 5 in order to eliminate images due to NSB which can trigger groups of 3 or 4 pixels; and a *distance* cut (see section 3.1.5) which eliminated images appearing at the edges of the camera which, even if due to gamma rays, are troublesome to reconstruct.

3.2.9 VERITAS Array Cuts “Image Shape Cuts”

At this stage we have a set of events from the data acquisition system full of array events that triggered a subset of telescopes. The quality cuts described above eliminated events that may have triggered the array but were actually only due to small NSB events (fluctuations, planes, satellites, etc.). We now need to eliminate as many events as possible from our set that are due to cosmic ray showers. For the Whipple 10 m, this was accomplished via the use of (primarily) *length* and *width* cuts (we no longer need a *length/size* cut due to our lack of muon showers thanks to the array trigger). Instead of using the standard *length* and *width* parameters for image parametrization and hadron rejection for array events, it is possible to utilize the vastly improved ability of stereoscopic arrays to determine the shower impact parameter (see section 2.7). This utilization comes via the observation that the *length* and *width* parameters strongly depend on

both the *size* and impact parameter of the event. Noting this, one can then produce large banks of Monte Carlo simulations of gamma-ray air showers at specific zenith angles and examine the resulting *length* and *width* as a function of *size* and impact parameter. These simulations are used to fill what are known as “look-up tables”, and by using them it is possible to define for each event (per telescope) the following modifications of *length* and *width* (Daum et al., 1997):

- Scaled Length and Width: SL/SW

$$SL \equiv \frac{length}{\langle length_{lit}(S_{event}, I_{event}) \rangle} \quad (3.7)$$

Where *length* is the image length, S_{event} and I_{event} are the size and impact parameter (determined from array level impact reconstruction) of the **observed** event. $\langle length_{lit}(S_{event}, I_{event}) \rangle$ is then the mean of the simulated *length* values (from the look-up tables) which also had the values of S_{event} and I_{event} . Similarly,

$$SW \equiv \frac{width}{\langle width_{lit}(S_{event}, I_{event}) \rangle} \quad (3.8)$$

With these in hand, we can then weight the SL/SW per i^{th} event and combine them over n telescopes to get:

- Mean Scaled Length and Width: MSL/MSW

$$MSL \equiv \frac{\sum_i^n S_{event}^i (SL^i)}{\sum_i^n S_{event}^i} \quad (3.9)$$

$$MSW \equiv \frac{\sum_i^n S_{event}^i (SW^i)}{\sum_i^n S_{event}^i} \quad (3.10)$$

The derived values of MSW and MSL are then used as a powerful cutting parameter with which to eliminate cosmic-ray showers from the data set. The usefulness of cutting on these parameters is shown in figure 3.28. After the data set has undergone the quality and image shape cuts, there is a final value of the shower image that is used as a cutting parameter. Called Θ^2 , it is the stereo equivalent of the *alpha* parameter used in Whipple 10 m analysis and is explained in detail in the next section.

3.2.10 Directional Cut: Θ^2

Since the image in each camera contains directional information about the shower (encoded in the orientation of the long axis of the shower) we can use this information to reconstruct, to a high degree of accuracy, the original impact position of the shower core. On the Whipple 10 m,

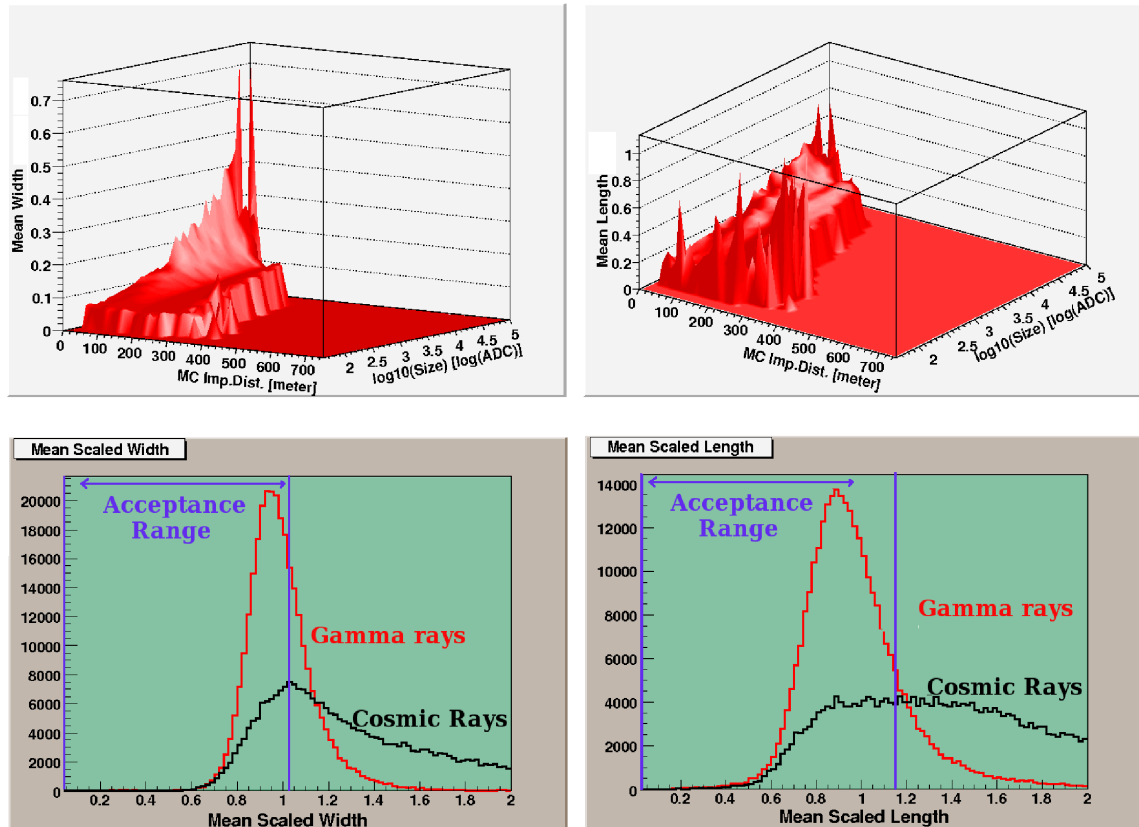


Figure 3.28: Demonstrating the computation and efficacy of the mean scaled parameters as they are explained in the text. The top row shows the look-up tables for MSW (left) and MWL (right). The calculation of MSW/MSL for an array event proceeds by averaging the length and width slices for a set size and impact parameter (given by the array reconstruction of the event) within these lookup tables. This average is then *size* weighted and summed over the equivalent calculation for the event as seen in all telescopes in the array. The bottom row shows the use of MSW and MSL as cut parameters for cosmic ray rejection. The red distributions shown are from gamma-ray simulations with the black distributions representing cosmic-ray simulations. The allowable range generated by the cuts are shown by purple lines. The gamma-ray distribution for both MSW and MSL is much more compact and limited in range.

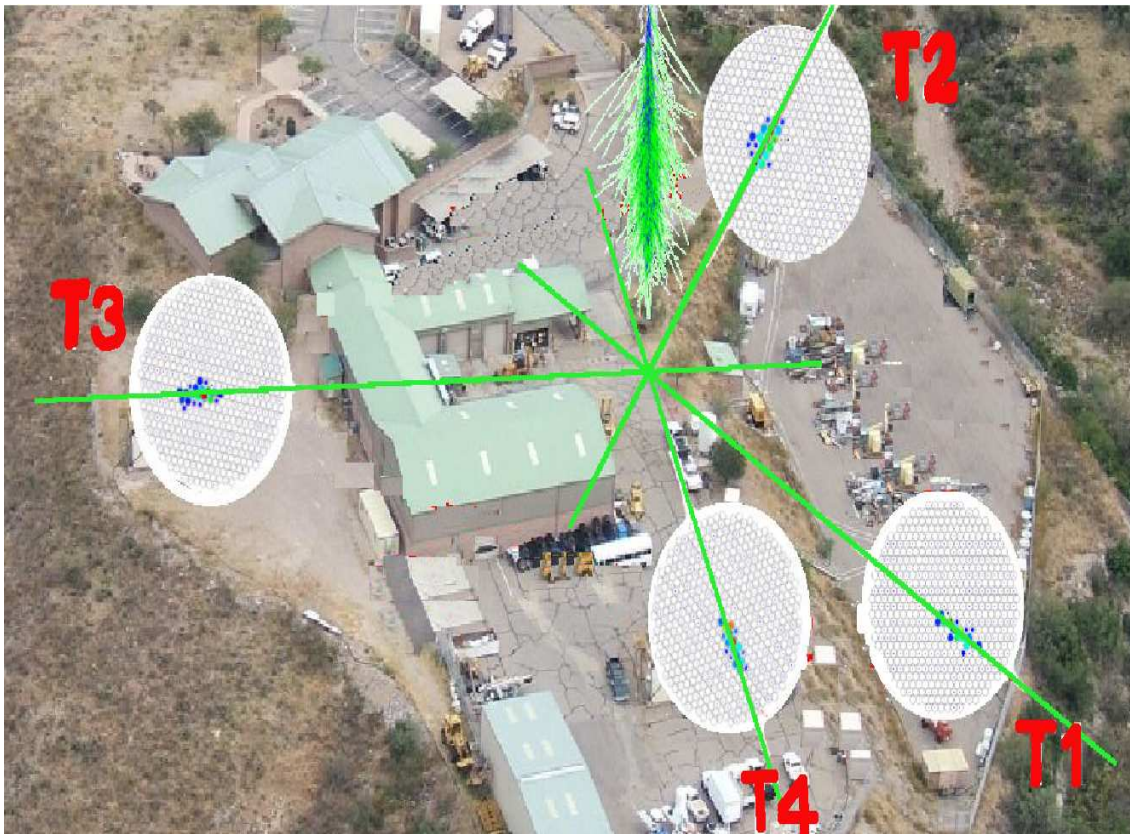


Figure 3.29: Four independent shower images can be used to locate the exact shower core impact position. This impact parameter is then used for calculation of MSW and MSL parameters, as well as calculation of the Θ^2 parameter. It should be noted that the direction of the images on each camera in reality would be reversed.

only a single image was available, therefore, the exact position of the shower core impact was not available (for example, for a single shower image the ellipse could be pointing in two totally opposite directions). However, with an array of images we can extrapolate the major axis lines of each shower image and measure their meeting point (see figure 3.29). In the case where the lines do not meet at a single point, the locations are weighted by the size of the contributing image (i.e. the axis from a brighter image will “have a stronger say” as to where the lines meet). By superimposing all camera images on a single camera (see figure 3.30), it is possible to measure the angular distance from this intersection point to the center of the field of view, or in the case of offset observations, to the point on the camera where the putative source is assumed to be (Daum et al., 1997b). This angle parameter is called Θ and its squared value Θ^2 is an extremely useful parameter to eliminate shower images that do not originate from the point on the sky that we are observing since the number of source events is linearly proportional to the area in the camera field

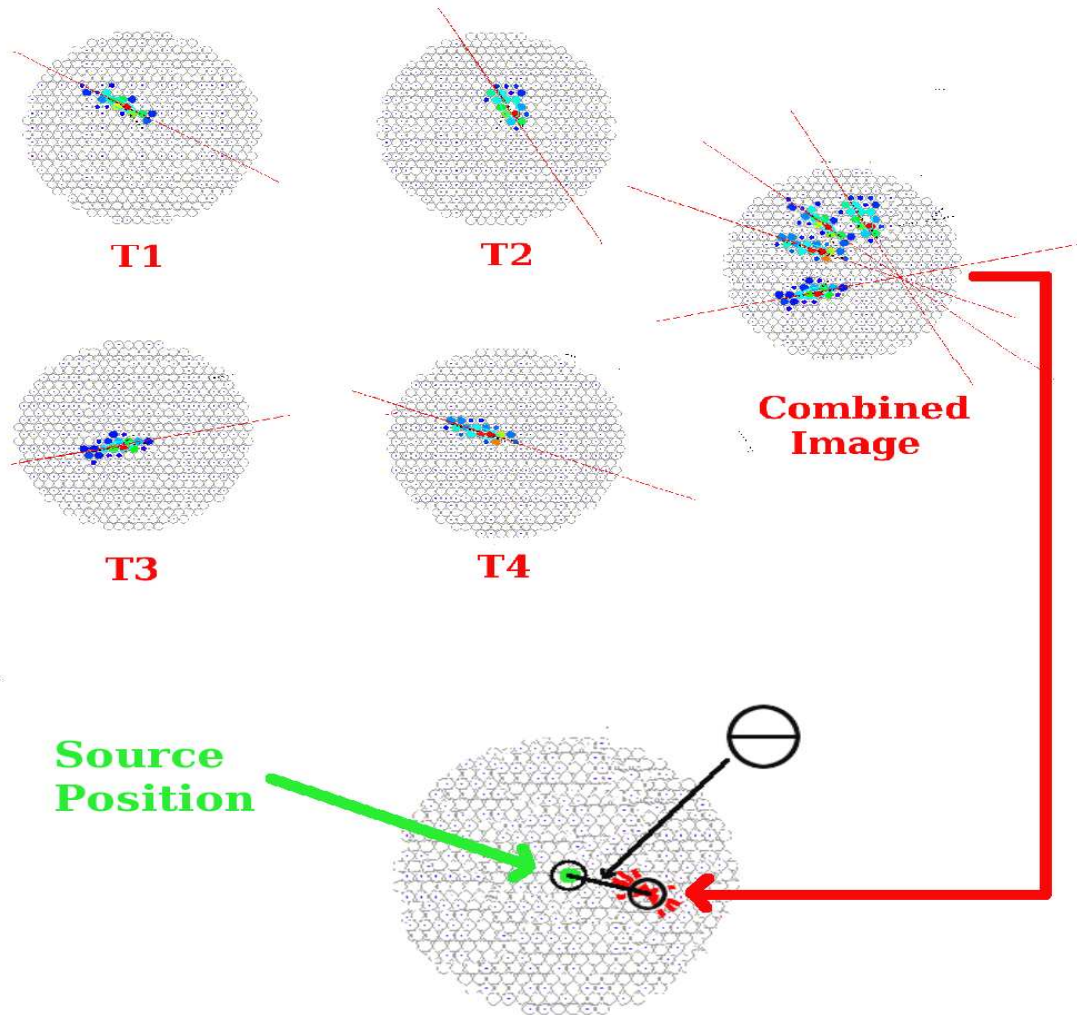


Figure 3.30: A demonstration of how the images from all telescopes are combined to locate the angular position (on the camera) where the shower is assumed to have originated from. This position is then used to compare to the position on the camera of the assumed source and its angular distance Θ is calculated. If the source is offset in the camera (as in Wobble mode), Θ will be then be measured to that offset position.

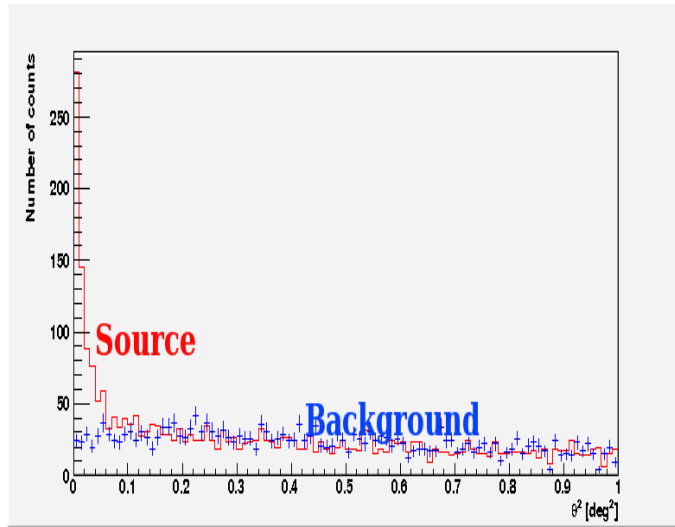


Figure 3.31: A Θ^2 distribution for ~ 1.5 hours of Crab Nebula data taken with 2 telescopes. Here the distribution from the source is clearly evident with counts increasing dominantly over the flat background at small Θ^2 values.

of view of radius Θ . Array images with a large values of Θ^2 will have originated away from the source position and will be discarded. The exact value of the Θ^2 cut will depend on what types of observations are being performed (extended sources such as large supernova remnants would require a large Θ^2 window), however a standard cut is $\Theta^2 \sim 0.025^\circ \rightarrow 0.035^\circ$.

3.2.11 Wobble Observations

Although VERITAS does still utilize both TRACKING (mostly for GRB ToO observations) and PAIRS observation, the primary mode of observations for VERITAS is what is known as “Wobble” or offset observations which has proven to be an effective observing method for other multiple telescope Cherenkov arrays such as H.E.S.S. and HEGRA (Bernlohr, 2003; Daum et al., 1997b). Although this targeting is possible for the Whipple 10 m also, the relatively limited off-axis response did not make it feasible for that telescope. However the VERITAS arrays’ superior off-axis performance and larger field of view allow for this mode of observation which maximizes what limited observational time is available each year. Wobble mode proceeds as follows: instead of the telescope pointing directly towards the center of the source, the source is offset in the field of view in all telescopes by a set amount of either $\pm RA$ or $\pm DEC$ (simulation studies of the VERITAS telescopes have shown that the optimal offset is 0.5° (Beilecke, 2007)). It does not matter *a priori* what direction the offset is taken in; however, for large sets of observations on the same target it is desirable to have equal numbers of observations in all offset directions used in order

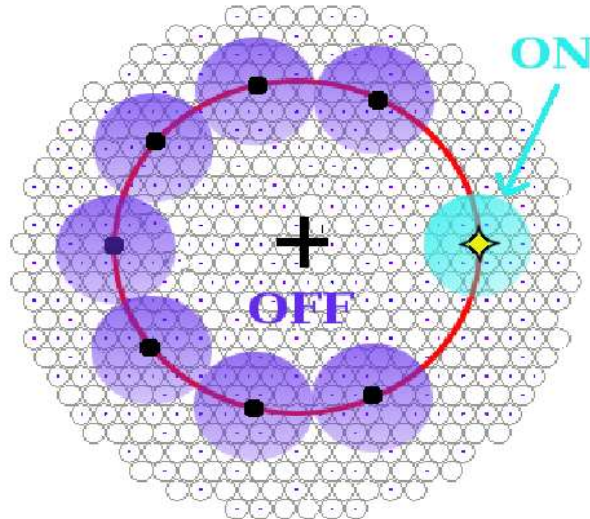


Figure 3.32: Wobble Mode Observing. The source (yellow star) is offset in the camera by a set amount in RA or DEC. Any events which are reconstructed within a set radius of the source position are considered ON events (blue region). A given number (in this case 7) of OFF regions are similarly constructed around the circle having a radius equal to the source offset. Similarly, events reconstructed as falling within these background regions (purple) are considered OFF events.

to eliminate any possible camera bias. VERITAS Wobble observations are taken in one of four Wobble directions: N,S,E,W- corresponding to 0.5° positive offset in RA, 0.5° negative offset in RA, 0.5° positive offset in DEC, and 0.5° negative offset in DEC.

The main advantage of wobble observations lies in the ability to observe both the signal and the background control region at the same time. The acceptance function of the camera goes down as you move away from its center; therefore by using source and background regions at identical radial distances from the center of F.O.V., one can utilize both signal and background regions with equal acceptance for gamma-ray signals. Shown in figure 3.32 is a representation of this concept. Both signal and background regions are defined as disc sections of the camera with radii that are set such that the regions do not intersect and they are smaller than the original wobble offset. Events that are reconstructed to fall within the source disc are considered source events (*ON*) and likewise for the background regions. In order to eliminate the possibility of background bias (if there are dim stars in a particular region of the camera), more than one background region is used and typically either 5 or 7 independent background regions are utilized for a wobble run. The number of background counts from all the regions *OFF* is averaged over the number of regions n to give an accurate representation of what the background counts are for the same sized region as the ON disc. Although the sensitivity of Wobble mode observations to the source flux is slightly

reduced (due to the source being offset from the center of the FOV), this is compensated for the more accurate background determination ($\sqrt{(n)}$ where n is the number of background regions).

In contrast to the calculation of gamma-ray rate and significance presented in section 3.1.6, the results from the VERITAS data set will use the formulation of these quantities as put forth later in Li and Ma (1983):

$$S = \sqrt{2} \sqrt{ON * \ln \left(\frac{(1 + \frac{1}{n})ON}{\frac{1}{n}(ON + OFF)} \right) + OFF * \ln \left(\frac{(1 + \frac{1}{n})OFF}{ON + OFF} \right)} \quad (3.11)$$

With the associated gamma-ray rate being defined as:

$$R_\gamma \pm \Delta R_\gamma = \frac{ON - \frac{1}{n}OFF}{\Delta t} \pm \frac{ON - \frac{1}{n}OFF}{S} \quad (3.12)$$

It is this definition that will be used in calculating the significance and gamma-ray rate for data taken in this thesis.

For 2-dimensional analysis, a slightly different method of measuring the background of wobble observations must be employed. Known as the **Ring Background Model** (Berge et al, 2006), this method provides significances for each bin within the field of view by providing both “source” and background counts for that bin. In this way, a 2-d image of the field of view can be constructed. To accomplish this, the observed field of view is broken down into two dimensional bins. Each of these 2-d bins is encompassed by an “ON” region disc which contains all the reconstructed events that will be considered to be originating from that bin. Surrounding this bin is an annulus of a set radius and width which is sufficiently larger than the ON disc to avoid events bleeding into the two different regions (see figure 3.33). This region will contain all the events considered to be “OFF” events for the chosen 2-d bin and a scaling factor α is applied to the background which is a function of the ratio of the sizes of the ON and OFF regions, usually chosen to be $\sim 1/7$ However, since the camera will have a different sensitivity to gamma-ray showers as a function of linear distance from the camera center (acceptance) and this background ring will contain regions of the field of view with different acceptances, an acceptance correcting function must be applied to the α factor for every bin of the background annulus. Equation 3.11 is then used to determine the significance of each bin. After this, image smoothing is applied via either a Gaussian or “Top-Hat” smoothing function which calculates the significance of each bin via a weighted average of the bins around it in a two dimensional region. The ring background model provides a method for calculating 2-d significances which is robust against arbitrary gradients (due to brightness of the sky or differing camera sensitivity) within the field of view (Berge et al, 2006).

3.2. THE VERITAS ARRAY

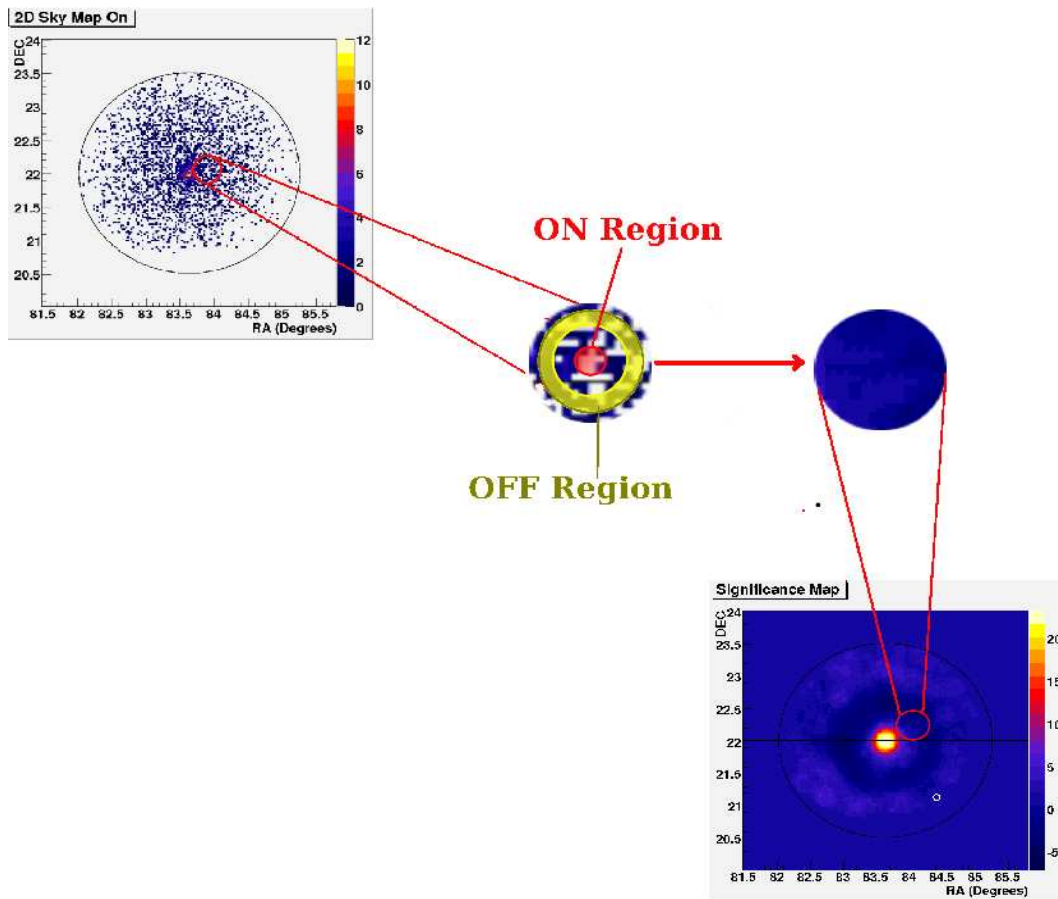


Figure 3.33: A demonstration of how the Ring Background Model works. For every region of the reconstructed 2-d sky map, an ON region is chosen (red) and an OFF region comprised of a surrounding annulus (yellow). The significance of each region is then calculated and a smoothed significance map is created.

3.2.12 Spectral Reconstruction

Possibly the most important physical quantity that can be derived from observations of high energy gamma-ray sources is the source spectrum. This information can inform us about acceleration processes within the source as well as, in the case of distant blazars, about the characteristics of the extragalactic background light absorption. The process involved in extracting the spectrum of a source is heavily dependent upon Monte Carlo simulations which are used for comparison to the observed data to estimate an incoming spectrum. The general method used is that detailed in Mohanty et al. (1998), which necessitates the ability to estimate the energy of each individual gamma ray as well as a method for determining the energy dependent collection area of the array. The former gives the raw information regarding how the observations reflected the intrinsic source spectrum and the latter allows us to disentangle this reflection from the observational process itself.

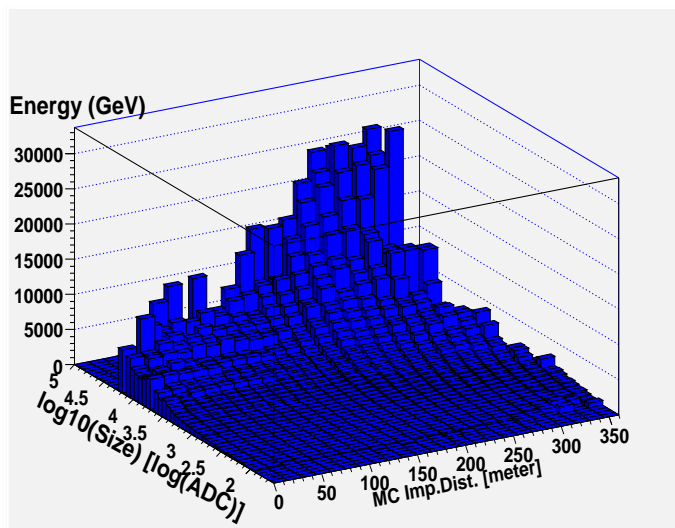


Figure 3.34: An example of the lookup tables used for determining the primary gamma-ray energy via its reconstructed impact parameter and measured *size* parameter.

Alternately, given a number of incoming gamma rays N_γ in each energy bin ΔE over a set area around the telescopes, the effective area tells us how likely it is that the array will trigger on these gamma rays.

- Energy Estimation** With a single telescope, there exists an inherent degeneracy in determining if a shower was energetic or just close by, with a multiple telescope array, we can do away with this uncertainty and isolate the shower energy based on its size and projected impact parameter. As in the determination of the shower impact parameter in section 3.2.8, the determination of the energy of the primary is accomplished by using simulations to produce “lookup tables”. Shown in figure 3.34 is an example of one of the lookup tables used to determine the primary energy. Once the size and impact parameter of the shower have been reconstructed, a specific lookup table for each 10° band of zenith angle will then provide an accurate estimation of the primary energy.

- Collection Area**

The effective collection area of the array will change depending on what elevation the observation is taken at since the array will have a larger effective area at large zenith angles due to the greater area that the light pool from the shower will cover. The effective area is also heavily dependent upon primary gamma ray energy. Since there is no test beam from outside the atmosphere that we can use to calibrate the effective area of the telescopes, we must rely instead upon simulations. Monte Carlo showers are produced from various angles

3.2. THE VERITAS ARRAY

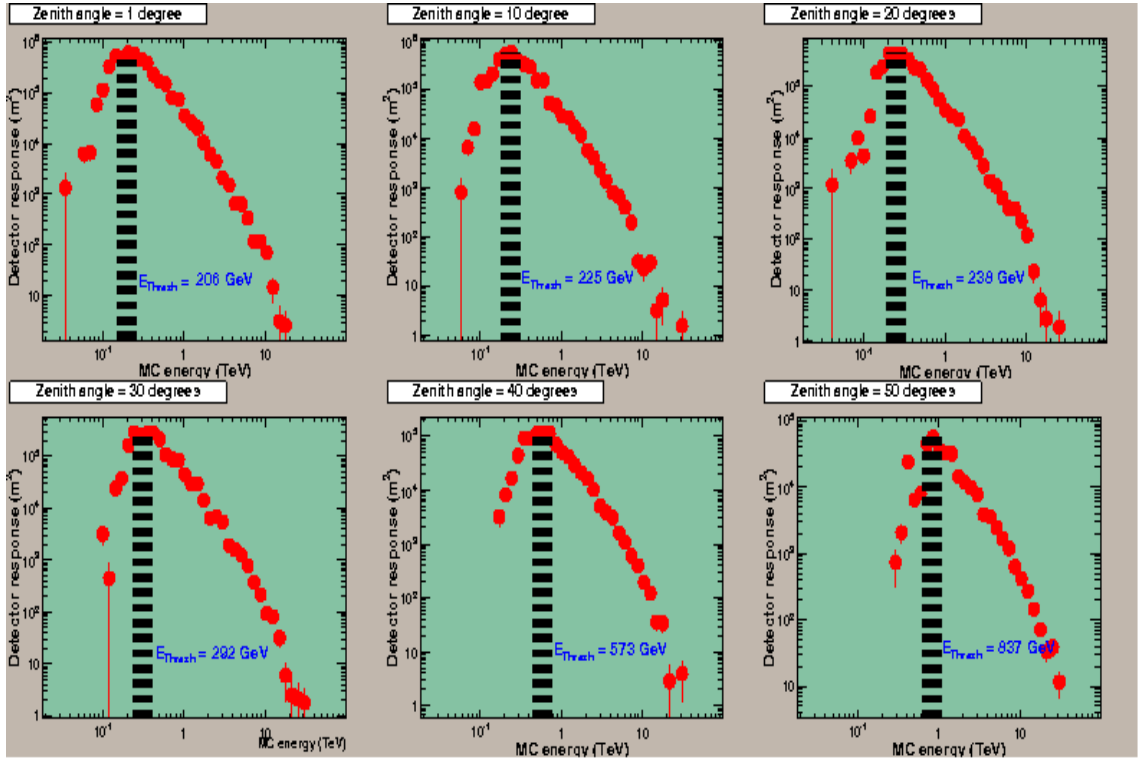


Figure 3.35: Examples of detector response versus primary energy for various zenith angles. These plots are from Monte Carlo simulations of the VERITAS-3 array. The threshold energies (E_{Thresh}) as defined earlier in this section are shown by thick dashed lines. These threshold energies represent the energies at which the array’s effectiveness in detecting a Crab-like source would have a maximum. Notice that this threshold does not increase significantly until quite large ($\geq 40^\circ$) observational zenith angles are reached.

and energies and are then fed through a simulated version of the array. The resulting triggers are then analyzed in just the same way as normal data. The effective area can then be estimated by looking at the ratio of the simulated showers versus the number that passed the analysis cuts. For gamma rays that are simulated as falling within an area A_0 (centered on the array), the effective collection area at a given energy (E) is given by:

$$A_E = A_0 \frac{N_{pass}}{N_{simulated}} \quad (3.13)$$

where N_{pass} is the number of simulated gamma rays that survive analysis cuts, and $N_{simulated}$ is the original number of simulated gamma rays. By folding the effective area curve with a Crab Nebula spectrum, one can achieve a “detector response” curve, which is a gauge of how responsive the detector will be to a Crab Nebula-like spectrum source viewed at different zenith angles. Several of these detector response curves are shown in figure 3.35.

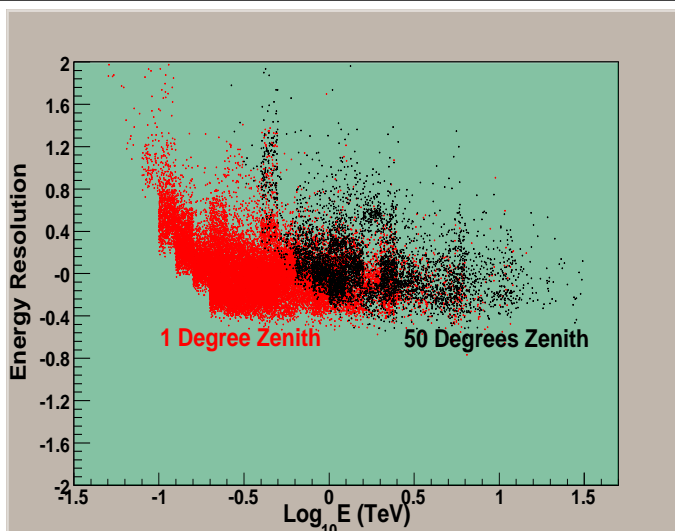


Figure 3.36: Comparison of the simulated energy resolution for incident gamma rays at 1° zenith angle (red) and 50° zenith angle (black). It is clear that the resolution of energies becomes much more efficient for lower energies at smaller zenith angles.

- **Energy Resolution**

Also taken into account in the process of spectral reconstruction is a gauge of how accurately the array (and associated analysis chain) is able to reconstruct the energy of the gamma ray. This is obtained by matching the results of analyzed Monte Carlo simulations with the properties that we know they had. In other words, if we simulate a 2 TeV gamma ray and via the detection simulation and analysis it is reconstructed as a 1.5 TeV gamma ray, then it is understood that our energy resolution is at the $0.5/2 = 25\%$ level. Of course, this parameter is energy and angle dependent, but extended Monte Carlo studies estimate the energy resolution of the VERITAS array to be at the 10-20% level (Maier et al. 2007a).

Given the above information along with a strongly detected source in our observations, how do we then go about extracting a spectrum from the dataset? With energy dependent effective area A_{eff} , X number of detected gamma rays of reconstructed energy E , and the time T_{obs} over which the observations were taken, we can construct our source spectrum as:

$$\frac{dN}{dE} = \frac{1}{T_{obs}A_{eff}} \frac{dX}{dE} \quad (3.14)$$

Which is then expressed in units of $\gamma s TeV^{-1} s^{-1} cm^{-2}$. By using this spectrum, we can then choose a threshold energy above which to integrate and extract an integral flux in terms of $ergs^{-1}$ or other comparable energy measurements. The simplest assumption to make about the intrinsic spectrum

(when we have no reason to believe otherwise) is that it can be fitted by a power law:

$$\frac{dN}{dE} = AE^{-\alpha}dE \quad (3.15)$$

Where A is a normalization constant and α is a differential spectral index. It should be noted at this time that since the entire process of spectral extraction (including the calculation of A_{eff}) is dependent upon Monte Carlo simulations, and these simulations were produced with some pre-defined spectral shape (usually that of the Crab Nebula spectrum), it would seem logical to expect that our reconstructed and fitted spectra should be heavily dependent upon the spectral shape of the simulations and not completely independently derived. This is only partially true. As it turns out, although there is bias effect of extracting spectra based on simulations with a defined spectral slope, this effect is estimated to result in an error of less than 5% (Aharonian et al., 2006c) for a wide range of reconstructed spectral indices and can be readily ignored.

3.3 Summary

In this chapter a comprehensive examination of both the Whipple 10 m telescope and the VERITAS array has been presented. The structural, hardware, and data flow configurations of both experiments have been examined and contrasted with each other. One of the goals of this chapter has been to demonstrate how the same experimental method for detecting high energy gamma rays can be improved by the implementation of a stereo array. To sum up, Table 3.2 shows the physical and performance characteristics of both experiments. Although no data from the full 4 telescope configuration will be used in this thesis, the characteristics are still presented for completeness. The data shown in the columns relating to the performance characteristics of the experiments as applied to Crab Nebula observations are examined in more detail in chapters 5 (Whipple 10 m) and 6 (VERITAS-2,3 array).

	Whipple 10 m	VERITAS-2	VERITAS-3	VERITAS-4
Optical Structure	10 m diameter; $f/0.7$	$2 \times 12\text{m}$ diameter; $f/1.0$	$3 \times 12\text{m}$ diameter; $f/1.0$	$4 \times 12\text{m}$ diameter; $f/1.0$
Mirrors	248/75 m^2	$2 \times 350/110 \text{m}^2$	$3 \times 350/110 \text{m}^2$	$4 \times 350/110 \text{m}^2$
Effective Area @350 GeV, @Zenith	$4 \times 10^4 \text{m}^2$	$5 \times 10^4 \text{m}^2$	$8 \times 10^4 \text{m}^2$	$> 10^5 \text{m}^2$
Slew Speed	1°/s	0.5°/s	0.5°/s	0.5°/s
Pointing Accuracy	0.1°	0.05°	0.05°	0.05°
Camera F.O.V	$379 \text{ pixel}/2.2^\circ$	$499 \text{ pixel}/3.5^\circ$	$499 \text{ pixel}/3.5^\circ$	$499 \text{ pixel}/3.5^\circ$
Readout Electronics	CFDs, QADCs	CFDs, FADCs	CFDs, FADCs	CFDs, FADCs
d.c./p.e ratio	3.3	5.3	5.3	5.3
Typical Trigger Rate	20-30 Hz	80-100 Hz	150-170 Hz	200-300 Hz
Data Size (30 min)	3MB	$\sim 1 \text{ GB}$	$\sim 3 \text{ GB}$	$\sim 5 \text{ GB}$
E_{thresh} @Zenith	400 GeV	200 GeV	200 GeV	200 GeV
5%Crab Sensitivity (5σ)	50 hrs	10 hrs	7 hrs	4 hrs
Photoelectron Trigger Level	7	4.5	4.5	4.5
Angular Resolution	0.15°	$\sim 0.05^\circ$	$\sim 0.05^\circ$	$\sim 0.05^\circ$
Energy Resolution	$\sim 30\%$	$\sim 10\%$	$\sim 10\%$	$\sim 10\%$
Avg. Crab Rate ys/min	3	3.5	6.5	8
Avg. Crab Rate $\frac{\sigma}{\sqrt{hr}}$	5	20.5	26	32

3.3. SUMMARY

Table 3.2: The properties of the Whipple 10 m and several versions of the VERITAS array. Data from Schroedter (2004), Fegan (2004), Maier (2006), Maier et al. (2007a), and Holder (2006).

Chapter 4

The Astrophysics of TeV Binaries

4.1 High Mass X-ray Binaries

Out of the roughly 10^{11} stars in the Milky Way, it is common thought that approximately 25%-50% of these will be in binary systems. Out of this population, only about 280 have been detected and classified as “X-ray binaries” (Liu and van Paradijs, 2006), or binary systems which present both transient and persistent X-ray emission. X-ray binaries are thought to be the pairing of a compact stellar object (neutron star or black hole) and a Main Sequence star. This group can be further subdivided based on the mass of the Main Sequence star placing those with masses below several M_{\odot} in the category of Low Mass X-ray Binaries (LMXBs) and those above in the category of High Mass X-ray Binaries. There are two classes of HMXBs which have been detected in TeV gamma rays and their configurations, as well as emission mechanisms, are appreciably different: binary pulsars and microquasars.

Binary Pulsars are HMXBs which contain pulsars that orbit the Main Sequence companion. The interaction between the energetic pulsar wind and the stellar wind then results in the observed X-ray to (sometimes) TeV emission. In contrast, in **microquasars** the compact object is not a pulsar and high energy emission results from accretion-related processes as the compact object pulls matter off of the Main Sequence star.

4.1.1 Binary Pulsars

An isolated pulsar consists of a highly magnetized neutron star (polar field strength of $\sim 10^{10}$ G for the main population of pulsars (Lynne and Graham-Smith, 1998)) where the axis of rotation is misaligned with the magnetic field axis. Pulsars have rotational periods ranging from about 1.5 ms to 8.5 s (Lorimer, 2001). Due to this fast rotation of the co-moving magnetic field lines, a strong electric field will be induced within the influence of the pulsar magnetosphere. This electric

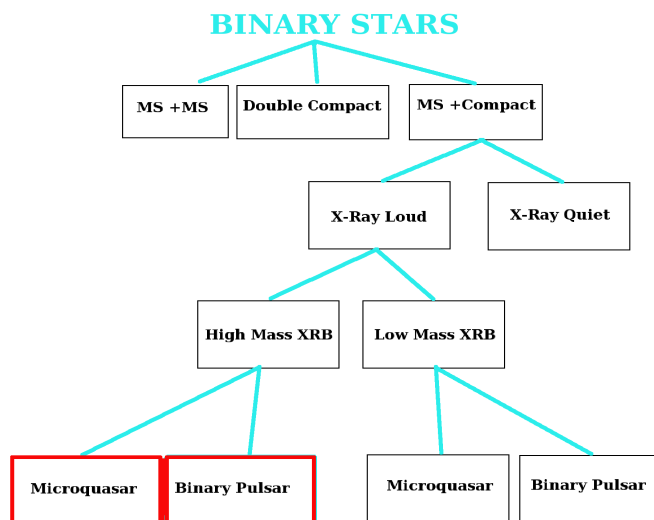


Figure 4.1: Classification of binary star systems. Those highlighted in red have members which are known TeV gamma ray sources.

field will lift particles off the surface of the neutron star and accelerate them to relativistic energies which (through pair creation cascades) will consequently create an electron/positron plasma within the magnetosphere. This plasma will eventually “leak” out of the magnetosphere creating a highly energetic plasma wind which continues until the termination shock, or the point where the particle flow goes from highly ordered to essentially isotropic.

Consider a pulsar rotating with an angular velocity Ω . It is common in pulsar studies to construct a cylindrical volume called the *light cylinder* near the pulsar of radius $R_L = \frac{c}{\Omega}$. An object co-rotating with the pulsar would reach the speed of light at this radius and it is within this volume that the rotating pulsar magnetosphere is contained. For a pulsar with a magnetic field B_* rotating with a period P , electron/positron pairs will emerge from the polar regions of the pulsar and travel along open field lines emerging from the light cylinder at a rate of (Kirk et al., 2007):

$$\frac{dN}{dT} \sim 2.7 \times 10^{33} \left(\frac{B_*}{10^{12} \text{G}} \right) \left(\frac{P}{1\text{s}} \right)^{-2} \text{s}^{-1} \quad (4.1)$$

which, for a typical pulsar can lead to an emitted pulsar wind energy of $\sim 10^{30}$ - 10^{40} ergs/s from the light cylinder, which will synchrotron radiate in the X-ray regime adding to the baseline X-ray emission (coming from material accreted onto the poles) from hot pulsars. However, it is believed that in the case of high mass X-ray binary pulsars, a more significant component of the observed X-ray emission results from the interaction of this energetic wind with the solar wind emitted by the massive Main Sequence companion.

The majority ($\sim 80\%$) of HMXBs contain Be Main Sequence stars (Liu and van Paradijs, 2006) (the remaining discussion will assume the presence of a Be Main Sequence companion) which are characterized by dense equatorial stellar wind outflows (Tavani et al., 1994). When the relativistic pulsar wind comes into contact with the stellar wind, it will set up a shock front at a distance r_s from the pulsar, found by equating the pressure from the two winds:

$$\frac{\dot{E}_{pw}}{\Omega_{pw} r_s^2 c} = \frac{\dot{M}_{Be} v_{sw}}{\Omega_{sw} (a - r)^2} \quad (4.2)$$

$$r_s = a \cdot \left(\sqrt{\frac{\Omega_{pw}}{\Omega_{sw}} \cdot \frac{\dot{M}_{Be} v_{sw} c}{\dot{E}_{pw}} + 1} \right)^{-1} \quad (4.3)$$

where Ω_{pw}, Ω_{sw} are the solid angles of the pulsar and solar wind. $\dot{M}_{Be}, \dot{E}_{pw}$ are the mass loss and energy loss rates of the Be star and pulsar. v_{sw} is the velocity of the solar wind and a is the pulsar-Be star separation. Magnetic instabilities on either side of this shock front will result in first-order Fermi acceleration of particles to relativistic energies. This process is found to be an efficient production mechanism for both X-ray (via synchrotron or inverse-Compton losses) radiation as well as gamma-ray (via inverse-Compton losses) radiation (Tavani and Arons, 1997). Since the emission from the system is dependent on the interaction between the two winds and this, in turn, is dependent upon the geometry of the individual system, the emission properties will vary on a system to system basis. In general, however, this model for HMXBs predicts that there will be extended radio emission from the pulsar wind synchrotron losses. The X-ray emission, which is provided by synchrotron losses will be of the power-law form, with a spectral index that will vary with changes in the orbital cycle of the binary, getting generally harder as the stellar wind at the shock becomes more tenuous (Murata et al., 2003). During close passages of the pulsar to the dense stellar wind (i.e. apastron), inverse-Compton losses will dominate as the electrons will upscatter the Be star photons to GeV-TeV energies (Dubus, 2006).

4.1.2 Microquasars

While binary pulsars can essentially be thought of as rotation-driven emitters (the main power in the system coming from the rotation-driven pulsar wind), microquasars can be thought of as accretion-driven emitters. These objects are the stellar mass analogues of AGN (see section 1.2.1) in that they consist of a central accreting compact object, an accretion disk, and symmetric relativistic jets originating at the accretion point. In the case of AGN, the accretor takes the form of a supermassive black hole ($M \sim 10^6 - 10^9 M_\odot$) whereas in microquasars the accretion is powered by either neutron stars ($1.4 M_\odot < M < 2.5 M_\odot$) or stellar mass black holes ($M > 2.5 M_\odot$). In these systems, the compact object accretes material from the Main Sequence star via either its stellar wind

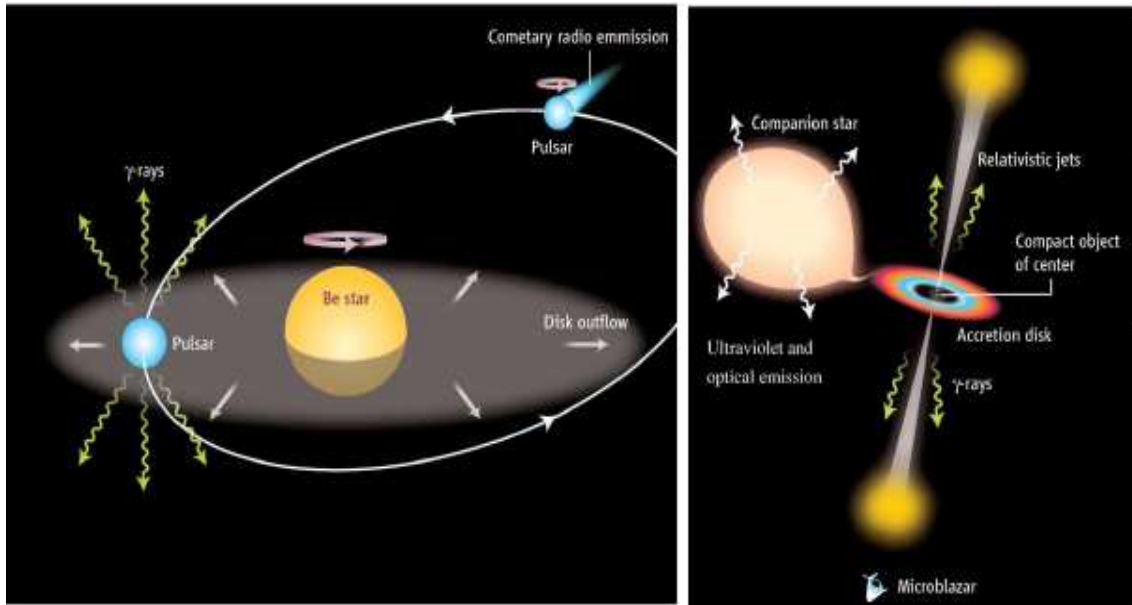


Figure 4.2: The binary pulsar model for TeV HMXBs (left) along with the microquasar model (right). Figure taken from Mirabel (2006).

or the overflow of the Main Sequence stars' Roche lobe (Massi, 2005). As material is captured by the gravitational force of the compact object, this material will have a distribution in angular momentum and will not fall directly onto the surface of the accretor. Viscous forces amongst the matter will further redistribute the angular momentum and an accretion disk will form. This disk has an inner radius R_{in} within which material will not have a stable orbit and will free-fall towards the accretor. Near this inner radius, strong frictional forces will result in the heating of the material to a temperature (Longair, 1994):

$$T \sim 2 \times 10^7 \left(\frac{M_{compact}}{M_{\odot}} \right)^{-1/4} K \quad (4.4)$$

which, for even a moderately sized neutron star accretor of $2 M_{\odot}$ results in thermal emission in the range of $2.37 \times 10^7 K$ which implies emission near 12 nm, well within the X-ray band (compared to the IR-UV emission that AGN supermassive accretors produce). Therefore in microquasar-type sources, the X-ray emission observed would be due to accretion processes and result in a thermal spectrum peaking near the mean temperature of the inner regions of the disk. This stands in direct contrast to X-ray emission from binary pulsars whose strongest X-ray emission comes from non-thermal processes such as synchrotron or inverse-Compton acceleration.

Another distinguishing feature of microquasars (similar to AGN) is the presence of well collimated, bilateral radio jets. These jets are formed in the special case of an accretion disk where the pressure exerted by the accretion disk plasma near R_{in} is greater than the pressure resulting from

the vertical magnetic field permeates the disk (Koide et al., 2000). The assumption of a weak magnetic field (i.e $B < 10^{12} \text{G}$) near R_{in} can be thought of as essentially a by-product of our assumption that the compact object is not a pulsar (since accretion processes such as those described above would not be possible in the region around a pulsar). Since the plasma pressure dominates, as the accreted material rotates around the compact object, the once vertical magnetic field lines become twisted in a helical fashion around the accretor. As the field lines compress and become stronger, a “lifting” effect takes place where the gas at the surface of the accretion disk (where the plasma pressure is lowest) begins to follow the twisted field lines extracting both material and angular momentum from the accretion disk. As a reaction to this, radial accretion in the disk increases which further twists the field lines and increases the lifting effect of material from the surface. This effect will produce bilateral jets of relativistically accelerated charged electrons streaming outwards (Koide et al., 2000). This theory of jet formation is known as “magnetohydrodynamic (MHD) jet theory”.

The already energetic electrons in the jet will be further accelerated by shocks (within the jet and at the external shear surface of the jet (Drury, 1983)) and become strong synchrotron emitters in the radio (and sometimes X-ray) band presenting a flat or inverted radio spectrum (van der Laan, 1966). These radio jets are the feature that when seen in radio observations, form a strong criteria for the identification of the system as a microquasar (Massi, 2005).

Additionally, HMXBs which do not contain pulsars are generally known to follow a relationship between their X-ray spectrum and flux called the **High:Soft/Low:Hard** correspondence (Tanaka, 1997). This correspondence is believed to be tied directly to the accretion rate of the system and thus in microquasars, it is believed that it is also tied to the radio jet behavior. During periods of normal or elevated accretion, the system will present a high flux of what is known as a “multi-color blackbody” spectrum (soft) which represents thermal emission from all parts of the differentially heated accretion disk (Mitsuda, 1984). In black hole HMXBs, this thermal spectrum is accompanied by a power-law tail ($2.1 < \alpha < 4.8$) (McClintock and Remillard, 2004) excess which is fuelled by inverse-Compton scattering of disk photons by electrons originating from a corona around the accretion disk (Coppi, 2000).

Following the High/Soft state, both black hole and neutron star HMXBs are known to suddenly switch to what is known as the Low/Hard state which is characterized by the replacement of the high flux, multi-component, soft blackbody X-ray spectrum with a low flux, single power-law, hard spectrum. This spectrum ranges from $\alpha = 1.5-19$ (McClintock and Remillard, 2004)(Tanaka, 1997) and it is not entirely clear what physical mechanism is responsible for this non-thermal emission (see McClintock and Remillard (2004) for a review of some of the proposed mecha-

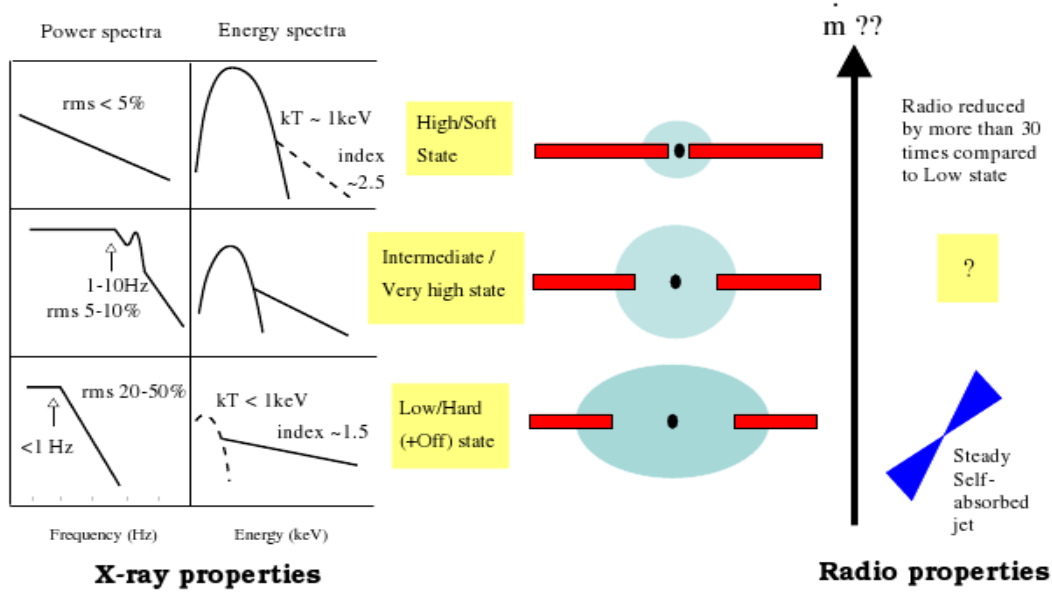


Figure 4.3: The accretion/ejection model and its associated spectral properties in both radio and X-ray as described in the text. Taken from Fender (2001).

nisms). By detailed resolution of the softer parts of the X-ray spectrum (during both High/Soft and Low/Hard states), one can determine the inner radius R_{in} of the accretion disk (see figure 4.3; Shakura and Sunyaev (2005); Mitsuda (1984)). By comparing these measurements during the different spectral states, it is found that R_{in} will grow out to an order of magnitude larger than it was originally (McClintock and Remillard, 2004) which implies that the inner regions of the accretion disk have been either completely removed or sufficiently modified so as to not be strong thermal X-ray emitters. By noticing that radio jet formation or flaring events only occur during these Low/Hard states (Fender, 2004), a possible picture of the emission evolution is created: during normal and increased accretion periods (such as passage through a dense region of stellar wind) from the Main Sequence star, a steady accretion rate feeds a soft multi-color blackbody X-ray spectrum (High/Soft) with no associated radio activity. This period of high accretion then feeds the inner regions of the disk (through MHD jet formation) into the production of a radio loud, relativistic jet. The X-ray spectrum during this time is a low flux, hard, power law resulting from either synchrotron or inverse-Compton scattering of stellar photons by the energetic jet electrons. This general picture of accretion/ejection is supported by observations of the galactic microquasar GX 339-4 (Fender et al., 1999) in which a Low/Hard X-ray state is shown to be highly correlated with the appearance of an expanding, inverted spectrum radio jet; while both features are shown to be highly anti-correlated with the switch back to a High/Soft X-ray state (see figure 4.3 for a graphical depiction of the evolution between these states). This model is supported even further by

the observations of intermediate states between the extremes of High/Soft and Low/Hard. These states are characterized by powerful quasi-periodic oscillations (QPOs) of the X-ray flux along with corresponding changes in the inner regions of the accretion disk (Belloni et al., 1997).

This accretion/ejection process may also play a strong role in the production of TeV gamma-rays within the microquasar framework. As will be explained in section 4.5.6.1, it is believed that TeV gamma-rays can be produced if the energetic electron population within the jet is exposed to a region of stellar UV radiation dense enough for efficient inverse-Compton scattering to TeV energies. Alternative methods for TeV production within the microquasar framework have also been proposed, such as jet/ISM shock interaction (Bosch-Ramon et al., 2006) and hadronic jet models (Romero et al., 2003; Romero et al., 2005). However, any successful model for TeV gamma-ray production within microquasars will almost inevitably utilize the extreme energetics of the jet which, in turn, is related to the overall phenomena of accretion/ejection processes.

The following sections will examine the firmly detected TeV binaries (PSR 1259-63, LS 5039, and LS I +61 303) as well as Cygnus X-3 which, although so far undetected by current IACTs remains an active target for TeV and multiwavelength observations. Special attention will be paid to LS I +61 303 as it is the main subject of this thesis and its exact nature- binary pulsar or microquasar- is still a matter of open debate.

4.2 PSR 1259-63

PSR 1259-63 is a pairing of a 48 ms pulsar in orbit around the Be star SS 2883. This pulsar crosses the stars' equatorial stellar wind twice every 3.4 yrs (see figure 4.4) (Johnston et al., 1992). It is believed that the system produces non-thermal X-rays by the interaction of the energetic pulsar wind (PSR 1259-63 has a spin-down luminosity of 8.3×10^{35} ergs/s) and the stellar wind of the Be star. Electrons are first-order Fermi accelerated within the shock fronts at the interaction point of the two winds and they subsequently emit in the soft X-ray to soft gamma-ray band through synchrotron losses (Johnston et al., 1999; Connors et al., 2002). This model is supported by X-ray and soft gamma-ray observations made by the ROSAT (Cominsky et al., 1994), ASCA (Kaspi et al. 1995), OSSE (Grove et al., 1995) and INTEGRAL (Shaw et al., 2004) which reveal a synchrotron spectrum. This synchrotron interpretation is also given credence by the detection of non-thermal radio emission coming from the system during periastron passage (Johnston et al., 1999; Connors et al., 2002). It is theorized that the same population of energetic electrons can upscatter UV photons from the Be star to TeV energies (Tavani and Arons, 1997).

This H.E.S.S. experiment detected PSR 1259-63 in the TeV gamma-ray regime during its

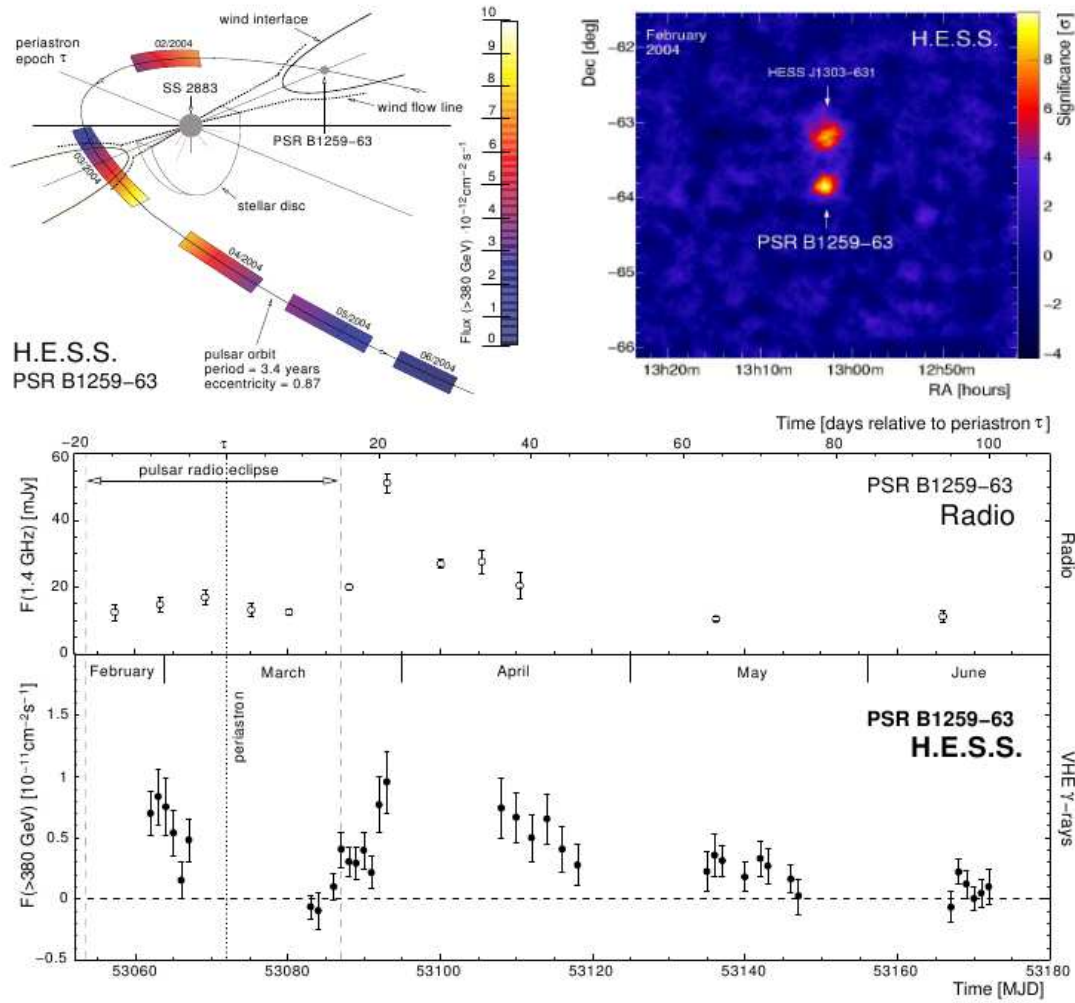


Figure 4.4: The H.E.S.S. observations of PSR 1259-63 in 2004. Top left shows the orbital geometry as well as the associated zones of the orbit that H.E.S.S. detected strong TeV emission from. Top right shows the 2-D sky map produced from the data including the unidentified source HESS J1303-631 discovered serendipitously within the field of view. The bottom panel shows the nightly light curve from both radio and TeV data. Figures taken from Aharonian et al. (2005c).

2004 periastron passage (Aharonian et al., 2005c) at a significance of 13.8σ over an exposure of 48.6 hours. The observations were made at the moderately large average zenith angle of 42.7° which resulted in a slightly elevated (for H.E.S.S.) energy threshold of 380 GeV with the strongest emission recorded after periastron passage (although the orbital coverage was not uniform). The source was found to have a spectral index of $\alpha=2.7\pm 0.2$ with integral flux of $F(>380 \text{ GeV}) = (4.0\pm 0.4)\times 10^{12} \text{ cm}^{-2} \text{ s}^{-1}$ equivalent to 4.9% of the Crab Nebula flux as measured by H.E.S.S. (Aharonian et al., 2006c). The extracted TeV spectrum from this source is consistent

with the hypothesis that the high energy emission is created by the bow shock between the pulsar wind and its external medium. This notion is also supported by associated 1.4 GHz radio observations carried out contemporaneously during the 2004 periastron passage (Johnston et al., 2005). These observations show a good correlation between high flux points in both radio and TeV bands indicating a common acceleration mechanism for both wavebands.

4.3 LS 5039

The first (assumed) microquasar to be discovered in TeV gamma rays, LS 5039 is an interesting laboratory for periodic high energy emission due to its relatively rapid orbital period of a compact object around a massive O6.5V star every 3.9 days (Casares et al., 2005a). Although the nature of the compact object is not clearly understood, there have been estimates placed on its mass in the $2.7\text{-}5M_{\odot}$ range if the system is inclined at a low angle ($\sim 25^{\circ}$), however, other estimates using larger inclination angles allow for the possibility of a neutron star (Dubus, 2006). The system was first identified as a high mass X-ray binary through ROSAT observations in 1997 (Motch et al., 1991) and was subsequently identified as a microquasar when bipolar relativistic radio jets were resolved in the system through VLA and VLBA observations in 1999 (Paredes et al., 2000) and were later confirmed by EVN and MERLIN observations (Paredes et al., 2002). The system was identified with the EGRET unidentified GeV source 3EG J1824-1514 (Paredes et al., 2000) and therefore was believed to be a possible source of TeV gamma rays (Bosch-Ramon et al., 2005).

This prediction was confirmed in 2004 by H.E.S.S. observations which serendipitously detected LS 5039 during a scan of the galactic plane (Aharonian et al., 2005d). This detection was followed up by dedicated observations of LS 5039 in 2005 which revealed the source to be a periodic, variable TeV gamma-ray source positionally coincident with the VLBA radio source (Aharonian et al., 2006d). The source was detected at a significance of 40σ over 69.2 hours of livetime observations. The short orbital period of the system allowed observations at all orbital phases to be taken with a clear correlation seen between orbital phase and both gamma-ray flux and spectrum. There is a clear flux increase when the system is in orbital phase $0.45 < \phi < 0.9$ (see figure 4.5) with a flux maximum occurring near where the compact object lies directly in front of the massive star with respect to our line of sight (or the *inferior conjunction* at $\phi = 0.716$). The observed flux minimum occurs near $\phi = 0.2$ which is slightly after the continuation of our line of sight to the other point of the orbit behind the OV star (known as *superior conjunction* or $\phi = 0.058$). By defining two orbital regions that encompass the entire orbit, **INFC** defined as $0.45 < \phi < 0.9$, and **SUPC** defined as $\phi < 0.45$ or $\phi > 0.9$, the VHE gamma ray behavior breaks into

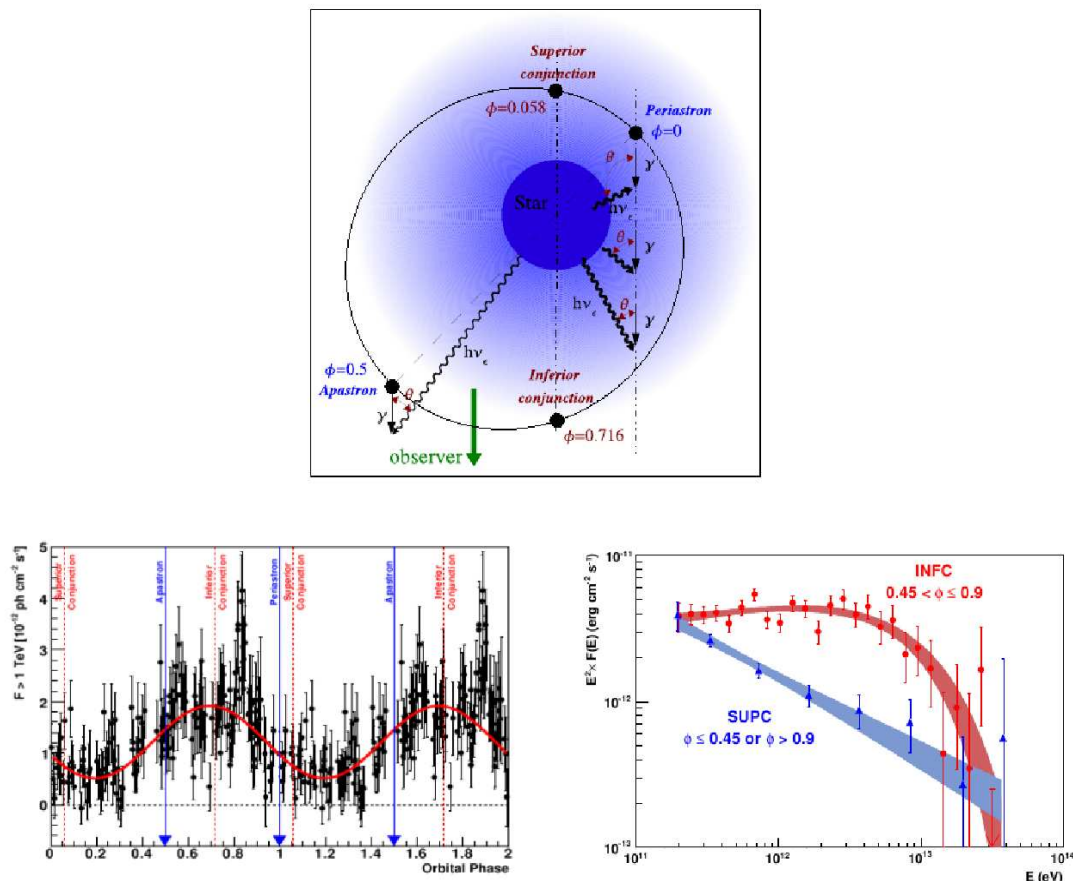


Figure 4.5: H.E.S.S. observations of LS 5039. Top shows a schematic of the orbital geometry of the system. Bottom left shows the modulation of the flux as a function of orbital phase. Bottom right shows the modulation of the spectra as a function of the orbital phase of the system. Figures taken from Aharonian et al. (2006d).

two exclusive modes. During **INFC** the system presents a VHE flux (>200 GeV) of $(2.28 \pm 0.1) \times 10^{-12} \gamma \text{ cm}^{-2} \text{ s}^{-1}$ (2.8% Crab flux) with hard power-law index of $\alpha=1.85 \pm 0.16_{\text{stat,sys}}$ and an exponential cut-off at (8.7 ± 2.0) TeV. During **SUPC**, however, the system is less active presenting a flux (>200 GeV) of $(0.91 \pm 0.1) \times 10^{-12} \gamma \text{ cm}^{-2} \text{ s}^{-1}$ (1.1% Crab flux) with a soft power law of $\alpha=2.53 \pm 0.17_{\text{stat,sys}}$ extending all the way to 20 TeV. This modulation in both spectrum and flux of VHE gamma rays echoes that observed in the X-ray band (Bosch-Ramon et al., 2005) which could indicate a common production mechanism for both bands.

The primary mechanism thought to generate the VHE flux from LS 5039 is through inverse-Compton scattering of stellar photons by energetic electrons within the jet. This TeV gamma-ray flux would be modulated by absorption due to pair creation within the photon field of the OV star. This modulation explains the peak of the flux observed near inferior conjunction (largest op-

tical depth along our line of sight); however, it cannot explain the observed emission at periastron ($\phi = 0.0$). There have been attempts to solve this problem by postulating that an accretion-ejection phenomena might play a part in the modulation of VHE gamma-rays within the system (Paredes et al., 2000), similar to that explained in 4.1.2. In this model, accretion maxima after passage through dense regions of the OV stellar wind fuel increased jet energetics which then fuel increased scattering of stellar photons to TeV energies by jet electrons. However, this model alone predicts an increased flux shortly after periastron passage which is also not observed. It is clear that within the jet model of TeV production, additional effects must be taken into account in order to accurately reproduce the observed TeV emission, such as attenuation of the TeV gamma-ray signal by pair-production with the optical photons from the Main Sequence star.

As an alternative to the jet models, models based on the binary pulsar scenario have been invoked in order to explain the high energy behavior of LS 5039 (Dubus, 2006) (see section 4.1.1). The high energy emission is then explained as arising from synchrotron or inverse-Compton losses from electrons accelerated at shock fronts between a pulsar wind and the stellar wind. The modulation of the high energy emission is explained by variations in pair-production absorption and shock location along the orbit. These models neither accurately reproduce the observed GeV flux from the associated source 3EG J1824-1514 (Dubus, 2006) nor satisfactorily explain the bipolar nature of the observed radio emission as synchrotron emission from a cometary pulsar wind.

4.4 Cygnus X-3

Cygnus X-3 is a pairing of an undetermined compact object ($M_c \leq 3.6M_\odot$) with (most likely) a Wolf-Rayet star ($M_{wr} \leq 7.3M_\odot$) (Stark and Saia, 2003) in a 4.8 hour orbital period (Parsignault et al., 1976). Cygnus X-3 is one of the most powerful X-ray sources in the galaxy and hence, also one of the first to be discovered by early rocket-based experiments (Giacconi et al., 1967). The source is also particularly bright in the radio band showing flares ranging from 0.1 to 1 Jy (Gregory et al., 1972). During these radio flares, observations by the VLA, Merlin, VLBA, EVN, and e-VLBI all indicate a two-sided relativistic jet (Tudose et al., 2007), which lead to the identification of the system as a microquasar. Although this source is the subject of intense observations in the X-ray and radio bands, a lack of understanding of its stellar environment and fundamental components (as well as being optically obscured by the galactic plane) inhibits comprehensive modeling of radio and X-ray emission.

However, due to the presence of a relativistic radio jet and some mechanism which produces hard X-rays, it is reasonable to expect that Cygnus X-3 might also be a high energy gamma-ray

emitter. The history of gamma-ray observations of Cygnus X-3 has been fraught with unconfirmed or retracted detections. The first gamma-ray detection was reported by the SAS-2 satellite which associated a 4.5σ excess of emission above 35 MeV with Cygnus X-3 along with a 4.8 hour periodicity (Lamb et al., 1977). However, although a detection in >50 MeV gamma rays consistent with the SAS-2 location, this periodicity was not confirmed by the subsequent (and far more sensitive) EGRET experiment (Mori et al., 1997). Moving to higher energy gamma rays, an initial detection by the Crimean observatory of Cygnus X-3 in 1982 (Stepanian et al., 1975) in TeV gamma rays showed a correlation with the 4.8 hour period of the system as well as a 9.22 ms period in the data associated with the presence of hypothesized pulsar within the system. Subsequent observations by the Durham Mark-6 experiment (Chadwick et al., 1985) reinforced a TeV detection, but instead detected a 12.59 ms periodicity in the TeV data. Despite the Crimean and Durham results, further observations by the more sensitive Whipple telescope failed to detect the source (O’Flaherty et al., 1990). At even higher energy ranges, Cygnus X-3 has been reported to be detected in the PeV range by the Kiel Observatory (Samorsky and Stamm, 1983), Haverah Park Air Shower Array (Lloyd-Evans et al., 1983) and even at the EeV range by the Fly’s Eye air shower experiment (Cassiday et al., 1989). Further observations by the more sensitive CASA-MIA experiment showed no hints of a source (Ong et al., 1991). Upon further inspection, all of the reported detections had questionable margins of significance and are considered now to be suspect (see (Weekes, 1988) for a review of these detections). However, since the source displays ultimately unpredictable behavior in radio outbursts as well as both hard and soft X-rays, it is conceivable that the source was flaring when these past experiments detected it and quieted down when more sensitive experiments were taking data on it. Using the motivation that if the source is indeed a microquasar, then its high energy gamma-ray emission could be produced by inverse-Compton scattering of the stellar photons by energetic jet electrons (as is believed to occur in LS 5039). In this case radio outbursts might be a good indicator of VHE gamma-ray emission. After years of relative quiescence in radio, in Fall 2006 Cygnus X-3 erupted again with some of the largest radio flares seen from the system repeatedly erupting to the 3 Jy level and at one point all the way to the 14 Jy level (McCullough, 2006). Motivated by this, the Whipple 10m telescope began taking data on the system again. The results of this campaign are presented in section 5.4.

4.5 LS I +61 303

When this thesis work was begun in early 2005, the binary system LS I +61 303 (referred to henceforth as LSI) was one of the most heavily studied binary systems in the Milky Way primarily

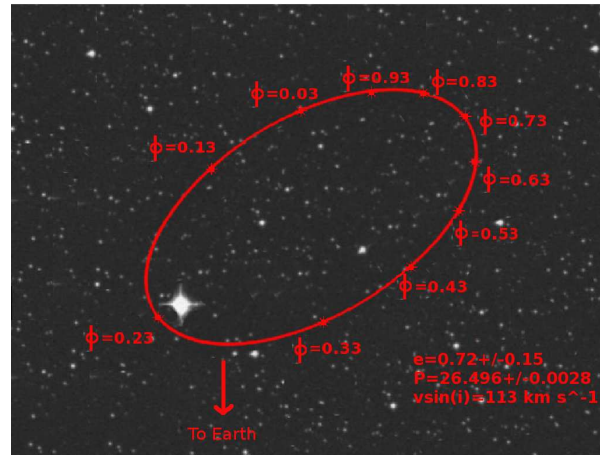


Figure 4.6: A schematic of the orbital geometry of LSI +61 303. The parameters quoted are from Casares et al. (2005b) and Gregory (2002).

due to its periodic outbursts in both radio and X-ray. However, despite years of observational scrutiny (dating back to the late 1970's) the identification of what the system actually was still remained a mystery. Putting aside (for the moment) the particulars of why astronomers believed what they believed about LSI, there were two competing views as to the physical nature of the system: was LSI a microquasar or binary pulsar? Or more phenomenologically, was the emission observed from LSI accretion or rotation driven? There seemed to be equal strengths and flaws to each supposition. Years of monitoring in radio, X-ray, optical, IR, and even GeV gamma rays did nothing to resolve the debate. The 2006 detection of LSI by the MAGIC collaboration in TeV gamma rays (?) was also ineffective at weighing in on either side because, as will be shown in this chapter, both scenarios can accommodate the observational properties. After briefly summing up the known physical properties of LSI +61 303, a history of the observations across the spectrum will be given.

4.5.1 Physical Properties

From optical and UV observations it is known that LSI +61 303, located at a distance of ~ 2 kpc (Hutchings and Crampton, 1981), is a binary system composed of a BO Ve star (Hutchings and Crampton, 1981; Casares et al., 2005b) paired with a compact object of unknown nature. The constraints placed on the orbital parameters of the system do not allow for sufficient determination to be made of the inclination angle i ($10^\circ \leq i \leq 60^\circ$) (Casares et al., 2005b) which leaves ambiguity in the determination of “which way were looking at the system” which can effect modeling certain aspects of the system, such as jet orientation. This ambiguity in the inclination angle also

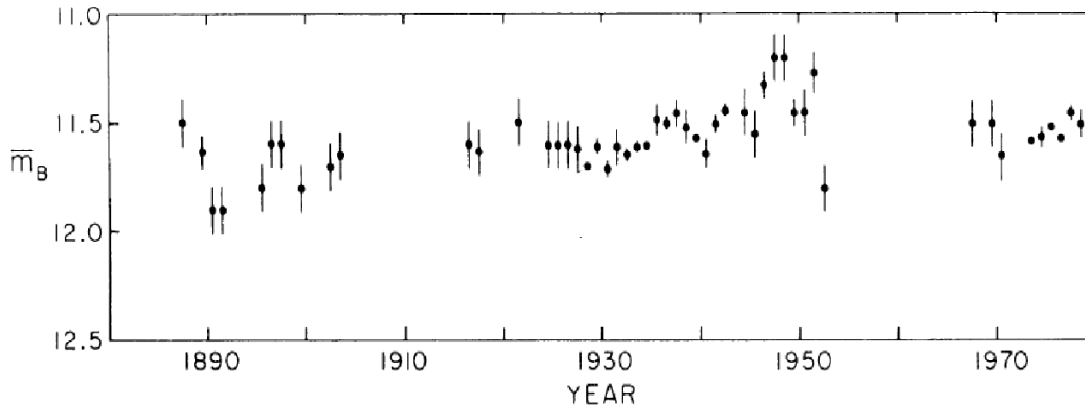


Figure 4.7: Analysis of 359 B band optical plates from Harvard College Observatory on LS I +61 303. These plates show punctuated regions of significant variability spread out over the timespan of years. Taken from Gregory (2002).

prevents an accurate determination of the mass function of the compact object and although, the system most likely possesses a neutron star, a black hole cannot be ruled out (Casares et al., 2005b; Hutchings and Crampton, 1981; Punsly, 1999). What is known very well about the compact object however, is that it is responsible for large radio outbursts every 26.5 day orbital cycle. While there is a slight modulation of the phase and flux of the bursts over a period of roughly 4 years (Gregory, 2002), these modulations occur at very regular intervals in the orbital cycle. Figure 4.6 shows the most accurate constraints on the orbital geometry. These come from Casares et al. (2005b) in which measurement of the He I & II lines from the Be star constrain the eccentricity of the orbit to be $e=0.72\pm 0.15$ and the phase of periastron to be $\phi=0.23\pm 0.02$ ($\phi=0$ is a relatively arbitrary definition set at JD 2443366.775 by Gregory (2002)). To further illustrate the complex nature of this source, it is beneficial to detail its observational history.

4.5.2 Radio

The oldest known observations on LS I +61 303 come from analysis (Taylor and Gregory, 1984) in which B band optical plate exposures taken from the Harvard College Observatory date back to 1887 (figure 4.7). These plates show LS I +61 303 to go through years of roughly constant optical emission, punctuated by significant variability. The source was first officially titled in the catalogue *Luminous Stars of the Northern Milky Way* as LS I +61 303. However, the high energy astrophysics community only first took interest in LS I +61 303 when it was discovered as a radio source during a 1977 survey of the galactic plane (Gregory and Taylor, 1978) with the VLA. The

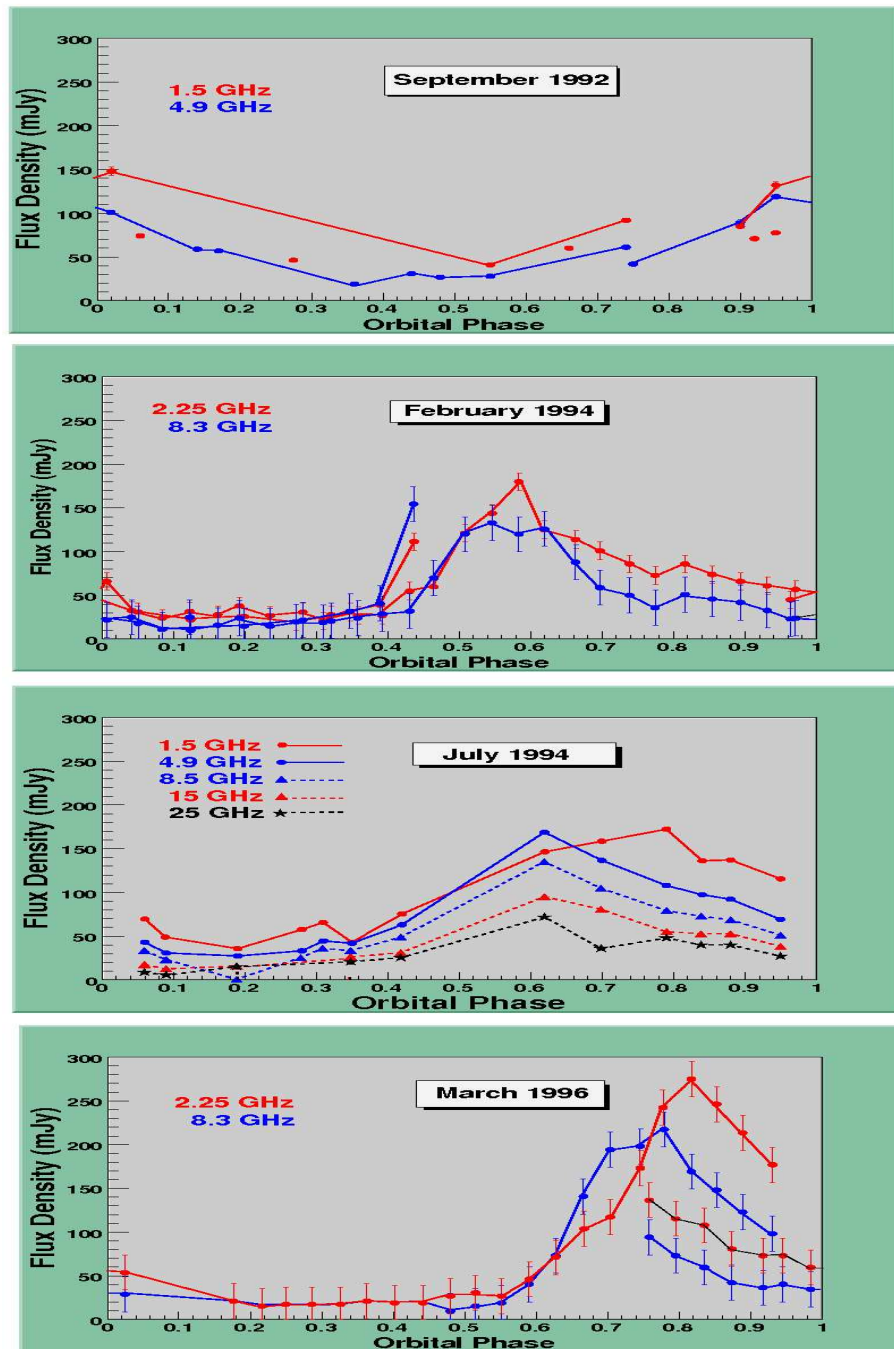


Figure 4.8: The results of several radio monitoring campaigns on LS I +61 303. The first figure shows VLA monitoring performed in 1992, a peak can be seen near phase 0.0 (taken from Taylor et al. (1996)). The second figure shows GBI monitoring two years later from (Leahy et al., 1997), a peak can be seen in both bands near phase 0.6. The third figure shows the VLA results later that same year (Johnson et al., 1993), all four bands show a peak shortly after phase 0.6. The final figure shows the 1996 GBI results from (Harrison et al., 2000). Here as peak in both bands is evident near phase 0.8-0.9. As is shown in Gregory (2002), the peak in radio moves over time with peak flux modulation occurring on a scale of 4 years.

source, GT 0236+610 as it was then known, was seen to have large variations in its radio flux; varying by up to a factor of 30 over 20 days. GT 0236+10 was subsequently identified with both LS I +61 303 and the COS-B gamma-ray source, 2CG 135 +01 (Hermsen et al., 1977). The COS-B observations report that the source was detected at 20-45% of the Crab Nebula flux above 100 MeV. However, this value should be taken with caution as the relatively large COS-B error margins do not preclude emission from nearby sources from contributing to this flux.

Subsequent analysis of the radio flux (Taylor and Gregory, 1980) revealed a 26.5 day period in the radio outbursts. This prompted the work of Maraschi and Treves (1981) in which the authors first proposed that the observed emission from LS I +61 303 could be explained by the periodic interaction between a young pulsar wind and the stellar wind from a massive star. It should be noted that at the time of that publication, it was not known that LS I +61 303 was even a binary system. The insight required to suggest that binary behavior was at the heart of LS I +61 303, as well as suggesting a model for emission that is still considered by many to be correct today (after decades of subsequent observations) is extremely impressive. Before moving to higher energy observations, it is useful to point out that this outburst modulation seen in radio is mimicked in all known observational bands. This includes the X-ray observations which are detailed below, as well as optical (Mendelson and Mazeh, 1989) and infrared (Paredes et al., 1997). As these lower energy bands are not the focus of this current work, they are only mentioned in passing as a demonstration of the overall periodic nature of this source.

Further radio monitoring carried over 20 years with various experiments (Paredes et al., 1998) shows that the peaks of the radio outbursts are not constant in phase (ranging from $\phi = 0.45-0.95$). In a Bayesian analysis performed in Gregory (2002), the authors used all available radio data from 1977 to 2000 and found that a period of 26.496 ± 0.0028 day provides the best fit to data (agreeing well with the later work in optical data of Casares (Casares et al., 2005b)). The Bayesian analysis also found that there was a peak flux modulation over a timespan of 1667 days.

Several multiwavelength campaigns on LS I +61 303 using radio observations were performed in the 1990s using the VLA and GBI (Taylor et al., 1996; Johnson et al., 1993; Harrison et al., 2000; Leahy et al., 1997). These observations document the variability of the radio light curve between 1.5 and 25 GHz. Figure 4.8 shows the results of several of these campaigns spread out from 1992 to 1996. As can be seen both the placement of the radio peak within the orbital phase as well as the peak flux value seems to change from year to year. (Gregory 2002) shows that this is also the case for individual orbital periods, although to a lesser degree. The first resolved radio imaging of LS I +61 303 was performed by EVN (Massi et al., 2001) in 2000. The observations revealed the presence of asymmetric 5 GHz radio emission extending up to tens of

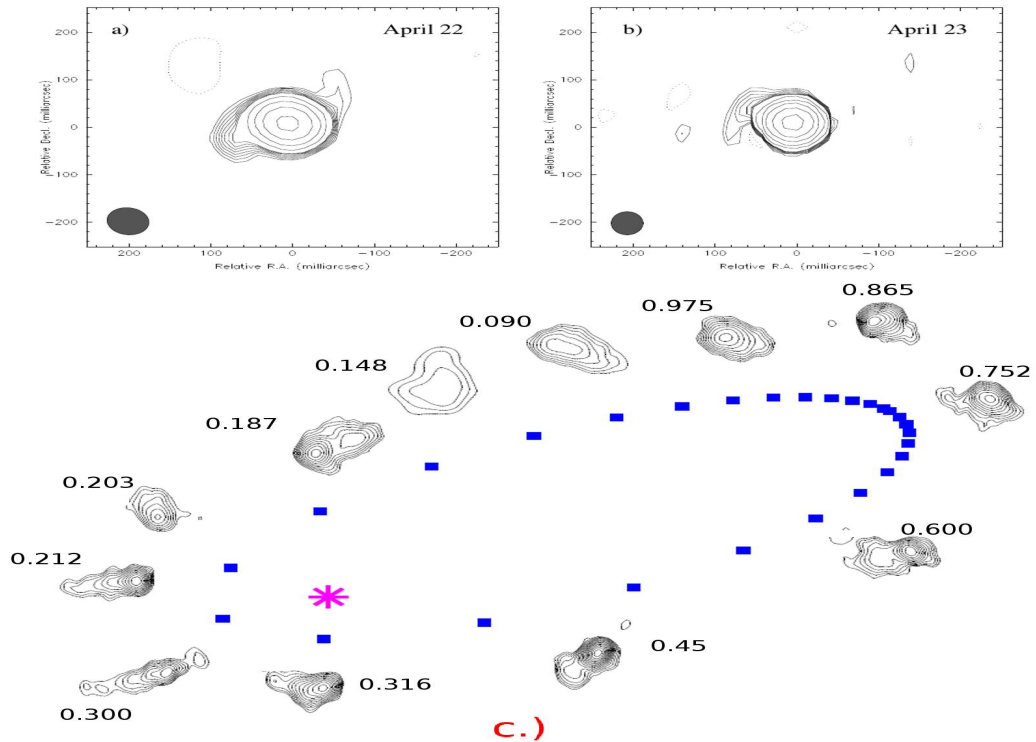


Figure 4.9: a.) The MERLIN image of LSI I +61 303 in 5 GHz radio. A significant one-sided extension is present. b.) One day later in the same band. This disappearance of the asymmetric extension was taken as strong evidence of a relativistic precessing jet. (both a.) and b.) taken from Massi et al. (2004)). c.) VLBA 8.3 GHz imaging showing extended radio emission changing directions as the source moves in its orbit. These changes were interpreted as the presence of a cometary radio tail formed by the interactions between the Be stellar wind and a pulsar wind structure, thus strongly asserting the binary pulsar model of LSI I +61 303 (taken from Dhawan (2006)).

milli-arcseconds in the southeast direction. The authors interpreted this result as a clear indication of the presence of a Doppler boosted relativistic jet in the system. This assertion was given further weight by the follow-up observation by the MERLIN radio telescope in 2004 (Massi et al., 2004). These observations (also at 5 GHz) show the aforementioned radio extension from LSI I +61 303 on the first day of observations, and then the extension is gone the next day (see figure 4.9). The authors interpret this as a precessing radio jet similar to those seen in other microquasars. This assertion was forcefully contradicted with VLBA observations on LSI I +61 303 in 2006 (Dhawan et al., 2006). These 8.3 MHz observations (figure 4.9 c) show extended radio emission from the source which changes direction as the orbital period progresses. Instead of being interpreted as a precessing jet, this time the extended emission was interpreted as the cometary tail of a pulsar

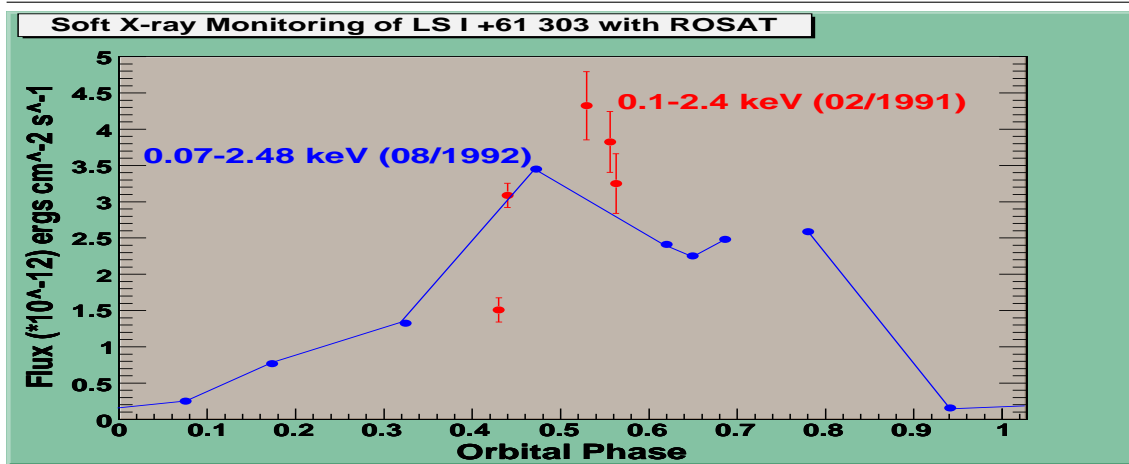


Figure 4.10: The results of two ROSAT monitoring campaigns on LS I +61 303 in soft X-rays. Red points with errors are taken from Goldoni and Mereghetti (1995). Blue points with no errors are taken from Taylor et al. (1996). Both sets of data points are accumulated from a single orbital period (note that the points from Taylor et al. (1996) begin at orbital phase 0.78). Both light curves imply a maximum in X-ray emission between 0.4 and 0.6.

wind being blown about by the equatorial wind of the Be star. Although these latest radio images present a very compelling case for the binary pulsar model, there are still remaining objections against this model which can explain the observed radio morphology. In fact, (Romero et al., 2007) presents MHD simulations showing that the interaction between the pulsar and stellar wind in the system does NOT exhibit the morphology observed by Dhawan (2006) and argues against such an interpretation.

4.5.3 X-ray Data

LS I +61 303 was first detected in X-rays by the Einstein satellite as a weak, non variable source (Bignami et al., 2001). The source was observed by Einstein twice during a period of over a year and a half in the energy range 0.2-5 keV. A flux of 2.1×10^{-12} ergs $\text{cm}^{-2}\text{s}^{-1}$ was compatible with both observations; however, the relatively poor energy resolution of Einstein (as compared to later X-ray satellites) make this flux measurement relatively obsolete. As was seen in subsequent observations by the ROSAT satellite in 1991 (Goldoni and Mereghetti, 1995), LS I +61 303 is indeed a variable X-ray source with flux values varying by a factor of 3 with average flux around 3.2×10^{-12} ergs $\text{cm}^{-2}\text{s}^{-1}$ in the 0.1-2.4 keV band (see figure 3). It was determined that a power-law model with spectral index (1.1 ± 0.3) provided the best fit to the spectrum extracted from the data. This implies that accretion processes are not at work in producing the X-ray emission from

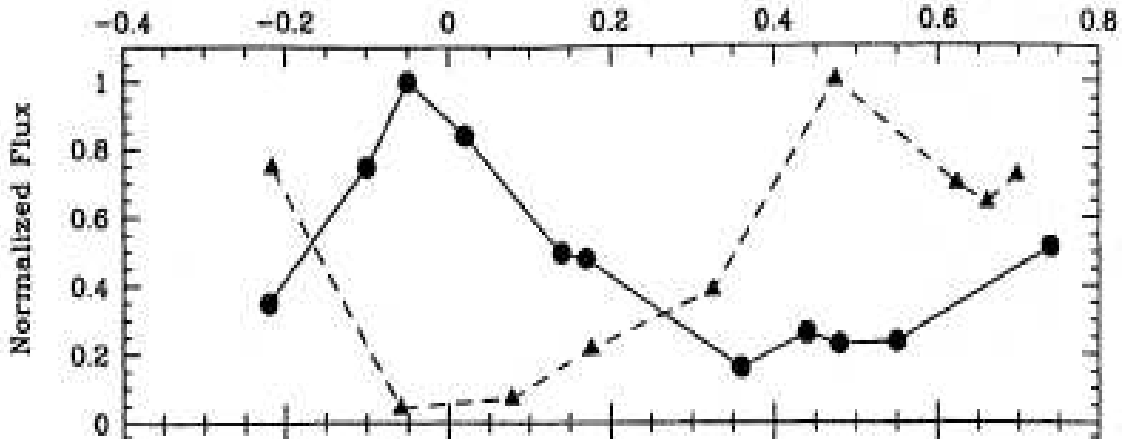


Figure 4.11: A comparison of the ROSAT soft X-ray flux (dashed lines) and the VLA 4.9 GHz radio flux (solid lines) taken contemporaneously on LS I +61 303. As can be seen, a radio flare is preceded by several days by a smaller flare in X-rays. Taken from Taylor et al. (1996).

LS I +61 303, as if this were the case, a general blackbody or “Raymond-Smith” (hot plasma disk) model would provide an acceptable fit. This lack of accretion-based X-ray spectral behavior is one of the arguments leveled against the microquasar model for LS I +61 303.

One year later in 1992, ROSAT was used along with the VLA as part of a multiwavelength monitoring campaign on LS I +61 303 in X-ray and radio (Taylor et al., 1996). The X-ray component of these observations in a similar energy range to (Goldoni and Mereghetti, 1995) (0.07-2.48 keV) also detected LS I +61 303 as a variable soft X-ray source with maximum flux occurring between orbital phases 0.4 and 0.6 (see figure 4.11). The combined X-ray and radio data set also showed a radio flare occurring at phase $\phi \sim 0.95$, several days after an X-ray peak (see figure 4.11). Both these observations show neither strong evidence for spectral hardening with increasing flux, nor evidence for X-ray pulsations.

These X-ray observations were followed up by pointings by the ASCA satellite in 1994 (Leahy et al., 1997). This data set consisted of two long (>30000 s) exposures which, for the first time, were able to measure the X-ray spectrum between 0.5 and 10 keV. Similar to the result of Goldoni and Mereghetti (1995), the authors found that an absorbed power-law model (a power-law altered by absorption by the estimate hydrogen column density along the line of sight) provided a much more suitable fit than a blackbody emission model to the 0.5-10 keV spectrum. Their fitted spectrum is in good agreement with the previous measurement in soft X-rays by ROSAT. The spectral index derived was in the range of 1.6-1.9, which is slightly softer than the ROSAT derived spectrum; however, the improved instrumentation may be responsible for this small shift. Their model

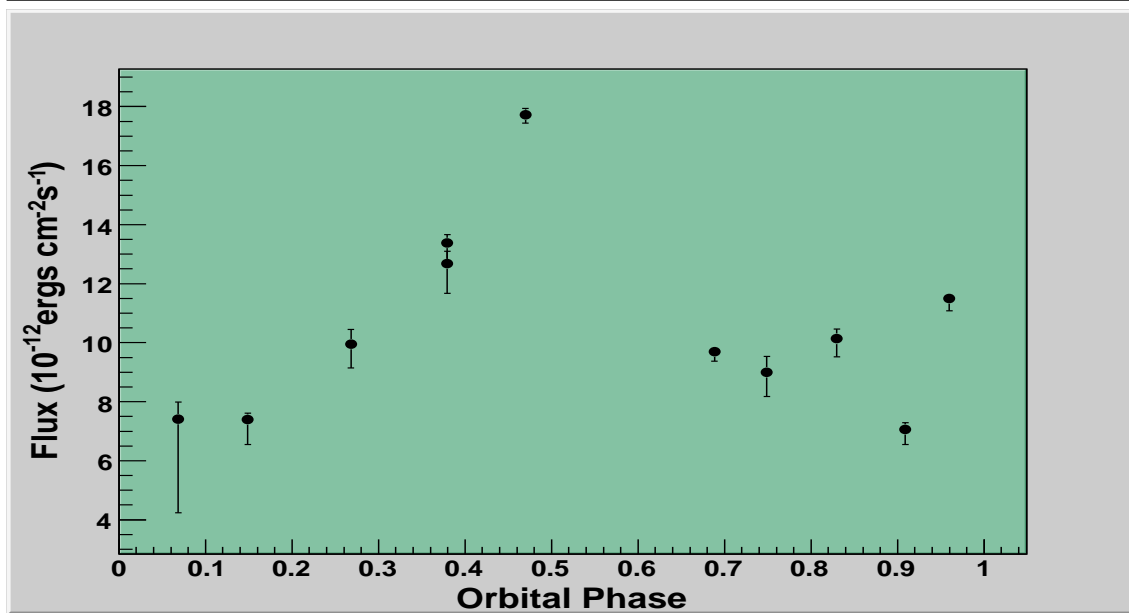


Figure 4.12: The first full orbital X-ray monitoring campaign on LS I +61 303 performed by RXTE. An increase in X-ray flux is clearly evident between orbital phases $\phi = 0.3 \rightarrow 0.5$.

fit also provided a value of the absorbing hydrogen column density along the line of sight to the X-ray emission site of $N_H = 0.6 \times 10^{22} \text{ cm}^{-2}$. The first RXTE monitoring of LS I +61 303 was carried out between March 1 and March 30 1996 as a part of a multiwavelength monitoring program in X-rays and radio (Harrison et al., 2000). Contemporaneous observations with RXTE PCA were carried out by the the Green Bank Interferometer (GBI) in the 2.25 and 8.3 GHz bands, and 15 GHz monitoring performed by the Ryle Telescope. The 11 RXTE pointings in the 2-10 keV band show significant variability, with a peak in X-ray flux preceding the radio peak by ~ 10 days. The X-ray data from RXTE PCA were analyzed in detail by two separate analyses ((Harrison et al., 2000; Greiner and Rau, 2001)), with both finding a peak in the 2-10 keV X-ray flux occurring between orbital phases $\phi = 0.45$ and $\phi = 0.6$ with no strong evidence for spectral variation. Both analyses found that a simple, absorbed power law provides the best fit to the observed data. Harrison et al. (2000) used a fixed spectral index of 1.8 to generate the flux values shown in figure 4.12. In a re-analysis of the same data set, Greiner and Rau (2001) found that the spectral index varies over the orbital cycle from 1.6 to 2.4., as well as generating a discrepancy in the values for integrated flux between 2-10 keV. However, the analyses are not strictly comparable since Greiner and Rau (2001) used the lower layers of the PCA units in their analysis, which provides for greater sensitivity to harder photons at the expense of lowered signal to noise ratio. Greiner and Rau (2001) also allowed the value of N_H to vary freely in their modeling process which resulted in finding a value of $3 \rightarrow 7 \times 10^{22} \text{ cm}^{-2}$, which is considerably higher than the ASCA result. This contradiction

in one of the fundamental parameters of the absorbed power law model seems troubling at first, however, RXTE has comparatively weak sensitivity in the energy range between 0.1 and 2 keV. This is exactly the same energy range over which the X-ray absorption by neutral hydrogen plays the most crucial role. Therefore, the RXTE measurements of N_H are not considered as accurate as those provided in Leahy et al. (1997) and further observations in softer X-rays by *XMM-Newton* (?) and Chandra (Paredes et al., 2007).

In a third published analysis of this data set (Neronov and Chernyakova, 2007), the authors fix a value of $N_H=0.49\times 10^{22}\text{cm}^{-2}$ in their modeling. The resulting flux values agree well with the analysis of Greiner and Rau (2001), however, the derived spectral values are much harder than previous analyses. Although this latest treatment of the data is the most consistent with overall measured values for N_H and α , their publication makes no statement about the analysis procedure used (cuts, energy ranges, etc). The author found during the work of this thesis, that using reasonable assumptions about quality criteria cuts and fitting energy ranges, the result of Neronov and Chernyakova (2007) was not reproducible. For this reason, it was decided to re-analyze this data set for the work in this thesis using the most up to date RXTE analysis software, background and emission models. This re-analysis is presented in chapter 7. For the time being however, the result of Neronov and Chernyakova (2007) is treated as an assumed correct black-box and thus, values of flux and spectral indices are shown in figure 4.15 for overall comparison with other X-ray satellite results.

Beppo-SAX carried out two long exposure pointings (12 ks and 8.6 ks) in September 1997 at orbital phases $\phi=0.31$ and 0.46, respectively (Sidoli et al., 2006). These observations, covering the energy range of 0.1-70 keV, took place near the orbital phases of $\phi=0.31$ and 0.46, respectively. The data were fitted with an absorbed power law model with $N_H=0.5\times 10^{22}\text{cm}^{-2}$ which resulted in spectral indices consistent with $\alpha=1.6$, similar to previous results. The results for the two observations in the 2-10 keV band are shown in figure 4.15.

In 2002, *XMM-Newton* was used to monitor LS I +61 303 in the 0.2-12 keV range. Four 5-6 ks pointings were taken spread out over a single orbit, with a single 6 ks pointing taken several months later. These pointings showed the 2-10 keV flux to be highly variable, having a minimum near periastron and peaking near phase 0.55. The spectral fitting used an absorbed power law model which resulted in a value of N_H of $0.49\times 10^{22}\text{cm}^{-2}$ being consistent with all observations. The resulting spectra was consistent with a value of $\alpha=1.5$ for 4 out of 5 of the pointings, with a much softer spectrum of $\alpha=1.78$ resulting for the data point just preceding the transition from a high to low X-ray flux. The authors of Chernyakova et al. (2006) interpret this as evidence for correlation between spectral behavior and flux states.

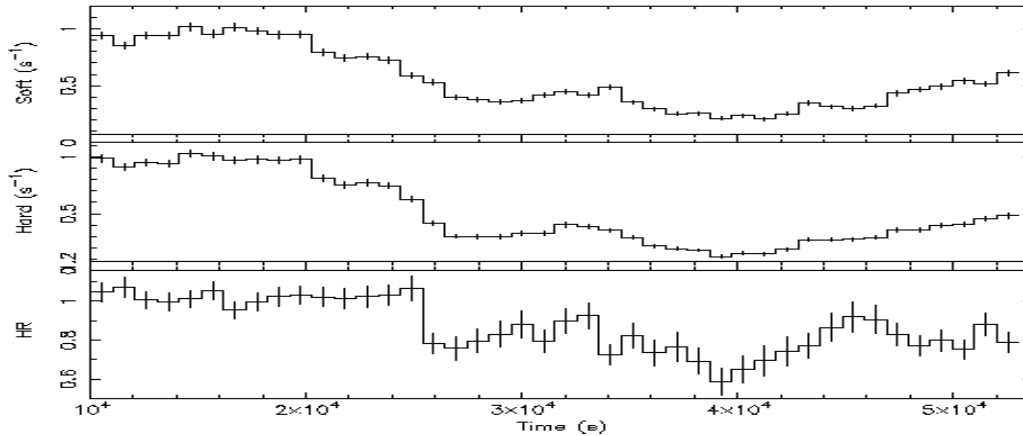


Figure 4.13: Background subtracted count rates and hardness ratio taken from the 2005 *XMM-Newton* long observation of LS I +61 303. The top panel shows the softer (0.3–2 keV) emission, the middle panel the harder (2–12 keV) emission, and the bottom panel the ratio between the two. A deviation to softer emission is seen roughly coincident with a switch to a lower flux state, although this correlation is not observed in subsequent observations with *Chandra*. Taken from Sidoli et al. (2006).

Several years later in 2005, *XMM-Newton* was again used for an extended pointing (48.7 ks) on LS I +61 303 during orbital phase 0.61 (Sidoli et al., 2006). This observation showed evidence for variation of the hardness ratio (defined as the ratio between 0.3→2 keV and 2→12 keV emission) over the timescale of hours. These observations also showed evidence for a correlation between harder emission and increased source flux, however, a strict statistical correlation study was not presented in that work. These observations also showed a sharp decrease in flux of the order of a factor of 3 over a time period of a few thousand seconds, with flux decreasing from $12 \rightarrow 4 \times 10^{12} \text{ ergs s}^{-1} \text{ cm}^{-1}$. These observations were the first to detail such rapid variability of the X-ray flux from this system (see figure 4.13).

Recently, the *Chandra* satellite carried out a 50 ks pointed observation on LS I +61 303 in April 2006 (Paredes et al., 2007) near orbital phase 0.04 (when the source is usually in a relatively quiescent state). These observations (in the energy band 0.3 to 10 keV) also reveal the presence of kilosecond scale miniflares in the source, with emission increasing by a factor of 2 over a timespan of roughly one hour. Similar to the *XMM-Newton* extended exposure, the *Chandra* observations also show an implied correlation between harder emission and increased flux. The spectral fitting carried out determined an absorbing column density of $0.7 \times 10^{22} \text{ cm}^{-2}$, consistent with previous fittings from soft X-ray observations. The flux was determined at $7.1_{-1.4}^{+1.8} \times 10^{12} \text{ ergs s}^{-1} \text{ cm}^{-1}$

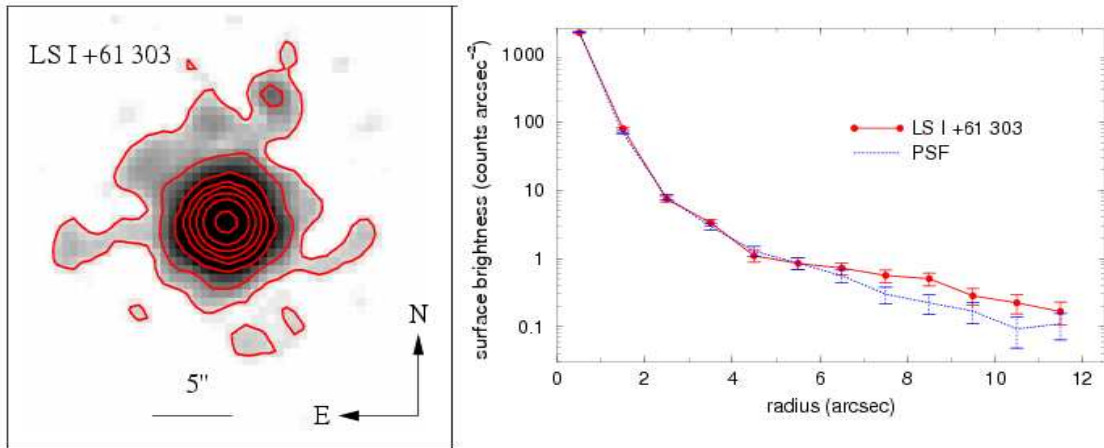


Figure 4.14: Left: The Chandra X-ray image of LSI +61 303 in the 0.3-10 keV band. Extended emission can be seen to the North of the central emission source. Right: A plot of the surface brightness counts of the source region versus the point source function. Extended emission is clear from 5 arcseconds outward. Taken from Paredes et al. (2007)

which is also consistent with previous measurements near that orbital phase. The derived spectral index, however, was determined at $\alpha=1.25\pm 0.09$, much harder than any previous measurements made. The Chandra exposure also detected extended emission between 5 and 12.5'' towards the North of LSI +61 303 (see figure 4.14). This detected emission has no definitively clear mechanism at this point in the frame of both the microquasar and binary pulsar models, however, it is evident from these observations that particle acceleration may be taking place as far away as 0.05-0.12 parsecs from LSI +61 303.

Moving to the harder X-ray regime, Harrison et al. (2000) presents the results of observations with RXTE (the same pointing as the PCA data set above) using the HEXTE instrument which provided coverage in the 15-150 keV band. The data shows a 7σ detection in this energy range from data integrated over the entire observational campaign. The HEXTE data is unable to provide a significant correlation between the harder X-ray emission and the softer PCA observations due to LSI +61 303 being too dim in the 15-150 keV band for individual detections on the same time scale as those obtained by the PCA.

The PDS detector (Phoswich Detection System) aboard Beppo-SAX also detected LSI +61 303 in hard X-rays during the same observational set in which the softer Beppo-SAX observations were made (Sidoli et al., 2006). The PDS detected LSI +61 303 between 15-70 keV at a significance of 4.4σ with an integrated flux of approximately $3 \times 10^{-11} \text{ erg cm}^{-2} \text{ s}^{-1}$.

In figure 4.15, all of the above discussed observations are combined. 4.15 (left) shows a plot of

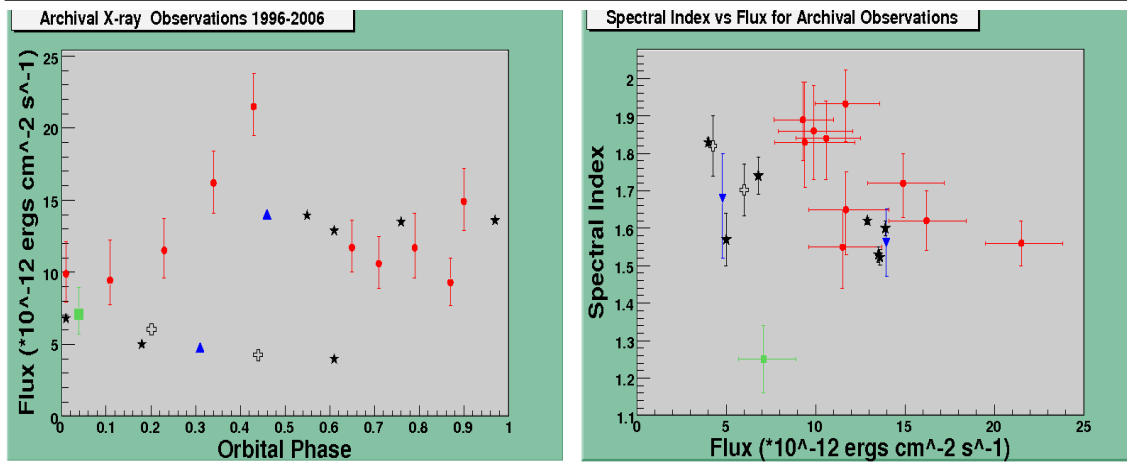


Figure 4.15: Left: Flux vs orbital phase of archival observations. Right: Flux vs spectral index for the same dataset. Red dots represent the RXTE data points in (Neronov and Chernyakova, 2007), Beppo-SAX and XMM-Newton data (Sidoli et al., 2006) are shown in blue triangles and black stars (respectively), the long Chandra pointing (Paredes et al., 2007) is shown by the green square, and the ASCA observations (Leahy et al., 1997) are shown by black crosses. All fluxes are in the 2-10 keV band, with the exception of the Chandra data point which is 0.3-10 keV.

the flux versus orbital phase in which a general trend towards higher emission later in the orbital phase can be seen. However, this feature does not always appear (XMM-Newton) and it is not clear that the increase in flux appears at the same region of the orbit every time. Despite the numerous data sets, no definitive conclusion (other than that it is obviously variable) can be made about the overall X-ray flux behavior of the system. 4.15 (right) shows a plot of the spectral index of the X-ray emission versus the flux level. Contrary to the claim of Sidoli et al. (2006), when all the available X-ray observations are taken into account, there is no statistically viable evidence for a correlation between spectral index and flux.

4.5.4 MeV Gamma Ray

In 1994 the OSSE experiment aboard the Compton Gamma Ray Observatory (CGRO) monitored LS I +61 303 as a part of a multiwavelength campaign involving radio, optical, and infrared measurements (Johnson et al., 1993). The source was observed three times over the year, with a detection in the 50-300 keV band resulting only during one observation window. The 4σ detection in this band was used to extract a spectrum with index $\alpha=1.6\pm 0.6$. Because of the faint detection and the long period over which the detection was made (orbital phase 0.3-0.84), no claim of modulation of the measured flux could be made.

Moving again to a slightly higher energy band, the COMPTEL experiment (again aboard CGRO) in observations from 1991-1994 detected a source which was positionally coincident with LSI +61 303 in the 1-30 MeV band (Schoenfelder et al., 1981). The peak flux from these observations comes in the 1-3 MeV band, with emission tailing off after this range. This turnover turns out to be consistent with the extrapolated spectrum from lower energy measurements when connected to the EGRET measurements (discussed below). Because of the large spread in time over which these measurements were made, as well as the uncertainty in flux measurements due to background corruption, no statement regarding orbital variability could be made with this data set.

The previously mentioned EGRET measurements of this source were the first gamma-ray measurements to be made which clearly showed signs of orbital variability. Flying aboard CGRO, the EGRET experiment detected a source 3EG J0241+6119 over the time period of May 1991 to October 1995. 3EG J0241+6119 was shown to be a strong, persistent source of >100 MeV gamma rays and was spatially coincident with LSI +61 303 (Kniffen et al., 1997). 3EG J0241+6119, showing an average >100 MeV flux of $(9.2 \pm 0.6) \times 10^{-7} \text{cm}^{-2}\text{s}^{-1}$ with strong evidence for short term variability (hour timescale), initially showed only marginal evidence for variations with respect to the orbital period which left the identification of it with LSI +61 303 somewhat in the air. Further observations of 2EG J0241+6119 in September 1996 reinforced the hypothesis of orbital scale variability in a full orbital monitoring of the source (Tavani et al., 1998), which was then referred to by its listing in the 3rd EGRET catalog, or 3EG J0241+6103. In these observations, the flux increased significantly over the period of observations, peaking at orbital phase 0.2 (see figure 4.16). A further analysis by Massi (2004) showed a strong peak for the data set at a period of 27.4 ± 7.2 days (at a chance probability of $<1\%$), which is consistent with the measured orbital period of the system of 26.496 days. When the data set is folded with the 26.496 day period, there are two peaks in emission located near $\phi=0.2$ and 0.5. This prompted Taylor et al. (1992) and Marti and Paredes (1995) to submit that a “two-peak” accretion model may be at work in the system. This model, while suffering from several drawbacks, is still a viable pathway within the microquasar framework and will be discussed in 4.5.6.1.

4.5.5 TeV Gamma Ray

Previous observations by the Whipple telescope detailed in Fegan (2004) and Hall et al. (2003) set upper limits of $22 \times 10^{-12} \gamma \text{cm}^{-2}\text{s}^{-1}$ and $8 \times 10^{-12} \gamma \text{cm}^{-2}\text{s}^{-1}$ for emission above 350 GeV and 500 GeV respectively. These results rely on a comparatively small dataset of 15 hours of livetime, which was the author’s principal motivation to increase the observational data set with

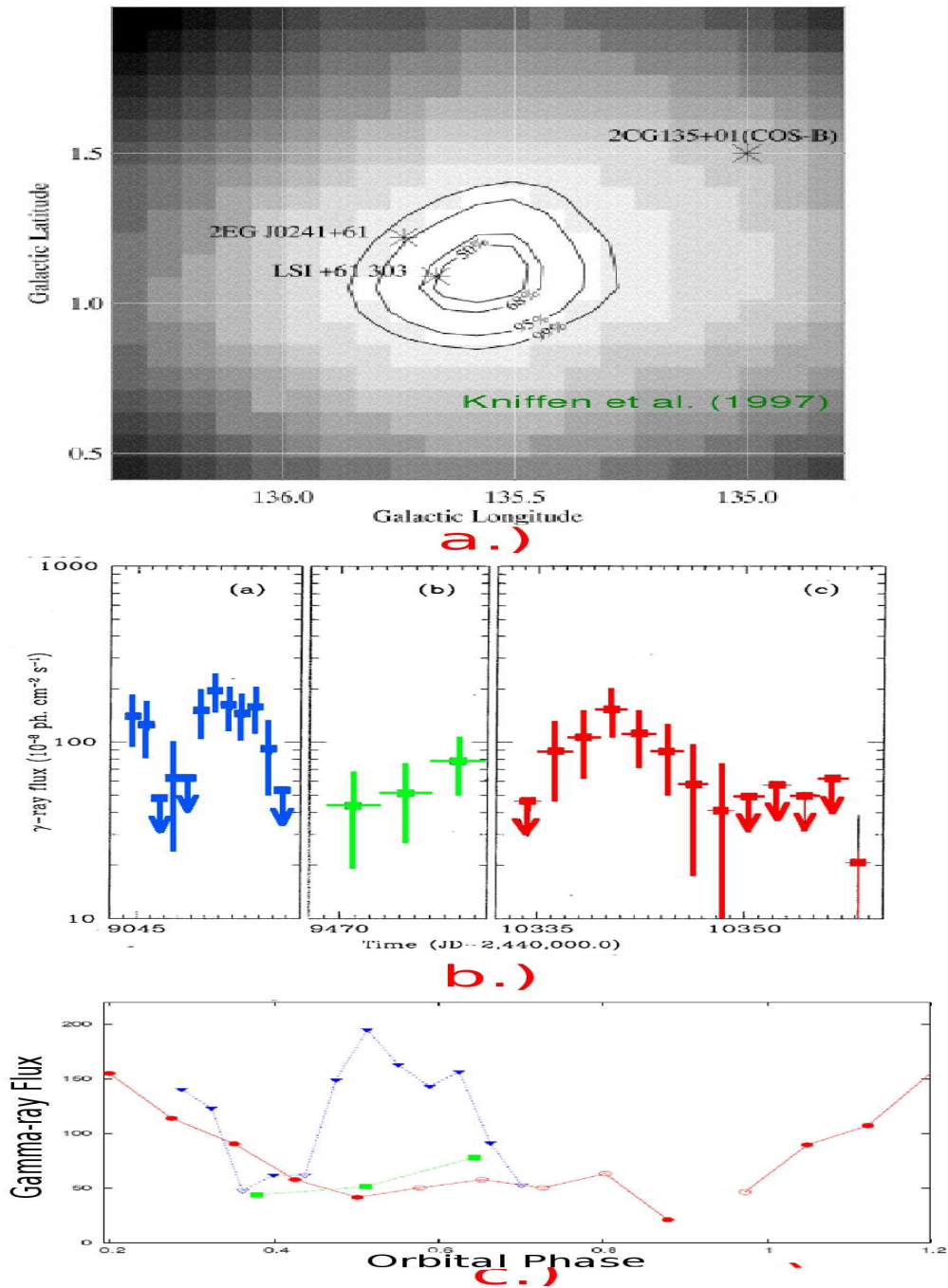


Figure 4.16: a.) The EGRET >100 MeV image of 3EG J0241+6130, positionally coincident with LSI +61 303. Also shown is the previous position of the source from the second EGRET catalog (Kniffen et al., 1997). b.) The observations detailed in the text, the first panel represents observations taken in 1993; the second, 1994; and the final panel covering the 1996 observations. (modified from Massi (2004) c.) The data points in b.) folded with a 26.496 day period. The data from separate orbital cycles are connected by lines. A variable nature can be inferred from the data with peaks near 0.2 and 0.5, however, error bars are not included (modified from Massi 2004)

4.5. LSI +61 303

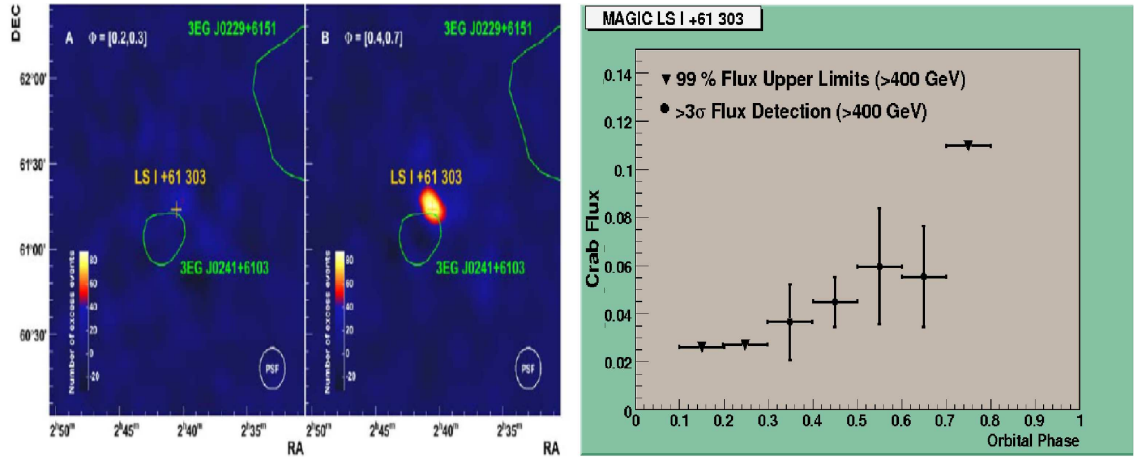


Figure 4.17: The MAGIC detection of LSI +61 303. Shown are the 2-D sky maps resulting from the $\phi = 0.2 \rightarrow 0.3$ (left) and $\phi = 0.3 \rightarrow 0.7$ (middle) from the data set shown in the overall light curve (right). Taken from Albert (2006).

the Whipple 10 m telescope on this target. The author was responsible for the initialization of a long term observational campaign taking place over the Autumn 2005/Spring 2006 timeframe which increased the dataset to 40 hours. The upper limits on emission above 350 GeV from this campaign are presented in section 5.5.

Coincidentally, the much more sensitive IACT MAGIC was observing LSI +61 303 during this same timeframe and did detect the source as a variable high energy source above 200 GeV (?). This 54 hour observation set covered six orbital cycles from phase $\phi=0.1 \rightarrow 0.8$ which detected a strong gamma-ray flux during orbital phases $\phi=0.4 \rightarrow 0.7$. This data set showed flux peaking at 16% of the Crab flux during phase $\phi=0.6$. The source however, was not detected during the other orbital phases (i.e. $\phi=0.1 \rightarrow 0.3$ and $\phi=0.7 \rightarrow 0.8$) which included the periastron passage. The extracted spectra from 0.2 to 4 TeV is fitted well by a power law with spectral index $\alpha = 2.6 \pm 0.4_{stat,sys}$.

The MAGIC detection has now been confirmed in TeV gamma rays by observations taken by the VERITAS array which are presented in section 6.

4.5.6 Models for High Energy Emission

Before examining the various models for high energy emission from LSI +61 303 it is useful to summarize the observational properties detailed above:

- **Radio:** The system presents outbursts in radio roughly every 26.5 days, coincident with the orbital period of the system. These radio outbursts go through a 4 year modulation in both the timing and orbital location of the outbursts, however, in general most outbursts

occur between orbital phases 0.4 and 0.9. High resolution radio observations of the system by MERLIN and EVN reveal the presence of a double sided extended structure extending from the object, interpreted to be a relativistic jet. This interpretation is challenged however by recent (2006) VLBA observations which show radio images of “cometary” structures extending from the system, interpreted as the synchrotron emission from the tail of a pulsar wind.

- **X-ray:** LS I +61 303 is even more puzzling in the X-ray regime. Although there have been numerous observational campaigns focused on the source, there has not yet emerged a single coherent picture of the X-ray behavior of the system. In general however, several properties can be extracted from the observations. First of all the X-ray emission “usually” increases significantly at later stages of the orbit with low flux states occurring before $\phi = 0.4$ and high states generally occurring afterwards. The spectra from the observations are very well fitted by an unbroken power law (implying a non-thermal X-ray mechanism) with typical spectral indices between 1.5 and 2 (with the exception of the very hard spectra Chandra observations of spectral index 1.2). Despite claims by some of the authors detailing the various observations, there is no clear evidence for a consistent relation between spectral index and flux when all the observations are taken into account.
- **Soft Gamma Rays:** The only reliable observations in this energy band come from EGRET. These observations show LS I +61 303 to be a variable source in the >100 MeV band. Phase analysis of this data infers the presence of two emission peaks, one located near periastron ($\phi=0.2$) and another later in the orbit ($\phi=0.4$ to 0.6).
- **TeV Gamma Rays:** The MAGIC detection of LS I +61 303 shows the source to be a variable TeV emitter with emission appearing between $\phi=0.4$ and 0.7 and a distinct lack of emission near periastron passage.

With all these observational properties taken into account, there have been two main models attempting to explain the high energy emission from this system based upon the differing premises: either this system is a microquasar or a binary pulsar. There are many variations on these two competing models and only two recent models are examined here, but these two are representative of the general mechanisms considered in the various emission models for this source and serve as a good template.

4.5.6.1 Microquasar Model

The most recent microquasar model that takes into account all available observations is that of Bosch-Ramon et al. (2006b). In it the authors model the system based on inverse-Compton emission from the jet. The model consists of the compact object embedded in an orbit co-planar with the circumstellar disk of the Be star with an initial density of $10^{-11} \text{ g cm}^{-3}$, exponentially falling off near $12 R_*$ (R_* = radius of the Be star). The energetics of the relativistic jet are dictated by the accretion rate (\dot{M}) of the system which is shown to have two maxima (Marti and Paredes, 1995):

$$\dot{M} \propto \frac{\rho_{wind}}{v_{rel}} \quad (4.5)$$

The first maxima occurs at periastron where the density of the stellar material is highest, and the second at a later orbital phase where the decrease in relative velocity compensates for the drop in stellar wind density ($\sim \phi = 0.5$). These accretion peaks feed a relativistic population of electrons ejected into the jet which then are further accelerated by the shock front created between the jet and the stellar wind in which the jet is embedded. Bosch-Ramon (2005b) takes the accretion rate changes into account and models both radio synchrotron and X-ray/gamma-ray inverse-Compton emission.

Electrons are injected from the jet into shocked regions, resulting in an overall electron energy spectrum of E^{-2} (first order Fermi acceleration), with a lower limit to E set at 1 MeV. An upper limit is set by equating radiative losses to the acceleration rate of the electrons within the e jet region of size s , here s is modeled as 2 homogeneous spheres of radius $R_{orbital}/3$, with $R_{orbital}$ representing the orbital distance. This leads to a constraint of $E_{max} < \eta qBs$, with η representing an acceleration efficiency. $\eta = 0.01$ and $B = 1G$ are set in order to reproduce the MAGIC TeV result of an $E_{max} \sim 4$ TeV. The luminosity of injected electrons L_{in} varies according to the accretion rate:

$$L_{in} = L_{norm} \frac{\dot{M}}{10^{18} \text{ g s}^{-1}} \quad (4.6)$$

with L_{norm} set (from observations) at $1.3 \times 10^{35} \text{ ergs s}^{-1}$. Synchrotron and inverse-Compton (both Thomson and Klein-Nishina) losses are modelled, the latter model taking into account both angular dependence and the separate process of pair-production effects on stellar fields. The target photon fields considered for inverse-Compton losses are dominated for most of the orbit by the thermal radiation from the Be star ($T=2.6 \times 10^4 \text{ K}$). The exception is near periastron where thermal emission from the densest regions of the stellar wind ($T=1.7 \times 10^4 \text{ K}$) dominates over the stellar radiation.

The resulting spectrum produced from this simulation fits the observed data reasonably well.

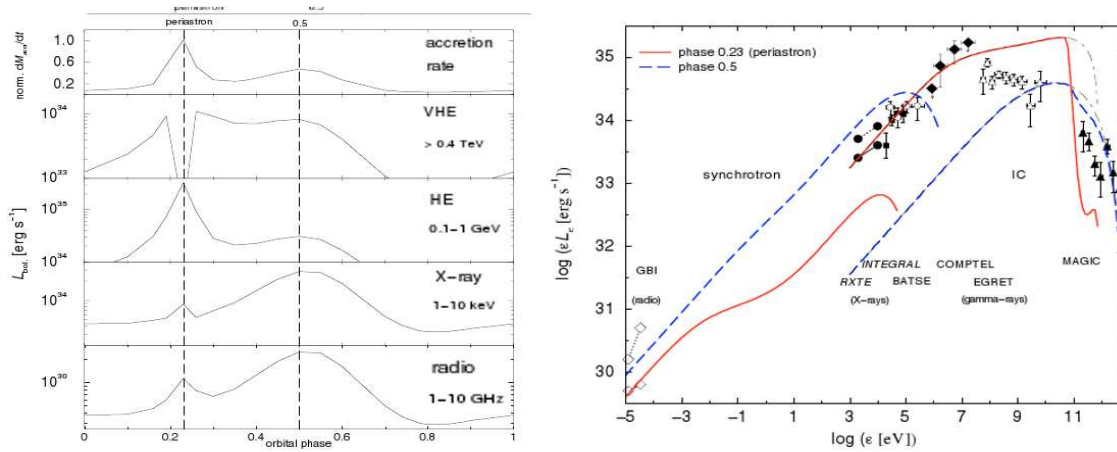


Figure 4.18: The phase dependent lightcurve generated by microquasar model of Boch-Ramon et al. (2006B) (left) and its spectral results compared to observations (right).

Figure 4.18 (left) shows the predicted accretion luminosity and consequent flux variability for the TeV, GeV, X-ray and radio bands. There is a severe dip in the TeV production due to photon-photon absorption, but an excess near orbital phase $\phi = 0.5$ which is seen in the MAGIC data set (albeit slightly later at $\phi = 0.6$). The MeV flux shows a peak at periastron as well as one near $\phi = 0.5$ which is present in the EGRET data set, although the two peaks in the EGRET data set are roughly equal in flux. The X-ray and radio behavior is also reproduced well showing deficits near periastron but excesses later in the orbit. From looking at the resulting spectrum (figure 4.18 right) the synchrotron and IC losses compete greatly near the hard X-ray regime, with the model slightly underpredicting the soft gamma-ray flux at $\phi = 0.5$ and overpredicting it at periastron. However, the TeV spectra agrees relatively well with the MAGIC results with the obvious effect of photon-photon scattering taking a toll on the TeV flux near periastron (the dashed lines show unabsorbed spectra). This model, however, only takes into account emission from the base of the jet and not the entire extension of it (defined as the total region of radio emission); this factor as well as alterations provided by the observed precession of the jet (Massi et al., 2004) could also introduce variations into this model.

4.5.6.2 Binary Pulsar Model

As an alternative to the microquasar scenario is the binary pulsar explanation for LS I +61 303 first proposed by Maraschi and Treves (1981) and developed extensively in Dubus (2006). In this model, a shock front that accelerates electrons to relativistic energies is set up at a “standoff distance” away from the pulsar R_s . This distance is the location (relative to the pulsar) at which

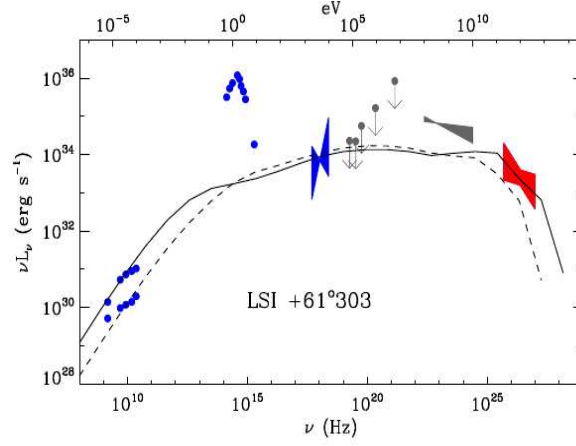


Figure 4.19: The spectrum produced by the binary pulsar model of Dubus (2006). The solid black lines represent emission at periastron and the dashed black line represent emission at apastron.

the pressures from the pulsar wind and stellar wind equate and varies along the orbit. It is given by:

$$R_s = \sqrt{\frac{\rho_w(v_w - v_p)^2 4\pi c}{\dot{E}}} \quad (4.7)$$

where ρ_w, v_w are the stellar wind density and velocity; v_p , and \dot{E} are the velocity and energy loss rate of the pulsar wind. At R_s a shock is formed which accelerates particles to relativistic energies, which then lose energy via synchrotron and inverse-Compton channels. Taking R_s to vary from 5×10^{10} to 2×10^{10} cm, this distance determines which particle acceleration process are dominant. At periastron, R_s is a minimum which increases the B field (coming from the pulsar) at the shock, increasing X-ray synchrotron losses and decreasing inverse-Compton contributions (lack of TeV emission at periastron agrees with observations).

This model, however, predicts a maximum of X-ray emission near periastron which stands against the observational evidence. Also, the fall off of synchrotron emission as well as the lack of inverse-Compton emission at MeV-GeV energies underpredicts the EGRET flux (see figure 4.19). However, the strengths of the model are recovered in the TeV and radio predictions. At apastron, the model predicts a maximal R_s which lowers the magnetic field and increases inverse-Compton losses. This model predicts a TeV maximum at apastron and provides a spectrum which slightly underproduces but is consistent with the MAGIC data. Near periastron the Bondi capture radius (distance at which the pulsar begins to accrete material from the stellar wind) is larger than R_s which results in mostly isotropic ram pressure surrounding the pulsar wind “bubble” resulting in weaker, symmetric synchrotron radio emission. At apastron, however, due to the large R_s , the Bondi radius is now within the standoff distance and results in a one sided ram pressure from

the direction of the stellar wind, resulting in a cometary form of the pulsar wind and associated synchrotron radio emission. This claim was seemingly justified by the VLBA results in Dhawan (2006) (see figure 4.9). However, recent simulation work (Romero et al., 2007) disagrees with this claim. Regardless, the prediction and subsequent observation of what appears to be cometary radio emission from LS I +61 303 stands as one of the main strengths of the binary pulsar argument.

4.6 Summary

In this chapter a description of the overall features of active high mass X-ray binaries was given within the context of both the binary pulsar and microquasar models. Brief observational summaries were given of two detected TeV HMXB systems PSR 1259-63 and LS 5039. A brief description and summary of the microquasar Cygnus X-3 (undetected at TeV energies) was given as background to the TeV upper limits that will be presented in the next chapter. An extended observational summary of LS I +61 303 is presented with the key characteristics highlighted in section 4.5.6. Two of the most prominent models for explaining high energy emission from LS I +61 303 are presented. The microquasar model of Bosch-Ramon et al. (2006b) is detailed showing that it reproduces the variable behavior of the system in radio, X-rays, and TeV gamma rays quite well; while slightly underproducing the soft gamma-ray spectrum during the later phases of the orbit. This model cannot explain the lack of accretion signatures in observations nor the apparent cometary shaped radio morphology detailed Dhawan (2006). The binary pulsar model of Dubus (2006) was presented which accounts for the above mentioned radio morphology in its predictions as well as the TeV variability observed from the system. However, the model lacks an ability to accurately produce the variability observed in X-rays as well as underpredicting the EGRET GeV flux. These models will both be revisited in chapter 8 and compared to the most recent results on LS I +61 303 with VERITAS and RXTE.

Chapter 5

Whipple 10 m Observations of Cygnus

X-3 and LS I +61 303

In 2005 and 2006 the Whipple 10 m was primarily used to monitor very high energy gamma-ray emission from a select group of AGN known to be TeV sources (Grube, et al. 2007). During this period, any spare time between blazar observations was dedicated to observing undetected sources that were believed to be possible TeV emitters. Among these were the galactic binaries Cygnus X-3 and LS I +61 303. Observations taken on these objects did not yield any cumulative (or in the case of LS I +61 303, phase resolved) significances; however, the data taken on these sources has been used to determine flux upper limits which are presented here.

5.1 Flux and Flux Upper Limit Calculations

In section 3.1.6 the method for determining both the rate and significance of a signal from a putative gamma-ray source was described. The significance of observations defined could be equivalently stated as the level of confidence at which the hypothesis “This is not a gamma-ray source” is rejected. It is customary to deem a source present if this hypothesis is then rejected at the 5σ confidence level (Weekes, 1999). If the data does not reveal a significance above this amount, the data can then be used to place upper limits on what the maximum flux could have been from the source during the observational time period. The customary method for performing this calculation is that presented in Helene (1983). This method provides a way to get the upper limit in terms of ON source counts for an arbitrary confidence level (usually 99.9% or greater). In other words, given an observation of duration T_s that resulted in source counts of C_{on} and background counts of C_{off} , the Helene method will give the number of excess counts C_{ul} which, to a 99.9% probability, the source could have presented and still have been consistent with a null detection.

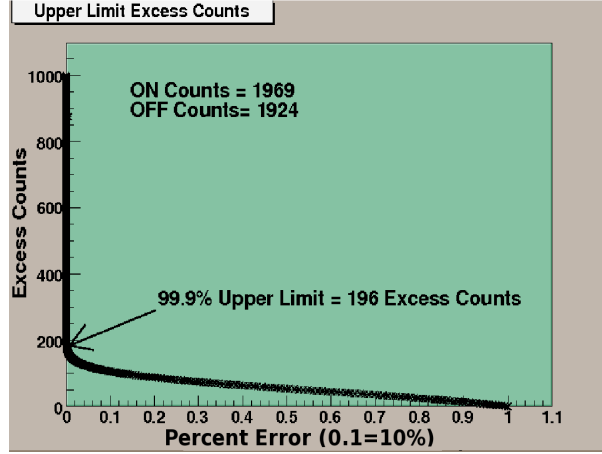


Figure 5.1: An example of the determination of the upper limits counts for a sample data set. Generated by solving for C_{ul} (y-axis) in terms of α for a given C_{on}, C_{off} and σ .

For the present work, these upper limit counts were translated into both a upper limit flux in terms of the Crab Nebula flux, and a physical flux upper limit in photons $\text{cm}^{-2}\text{s}^{-1}$. The separate steps are presented below:

- **Helene Count Upper Limits:** Given source counts C_{on} and background counts C_{off} from signal and background regions of the same area, it is possible to find the probability α that a given excess count level C_{ul} was due entirely to Gaussian fluctuations (Helene, 1983):

$$\alpha = \frac{ERFC\left(\frac{C_{ul}-C_{on}+C_{off}}{\sqrt{C_{on}+\sigma^2}}\right)}{ERFC\left(\frac{-C_{on}+C_{off}}{\sqrt{C_{on}+\sigma^2}}\right)} \quad (5.1)$$

where σ is the standard deviation of the background counts and

$$ERFC(x) = \frac{1}{\sqrt{2\pi}} \int_x^{\infty} e^{-z^2/2} dz \quad (5.2)$$

Theoretically, equation 5.1 can then be rearranged to solve for C_{ul} , in practice, the input values of C_{on} , α , C_{off} , and σ are fixed and input into a ROOT code macro and the resulting value of C_{ul} is found. See figure 5.1 for a graphical example of this concept. Following de la Calle Perez (2002), in the case where $C_{on} < C_{off}$, then C_{on} is set equal to C_{off} in order to give conservative results.

- **Crab Flux Upper Limits:** After C_{ul} is found for a given observation, this value is then converted to an upper limit in terms of a flux from the Crab Nebula. Given a source observation set of duration T_s (resulting in a count upper limit C_{ul}) and a Crab observation set of

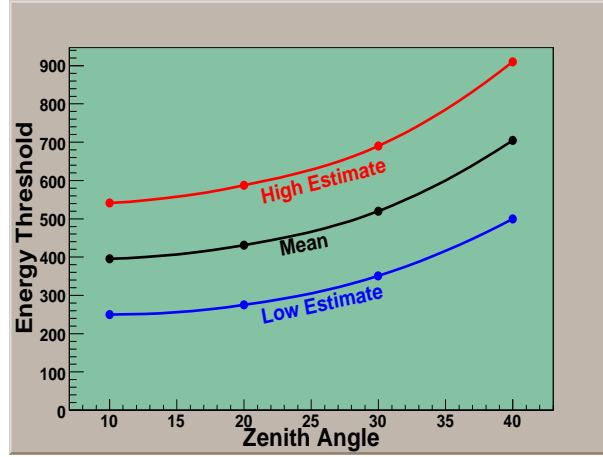


Figure 5.2: The estimation used for energy threshold vs elevation for Whipple 10 m data. Data taken from Grube (2007).

duration T_c (resulting in excess counts C_{Crab}), the upper limit in terms of Crab flux (UL_C) is defined as:

$$UL_C = \frac{C_{ul}}{C_{Crab}} * \frac{T_c}{T_s} \quad (5.3)$$

- **Absolute Flux Upper Limits** After UL_C is determined, this value can be easily converted to an absolute flux upper limit UL_{abs} (in $\gamma \text{ cm}^{-2}\text{s}^{-1}$) by knowing what the Crab absolute flux (F_{Cr}) above an energy threshold (E_{th}) is (de la Calle Perez, 2002):

$$\begin{aligned} UL_{abs} &= UL_C * F_{Cr}(> E_{th}) \\ &= UL_C * A * \int_{E_{th}}^{\infty} E^{-\Gamma} dE \end{aligned} \quad (5.4)$$

where A is a flux normalization constant such that:

$$F_{Crab}(> 1\text{TeV}) = A * \int_{E_{1\text{TeV}}}^{\infty} E^{-\Gamma} dE \quad (5.5)$$

Combining equations (5.4) and (5.5):

$$UL_{abs} = UL_C * F_{Crab}(> 1\text{TeV}) * E_{th}^{-\Gamma+1} \quad (5.6)$$

Therefore, the determination of the flux upper limit depends solely on measured data from the Crab Nebula and not on simulations. However, this method assumes that the putative source flux has the same spectral shape (index) as the Crab Nebula. Since we are integrating the Crab spectrum above a given energy threshold, and the threshold of observations will change as a function of the zenith angle of observations, the observations must be compared

to a Crab Nebula data set which was taken over a range of zenith angles similar to those of the actual data. For the LS I +61 303 data set examined in this chapter, the flux upper limit was calculated by comparing it to a subset of the Crab nebula observations described in this chapter which had similar zenith angles to the LS I +61 303 observations. The Cygnus X-3 observations were compared to the entire Crab data set as its range of zenith angles were comparable to those of the entire Crab data set. To compute the energy threshold for observations at a given zenith angle, recent Monte Carlo simulations described in Grube (2007) are shown in figure 5.2 and these values will be used for the energy thresholds used in this analysis. The red line in figure 5.2 represents restrictive cut values used to determine the threshold while the blue line represents more relaxed analysis parameters. For the current work, the mean of the two values will be used. A similar method was used to produce the upper flux limits for LS I +61 303 from 2005-2006 published in Smith et al. (2006) by using the Crab spectral index of -2.49 and flux at 1 TeV of $2.1 \times 10^{-11} \gamma \text{ cm}^{-2} \text{ s}^{-1}$ (Hillas et al., 1998), this method is updated here for the newest determinations of the energy threshold of the observations and Crab spectral parameters observed with the Whipple 10 m between 2000-2006, detailed in Grube (2007). That work gives an average value of spectral index of -2.63 (averaged between restrictive and relaxed analysis parameters) and of flux above 1TeV of $1.99 \times 10^{-11} \gamma \text{ cm}^{-2} \text{ s}^{-1}$.

5.2 Data Quality Selection and Analysis Parameters

In section 3.1.6 the various modes of observing for the Whipple 10 m telescope were described. The preferred mode of observation for the detection of new sources is the PAIRS mode and it is this mode that was used for the data selection for the Crab, Cygnus X-3, and LS I +61 303 observations. The quality selection criteria that were used for these data sets were the following:

- **Elevation $>50^\circ$:** Below this elevation, the telescope's sensitivity drops due to the larger energy threshold as well as additional noise from scattered city lights etc. that become more significant with larger zenith angles.
- **Weather:** Each night the observers at the Whipple 10 m will include (on a run by run basis) a judgment of what the weather looked like for observing (graded A \rightarrow C). Of course the preferred weather grade for data is A; however, anything above B- is usually usable for analysis and is judged by its rate stability on a run by run basis. For the analysis of the 10 m data presented here, any run above a B- grade is used (after the additional below criteria are applied).

- **Rate Stability:** However, the observers evaluation of the weather conditions have been notoriously inconsistent. Therefore, a more useful gauge (combined with the observer’s weather grade) of the quality of each data run is gained by looking at the signal trigger rate from the data acquisition chain. Although different sky conditions as well as hardware configurations (such as CFD threshold) will introduce variations in the raw trigger rate, the standard deviation of this trigger rate (σ_{rate}) is an effective gauge of how stable the data is. A large standard deviation implies that the telescope was triggering erratically or there were major deficits or excesses in trigger rates due to weather. All of these will add biases to the analysis, for example, if an ON run had a consistent rate and its associated OFF run had an erratic trigger rate with deficits (say due to clouds), this would bias the ON data run and possibly result in a false positive excess. In order to remove the possibility of allowing these biases into the analysis chain, the post-analysis trigger rate of each ON and OFF run is examined and any run showing a standard deviation of larger than 3 Hz is discarded (a typical mean rate for a dark sky run is of the order of $\sim 20\text{-}30$ Hz). Although this is a particularly liberal allowance ($\sim 4\text{-}5\sigma$ effect) for rate stability, it was determined that poor weather conditions would result in values much higher than 3 Hz and thus justifies this cut value. For the datasets analyzed in this work, there were several exceptions to this criteria in the case where the high voltage supply of the 10 m temporarily dropped out, which would give large rate deviations (rate cut in half or more) but only temporarily, and thus would not effect the overall data quality since these dropouts were very short (less than 30-40s).
- **Analysis Cuts:** The cuts used for this analysis are based on discriminating the second moment parameters of each individual image recorded by the data acquisition system on the Whipple 10 m (see section 3.1.4). The specific set of cuts used has been in use at the Whipple 10 m since 2000 and is known as *SuperCuts 2000*. These cuts were optimized on Crab Nebula data in order to maximize the resulting rate and significance. Although there have been several variations on these cuts used at the Whipple 10 m in order to optimize cuts for specific tasks (such as sources at large zenith angles)(Kosack, 2005) *SuperCuts 2000* has remained as the default set of cuts to analyze any given source without respect to its individual properties. See table 3.1 for a list of these cuts.

5.3 Crab Nebula Data Set

For calibration purposes, observations of the Crab Nebula are performed every season. These observations are also necessary in order to carry out the flux upper limit calculation described above.

5.3. CRAB NEBULA DATA SET

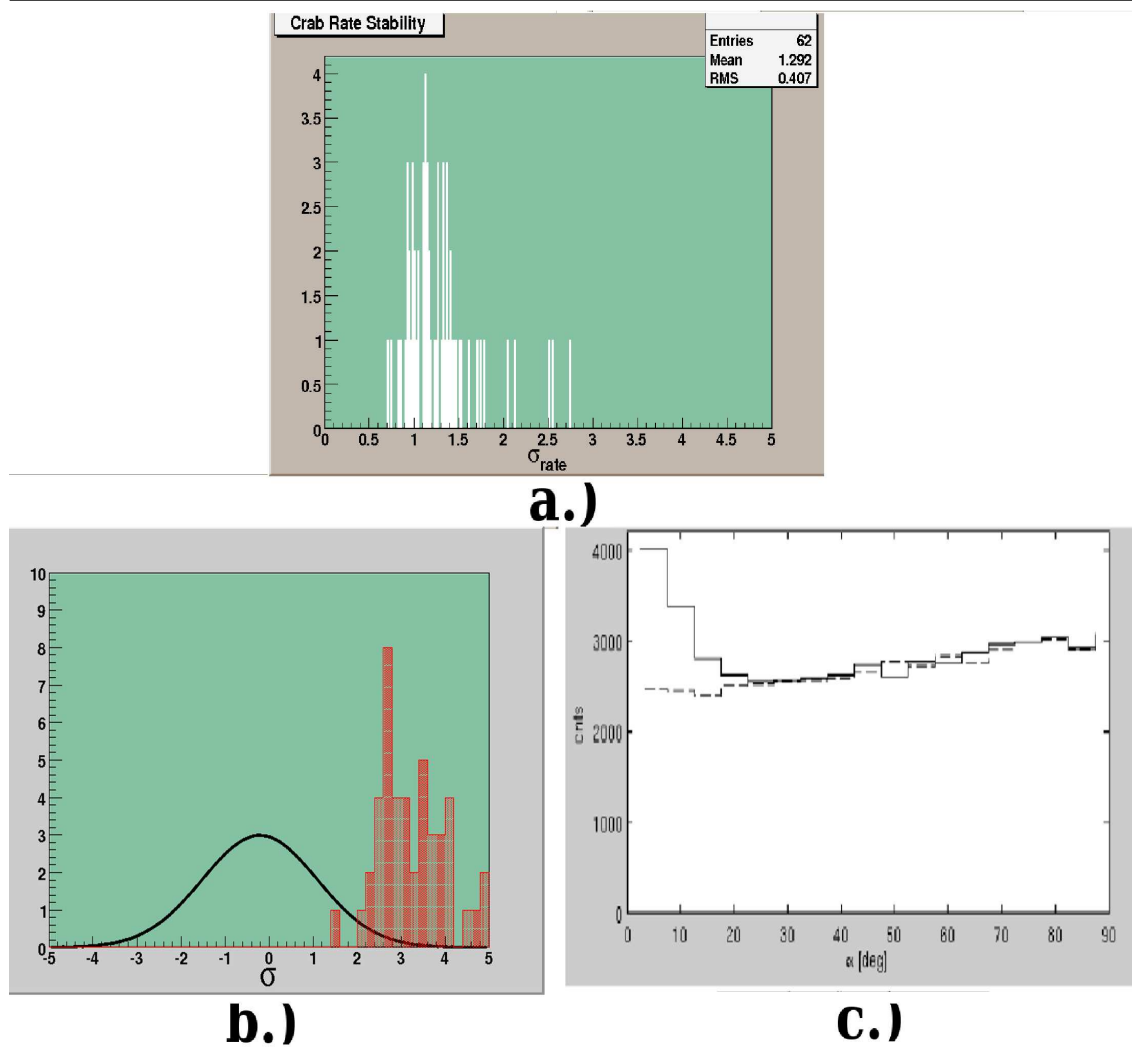


Figure 5.3: The results of the selected Crab Nebula observations from 2005-2007. a.) Shows the rate stability standard deviation on a run by run basis (the large deviations are associated with temporary drops in the high voltage supply). b.) Shows the distribution of significances along with the distribution expected for a non-detection (Gaussian). c.) Shows both the alpha parameter distribution for ON (solid lines) and OFF (dashed lines).

In the 2005-2007 observing season, a data set consisting of 18.43 hours of pointed observations (along with the corresponding 18.43 hour OFF observations) were taken in PAIRS mode. The data were taken from October 2005 until December 2006 at a variety of elevations ranging from 50° to 80° . The full data set resulted in a detection of 21.94σ at a gamma-ray rate of $(2.63 \pm 0.12) \gamma \text{ min}^{-1}$, which is consistent with previous results from observations taken at similar zenith angles. The alpha distribution and two dimensional significance map are shown in figure 5.3.

5.4 Cygnus X-3 Observations

In Autumn 2006, observers at the Whipple 10 m telescope were alerted by staff at the Harvard-Smithsonian CfA that Cygnus X-3 was particularly active in both radio and X-ray regimes (McCullough, 2006). As a response to this alert, the Whipple 10 m began monitoring the source which was visible in October and November. These observations resulted in a usable data set of 5.08 hours of pointed ON observations with an associated 5.08 hours of OFF observations. Although these observations did not result in any detections of reliable significance, the data were used to derive an upper flux limit. This resulted in an upper limit of 16.6% of the Crab Nebula flux on Cygnus X-3 during this time.

For absolute flux upper limits, equation 5.6 is used. The approximate elevation of the data set was determined to be 70° , which by figure 5.2, implies an average energy threshold of 460 GeV. The upper flux limit for the observation set is therefore:

$$\begin{aligned} F(> 460\text{GeV}) &= 0.166 * 1.99 * 10^{-11} \gamma \text{ cm}^{-2} \text{ s}^{-1} * \frac{0.46^{-1.63}}{\text{TeV}} \\ &= 2.35 * 10^{-11} \gamma \text{ cm}^{-2} \text{ s}^{-1} \end{aligned} \quad (5.7)$$

Which, although not ruling out periodic flaring from this source, does rule out steady emission at the level reported previously by other TeV experiments. It is assumed that the same electron population which gives rise to the hard X-ray outbursts in Cygnus X-3 might also create TeV gamma rays through non-thermal processes described in the previous chapter. To explore this, the hard X-ray data taken by the ASM during this time period is shown compared to the nightly binned fluxes observed by Whipple in figure 5.5. It is clear that in X-rays, the source goes through large variations in count rates. Since no detection in the TeV regime were made during this time, there can be no strong conclusions drawn about correlations with the X-ray behavior. However, if the X-ray flux is in fact correlated with a TeV flux, it is not present at the level of sensitivity of Whipple. Further long term, high density monitoring in both TeV and X-ray regimes is necessary to derive more constraining upper limits on both the TeV flux and any possible correlation between it and a hard X-ray flux.

5.5 LS I +61 303 Observations

From September 2004 to January 2007, a total of 55.85 hours of ON source observations (along with the accompanying 55.85 hours of OFF observations) which passed all selection criteria were taken on LS I +61 303. Initially, the data from September 2004 to February 2006 were analyzed

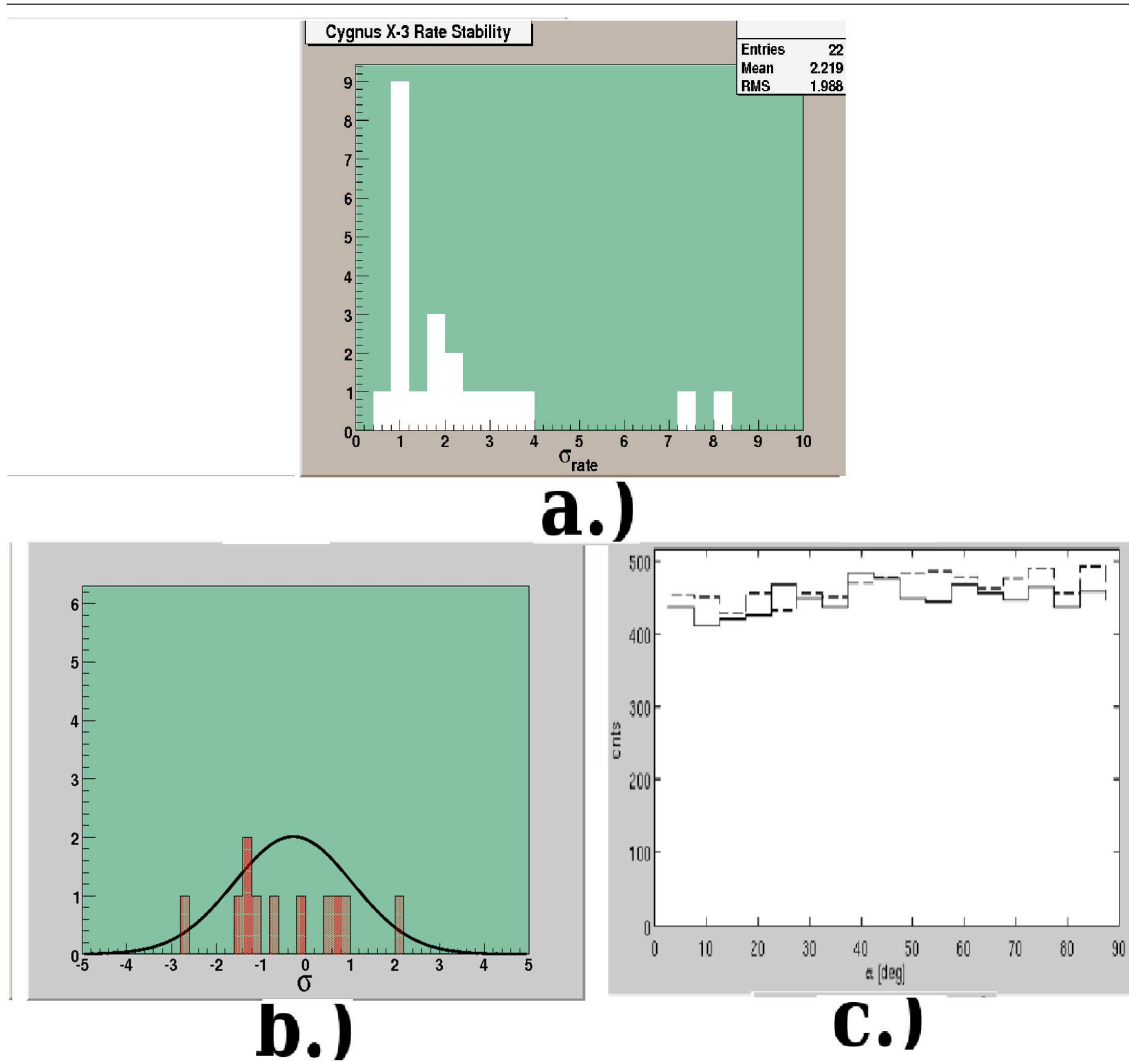


Figure 5.4: The results of the Cygnus X-3 observations described in the text. The associated figures are the same as in figure 5.3. All data is consistent with a null detection.

and presented in Smith et al. (2006). Later in 2006 and 2007 additional data was accumulated on LS I +61 303 with the Whipple 10 m and it is the union of that data with the original analysis that is presented here. The same set of analysis parameters described above for Cygnus X-3 were used for offline analysis of both data sets.

Because of the inability to observe during moonshine, not all orbital phases could be covered with equal exposure time (see figure 5.7). Coincidentally (or unfortunately) the orbital phases that are now known (from the MAGIC observations (?) and VERITAS observations (Maier et al., 2007b)) to be the phases with the greatest amount of high energy gamma-ray emission, were not covered in as good detail as some other orbital phases. These observations did not yield any detection at the total data set level, nor the individual bin level (binned by 0.1ϕ). Since there

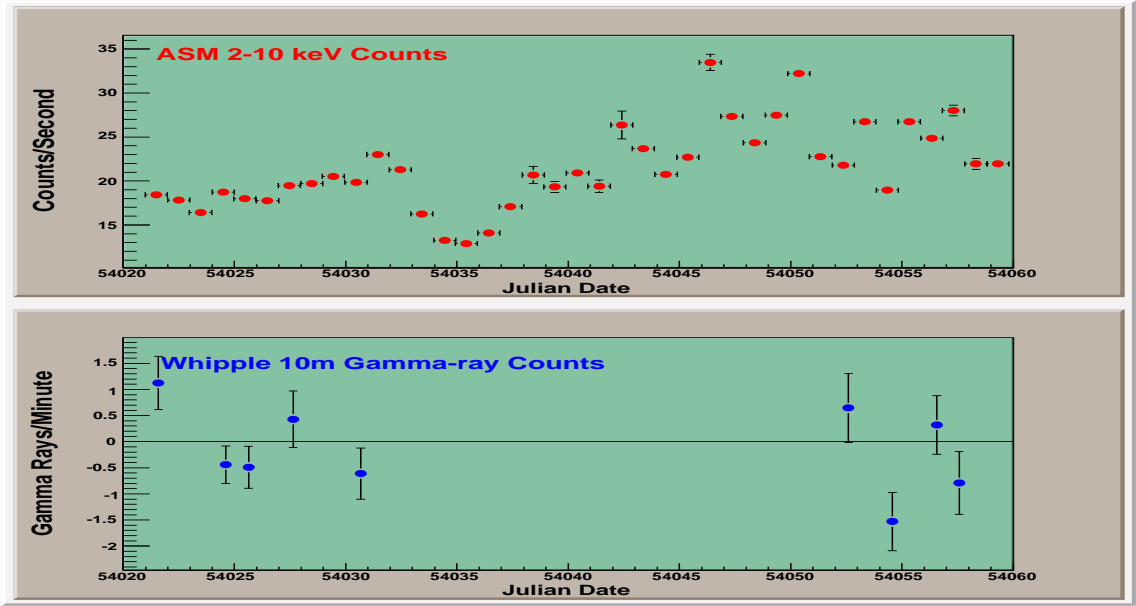


Figure 5.5: Nightly ASM 2-10 X-ray fluxes from Cygnus X-3 (top) compared to the nightly binned TeV fluxes by Whipple (bottom).

was no detection found, flux upper limits were produced using the same Crab Nebula data set presented above. For consistency however, since the elevation range of the LS I +61 303 data set was much lower ($50^\circ < \text{elevation} < 60^\circ$), only the subset of the Crab data set covering elevations from $50^\circ \rightarrow 60^\circ$ was used (4.15 hours). From these reduced elevation observations, the Crab Nebula flux is then modified to 1.96 ± 0.25 gamma rays per minute at a significance of 7.82σ . Using this large zenith angle Crab set, the upper limit in terms of Crab flux for the total LS I data set is derived at 8%. This value and the values for the individual phase bins are shown in figure 5.7 and table 5.1. For the total data set, an absolute flux limit can be derived using the average elevation of the dataset (58.46°), which implies an energy threshold of 540 GeV (see figure 5.2). The total absolute flux upper limit derived is therefore:

$$\begin{aligned}
 F_{total}(> 540\text{GeV}) &= 0.08 * 1.9910^{-11} \gamma \text{ cm}^{-2} \text{ s}^{-1} * \frac{0.54^{-1.63}}{\text{TeV}} \\
 &= 0.434 * 10^{-11} \gamma \text{ cm}^{-2} \text{ s}^{-1}
 \end{aligned} \tag{5.8}$$

In order to more accurately compare this upper limit to the flux seen by the MAGIC result, a separate upper limit only derived from the data between orbital phases 0.4 and 0.7 (the regions in which MAGIC detected the source. The data set used to derive this upper limit consisted of 23.08 hours and resulted in a Crab flux upper limit of 12%. The average elevation of this data set alone was 58.55° which implies the same energy threshold as the total data set of 540 GeV. The absolute

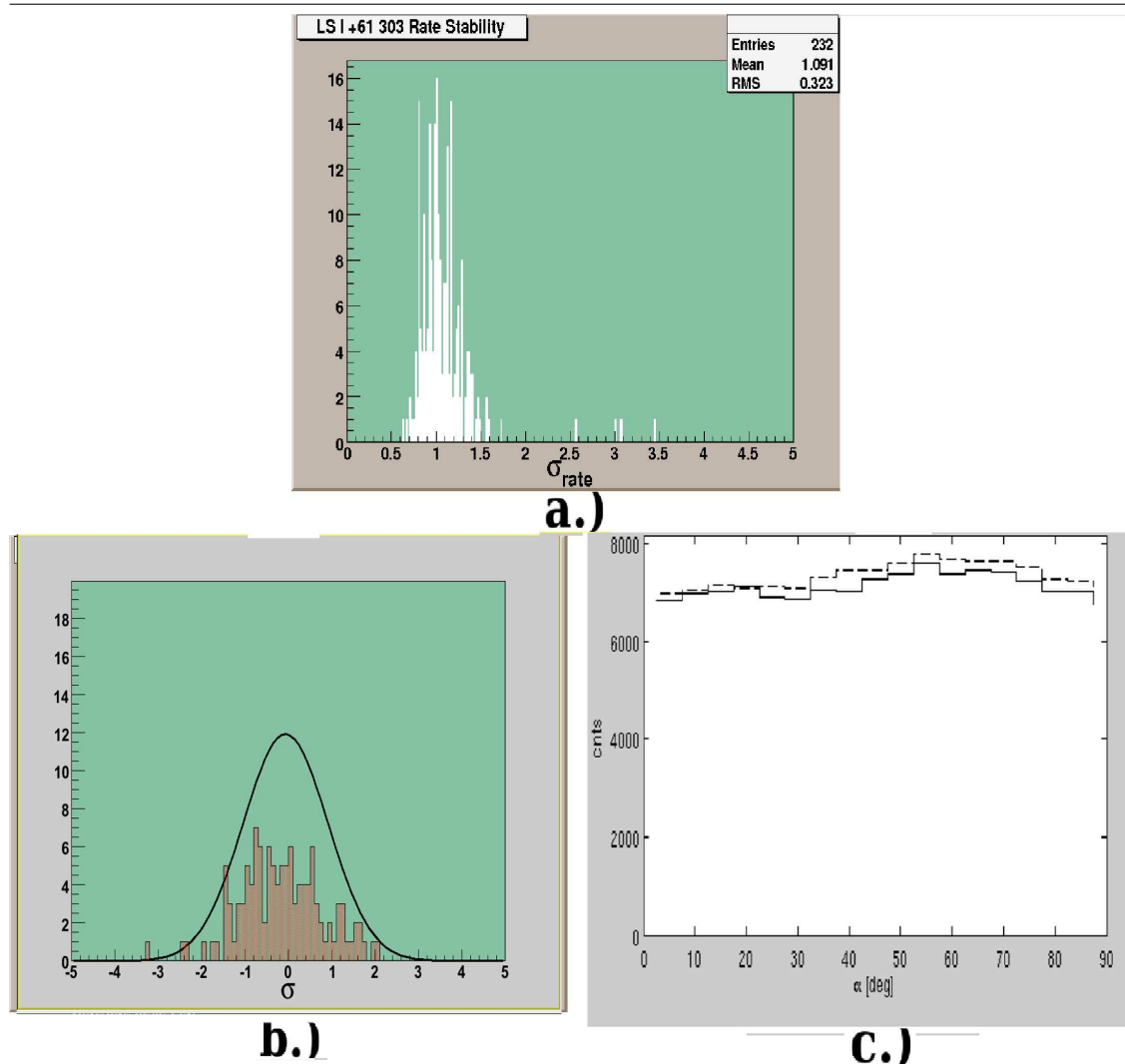


Figure 5.6: The results of the Whipple 10 m dataset on LS I +61 303 recorded in 2004-2007. Figure quantities are the same as in figure 5.3 and 5.4.

flux upper limit for the reduced data set is therefore:

$$\begin{aligned}
 F_{\phi=0.4 \rightarrow 0.7}(> 540 \text{ GeV}) &= 0.1198 * 1.9910^{-11} \gamma \text{ cm}^{-2} \text{ s}^{-1} * \frac{0.54^{-1.63}}{\text{TeV}} \quad (5.9) \\
 &= 0.651 * 10^{-11} \gamma \text{ cm}^{-2} \text{ s}^{-1}
 \end{aligned}$$

This close limit is still consistent with the MAGIC detection. In figure 5.7, the upper limits derived in this chapter are compared to the MAGIC detection. Although it appears that the Whipple upper limits might be in contradiction to the MAGIC detection, there are two effects which need to be taken into account. First, the MAGIC energy threshold for their detection was 400 GeV compared to the Whipple upper limit threshold of 540 GeV; this extra 140 GeV is most likely responsible for a significant excess of gamma ray events that were not detected by Whipple.

Table 5.1: 2004-2007 LSI +61 303 Observations

ϕ	T_{Obs}	ON Counts	OFF Counts	99% Flux Upper Limit
	(minutes)			Crab(%)
0.0→0.1	275	1865	1965	22.3
0.1→0.2	276	1893	1999	22.45
0.2→0.3	304	2095	2045	25.7
0.3→0.4	526	3394	3342	18.2
0.4→0.5	720	4370	4440	12.8
0.5→0.6	416	1996	2054	15
0.6→0.7	249	1590	1612	22.3
0.7→0.8	221	1516	1567	24.7
0.8→0.9	166	926	988	26.2
0.9→1.0	193	1182	1192	24.7
0.0→1.0	3351	20827	21204	6
0.4→0.7	1385	7956	8106	11.98

Additionally, it is clear that this object is a variable emitter across the electromagnetic spectrum, therefore it is not unreasonable to expect that the same may be true of its TeV emission properties. With this in mind, it is altogether possible that the 2006 MAGIC observations had just slightly better luck and happened to be looking when the source was particularly active during phases 0.4→0.7, and the Whipple observations didn't cover the same time span. It is encouraging, however, that the Whipple 10 m telescope was apparently exceptionally close to detecting a source which is only readily detected by the newest generation of IACTs.

Since no definitive detection was made in this dataset, any physical conclusions based on this dataset would only be weakly supported. However, this dataset does reinforce the claim of Albert et al. (2006b) that the source is a variable emitter of VHE gamma rays. The flux upper limit produced for the dataset as a whole supports this claim by proving that the source is not a constant emitter (at 6% Crab flux) at the 99.9% confidence level (see table 5.1). This claim will be examined further by the VERITAS observations detailed in the following chapter.

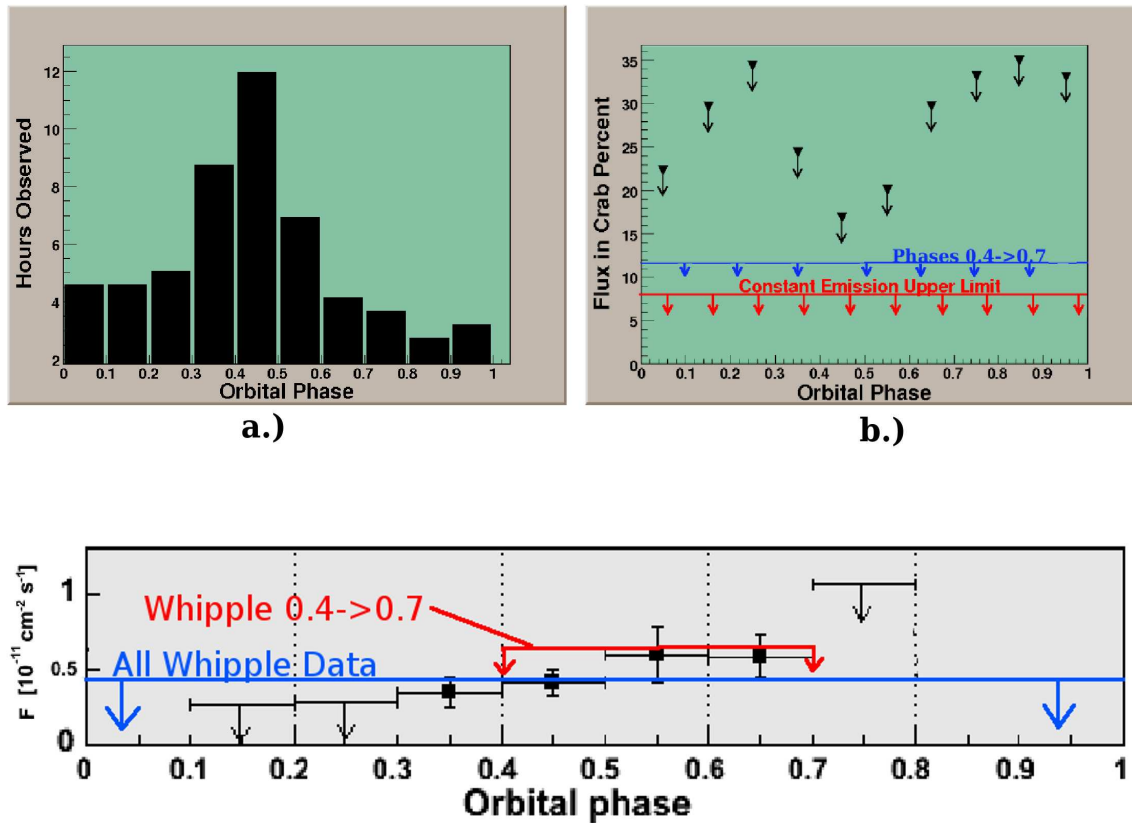


Figure 5.7: a.) The distribution of observation times by orbital phase on LS I +61 303 from 2004-2007 with the Whipple 10 m. b.) The derived upper limits as explained in the text. c.) Comparison of the total upper limit (blue lines) and “active” phase (0.4→0.7, red line) upper limit with the data points and upper limits from MAGIC observations (black points).

Chapter 6

VERITAS Observations of LS I +61 303

Spurred on by the MAGIC detection of LS I +61 303, in the autumn of 2006 the author requested LS I +61 303 be made a priority target for observations with the newly operational two telescope VERITAS array. These observations were taken from September to December 2006 at which point the array was then temporarily decommissioned for an upgrade to the three telescope system. When this upgrade was completed, three telescope observations were taken on LS I +61 303 from January to February 2007. These combined observations covered a total of 5 separate 26 day orbital phases, during which the source was reliably detected at TeV energies for 3 of these phases. The spectral energy distribution extracted from these observations is consistent with the previous MAGIC detection, although the energy range over which the spectrum is fitted is larger and indicates a harder spectral index.

6.1 Data Selection and Reduction

6.1.1 Quality Criteria

Since the LS I +61 303 data were taken while the 2 and 3 telescope arrays were still undergoing “shakedown” and were subject to variations in observation conditions, it is important to subject the data to a stringent quality selection in order to only keep the most consistent data. There is also an astrophysical justification for this as the variability of LS I +61 303 is not an a priori known quantity and there is inherent danger in introducing further variability into the data due to instrumental variations. The first pass at selecting runs was to group all the data runs taken with the configurations which were to become the “standard” operational parameters for the array. These parameters were:

- **Observing Mode:** All data used for this work were taken in “Wobble” mode (see section

3.2.11), with the wobble offset varying (either 0.3° or 0.5°).

- **L1 CFD Trigger:** All data used for this work were taken with a CFD threshold setting of 50 mV for all telescopes.
- **L2 Pattern Trigger:** All data used for this work were taken with a 3-fold multiplicity trigger setting in the L2 pattern triggers.
- **L3 Array Trigger:** All 2 telescope data used for this work were taken with a 2/2 array trigger configuration, while all 3 telescope data were taken with a 2/3 array trigger configuration.

After these configuration criteria were imposed, the data selection criteria based on several factors were imposed:

- **Weather:** As with Whipple data, every night the observers enter into the log a judgment of how good the sky looked based on an A→C scale. Since this is not always the most accurate gauge of actual sky condition, it is only used as a perfunctory quality check; however, any runs given a grade of C+ or less were not accepted unless all other quality selection criteria described here were satisfied.
- **FIR data:-** VERITAS is equipped with a Far Infrared Pyrometer which can measure the temperature of the middle to upper atmosphere. This temperature is a direct indicator of the sky quality as a rapidly varying or generally high temperature (-20°) will indicate the presence of clouds. Therefore, any data showing an FIR temperature of $> -20^\circ$ or a significantly varying FIR rate were not used (see figure 6.1).
- **L3 Rate:** Although an individual telescope's L2 rate can vary significantly over a run, as long as the overall array trigger is stable the data quality is not significantly affected. Using diagnostic plots generated for every run via software written by VERITAS collaboration member S. Fegan, each run can be inspected for L3 rate variations as well as overall L3 rate and any runs with low or wild rates are discarded. The acceptable trigger rate for 2 telescope runs was taken as 80-100 Hz and for 3 telescope runs 150-170 Hz (see figure 6.2).

6.1.2 Analysis

Analysis for VERITAS data was carried out using the **VEGAS** (Very Energetic Gamma-Ray Analysis Suite) software package which was written to be the default analysis package for all VERITAS

6.1. DATA SELECTION AND REDUCTION

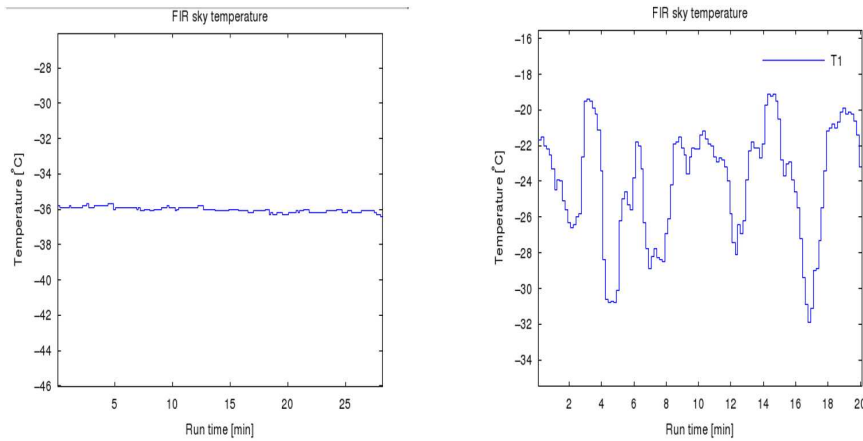


Figure 6.1: Left: FIR data from an acceptable night of data. Right: The FIR rate is wildly varying, disqualifying any data taken during this night from use.

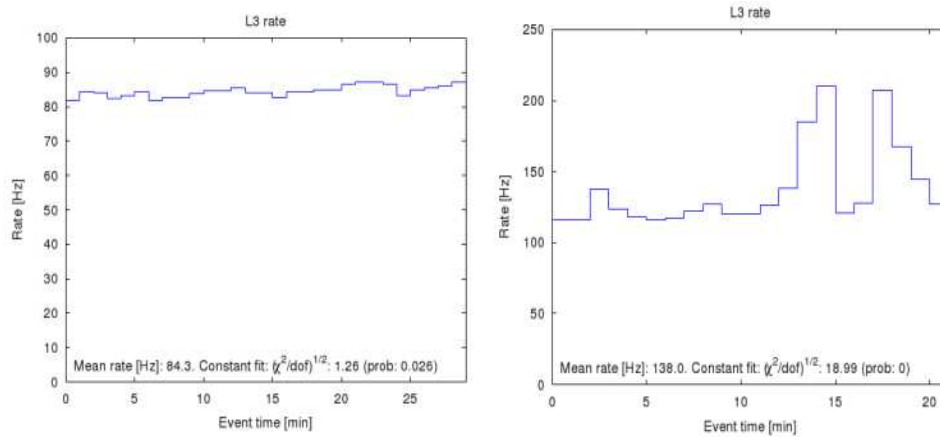


Figure 6.2: Left: The L3 rate from an acceptable run. Right: The L3 rate from a discarded run. Plots courtesy of UCLA diagnostic software.

data. It should be noted at this stage that LS I +61 303 was the first VERITAS source to be formally analyzed (other than the standard candle of the Crab Nebula) using this software package. As such, this analysis provided a functional test bed for the overall effectiveness and capabilities of the package. The software consists of 6 distinct stages which perform all analysis tasks from the cleaning and calibration, to event reconstruction and event selection for an individual data run. The general breakdown of tasks is given below as well as the analysis parameters chosen (also shown in table 6.1) for this work:

- **Stage 1:** For a given data run, this stage contacts the database of run information for all VERITAS runs and retrieves information such as pointing, observing mode, and general

Table 6.1: VEGAS Analysis Parameters

	Stage 1	Stage 2	Stage 3	Stage 4	Stage 5	Stage 6
Cuts	N/A	N/A	Picture/Boundary: $5/2.5\sigma$	$N_{\text{Tubes}} \geq 5$ $0.05 \leq \text{dist} \leq 1.3$ $\text{size} \geq 400$ d.c.	N/A	$\theta^2 \leq 0.025$ $0.05 \leq \text{MSW} \leq 1.02$ $0.05 \leq \text{MSL} \leq 1.15$

configuration settings (such as PMT voltages). This information is attached in a separate data file as is necessary for later stages of analysis. Stage 1 then analyzes the data files and calculates fundamental calibration constants such as the pedestal variance and T_{offsets} . This stage is also used to produce relative gains for the data file by running Stage 1 on the laser run taken the same night as the data.

- **Stage 2:** Stage 2 takes the calibration information from Stage 1, and the relative gain information from the laser run and applies this information to the actual data. The FADC trace window is set in this stage and the traces are analyzed producing an integrated charge per pixel for each event.
- **Stage 3:** Stage 3 cleans the events, applying a picture/boundary cut (described in 3.2.7) for images. For this analysis, picture/boundary selection criteria of $5/2.5\sigma$ per pixel were applied. This stage also parametrizes each image by the parameters such as *length*, *width*, *distance*, and other similar moment parameters described in section 3.2.9.
- **Stage 4:** Stage 4 takes the parametrized images from Stage 3 and first applies a set of image quality cuts to remove images which are unlikely to be accurately reconstructed. For this work, the quality cuts used removed any images which had less than 5 contributing pixels, any image whose *distance* parameter was not in the range of 0.05° - 1.3° , and any image whose *size* parameter was less than 400 digital counts. Stage 4 then takes the image parameters generated by Stage 3 and uses them to reconstruct the shower core location, the point of origin of the shower primary in the field of view, and (via lookup tables) the MSL/MSW parameters described in 3.2.9. These stages of event cutting result in a hadronic shower rejection rate of 99% and a gamma-ray shower acceptance rate of 50% (Daniel et al., 2007).
- **Stage 5:** Stage 5 performs various specialized routines on stereo parameters. This stage was not used in this analysis and all the cutting on stereo event parameters is performed in stage 6.

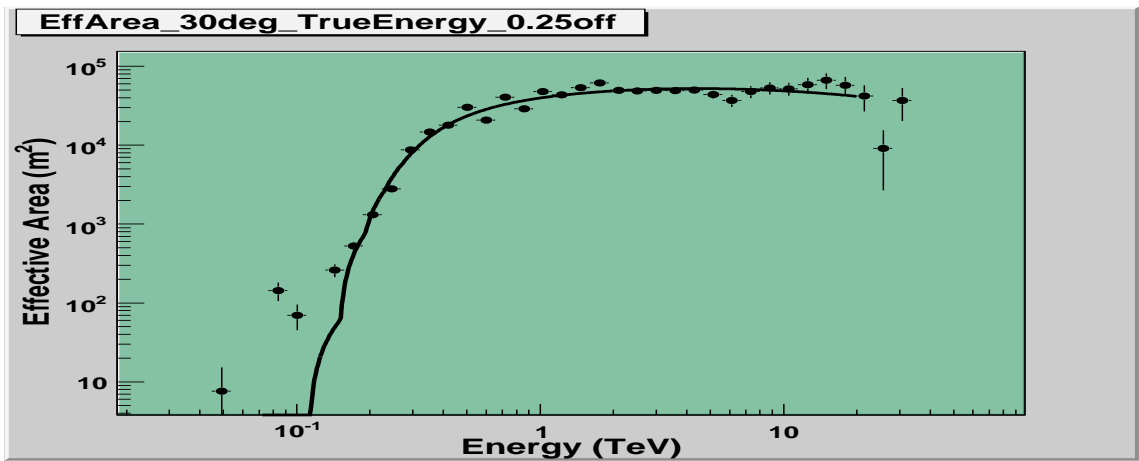


Figure 6.3: Example effective area (right) and energy bias (left) plots from the KASCADE simulations used in this analysis.

- Stage 6:** Stage 6 takes the reconstructed events from stage 4 and applies any user supplied cuts to them in order to discriminate between source events and background. The cuts used for this analysis are shown in table 6.1. This stage performs both the ring background and wobble analysis described in 3.2.11. For this analysis, all numerical results (such as rates and significances) are produced via wobble analysis with 3 background regions resulting in a background scaling factor of 1/3. All sky maps are produced via the ring background model. All final analysis results such as 2-d sky plots and θ^2 distributions are produced in this stage. The spectral analysis described in section 3.2.12 is also performed within this stage.

6.1.3 Spectral Derivation

As was described in section 3.2.12, there are several steps which are necessary to derive an energy spectrum from a given set of observations. The overall goal is to be able to examine a data set and derive how many gamma-rays of a given energy are present, number of background cosmic rays of a given energy are present, and the effective collection area of the observation. The spectral analysis code used for this work is contained within the Stage 6 module of VEGAS. Along with the data, this code requires effective collection areas as a function of energy. These effective areas are produced for different zenith angles in steps of 10° (i.e. an effective area plot for 10° zenith, 20° zenith, 30° zenith and then interpolation between two steps for real values of zenith falling in between). These effective areas are produced by analyzing batches of simulated gamma-rays by the same analysis routine prescribed above for real data (see figure 6.4).

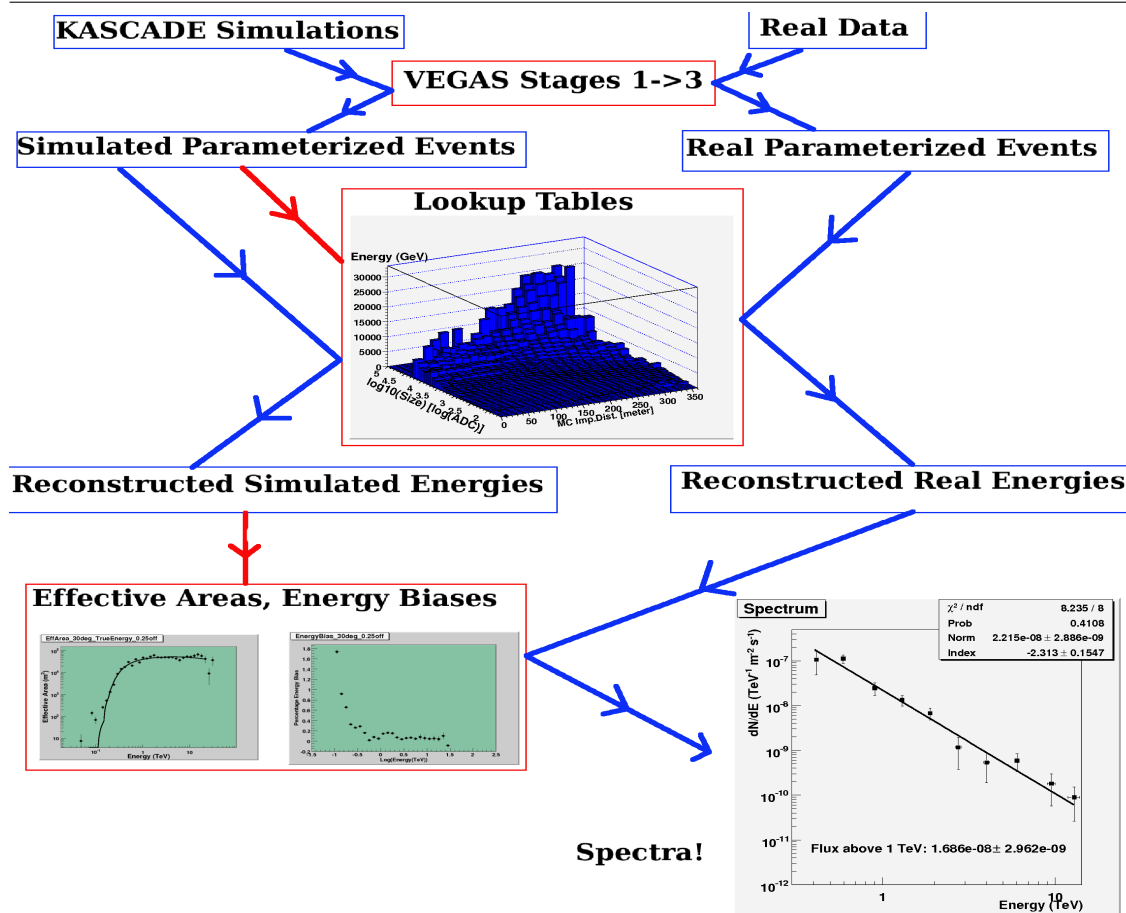


Figure 6.4: A graphical representation of the production of spectra used in this analysis. Blue lines represent the use of the item, whereas red lines represent the production of something. For example, the simulated parametrized events are used to produce the lookup tables and they also use them to produce the reconstructed simulated energies.

The analysis of simulations results in two sets of energies for each file: the energies of the original simulated gamma rays (“true” energies) and the energies that the software reconstructed from the simulation (“reconstructed” energies). With perfect reconstruction, these two sets of energies should be nearly identical (modulo statistical uncertainties); but in practice, due to uncertainties in reconstruction processes, they are not. The accuracy of the reconstruction process will be a function of energy and elevation (less energetic gamma rays will be reconstructed poorly, especially at large zenith angles) and are represented by “energy bias” plots; an example is shown in figure 6.1. It is customary to accept only energy regimes for each zenith angle where the energies are being reconstructed to within a 10% accuracy. For this work however, any reconstructed energy showing a bias of 30% or less was used. Although this is a very liberal allowance for spectral reconstruction, problems with the VEGAS spectral reconstruction code at the time of writing necessitated its

use. Since this method has the potential to introduce unnatural results into spectral reconstruction, it was first tested on Crab Nebula data to ensure that the reconstructed spectrum of the best known gamma-ray source remained consistent with previous results.

For the current analysis the lookup tables used for analysis of both real and simulated data were produced by G. Sembroski at Purdue University. These lookup tables are similar to those resulting from a simulated Crab spectrum; however, they are more heavily populated at higher energies in order to compensate for the slightly decreased sensitivity of VERITAS to higher energy showers (this is principally related to the camera size).

To produce effective areas and energy biases, a set of simulated gamma-rays (again, courtesy of G. Sembroski) produced with an intrinsic Crab Nebula spectrum were processed through VEGAS. Since the aim of this analysis was to produce a spectrum for the LS I +61 303 observations, and these observations were only taken at zenith angles of 28-38°, the analysis only used simulations covering 30→40° zenith angles. This is justified in the following section by extracting a Crab Nebula spectrum from observations taken at similar elevations using this method. The Crab Nebula spectrum extracted here agrees quite well with the canonical results.

6.2 Crab Nebula Observations

In order to provide a check of the accuracy of the analysis procedures described above, these same methods were applied to a set of 2 telescope Crab Nebula observations. There were no 3 telescope Crab observations at the same range of zenith angles as the LSI data set; therefore only 2 telescope Crab observations are presented here. However, it is assumed that the 2 telescope Crab observations provide an accurate calibration for the stereo methods used here.

The same run selection criteria explained above were used to select 8 “good” Crab Nebula observation data runs taken from September to November 2006. These runs were taken between 35° and 21° zenith angle resulting in a total of 19.9 hours of observation time. All of these runs were taken in wobble mode with an offset of 0.3°. The gamma-ray count analysis to determine the run-by-run and overall rates and significances was performed by the wobble analysis method, with a total number of 3 off source regions used to determine the background counts; these results are shown in figure 6.5. The production of the θ^2 distribution as well as the 2 dimensional analysis was performed by the ring background method with a inner/outer ring radius of 0.5°/0.8° resulting in the two dimensional sky map shown in figure 6.5. For spectral analysis, KASCADE simulations for 20→40° zenith angle at an wobble offset of 0.25° were used to produce effective areas and energy biases. Any reconstructed energies showing a bias of less than 15% were allowed

6.2. CRAB NEBULA OBSERVATIONS

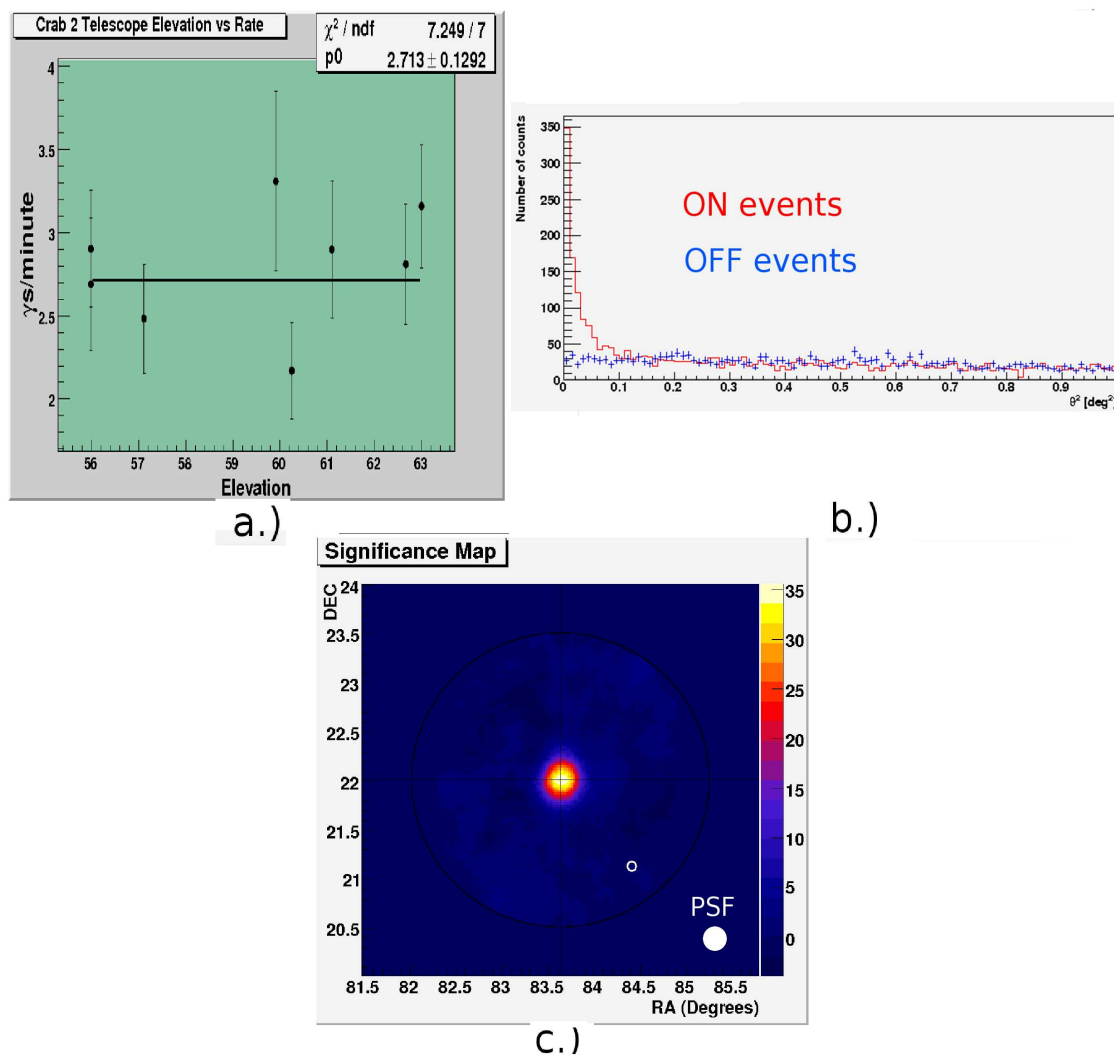


Figure 6.5: a.) Observational zenith angle versus gamma-ray rate for 2 telescope Crab data. b.) The θ^2 distribution for the same data set. c.) 2 dimensional sky map derived from the data set, consistent with a point source. This 2d map shows a slightly higher significance of detection than that shown in the text due to the method of the Ring Background Model being used for the 2d plots, whereas the text uses the Wobble analysis method. However, these two significances are comparable. The white ring represents a bright star excluded from the analysis. The 0.22° point spread function is shown for comparison.

to participate in spectral reconstruction resulting in an analysis threshold of 310 GeV. The source is easily detected by the 2 telescope array at a total significance of 28.98σ at a rate of 2.77 ± 0.13 gamma-rays per minute. Although there were slight variations in the measured gamma-ray rate per minute due to elevation differences between the observations, the rate distribution can be fitted quite well ($\chi^2/\text{n.d.f.} = 7.249/7$) with a straight line indicating a constant rate fit of 2.71 ± 0.13 γ/min ,

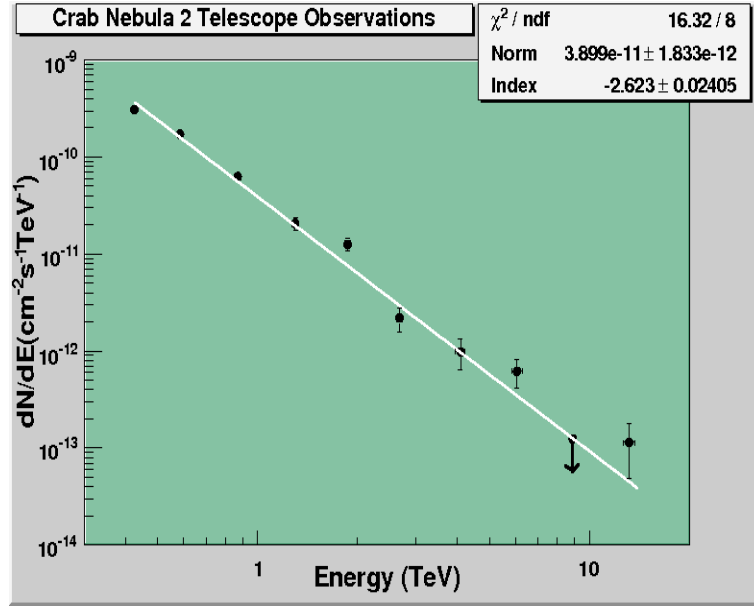


Figure 6.6: Differential energy spectrum for the Crab Nebula observations detailed in the text (only statistical errors are shown). The upper limit point at 8.9 TeV is a 99% flux upper limit calculated by the Helene method described in chapter 5.

consistent with the overall rate calculated from events. (see figure 6.5). The θ^2 distribution (also shown in figure 6.5) shows a clear excess near 0° , indicating a strong point source distribution of gamma rays. This is reinforced by the two dimensional sky map also shown.

For spectral reconstruction, KASCADE simulations for 2 telescope gamma-ray events at 30° and 40° zenith angle were processed through the necessary stages of VEGAS in order to produce effective areas for the data set in question. Although there were several runs at zenith angle less than 30° , they were only slightly less and it is considered valid to analyze them with 30° simulations. The effective areas produced from these simulations indicated a lower energy threshold of 310 GeV with the upper threshold determined solely by event statistics. The resulting spectrum from 400 GeV to 14 TeV (shown in figure 6.6) has the shape of a power law of the form $dN/dE = \text{Constant} \times E^{-\Gamma}$ with $\Gamma = 2.629 \pm 0.025_{stat} \pm 0.2_{sys}$ and a flux constant of $3.86 \times 10^{-11} \pm 0.18 \times 10^{-11} \text{ s}^{-1} \text{ cm}^{-2} \text{ TeV}^{-1}$ with a χ^2 fit of 17.45 for 8 degrees of freedom. The systematic error is assumed to be the same as in Maier et al. (2007b) as this paper describes observations taken in the same time period at similar zenith angles and array conditions. In general, these systematic errors are a result of atmospheric uncertainties, analysis cuts, and simulation uncertainties for observations taken at similar zenith angles.

To compare this spectrum with results from other IACT experiments, the spectrum is plotted along with results from the MAGIC (Albert et al., 2007), HESS (Aharonian et al., 2006c), and

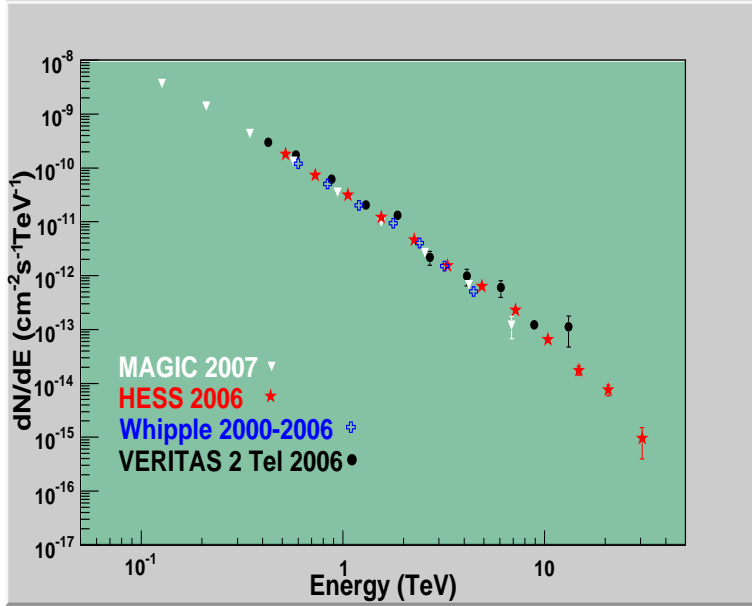


Figure 6.7: The VERITAS Crab Nebula differential energy spectrum points plotted along with results from other experiments.

Whipple 10 m Crab Nebula observations (Grube, 2007). The current result is in excellent agreement with these data points. Given this agreement, it is reasonable to assume that the method presented here for both basic and spectral analysis is valid and can be applied to other sources, such as LS I +61 303, detailed in the next section.

6.3 LS I +61 303 Observations

6.3.1 Dataset

From September 2006 to February 2007, LS I +61 303 was observed covering five separate orbital phases. After data selection criteria were implemented, a total of 41.26 hours of viable data was accumulated. This dataset covered the phase bins of $\phi = 0.2 \rightarrow 0.9$, although not with equal coverage. The distribution of observation time by phase bins is shown in figure 6.8. As can be seen, phases $0.4 \rightarrow 0.7$ have good coverage with the other phases observed only getting weak coverage. There were no observations possible between phases $0.9 \rightarrow 0.2$ because of the appearance of the full moon coinciding with these orbital phases during this time period. The data were taken with 2 (3) telescopes in wobble mode with an offset of 0.25° (0.5°). Since the wobble offset was larger in the three telescope data, this implies that a larger number of background regions can be fit within the field of view without overlapping, however, the same number and size of background regions in 2-telescope analysis would cause an overlap in background regions and they would no longer

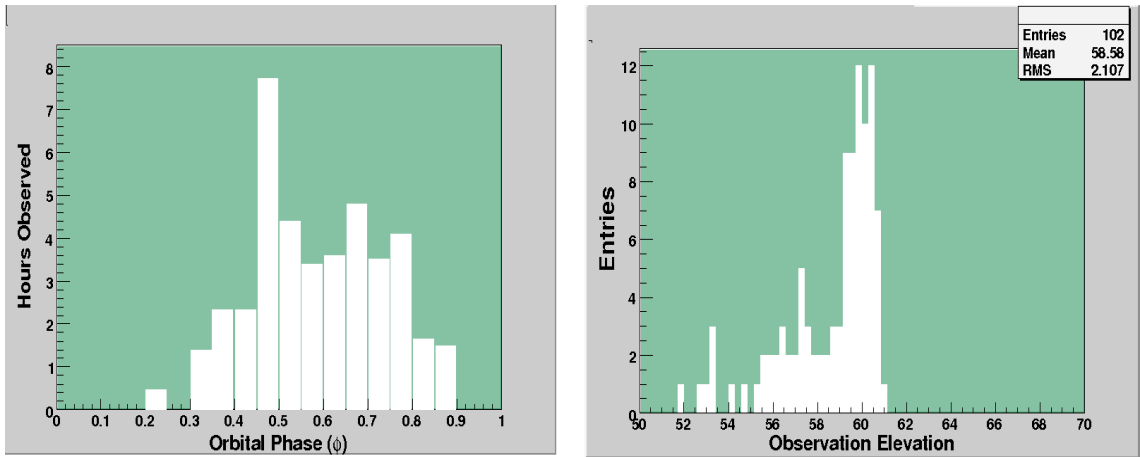


Figure 6.8: Properties of the LS I +61 303 dataset detailed in the text.

be considered independent. To facilitate the combination of data taken with 2 and 3 telescopes, the number of background regions for the analysis in both sets was constrained to 3. Similarly to the Crab Nebula data set described above, this data set was taken between 52° and 62° elevation.

6.3.2 Results

Analyzed as a whole, the dataset results in a firm source detection above 310 GeV of 7.23σ ; the average rate was $0.101 \pm 0.014 \gamma/\text{min}$. The θ^2 distribution as well as the two dimensional sky map resulting from this data set are shown in figure 6.9. Both are consistent with a point source of gamma rays, showing no evidence for source extension. Although the source is strongly detected, it is clear from examining the resulting lightcurve that the emission is not constant. A straight line fit to the lightcurve from the entire dataset, shown in figure 6.9, gives a reduced χ^2 fit of 3.44 which strongly implies that the source is variable in nature.

To investigate the variability seen in the data, the first step is to bin the data by its orbital phase. This is shown in figure 6.10 with the various colors representing different months. As can be seen, there is clear activity between the orbital phases of $\phi = 0.5 \rightarrow 0.8$ with no real significant activity outside of this range. It would appear that the source peaks in emission near $0.6 \rightarrow 0.7$ every phase with the exception of February. The data set from February however does not sample the regions of orbit where the observations from other months saw a clear increase in emission. Therefore, this variation in peak flux location presented by the February data is not considered to be significant as there is no way to separate its features from any possible sampling effect. The existence of a possible variation in peak flux location is a key open question surrounding LS I +61 303 and will be discussed in chapters 8 and 9. To further investigate the features of the lightcurve presented in

6.3. LS I +61 303 OBSERVATIONS

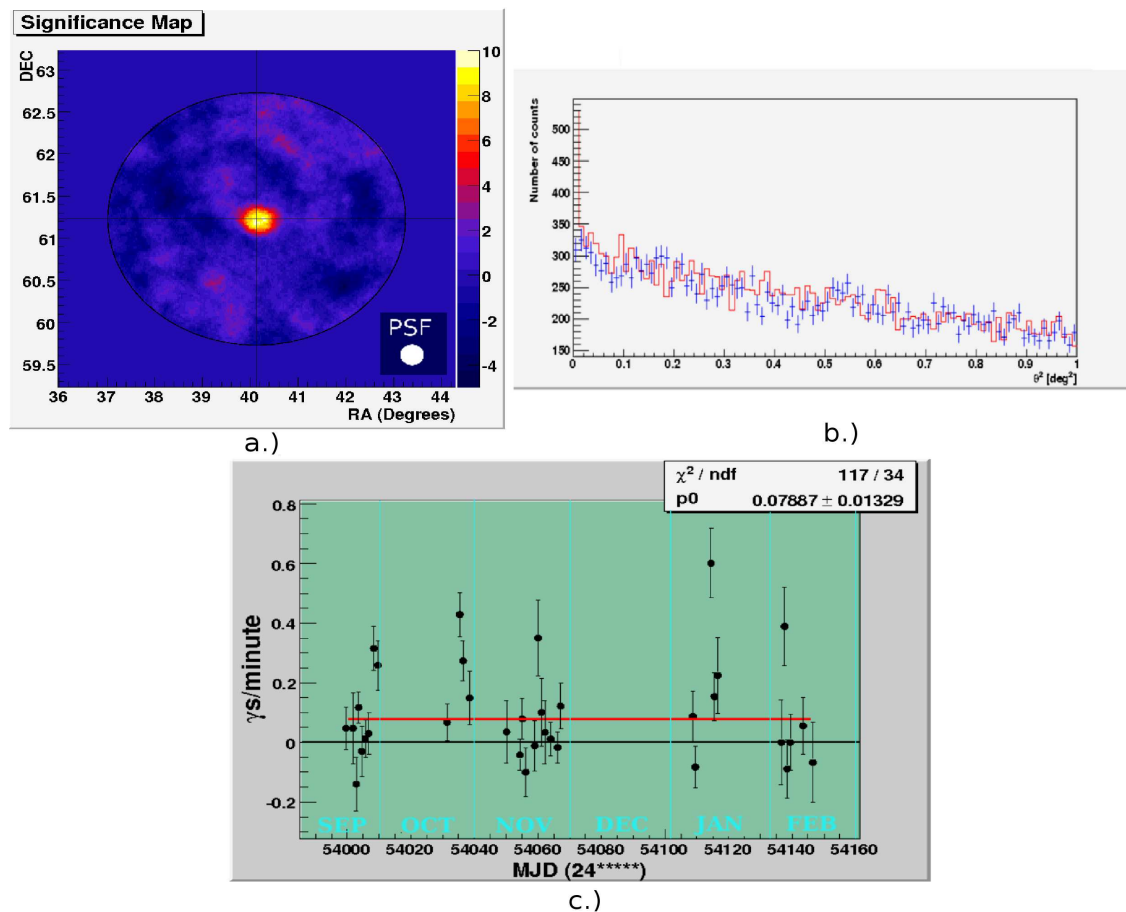


Figure 6.9: The significance skymap (a.), θ^2 plot (b.), and lightcurve (c.) from all the LS I +61 303 observations, September 2006 to February 2007

figure 6.10, all data are combined and binned in steps of $\phi = 0.1$ (shown in 6.11 left). It is clear that while there is little significant activity in the phase bins of 0.2→0.5 and 0.8→0.9, there is a clear excess of positive gamma-ray rates within the bins 0.5→0.8, particularly within 0.6→0.7. To further this investigation and search for possible finer structure within these bins, the data is re-binned by $\phi = 0.05$ and shown in figure 6.11 (right). Since this method seems to reveal a finer structure of the flux rising and falling, the analysis was continued with this finer orbital binning.

After binning all the data by orbital phase, any flux point showing a positive significance of less than 3σ was recast as a 99% flux upper limit. The method used to calculate this upper limit is the same as in the previous chapters, i.e. that of Helene (1983). These flux points and upper limits are shown in figure 6.12 as well as in Table 6.2. The two dimensional sky maps resulting from all of the phase bins are shown in figure 6.13. Although the source is only reliably detected between 0.6→0.8, the presence of a marginal signal in the phase bin between 0.5→0.6 motivates the treatment of the entire region of $\phi = 0.5 \rightarrow 0.8$ as the “active” region for the source. The

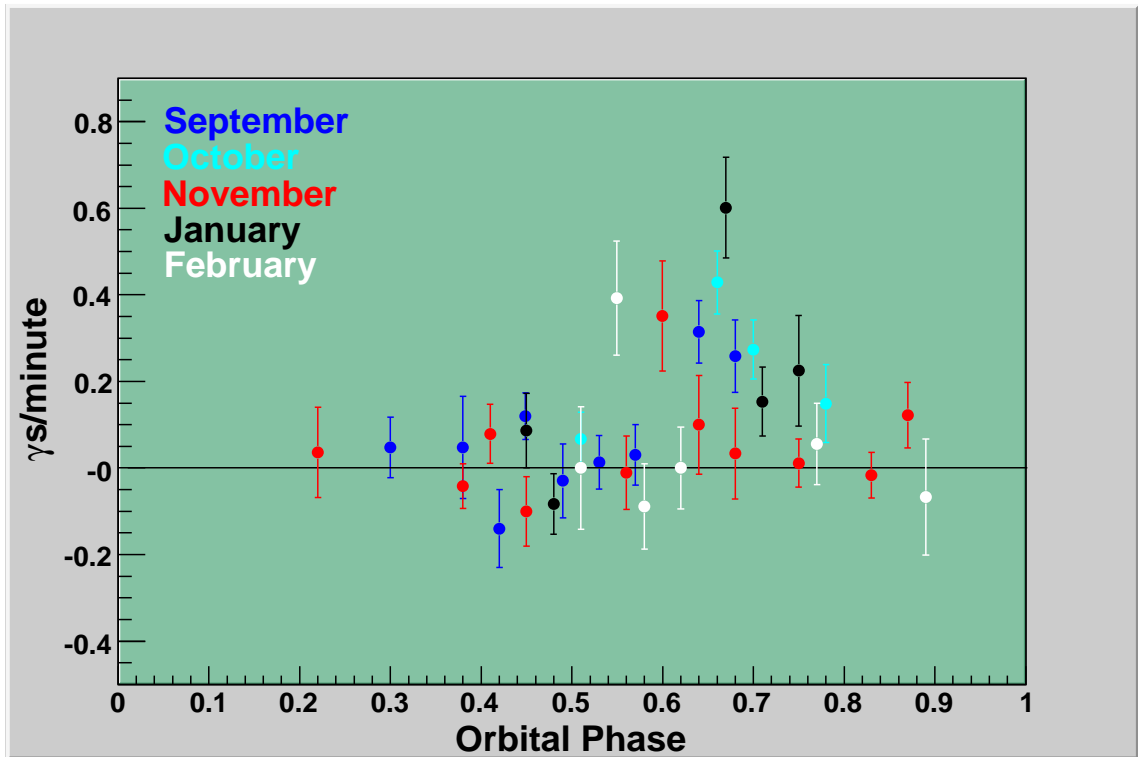


Figure 6.10: The TeV lightcurve from the 2006-7 LSI data plotted by orbital phase.

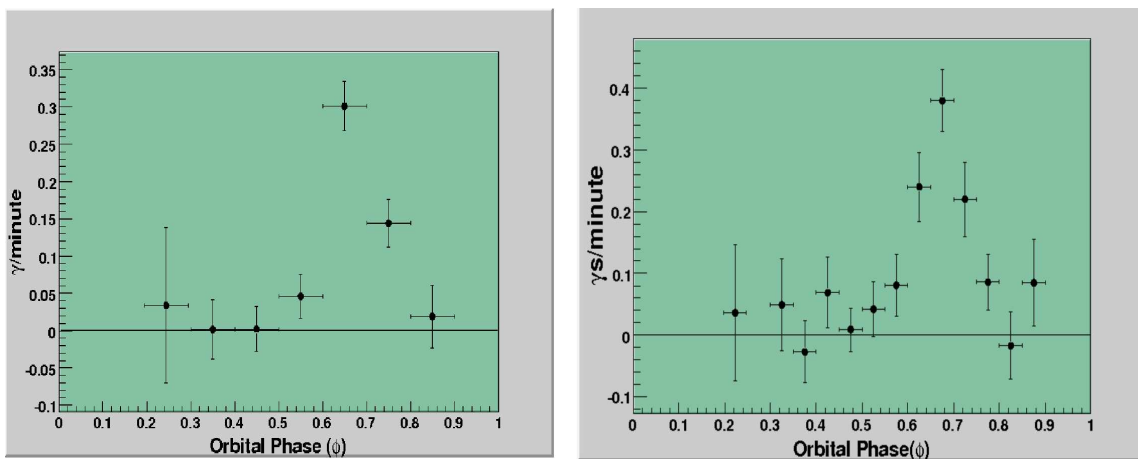


Figure 6.11: LSI +61 303 gamma-ray lightcurve binned by orbital phase in steps of 0.1 (left) and 0.05 (right).

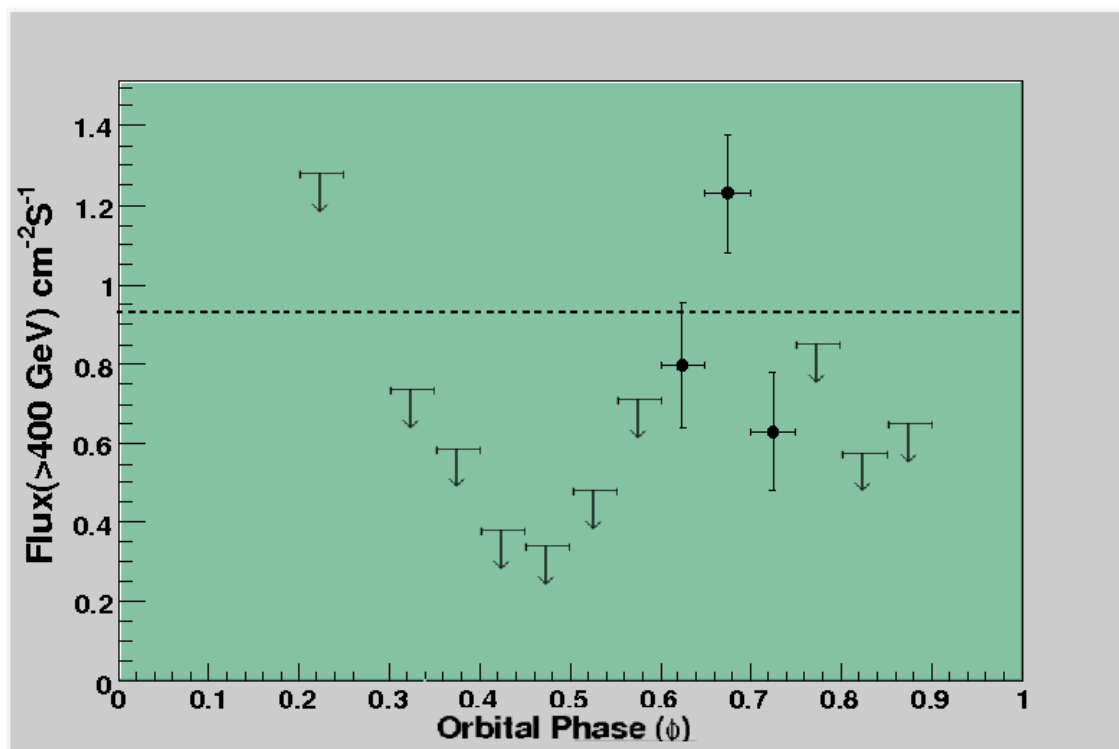


Figure 6.12: The above plot recast with points showing less than 3σ significance recast as 99% flux upper limits. The dashed line represents the 10% Crab Nebula flux level.

significance and rate for this region is also shown in table 6.2, with the two dimensional sky map resulting from this region shown in figure 6.12. The position of the optical counterpart of LS I+61 303, as well as the position of the TeV excess reported by MAGIC is also shown in this figure. The two dimensional distribution of gamma rays from the VERITAS data is consistent with the locations of both of these. It is clear that although the source is detectable during orbital phases $0.6 \rightarrow 0.8$, both the exact phase position and flux level appears to vary from cycle to cycle. Contrary to the MAGIC results (?), the source was not strongly detected between $0.4 \rightarrow 0.6$, although, this may also be related to some intrinsic source variability in the TeV band. This will be discussed further in the interpretation of this data set in chapter 8.

6.3.3 Spectral Results

To produce an energy spectrum for this source, the data set corresponding to $\phi = 0.5 \rightarrow 0.8$ was chosen as the strongest signal region. This choice is related to the observational results as well as physical motivation. Although the region of $\phi = 0.5 \rightarrow 0.6$ shows only a small indication of positive excess, the region of $0.5 \rightarrow 0.8$ corresponds to the apastron passage of the compact object in its orbit; this orbital region has been traditionally identified with the most activity in non-

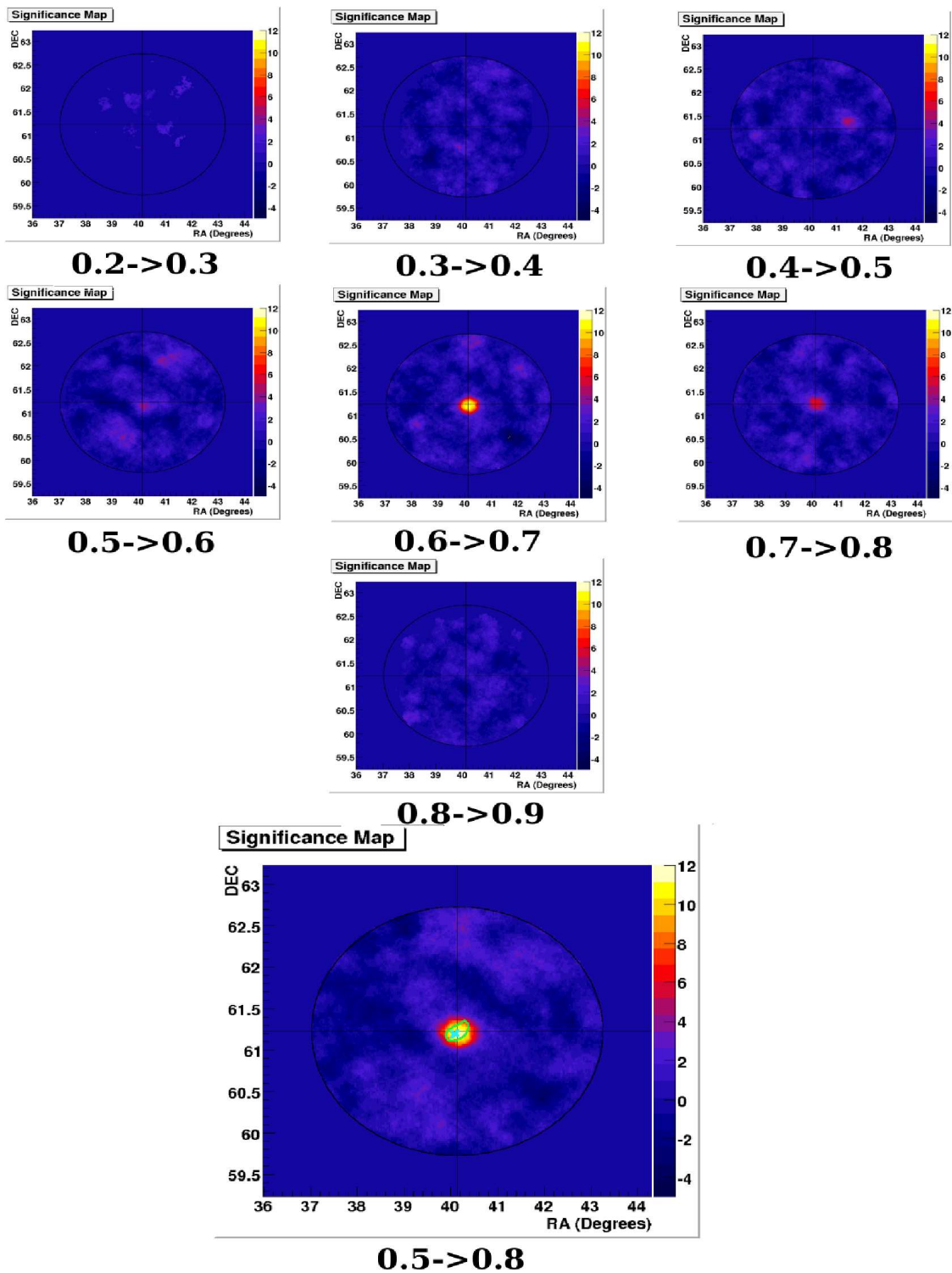


Figure 6.13: Two dimensional significance maps generated by orbital phase. The bottom plot ($\phi = 0.5 \rightarrow 0.8$) also shows the position of the optical counterpart (blue cross) and the MAGIC excess (green contour).

Table 6.2: LS I +61 303 Phase Binned Results

ϕ	$>3\sigma$ Detection Flux	99%Flux Upper Limit	Crab %
	$10^{-11} \text{cm}^{-2} \text{s}^{-1}$	$10^{-11} \text{cm}^{-2} \text{s}^{-1}$	
0.2→0.25		1.18	10
0.25→0.3		n/a	n/a
0.3→0.35		1.037	8.87
0.35→0.4		0.725	6.2
0.4→0.45		1.04	8.89
0.45→0.5		0.523	3.42
0.5→0.55		0.4	5.07
0.55→0.6		1.009	8.63
0.6→0.65	0.974 ± 0.22		8.33 ± 1.8
0.65→0.7	1.57 ± 0.2		13.4 ± 1.7
0.7→0.75	0.864 ± 0.23		7.4 ± 1.9
0.75→0.8		0.952	8.14
0.8→0.85		0.917	7.8
0.85→0.9		1.07	9.15
0.5→0.8	0.77 ± 0.1		6.5 ± 0.8

thermal emission including GeV and TeV gamma-rays (?), radio (Taylor et al., 1996), and hard X-rays (Harrison et al., 2000; Leahy et al., 1997; ?).

To proceed with spectral analysis, the same procedure and analysis cuts used to produce the Crab Nebula spectrum as above were used. KASCADE simulations for gamma-rays over the energy range of 50 GeV→30 TeV and zenith angles of $30^\circ \rightarrow 40^\circ$ were analyzed in order to produce effective areas for spectral analysis. Simulations produced at a wobble offset of 0.25° (for 2 telescope runs) and 0.5° (for 3 telescope runs) were utilized. The energy spectrum, fitted from 400 GeV to 14 TeV is shown in figure 6.14 along with the extracted Crab Nebula spectrum for comparison. The spectrum is well fitted (reduced χ^2 of 0.709) by a power law function as follows:

$$dN/dE_{0.5 \rightarrow 0.8} = (2.64 \pm 0.3_{stat}) * 10^{-13} \times E^{(-2.38 \pm 0.13_{stat} \pm 0.3_{sys})} \text{cm}^{-2} \text{s}^{-1} \text{TeV}^{-1} \quad (6.1)$$

Systematic errors quoted are as above for the Crab Nebula calculation and are those presented in Maier et al. (2007b).

In figure 6.15, this extracted spectrum is compared to that derived from the MAGIC observations taken in 2005-2006 which gave a spectrum of $\Gamma = 2.6 \pm 0.2$ which was slightly softer,

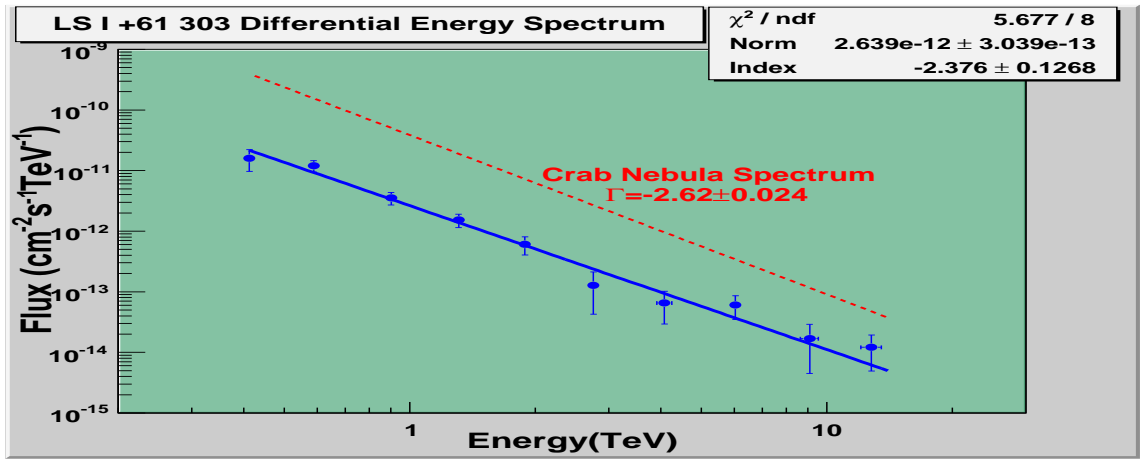


Figure 6.14: The derived LS I +61 303 differential energy spectrum from VERITAS observations along with the Crab Nebula spectrum for comparison.

yet consistent with the present one. This difference in spectral index, however, may be resulting from the slightly different energy ranges over which the MAGIC spectrum is fitted (0.2→5 TeV). Motivated by the HESS result (Aharonian et al., 2006d) in which the TeV spectrum of the microquasar LS 5039 showed large variations between different states of activity, the present data was analyzed in greater detail to search for similar variability. The active data was split into two parts: the high active phase of $\phi = 0.65 \rightarrow 0.7$ and the low active phase of $\phi = 0.6 \rightarrow 0.65 + 0.7 \rightarrow 0.75$. These two sets represented TeV fluxes equivalent to 13.4% and 7.86% of the Crab Nebula flux respectively. Because of the lowered sample time for both of these subsets, the resulting spectra could only be fitted between 0.4 and 5 TeV, instead of the full spectral range used in the previous extraction. However, if there is an appreciable difference in spectra between the two data sets, it will be evident in the reduced spectral range.

Both spectra are shown in figure 6.16 with consistent spectral indices. The higher flux spectrum is fitted well (reduced χ^2 of 0.935) by a power law,

$$dN/dE_{0.65 \rightarrow 0.7} = (5.4 \pm 0.79) * 10^{-12} E^{(-2.27 \pm 0.17_{\text{stat}} \pm 0.2_{\text{sys}})} \text{cm}^{-2} \text{s}^{-1} \text{TeV}^{-1} \quad (6.2)$$

With the lower flux spectra fit (reduced χ^2 of 0.792) by:

$$dN/dE_{0.6 \rightarrow 0.65, 0.7 \rightarrow 0.75} = (3.26 \pm 0.57) * 10^{-12} E^{(-2.54 \pm 0.26_{\text{stat}} \pm 0.2_{\text{sys}})} \text{cm}^{-2} \text{s}^{-1} \text{TeV}^{-1} \quad (6.3)$$

Although the higher flux spectrum shows a slightly harder spectral index ($\Gamma = -2.27$ versus $\Gamma = -2.53$), the error bars on both of these indices are overlapping and thus there is not sufficient evidence for any variation of spectral index between the two phases at this time.

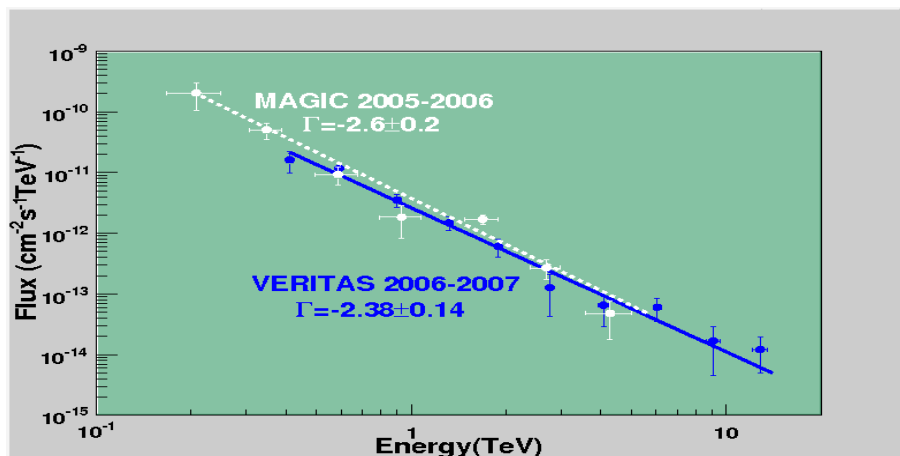


Figure 6.15: The VERITAS differential energy spectrum compared to that derived by MAGIC observations in 2005-2006.

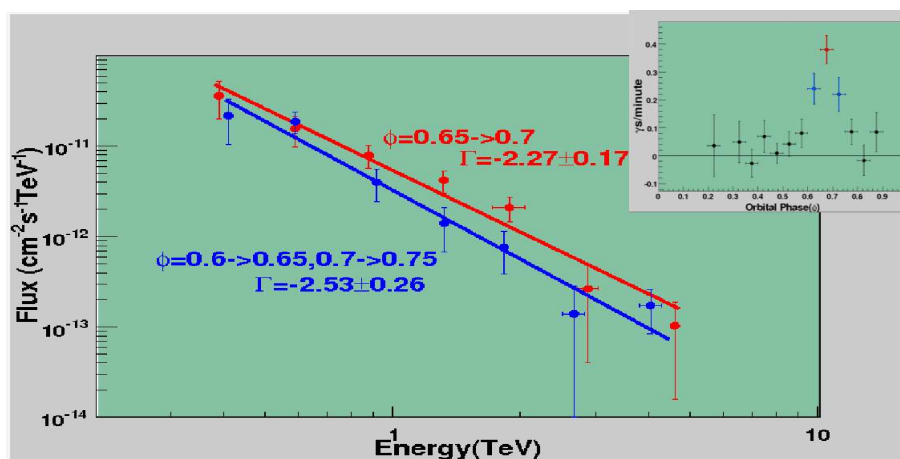


Figure 6.16: The high active region spectrum (red) compared to the low active region (blue). No significant evidence for deviation between the two are present.

To further investigate any possibility of spectral variation occurring during periods of increased flux, the night of October 27, 2006 was investigated. This night's observations consisting of 1.79 hours of livetime data resulted in a 5.87σ detection and showed a flux of $(1.53 \pm 0.25) \times 10^{-11} \text{ cm}^{-2} \text{ s}^{-1}$ above 310 GeV, or 16.5% of the Crab Nebula flux for the same energy range and observational elevation. The spectrum derived from this night only contains 42 excess events and such a spectrum reconstructed from such a low sample is fraught with uncertainty; however, if there was evidence for spectral variability during this high state of flux, it might appear. The spectrum is well fitted by a power law:

$$dN/dE_{10/27/06} = (6.83 \pm 1.37) \times 10^{-12} E^{(-2.15 \pm 0.25_{stat} \pm 0.2_{sys})} \text{ cm}^{-2} \text{ s}^{-1} \text{ TeV}^{-1} \quad (6.4)$$

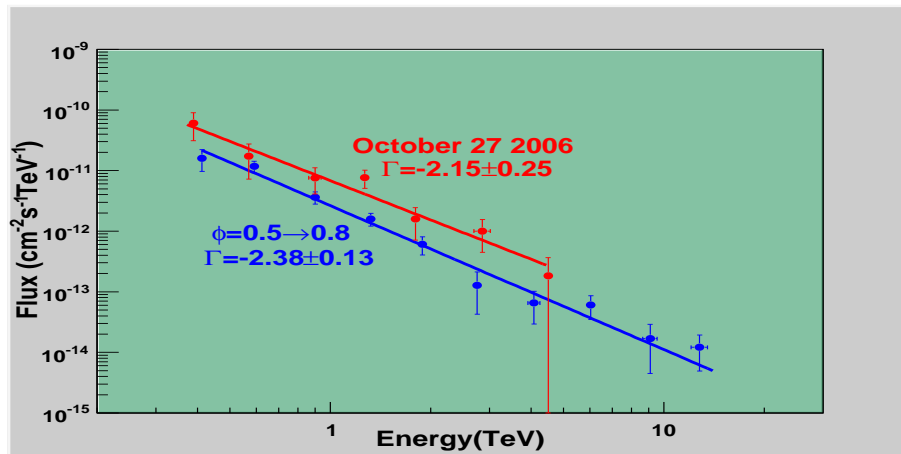


Figure 6.17: The spectrum derived from a night’s observations (10/27/06) which showed the strongest TeV for any single night in the entire dataset (red). For comparison the spectrum derived from the entire active region of the dataset is shown (blue).

This spectrum is shown along with the spectrum derived from the entire “active” region of the dataset for comparison in figure 6.16. The derived spectral index of $\Gamma = -2.15 \pm 0.25$ is, like the higher flux spectrum, slightly harder than the overall spectrum. However, the errors on the spectrum place it into consistency with the earlier derived indices. With further TeV observations of this source during flaring states, this investigation for spectral variability might continue with greater certainty; however, at the present time there is not enough observational time nor statistical evidence to place much of a constraint on spectral variability.

6.4 Summary

The galactic binary LS I +61 303 was reliably detected by the VERITAS array in both its two and three telescope configurations. These observations, comprising a 42.26 hour data set cover 5 separate orbital phases from September 2006 until February 2007. They reveal the presence of TeV gamma-ray emission peaking at 13% of the flux from the Crab Nebula during orbital phase 0.65→0.7. This emission is shown to be detected only between orbital phases 0.6→0.8. Although there is evidence for the exact peak of the emission changing from phase to phase, the sampling of the TeV data was not uniform and no definitive statement can be made about the movement of the flux peak at this time. The differential energy spectrum extracted from the data set is well fitted by a power law with spectral index $\Gamma = -2.38 \pm 0.13$, consistent with the energy spectrum derived from MAGIC observations in 2006. The energy spectra derived from the relatively low and highly active states show no evidence for variability. The spectrum from the strongest single

6.4. SUMMARY

night of observations in the dataset (10/27/06) is examined in further detail. The data show a particularly strong TeV signal (corresponding to 16.5% of the Crab Nebula flux) with no evidence for deviation in spectral index from the main TeV emission in the rest of the active dataset.

Chapter 7

X-ray Observations of LS I +61 303

After it was clear that TeV observations taken with VERITAS in September 2006 were showing a clear detection of LS I +61 303, the author filed a Target of Opportunity (ToO) request with the Rossi X-ray Timing Explorer (RXTE)(Swank, 1994) for monitoring in the 2-10 keV X-ray band to search for possible correlations between TeV and X-ray activity. This request was approved for a total of 10 nights of observing (1 ksec pointing each night) every other night from 10/13/06 until 10/31/06. These observations spanned the orbital phase bins of $\phi = 0.14 \rightarrow 0.83$ in the hopes of being able to monitor X-ray changes correlated with the apparent increase in TeV emission over the same range in orbit. The properties of the observations are shown in table 7.1. During the autumn of 2006, X-ray monitoring of LS I +61 303 was also carried out by the Swift satellite which observed the system over three separate orbital cycles in the 0.1-10 keV band (Holder et al., 2007). In addition to this, full orbital monitoring of LS I +61 303 has been performed in previous years by RXTE (Harrison et al., 2000) and the XMM satellite in 2002 (?). Although the archival RXTE and XMM data had no complimentary TeV observations, they are examined in this chapter as a comparison to the Swift and most recent RXTE data sets.

7.1 RXTE Data Reduction and Analysis

Analysis of this data was carried out using the NASA FTOOLS package obtained from the RXTE Guest Observer Facility. For each 1ks observation, a routine (xtefilt) was used to create filter files which encompass all the properties of the data file that would be subject to cutting (i.e. filtering by pointing too close to the Earth's limb, electron noise corruption, etc...). Since RXTE observations do not have dedicated background observations, the background for each observation must be simulated based on models (created from actual observations) combined with the actual properties of the particular observation. For this work, a background model based on a weak source was

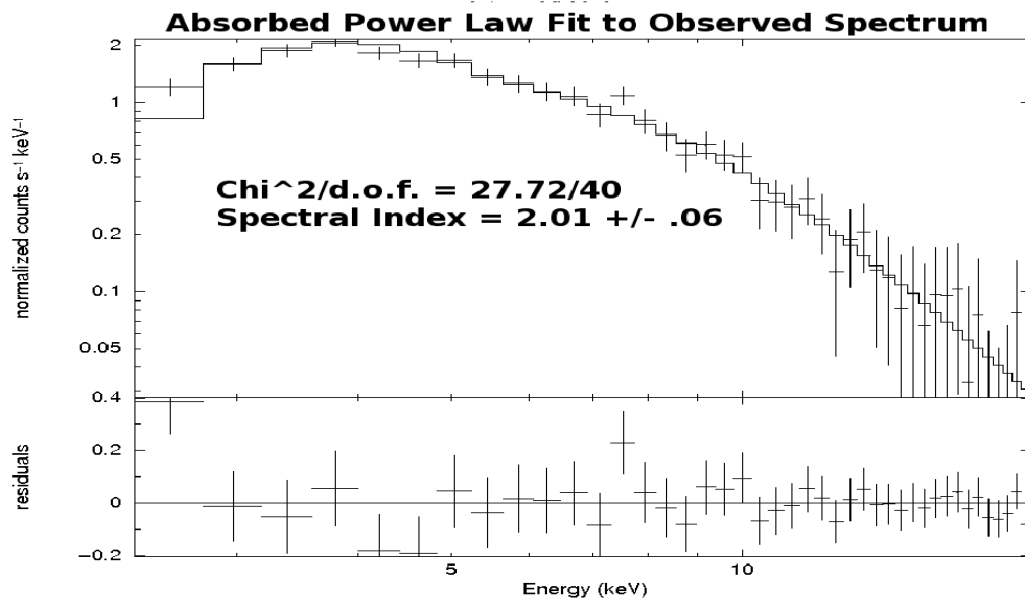


Figure 7.1: The integrated spectrum from all 9 observations with RXTE fit with an absorbed powerlaw model. This same fitting procedure was carried out for each individual observation spectra resulting in the data shown in table 7.1

chosen, *faint17eMv20051128.mdl*. Next a filtering routine was run on both the observation and the background file to create a list of observation times that correspond to usable data “Good Time Intervals” (or GTIs). The standard cuts used are the following: remove all of the data in which the pointing lay less than 10° away from the Earth (elevation cut); remove all data where the pointing error was less than 0.02° (pointing cut); and remove all data where the electron contamination per channel was <0.1 (electron contamination cut). After these data cuts are made, the “saextract” routine was used to extract both source and background spectra. This procedure was completed once for every night of observation in order to gauge how the X-ray behavior of the source was changing over the orbital period. Several issues affected the continuity of the data used for this analysis. First, for three of the ten observations, only 1 of 5 PCU units was turned on. For the rest of the observations, varying numbers of PCU units were used. Secondly, since the elevation cut of $<10^\circ$ eliminated all but 224 seconds of observation from the first night (10/13), it was decided to eliminate this observation from the analysis due to the extremely short exposure. For spectral analysis of this data, several additional steps are needed. While the initial analysis steps performed above generate both source and background spectra, to fit a model spectrum to the data, we also need a gauge of how each channel of the instrument responds to photons, or a “response matrix”. For this work, instrument response matrices were generated within the FTOOLS architecture using the PCARSP function, which was used to generate responses from the top layer of PCU 2 only.

The choice of only utilizing the top layer data came from the motivation that this choice would give the highest signal to noise ratio (Harrison et al., 2000). Spectra were produced for all 9 good observations in the energy range of 2-15 keV as RXTE is not reliably responsive below this range and above this range noise dominates for this source at lower flux levels.

Spectral modeling and fitting was carried out with the XSPEC package (Arnaud, 1996) utilizing the data spectra, background spectra, and response matrices to generate individual fits of chosen models to the background subtracted data. It was decided to model the data based on a simple absorbed power law which is shown to be the best fit to previous RXTE data on LS I +61 303 (Harrison et al., 2000; Greiner and Rau, 2001). Furthermore, the model has the advantages of being relatively simple (only 3 free parameters) and quite well suited to what is believed to be going on physically in the system (i.e. non-thermal processes such as IC scattering). The absorbed power-law model consists of three parameters: the density of the neutral hydrogen column along the line of sight to the source n_H , the photon spectral index α , and a normalization constant K which represents the source emission at 1 keV in photons $\text{keV}^{-1}\text{cm}^{-2}\text{s}^{-1}$. The model generates a spectrum:

$$M(E) = e^{-n_H\sigma(E)}KE^{-\alpha} \quad (7.1)$$

where $\sigma(E)$ is the photo-electric absorption cross-section for neutral hydrogen. Two approaches were taken in modeling the spectra of these observations. The first, taking the previous results (Leahy et al., 1997; ?) into consideration, fixes a value of $n_H = 0.5 \times 10^{22} \text{cm}^{-2}$ in the modeling process and therefore the only variable parameters were taken to be the spectral index α and the normalization constant K . The second approach was to allow the value of N_H to vary freely in the model. However, after examining the data, it was determined that the exposure lengths would not allow for reasonable fits using a freely varying N_H model (i.e. the resulting fit statistics had huge error bars and were thus irrelevant). It was decided, for this data set, that a reasonable approach would be to only fit the model with a fixed value of N_H . The fit statistics of this modeling processes are shown in table 7.1. Also, using these spectra, one can produce integrated flux values in the energy range of interest (2-10 keV in most cases); these are also shown in table 7.1 as well as figure 7.2.

7.2 Results

The lightcurve generated by integrating the absorbed power law fit over 2-10 keV is shown in figure 7.2 as well as the background subtracted instrumental count rate for comparison. The dominant systematic source of error for weak sources such as this is the variation in the X-ray background

7.2. RESULTS

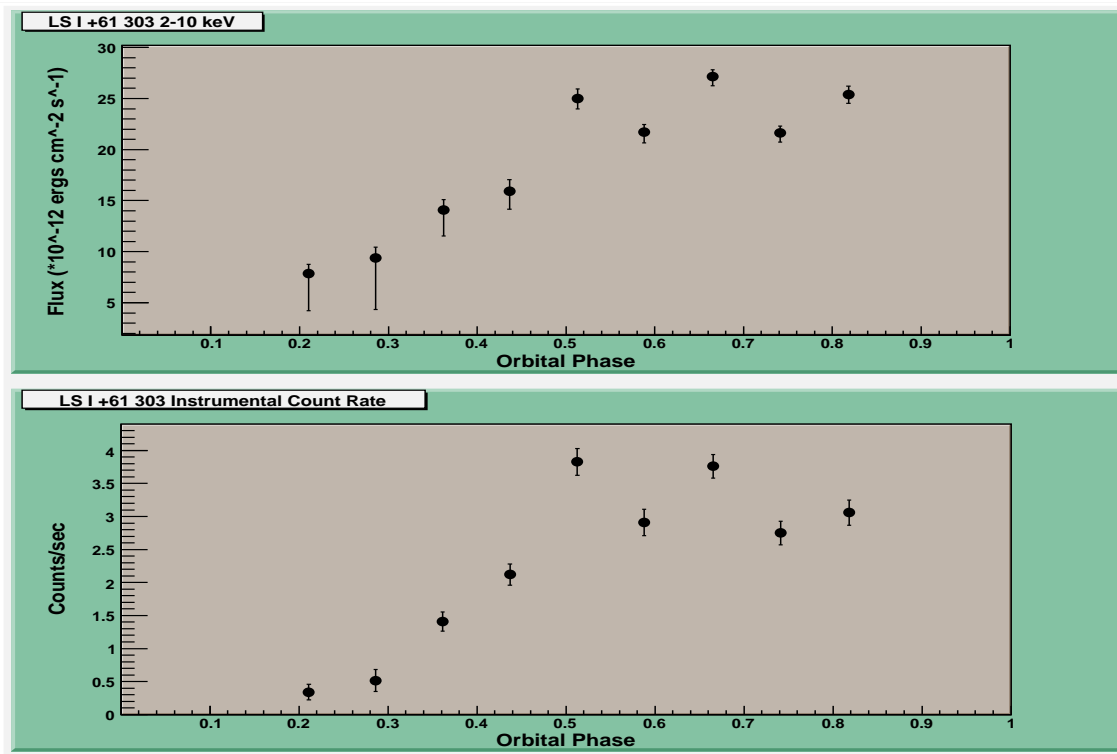


Figure 7.2: Top: X-ray lightcurve in 2-10 keV band extracted from absorbed power-law spectral fitting. Bottom: The associated background subtracted instrumental count rates for comparison. This count rate was taken from PCU 2 only as this was the only unit in operation for the entire data set. The two curves are satisfactorily in agreement with a flare evident in both data, peaking at around orbital phase 0.66 and persisting until the end of the data set.

(Harrison et al., 2000) of approximately 2×10^{-12} ergs cm^{-2} s^{-1} with variations expected in the 10% range. This error is included in the flux values plotted in figure 7.2 as a 0.2×10^{-12} ergs cm^{-2} s^{-1} addition to the statistical error, which is the dominant source of error for these data points. As can be seen from the data, as the source advances through its orbital cycle, a flare is seen in the data which peaks at orbital phase 0.66 and persists until the end of the data set. During this time, the 2-10 keV flux increases significantly with no clear indication of spectral hardening (see figure 7.3). However, the spectra derived from the first few nights of observations should be taken cautiously as the flux values are relatively low and have large error bars associated with them. This, combined with the reduced sensitivity of only using a single PCU for these observations, introduces a significant margin of error which may affect the spectra. The flux values later in the observations are significantly strong that the derived spectral values should be taken as very accurate measurements. A glance at the error bars on the flux values in figure 7.3 reinforces this assumption. The data taken indicate that a spectral index value of 2.1 fits most of the data points

7.2. RESULTS

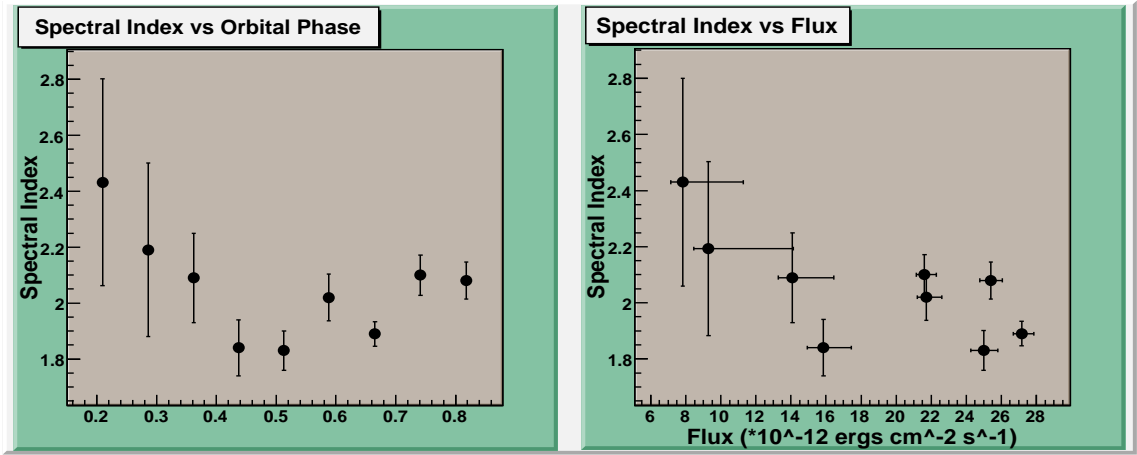


Figure 7.3: On the left is shown the fitted spectral index values from an absorbed power-law model versus the orbital phase. On the right is shown a comparison of the integrated flux values derived from the model in the 2-10 keV band versus the derived spectral index.

Table 7.1: RXTE October 2006 Results

JD Start (245****)	Orbital Phase	Spectral Index	Flux (\pm error _{stat,sys}) (10^{-12} ergs cm $^{-2}$ s $^{-1}$)	χ^2 /d.o.f.
4021.804	0.141	n/a	n/a	n/a
4023.651	0.211	-2.43 \pm 0.37	7.834 +0.88 -3.65	17.16/28
4025.685	0.286	-2.19 \pm 0.316	9.32 +1.03 -5.05	15.73/28
4027.64	0.362	-2.09 \pm 0.16	14.09 +1.0 -2.55	15.28/28
4029.721	0.437	-1.84 \pm 0.1	15.86 +1.14 -1.78	16.84/29
4031.685	0.513	-1.83 \pm 0.071	24.99 +0.94 -1.0	33.86/29
4034.023	0.588	-2.02 \pm 0.083	21.73 +0.72 -1.07	37.61/29
4035.745	0.6653	-1.896 \pm 0.044	27.16 +0.67 -0.90	47.09/29
4038.002	0.7413	-2.10 \pm 0.0717	21.62 +0.68 -0.87	27.16/29
4039.994	0.8181	-2.08 \pm 0.066	25.4 +0.83 -0.86	34.71/29

with the exception of several harder spectral points, which is consistent with (if not identical to) previous measurements of the X-ray spectrum (Harrison et al., 2000; Greiner and Rau, 2001; ?). Comparing the data points from figures 7.2 and 7.3 at higher flux, it is possible that the spectrum may be hardening with increased flux, however no definite statement can be made about this, primarily due to low statistics and large error bars in the first few observations. To further explore this, plotted in figure 7.3 is a comparison of flux values versus spectral indices. No clear correlation is evident.

7.3 Re-Analysis of Archival RXTE Data

RXTE previously monitored LS I +61 303 for a full orbital cycle in March 1996. The data set consisted of 11 pointed observations of between 7.9 and 12.9 ks. These data were taken along with radio data as a part of a multiwavelength campaign with the Green Bank Interferometer (GBI) and Ryle Telescope. Spectral fitting of this data set (Harrison et al., 2000; Greiner and Rau, 2001; Neronov and Chernyakova, 2007) are presented and summarized in chapter 4. The motivation to perform a fourth analysis of the data comes from the inconsistent spectral fitting performed by all three previous analyses. This inconsistency arises from the fact that the best fit model to the spectrum of LS I +61 303 is a power law whose spectral index is heavily modified in the low X-ray energy (<2 keV) range by photoelectric absorption (see previous section). Therefore, setting the value of N_H (or equivalently the degree of photoelectric absorption) will strongly modify the resulting spectral fit. However, RXTE is less sensitive in the range that would allow accurate determination of N_H (<2 keV); therefore, when carrying out spectral analysis of RXTE data, it is preferable to model the fit using a pre-determined value of N_H coming from other experiments which are more sensitive in the <2 keV range.

It should be noted that all three previous analyses used the same software package as is used for the current analysis (presented in the previous section), XSPEC. Although the various releases of XSPEC used may introduce slightly different spectral fitting results, it is assumed that the primary source of variation in results comes from analysis procedures, and not differences in software releases. The first analysis (Harrison et al., 2000) modelled the data with an absorbed power law with spectral index 1.8 (obtained by previous ASCA observations) and then extracted flux values from this fit in the 2-10 keV range. The second analysis (Greiner and Rau, 2001) took into account data from the lower PCU layers which allowed harder photons to be included in the analysis. The fitting routine was performed between 2 and 25 keV and allowed all three free parameters (N_H , α , and K) to vary. Although producing reasonable fits to the data, this analysis also produced values for N_H as high as $6.5 \times 10^{22} \text{cm}^{-2}$. This is seen to be an unreasonable value in light of more recent determinations of $N_H = 0.5 \times 10^{22} \text{cm}^{-2}$ (?), which agree with the previous ASCA measurement of $0.4\text{-}0.6 \times 10^{22} \text{cm}^{-2}$ (Leahy et al., 1997). The most recent analysis of this data (Neronov and Chernyakova, 2007) fixes the value of N_H at $0.5 \times 10^{22} \text{cm}^{-2}$ in the spectral fitting performed (of only the top PCU layer) and detected spectral variability. However, in the publication, the authors do not state over which energy range their spectral fitting is performed, nor their data selection criteria. Their values of $\frac{\chi^2}{d.o.f.}$ imply a fitting range which is much smaller than the good responsive range of RXTE for this source and length of exposure. For exposures as

7.3. RE-ANALYSIS OF ARCHIVAL RXTE DATA

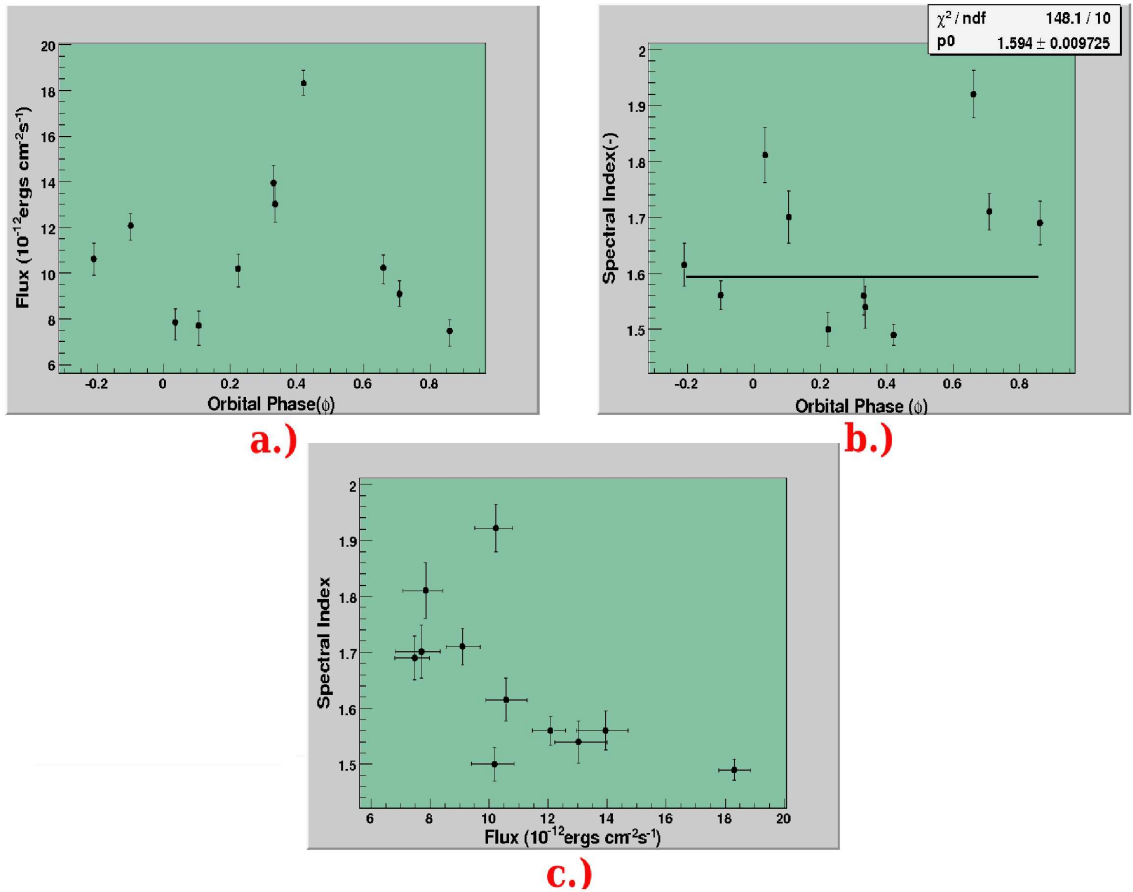


Figure 7.4: Results of the re-analysis of archival RXTE data on LS I +61 303. a.) Flux vs orbital phase. b.) Spectral index vs orbital phase with a straight line fit. c.) Spectral index vs flux.

long as those in this data set (> 5 ks), RXTE can reliably detect LS I +61 303 over the range of 2-20 keV; it is this range over which the spectral fitting should be performed. This is the approach taken in the current re-analysis of the data set.

The analysis procedures carried out on the 1996 data set are identical to those detailed in the previous section, namely, fluxes in the 2-10 keV range were extracted from fitted spectra (from 2-20 keV) to each night's observations (figure 7.4a). This fitting was carried out with N_H fixed at a value of $0.5 \times 10^{22} \text{cm}^{-2}$. The flux values from this data set show a clear flux peak near orbital phase 0.4, which is considerably earlier than that observed in the most recent RXTE data set, although consistent with previous results. The data also show a secondary flux peak near $\phi = 0.8$. The spectral index versus orbital phase is shown in figure 7.4b with a straight line fit only resulting in a χ^2 fit of 148.1/10, strongly indicating variability with orbital phase. The spectral index versus flux level is shown in figure 7.4c showing a trend towards harder spectral values with flux increase. This correlation is not concrete however, due to the highest flux point having a similar spectral

Table 7.2: Table 2: RXTE March 1996 Results

JD Start (245****)	Orbital Phase	Spectral	Flux (\pm error _{stat,sys}) (10^{-12} ergs cm $^{-2}$ s $^{-1}$)	χ^2 /d.o.f.
0144.088	0.79	-1.615 \pm 0.038	10.58 $^{+0.7}_{-0.69}$	54.89/54
0147.401	0.90	-1.56 \pm 0.026	12.08 $^{+0.52}_{-0.62}$	115.32/54
0150.67	0.034	-1.81 \pm 0.049	7.85 $^{+0.58}_{-0.78}$	58.37/54
0152.538	0.105	-1.70 \pm 0.047	7.71 $^{+0.64}_{-0.88}$	61.10/54
0155.660	0.223	-1.50 \pm 0.03	10.19 $^{+0.65}_{-0.80}$	62.09/54
0158.516	0.33	-1.56 \pm 0.035	13.94 $^{+0.76}_{-0.97}$	68.37/54
0158.641	0.335	-1.54 \pm 0.038	13.027 $^{+0.97}_{-0.81}$	68.46/54
0160.936	0.42	-1.49 \pm 0.019	18.3 $^{+0.56}_{-0.52}$	171.78/54
0167.463	0.66	-1.92 \pm 0.042	10.23 $^{+0.58}_{-0.70}$	66.56/50
0168.536	0.708	-1.71 \pm 0.033	9.10 $^{+0.59}_{-0.55}$	32.24/50
0172.665	0.86	-1.69 \pm 0.039	7.48 $^{+0.50}_{-0.67}$	77.67/50

index to some of the lower flux points. These results are in general agreement with previous X-ray monitoring campaigns, although not showing the definitive evidence for spectral hardening with increased flux claimed in the work of Neronov and Chernyakova (2007). Both the flux behavior and spectral variability of these observations will be discussed in greater detail in the final chapter.

7.4 *Swift* Contemporaneous Observations with VERITAS

Contemporaneous with the VERITAS TeV observations, X-ray observations with the Swift X-ray satellite were carried out in September 2006, and then resulting from a ToO request from the VERITAS collaboration, in November/December 2006 (Holder et al., 2007). A total of 56 kiloseconds of observations were taken over 24 days from September to December 2006. These observations, ranging in duration from 700-4700s, were taken by the XRT instrument aboard Swift, sensitive in the energy range of 0.3-10 keV. The analysis of these data was performed by Jamie Holder and Abe Falcone, both VERITAS collaboration members. The XRT data were taken in “photon counting mode” which is a mode which retains all imaging and spectroscopic capabilities but only has a time resolution of 2.5s, a mode commonly used for weak sources (see heasarc.nasa.gov/docs/swift/analysis/xrt_sguide_v12.pdf for details of XRT data modes). The counts were converted into an energy flux using the XRT count rate to flux conversion factor of $5.7e-11$ (erg/cm 2 /s 1)/(c/s). This conversion factor was obtained using the mean spectral fit

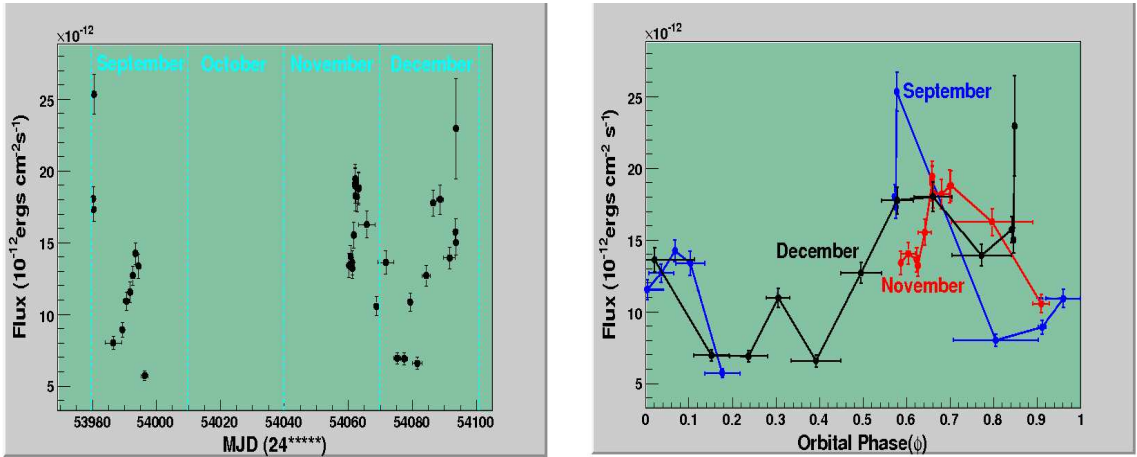


Figure 7.5: Swift X-ray observations in Fall 2006 binned by both MJD and orbital phase.

parameters for these data. The data binned by both date and by orbital phase are shown in figure 7.5. The data show a clear variability by a factor of 4-5 in flux over single orbital phases. The flux has a peak between orbital phases 0.5→0.8, although the location of the peak changes from cycle to cycle. There also is a secondary flux peak located between orbital phases 0.0→0.1, similar, but shifted in phase to the secondary peak observed in the 1996 RXTE observations.

The cumulative data set is fitted well ($\chi^2=377/370$) by an absorbed power law with $N_H=0.576^{+0.019}_{-0.018}\times 10^{22}\text{cm}^{-2}$, which is consistent with previous measurements. The parameters of the fit were a differential flux at 1 keV of $1.334^{+0.019}_{-0.020}\times 10^{-11}\text{ergs cm}^{-2}\text{s}^{-1}$ and a spectral index of $\Gamma = -1.73 \pm 0.03$ which is also consistent with previously measured values. At the time of writing, a full spectral analysis searching for variability linked to orbital phase changes had not been performed; however, a hardness ratio study (Holder et al., 2007) showed no evidence for spectral hardening correlated with flux level.

7.5 X-ray Behavior in Perspective

In summary, these X-ray data presented here vary in their description of both the phase location of the peak flux as well as the value of the peak flux itself. All the data sets show a clear increase in flux level by a factor of 4-5 from the lowest flux level of $5\text{-}10\times 10^{-12}\text{ ergs cm}^{-2}\text{ s}^{-1}$; however, the location of the peak flux is near orbital phase 0.4 in the archival RXTE data whereas the peak location is closer to 0.5→0.8 in the most recent RXTE and Swift data. The latest RXTE data only shows weak evidence for spectral variation with orbital phase (the Swift data does not address this issue), but the archival RXTE data shows strong evidence for spectral variation with orbital phase. Additionally, this spectral variability is seen in the observations taken with XMM-Newton in 2002

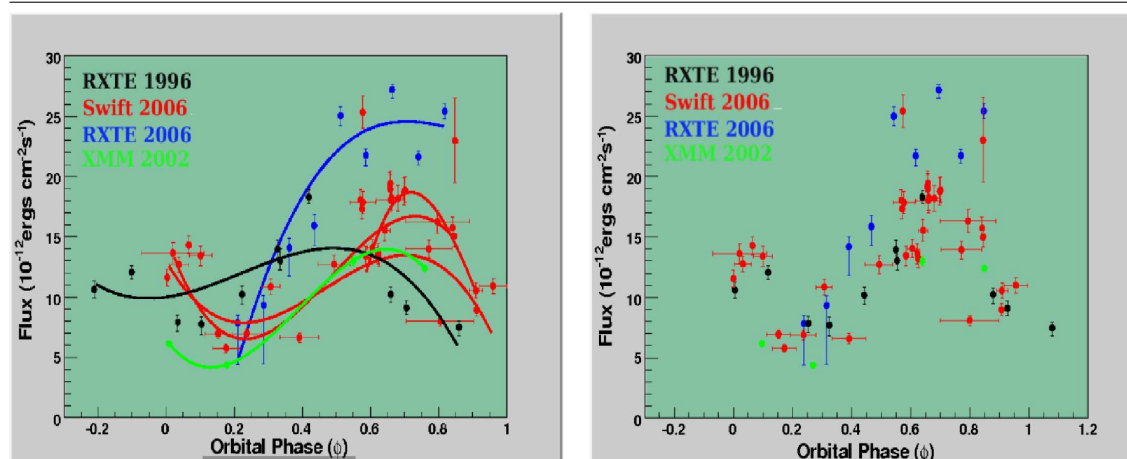


Figure 7.6: The combined X-ray lightcurves discussed in this chapter, plotted as a function of orbital phase. The three red curves represent the three continuous Swift observation sets. The left figure shows a polynomial fit to each light curve, the right shows the results after these polynomial fits are “aligned” (see text). A general characteristic trend can be inferred.

(?). Between February 5 and 21, 2002, LS I +61 303 was monitored in the 0.5-100 keV band. The observations showed LS I +61 303 to be variable in both flux and spectral index (see figure 7.7), peaking at orbital phase 0.55, with a spectral index that changed from 1.78 to 1.52 over a single orbital period. In an exploratory fashion this dataset, along with all the others discussed in this chapter, are shown in figure 7.6. As can be seen, the flux from all the XMM, Swift, and recent RXTE datasets show peak levels near orbital phases 0.5→0.8 with a secondary peak near 0.0→0.2. The archival RXTE data show nearly identical behavior but shifted back by about 0.2 in phase. To test how well the overall characteristic shapes of each light curve matched up, the lightcurves were fitted with a 3-dimensional polynomial function which is the simplest function which will provide two peaks (shown in figure 7.6). The maxima of all three continuous Swift dataset fits match up well and it was therefore decided to use their mean maxima ($\phi = 0.65$) as a reference point to align the other lightcurves up to. This resulted in a shift of orbital phase of 0.03 for the 2006 RXTE data, 0.11 for the XMM data, and 0.22 for the archival 1996 RXTE data. The result of this shifting is shown in figure 7.7. It is clear that the alignment of the light curves gives rise to a characteristic shape of a small peak early on leading to the main flux peak later in the orbit. Possible interpretations of this lightcurve behavior will be discussed in greater detail in the next chapter.

The spectral indices derived from the RXTE and XMM datasets as a function of orbital phase are shown in figure 7.7, both before and after the alignment of the light curves. There was no similar information available at the time of writing from the Swift dataset. After alignment of the

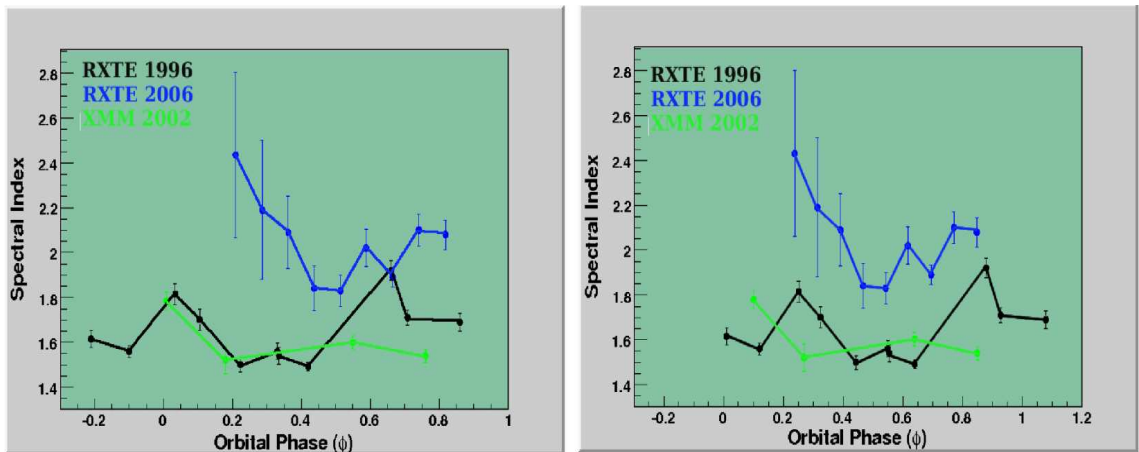


Figure 7.7: The spectral indices as a function of orbital phase for the XMM and RXTE datasets before (left) and after (right) the lightcurves were aligned.

light curves, the spectral indices do not line up as well as the flux light curve, however it appears that the same general shape is present in the two RXTE lightcurves, and may be present in the XMM lightcurve. That is, there is a soft spectral state early which appears to harden later in phase. The XMM spectral curve shows hints of this shape but it is not well enough sampled to correlate with the two RXTE curves. Overall, because of the error bars on the recent RXTE data and the lack of full orbital sampling in the XMM dataset, it is not possible to draw any definite conclusions about the behavior of the spectral variability in LS I +61 303; it appears conclusive however, that some form of spectral variability is indeed present within the X-ray datasets with straight line fits to the new RXTE data, archival RXTE data, and XMM light curves giving reduced χ^2 values of 2.22, 14.82, and 8.71 respectively.

7.6 Comparison of X-ray and TeV Data

Since both the TeV and the hard X-ray emission observed by VERITAS, RXTE, and Swift are non-thermal in nature and due to some as-of-yet undefined particle acceleration, it is reasonable to hypothesize that the behavior in the two bands may be related. To explore this idea, this section will deal with the comparison of the data in both the TeV and the hard X-ray band during the same time frame. Although the previous section dealt with X-ray observations which included archival RXTE data as well as XMM data taken in 2002, only the X-ray datasets which were taken contemporaneously with the VERITAS TeV data will be used for this comparison.

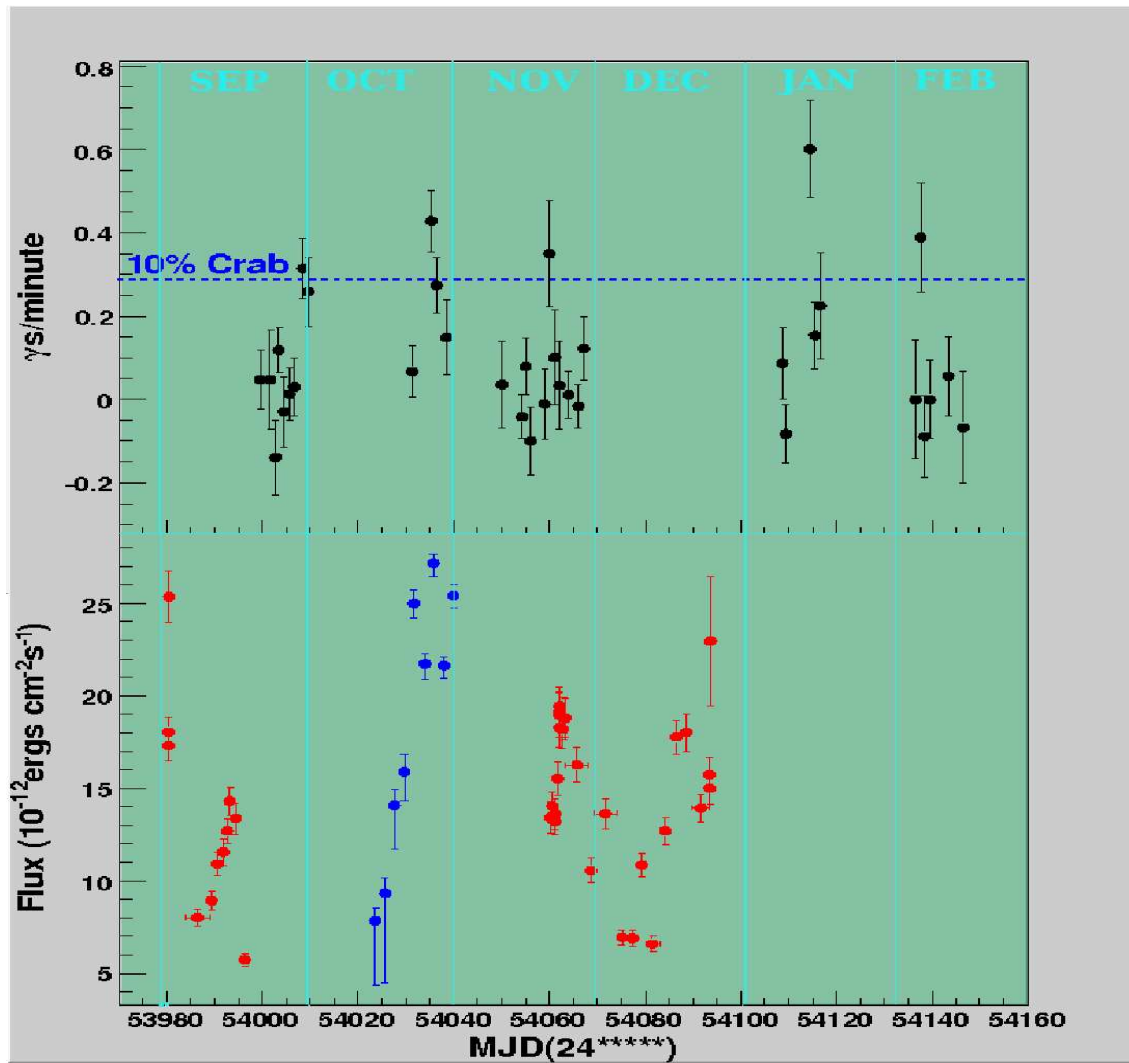


Figure 7.8: The VERITAS TeV data (black points in top graph) shown along with the X-ray data points (Swift in red, RXTE in blue).

7.7 Total Dataset Comparison

Figure 7.8 shows all the lightcurves (binned by MJD) for both the Swift and RXTE datasets taken in 2006 as well as the VERITAS TeV set taken in 2006-2007. By re-binning this data by its orbital phase, figure 7.9 is generated. Included in this figure are Gaussian fits (used solely under the assumption of the data set containing a single peak) to the TeV data as well as the combined X-ray data set. Since the goal is to understand how the rise time of the peak flux in both bands is possibly related, the X-ray data is only fitted over a range of $\phi = 0.2 \rightarrow 0.9$ since this is the only coincidence window between the two sets and the secondary bump in the X-ray data at earlier phases would distort the clarity of a Gaussian fit to the primary X-ray peak. The light blue lines in figure 7.9 represent the mean value of the Gaussian fit for both datasets. For the TeV data set, the

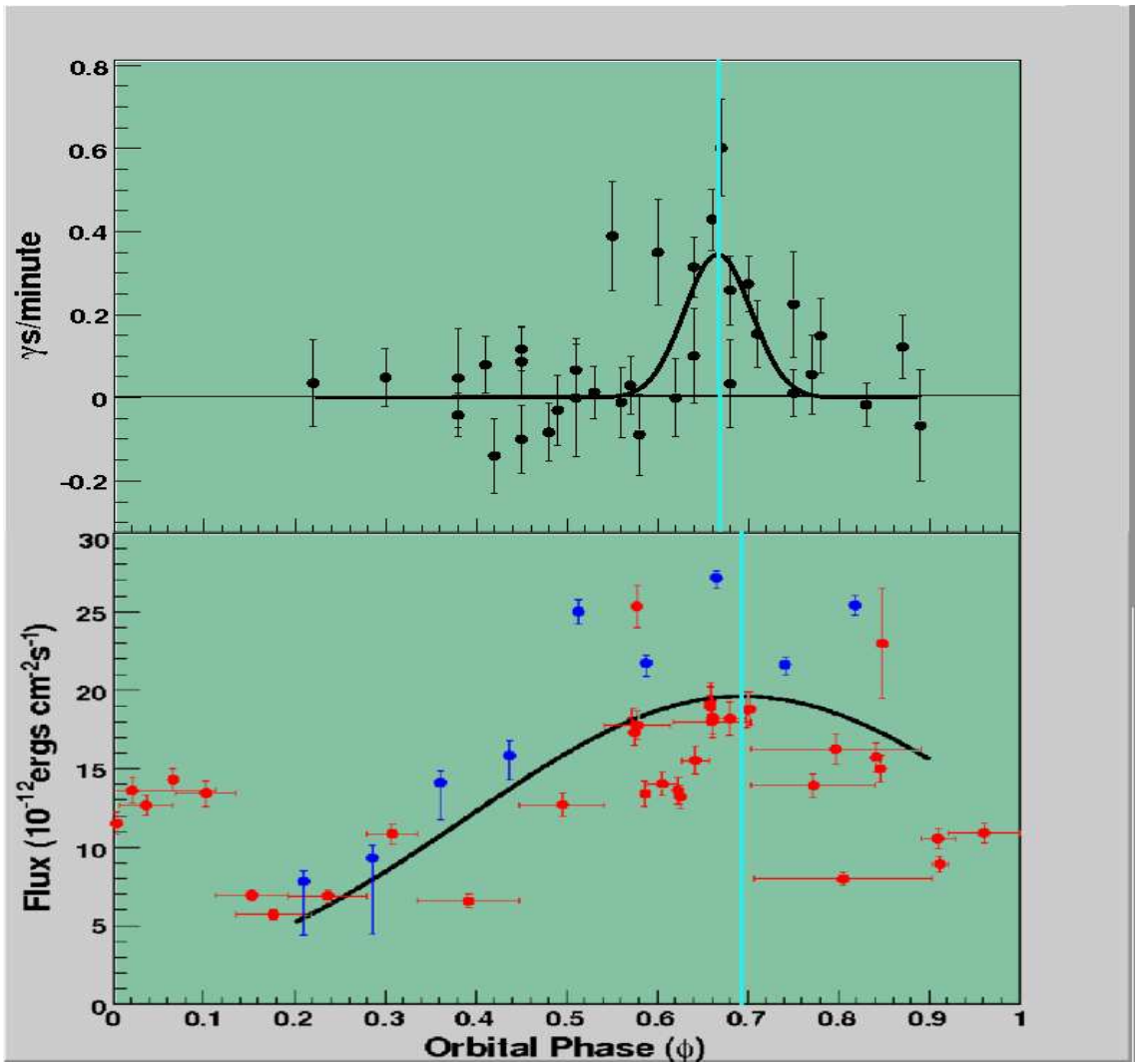


Figure 7.9: As in figure 7.8 but binned by orbital phase. The black lines represent Gaussian fits to the datasets with the light blue lines representing the peak of the fits.

fit peaks at a value of $\phi = 0.66$ whereas for the X-ray data the peak lies at $\phi = 0.692$. Although a definitive statement of correlation is not possible at this time, the short time difference between these two peaks implies that the behavior in each band may be possibly linked.

To investigate this further, a correlation study between the data in the two bands was performed utilizing the z -transform *Discrete Correlation Function* which is shown to give a much more sensitive gauge of correlation between two sparsely populated lightcurves than the standard discrete correlation method (Alexander, 1997). Standard discrete correlation tests on two sparsely populated lightcurves x and y proceed by ordering each point x_i, y_j according to their time differences τ_{ij} . This results in a cross-correlation function which determines a value r_{dcf} :

$$r_{dcf}(\tau) = \frac{1}{N} \sum_{\tau_{ij}} \frac{(x_i - \bar{x})(y_i - \bar{y})}{s_x s_y} \quad (7.2)$$

for each bin, where \bar{x}, s_x^2 are the mean, and variances of the parent distributions respectively. This method offers no errors on the individual r_{dcf} values for each bin and thus no gauge of the significance of any apparent correlation. To overcome this the ZDCF assumes that each lightcurve is drawn from a bi-normal distribution for which the z-transform ((Fisher, 1921)) function:

$$z = \frac{1}{2} \log\left(\frac{1+r}{1-r}\right) \rightarrow r = \tanh(z) \quad (7.3)$$

has a well understood mean and variance ($\bar{z}(r), s_z^2(r)$) which allows for the error to be determined on the correlation function for each bin. The Z DCF results in a correlation for each bin of (Alexander, 1997):

$$r_{zdcf}(\tau) = r_{-(r-\tanh(\bar{z}-s_z))}^{+\tanh(\bar{z}+s_z)-r} \quad (7.4)$$

The ZDCF also tests for correlations on bins selected by equal population instead of equal $\delta\tau$ which is desirable for lightcurves with erratic sampling.

Larger values (i.e. close to 1) of the ZDCF function for a given time delay imply strong correlation between the two lightcurves if they are separated by that time delay. In the case of an auto-correlation test, a single lightcurve is duplicated and a copy is delayed by a given lag and those two are tested for correlation. For example, a large value of the ZDCF function at a value of 3 days delay in a cross-correlation would imply that the two lightcurves are strongly correlated by a feature present in one lightcurve that appears 3 days later in the other light curve. In the case of an auto-correlation test, this same result would imply the presence of a periodic feature appearing every 3 days. The converse is true for negative values of the ZDCF, i.e. this implies anti-correlation for a given lag. To demonstrate the ZDCF efficacy in finding correlations between sparsely populated lightcurves, a test was carried out on two simulated lightcurves. In figure 7.10 (left) are shown two lightcurves simulated with sinusoidal behavior and degraded to mimic sparsely populated curves. The red lightcurve precedes the blue lightcurve by one day. The results of the ZDCF test (blue points vs red) on these two lightcurves is shown in figure 7.10 (right). As can be seen there is a significant peak near -1 and 2, implying that the red lightcurve leading the blue lightcurve by one day (and anti-correlated at a positive 2 day shift).

As an initial test on the data, both lightcurves (TeV and all X-ray data combined) were tested using the ZDCF for auto-correlation. The X-ray lightcurve flux was normalized to the maximum measured in the Swift data. Figure 7.11 (left) shows the X-ray lightcurve binned by successive orbital phases as the data occurred. In figure 7.11 (right) is shown the ZDCF for this light curve and as can be seen there is a clear excess of high ZDCF near 0 time delay. This implies that

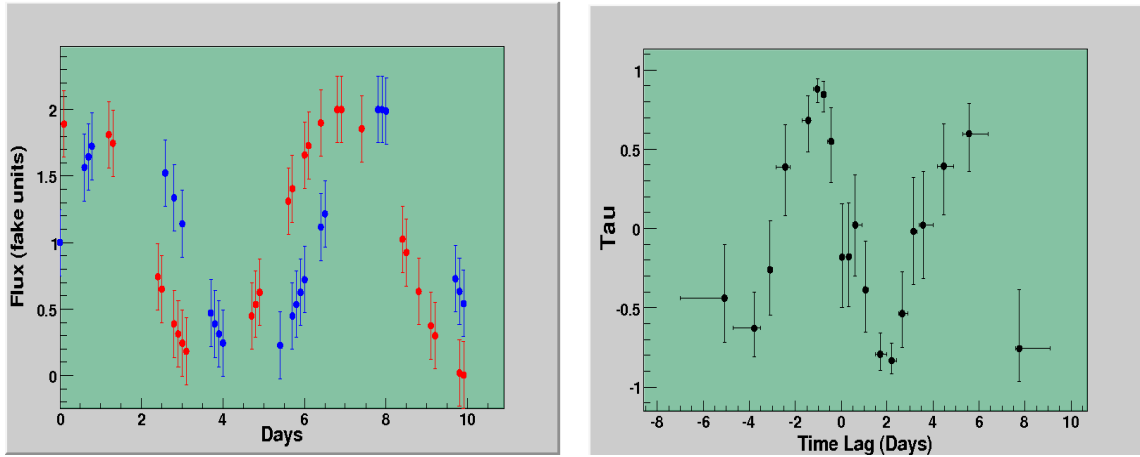


Figure 7.10: The simulated sinusoidal lightcurves (left) and the result of a ZDCF correlation test on them. Negative values indicate that the first lightcurve (blue in this case) lags the second and vice versa. A significant feature in the ZDCF test appears at the built-in lag of the curves with the red curve preceding the blue by one day.

the X-ray lightcurve is correlated with itself. By examining this ZDCF plot further there also appears to be hints of both excesses at whole values of the orbital cycles and deficits at half values. This would imply the presence of a periodic feature in the X-ray lightcurve in each phase—i.e. the lightcurve is correlated with itself when shifted by a whole orbital cycle, and strongly anti-correlated when shifted by half orbital cycles. However, since this lightcurve is not evenly sampled and has a gap from $\phi = 1 \rightarrow 2.2$, the presence of this periodic behavior is diluted and it is difficult to extract any concrete conclusions. To investigate this further in an exploratory fashion the X-ray lightcurve was altered so that it offered continuity between these values. This was accomplished by shifting all the data in $\phi > 2$ backwards by $\phi = 1$ (compare figures 7.11a and 7.12a). The resulting ZDCF graph on this continuous light curve shows the presence of a clear periodic sine-like feature. Although this is not a definitive proof of the periodic behavior of the X-ray lightcurve due to the alteration of the data needed to get this results, it is a clear indication that on the short term (several months) the X-ray behavior of LS I +61 303 may be relatively stable, albeit shifting slightly in maxima and minima. Therefore, if the TeV and hard X-ray behavior are strongly linked, this would imply that the TeV lightcurve should present the same periodicity and apparent regularity of the periodic nature of this source in hard X-rays.

This same auto-correlation test was applied to the TeV data. The original TeV flux was normalized to the maximum flux value of $0.6 \text{ } \gamma/\text{min}$ (7.13a). The ZDCF was applied to this function with the result shown in figure 7.13b. Although there are groupings of points with positive ZDCF

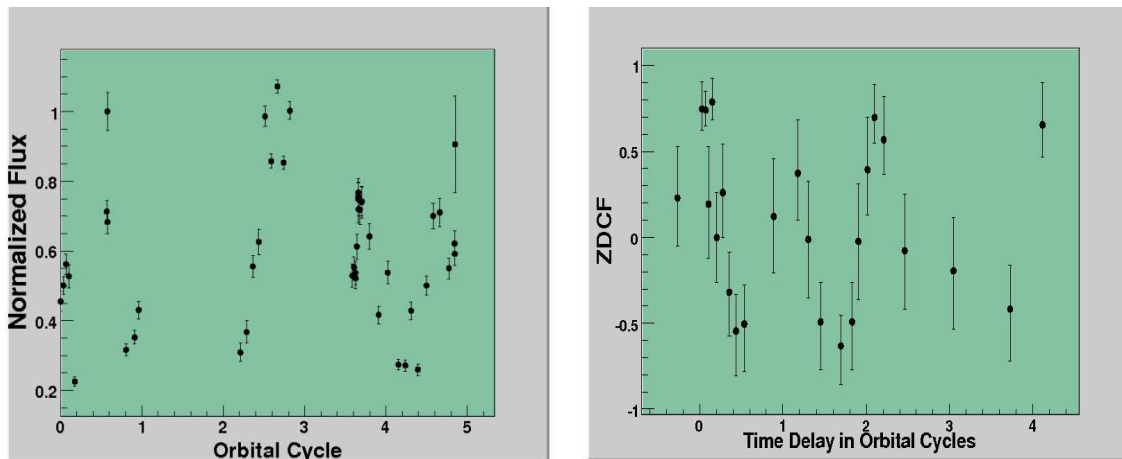


Figure 7.11: The X-ray lightcurve (left) tested for auto-correlation and the resulting ZDCF distribution (right) for various time delays of the lightcurve with itself.

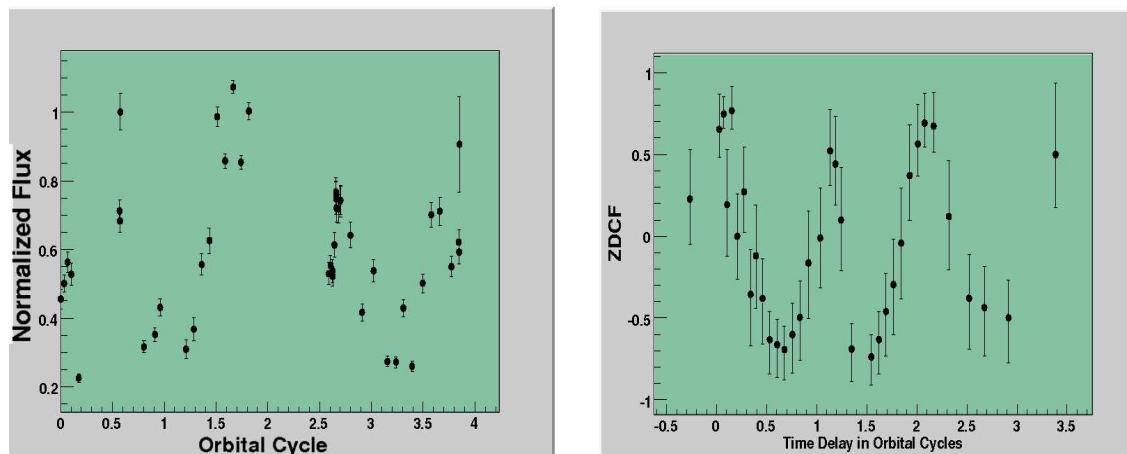


Figure 7.12: The same as in figure 7.11 with the X-ray lightcurve altered for greater continuity. The resulting ZDCF shows a much clearer indication of period behavior.

values near zero, the errors on the points do not allow for any statistically significant information to be drawn from this distribution. This is most likely due to the erratically sampled and gap filled nature of the TeV data set. To explore if there is any evidence of statistically self-correlated structure within the data, the TeV lightcurve was altered similarly to the X-ray data in order to make the lightcurve more continuous. This implied shifting the TeV data point in January and February back by a single orbital phase in order to create a curve with less data gaps. The result of this is shown in figure 7.14a. The ZDCF distribution is not improved by this alteration of the lightcurve, and there still are no statistically viable structures with which to state a correlation (figure 7.13b). This is most likely due to the extremely irregular sampling of the TeV data and the large error bars

7.7. TOTAL DATASET COMPARISON

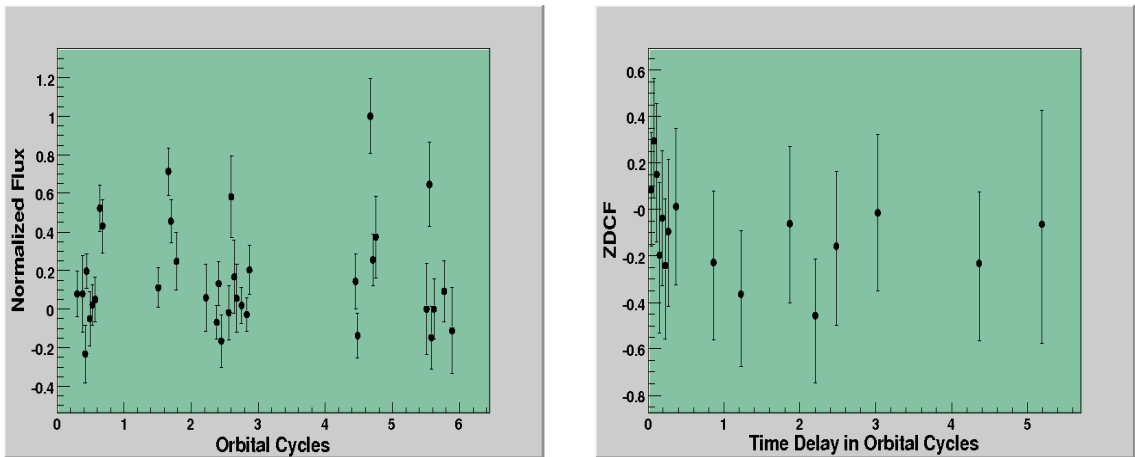


Figure 7.13: The unaltered TeV lightcurve (left) on which the ZDCF auto-correlation test was performed (right). There are no statistically reliable structures evident.

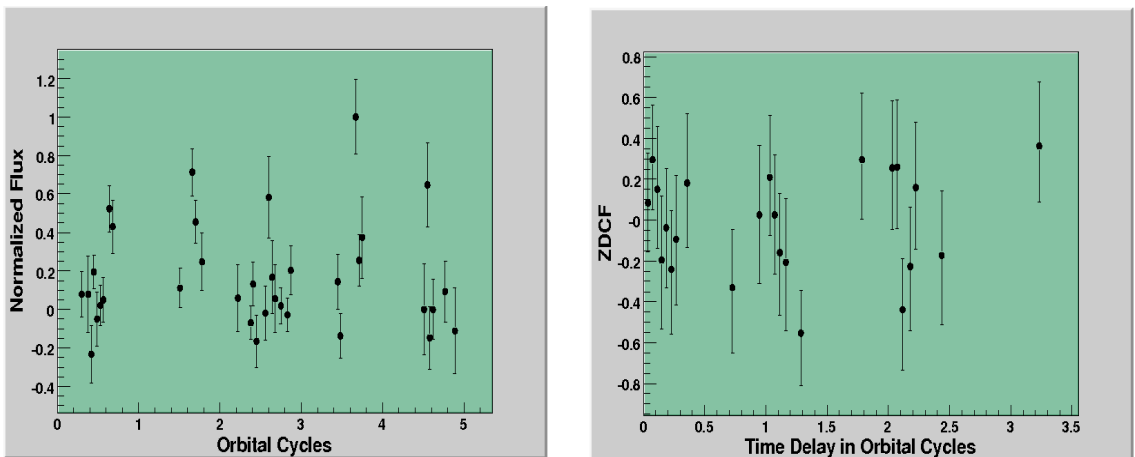


Figure 7.14: As above in figure 7.13 except using the altered TeV lightcurve as described in the text. There are no reliable structures evident.

on most of the data points.

Since the both the TeV and X-ray data are erratically spaced and only overlap twice in the entire union of both sets, it was decided to perform a cross-correlation test on the datasets binned by their orbital phase (expressed in days elapsed since $\phi = 0$ in figure 7.15). Moreover, since the TeV data only runs from $\phi = 0.2 \rightarrow 0.9$, the X-ray dataset used for the cross-correlation only included data points between these values. The lightcurves used for cross correlation are shown in figure 7.15 (left). The ZDCF correlation distribution performed on these two curves is shown in figure 7.15 (right). As can be seen, there are no statistically viable structures within this distribution due to large error bars in the TeV data and sporadic sampling in both data sets. The

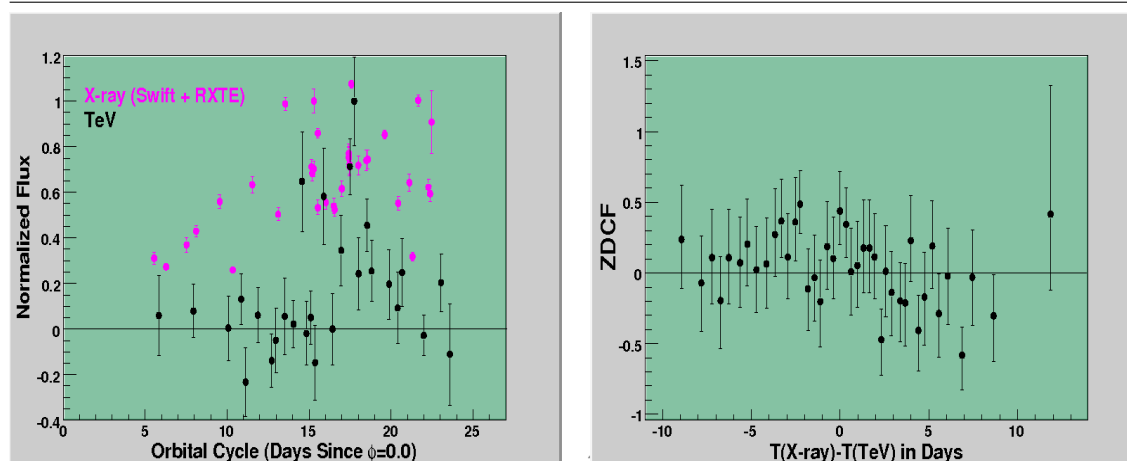


Figure 7.15: On the left is shown the X-ray (purple points) and TeV (black points) light curves, binned by location within the orbital cycle (left). On the right is shown the result of a ZDCF cross-correlation test performed on these two lightcurves.

obvious solution to this would be to reiterate these correlation tests using the lightcurves reduced in larger bins (i.e. data binned in 0.05ϕ bins); however, this reduces the number of overall points by a considerable factor rendering correlation tests (which require a good number of points) useless. Further, more in-depth coverage in both bands is necessary for any statistically viable statement about correlation between the two lightcurves to be made.

7.8 Combined Spectra

Shown in figure 7.16 is the broadband LS I +61 303 spectrum as observed by various instruments. Radio data points (crosses) (Strickman et al., 1998) show both low (blue) and high (red) radio states, the optical and UV points (Maraschi et al., 1981; Marti and Paredes, 1995) are from the optical companion in the system, the X-ray points (triangles) represent the total integrated Swift spectrum (blue) and the single night spectrum from 10/27/2006 observed by RXTE (red), the EGRET GeV data points (stars) are taken from Hartman et al. (1999). The TeV data points are the spectra detailed in chapter 6 with both the total integrated spectrum from phases $\phi = 0.5 \rightarrow 0.8$ (blue circles) and the single night spectrum from 10/27/2006 (red circles).

This figure shows the spectral behavior of LS I +61 303 in various states of activity using blue points to denote the relatively low flux states for each respective band and red points to denote the more active states. However, in the case of the TeV data, since there is no flux available for the low activity regions, the blue points should be considered as active already with the red points considered *very* active. It appears in general that the spectral indices of both the low and high

states do not appreciably change despite the flux increasing in the bands in which both states are observed. However, there are various caveats to extracting any reliable conclusions from this plot. First of all the radio data points were not taken contemporaneously with the X-ray and TeV data (in fact they were taken over a decade before the other two data sets). Additionally, the total integrated X-ray spectrum, is not extracted from the same time frame as the total integrated TeV spectrum. Finally, the active state X-ray spectrum (from 10/27/2006) was taken from the RXTE data set which is most likely prone to large systematic errors and gives a spectrum which is harder than the other data sets explored in this chapter (such as Swift and XMM). Given the Swift and XMM results, which were derived with much more sensitive instruments, it is likely that the X-ray spectrum during the high flux active states is harder than that derived from the 10/27/2006 RXTE data.

Moreover, it is not clear that the high flux states of any of these bands are inextricably linked to the high flux states in others, so comparing the high flux point of any two different bands is a very fragile endeavor. However, the combination of all these data sets shown in figure 7.16 does function as a base for comparing some of the various models proposed to explain the high energy emission from LS I +61 303. In the next chapter, some of these models will be compared and contrasted as they apply to the results derived in this work.

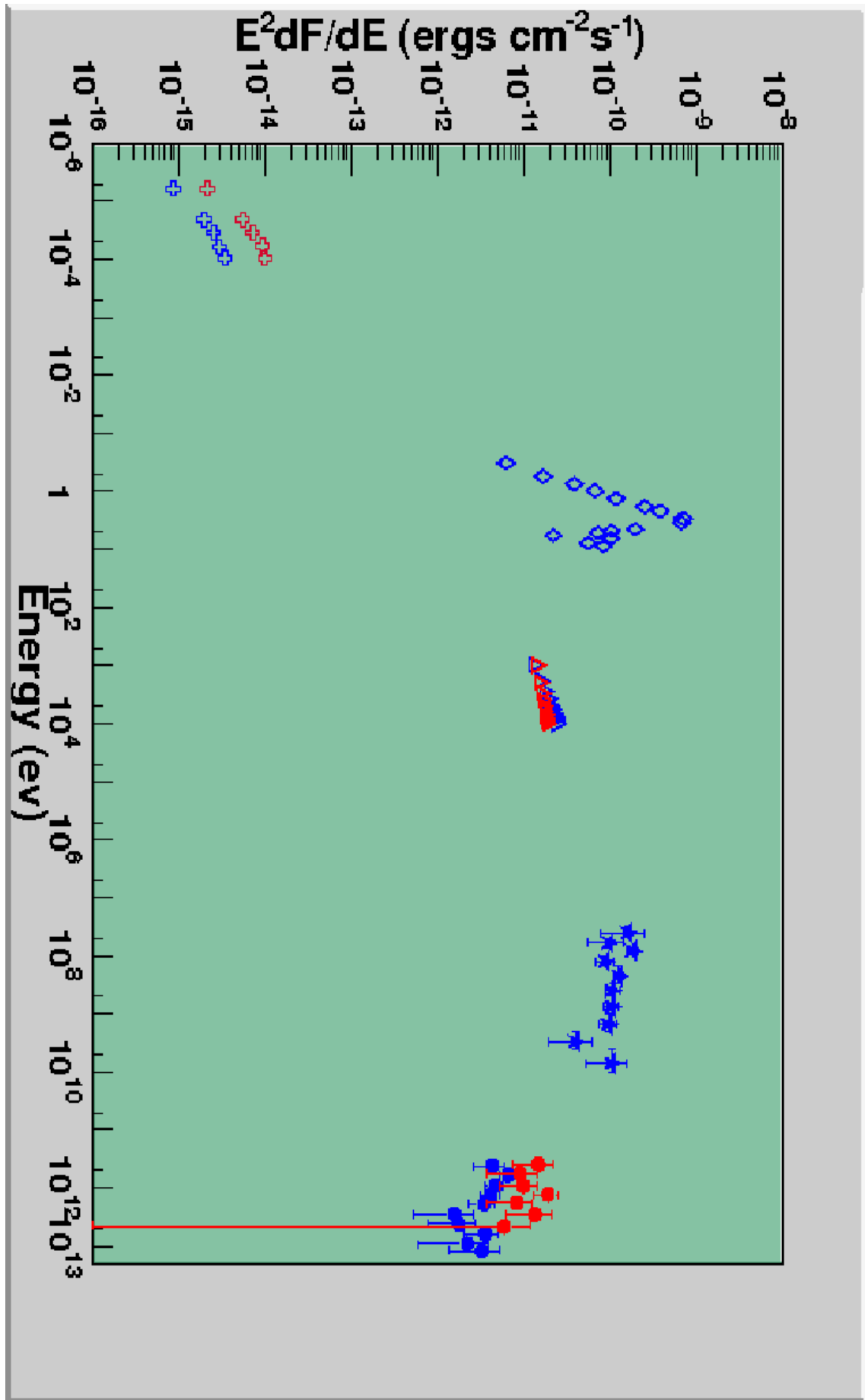


Figure 7.16: The broadband spectra of LS I +61 303 during both “low” and “high” states as explained in the text.

Chapter 8

Comparison to Emission Models

In this chapter several basic models created to explain the high energy emission properties of LS I +61 303 are compared to the most recent X-ray and TeV data available as presented in this thesis. There have been two main model classes invoked to explain the emission properties of this system, describing it either as a microquasar or as a binary pulsar.

8.1 Microquasar Model

In the generalized microquasar framework used to describe the high energy behavior of LSI, the emission is a result of the compact object in the system accreting material from the main sequence star (via stellar wind flow) onto an accretion disk. Magneto-hydrodynamical processes near the accretion disk inner regions will expel part of the accretion disk via jet ejective events. These jet ejections will accelerate electrons (via internal shocks) to relativistic energies. These electrons will radiate at synchrotron energies (resulting in radio and X-ray emission) and also inverse-Compton scatter local stellar photons from the Main Sequence star to X-ray and TeV energies. Since this model is based upon the accretion properties of the system, the regions of the orbit which have high rates of accretion will also have associated large high energy emission. There are two orbital regions in which this is generally thought to occur, the first located at periastron where the density of stellar wind material is the highest. The second will be located appreciably later in the orbit in a region where the slower orbital velocity (and associated increase in accretion rate) will compensate for the smaller density of stellar material (see section 4.5.6.1).

The general accretion-based model would then predict two peaks in high energy emission, one near periastron and one later in the orbit. The X-ray data detailed in this thesis, as well as the archival data, do show flaring behavior at later phases of the orbit (near apastron passage) but a lack of appreciably strong (compared to the rest of the orbit) X-ray emission near periastron

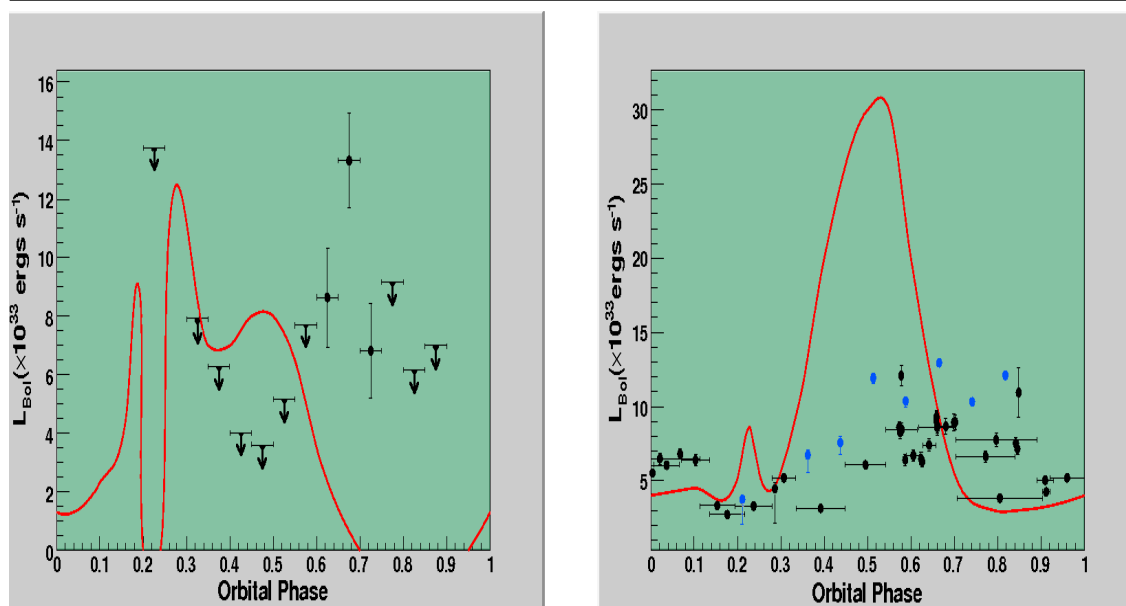


Figure 8.1: The prediction of the TeV (left) and X-ray lightcurves (right) from Bosch-Ramon et al. (2006b) (red lines) compared to data presented in Chapter 7. The bolometric luminosities calculated for the VERITAS, TeV, and X-ray data are estimated assuming a distance to LS I +61 303 of 2 kpc. It can be seen that the behavior of the TeV emission is not well matched. The general shape of the X-ray emission (Swift=black points, RXTE=blue point) is predicted well, but as large of variations in flux levels are not seen in the data.

passage. This is echoed in the TeV data: both the VERITAS and MAGIC results show no indication of TeV emission near periastron, but a strong TeV signal appears at later stages of the orbit. In addition to this, the Swift X-ray data shows a secondary peak occurring at orbital phases $\phi = 0.0 \rightarrow 0.1$, a feature which appears in past X-ray observations also. At this time, there are no TeV observations for this orbital range and no statement can be made about emission during this phase. However, any standard accretion-based scenario must be able to explain the lack of strong TeV and hard X-ray emission near periastron passage as well as the appearance of this secondary peak in the X-ray data. The microquasar model (Bosch-Ramon et al., 2006b), described in Chapter 4 is a prototypical microquasar model based upon this standard “Bondi-Hoyle” accretion model. By making reasonable assumptions about the physical properties of the system (such as magnetic field strength and injected electron spectra), this model can be used to predict both a broadband lightcurve and spectrum for LS I +61 303. Shown in figure 8.1, the various lightcurves for emission are compared to the resulting TeV and X-ray lightcurves derived from the observations in this thesis. During the near-periastron accretion peak, due to the increased target photon density, the inverse-Compton channel dominates over the synchrotron channel, shifting the dominant emission

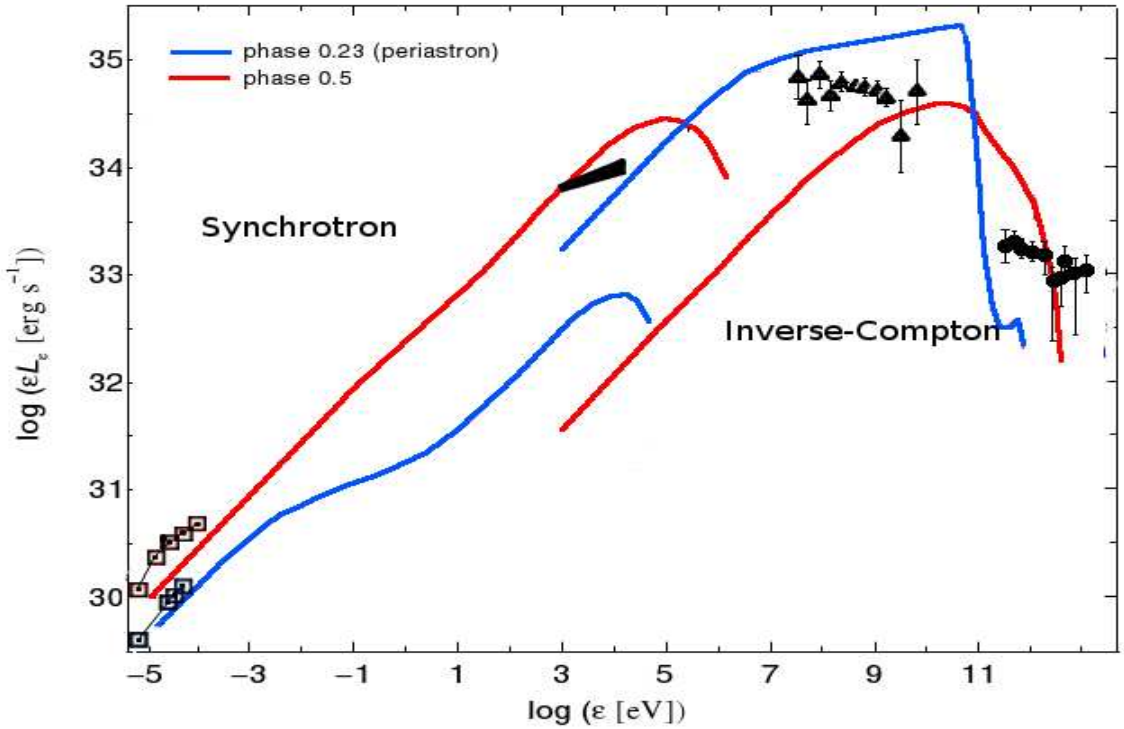


Figure 8.2: The spectral behavior predicted by the model of Bosch-Ramon et al. (2006b) for two separate regions of the orbital cycle. The TeV data is not well predicted.

band to the gamma-ray regime. TeV emission is strongly attenuated due to pair-production with local photons from the Be star, while GeV emission is elevated (not shown in figure 8.1) due to the increased IC channel. This prediction is consistent with the EGRET observational result (Tavani et al., 1998). The hard X-ray emission is still present at this accretion peak although not experiencing as strong of a flux amplification due to the primary mechanism of radiation (inverse-Compton) shifting to higher energy regimes. The model seemingly explains quite well the observational character of the system; however, the predicted differences in low versus high emission states in the X-ray band are several orders of magnitude larger than the differences seen in the X-ray and TeV data. In addition to this, the model predicts a level of TeV emission from periastron passage to $\phi = 0.5$, which if it were present, would have been detected by the TeV observations conducted by MAGIC and VERITAS. Although this could be a result of a relatively poor understanding of the fundamental parameters of the system (such as stellar wind and circumstellar disk density parameters, and effects related to the relative inclination between the compact object's orbit and the stellar wind/disk plane) the model still would fail to explain the presence of the secondary X-ray peak seen in the data. How well does this same model perform when computing the spectral parameters of the system? Shown in figure 8.2 is the model's prediction for the broadband spectral

energy distribution. This distribution is calculated in Bosch-Ramon et al. (2006b) for the two regions in the orbit with large accretion peaks ($\phi = 0.23, 0.5$) taking into account the effect of photon-photon absorption present at these two stages. The blue line, which represents the predicted spectrum during periastron passage, shows a strong shift towards inverse-Compton losses due to the enhanced ambient photon field close to the Be star. This same enhanced photon field, however, results in a strong attenuation of the TeV flux in this channel during periastron passage. During the later accretion peak at $\phi = 0.5$, the photon field from the Be star is smaller, resulting in a more efficient synchrotron loss channel, which lowers the TeV baseline emission. However, since the smaller ambient photon field at $\phi = 0.5$ results in little TeV attenuation, the overall TeV emission at this phase is greater than at periastron. Plotted over the model prediction in figure 8.2 are the observational data sets detailed in figure 7.15 for radio, X-ray, MeV, and TeV gamma-rays. The radio data (from VLA observations (Strickman et al., 1998)), shown during both quiescent and flaring states, agrees relatively well with the model prediction, although the actual flaring episode from the observational dataset occurred later than $\phi = 0.5$. The X-ray dataset shown is the combination of both the RXTE and Swift spectral results detailed in chapter 7 taken over a range of orbital phases. The overall flux level and spectral behavior is consistent with the model prediction. The EGRET spectrum (Tavani et al., 1998) corresponds to averaged values for different orbital periods, and could therefore be generally consistent with the average model prediction. The TeV spectrum taken from VERITAS data is not sufficiently predicted by this model however. It underpredicts the flux at > 10 TeV as well as predicting a much softer TeV spectrum than that observed by VERITAS.

As an alternative to the leptonic gamma-ray production mechanism (i.e. inverse-Compton scattering) invoked in most microquasar models for LS I +61 303, is the possibility that a hadronic mechanism could be at the root of the gamma-ray emission. Relativistic protons produced within the jet would interact via p-p collision with cold protons from the stellar wind producing GeV and TeV gamma-rays via the resulting pion decays (Romero et al., 2005; Bosch-Ramon et al., 2006; Orellana et al., 2006). By equating radiative losses to acceleration efficiency, the highest energy of a given accelerated particle population can be derived. Although protons are in general much less efficiently accelerated, their radiative losses are much less than an equivalently energetic population of electrons. Therefore, relativistic protons are able to be accelerated to higher energies and will thus result in harder TeV spectra than purely leptonic models. Thus, a hadronic mechanism could be invoked to explain the TeV spectrum observed by VERITAS which extends above 10 TeV (whereas typical leptonic models for LSI predict a spectral break occurring around a few TeV (Orellana et al., 2006)). However, such models rely heavily upon relatively poorly known proper-

ties of the system, (such as the magnetic field at the base of the jet) and currently such hadronic models (Orellana et al., 2006) overproduce TeV emission by an order of magnitude.

There has also been work done within the microquasar framework utilizing accretion processes which do not fall under the standard “Bondi-Hoyle” model. Through detailed three dimensional simulations of the system (Romero et al., 2007), the authors propose that the accretion disk viscosity is such that apparent \dot{M} changes, due to passage through regions of higher stellar wind density, occur over a much longer timescale than is expected through standard in-fall accretion. In other words, even though the compact object passes through a region of higher stellar wind density, the effective accretion rate does not appreciably change until a density wave can propagate through the accretion disk. In their model, the density wave resulting from periastron passage would not feed the jet until several days later, or around $\phi = 0.5$. This would explain both the lack of TeV emission near periastron (without invoking photo-absorption) as well as the presence of the TeV peak later in the orbit. However, at the time of writing, this model had not produced a TeV nor X-ray lightcurve with which to compare the available observational data.

8.2 Binary Pulsar Model

As described in chapter 4, the alternative to the microquasar scenario for this object relies on the assumption that the compact object is a young, energetic pulsar with spindown power on the order of $\sim 10^{35}$ ergs s^{-1} . This pulsar powers a relativistic wind of e^+/e^- pairs which stream away from the neutron star forming the “pulsar wind” with an energy of $\sim 10^{36}$ ergs s^{-1} . When this wind interacts with the Be star wind, a shock front will form which can accelerate electrons energies at which they will produce synchrotron X-ray radiation. These same electrons can up-scatter stellar photons to TeV energies. As the pulsar wind trails in the opposite direction of the shock, particles will cool via synchrotron processes resulting in a cometary tail of radio emission. Perhaps the strongest evidence for this model comes from Dhawan (2006) in which milli-arcsecond scale radio imaging of LS I +61 303 revealed what appeared to be the cometary tails of the pulsar wind being blown about in different directions over the orbital cycle. The emission properties of the shock acceleration between the two winds depend heavily upon the “standoff distance” R_s explained in Chapter 4, which is the distance between the pulsar and the shock front. As in chapter 4, $B \propto \frac{1}{R_s^2}$, therefore, as R_s changes this will alter the magnetic field near the shock front which then changes the overall emission properties. Near periastron where the stellar wind density is highest, R_s will be small which results in a higher magnetic field density, increasing synchrotron losses and decreasing the inverse-Compton losses, lowering the TeV emission component. Later in the orbit

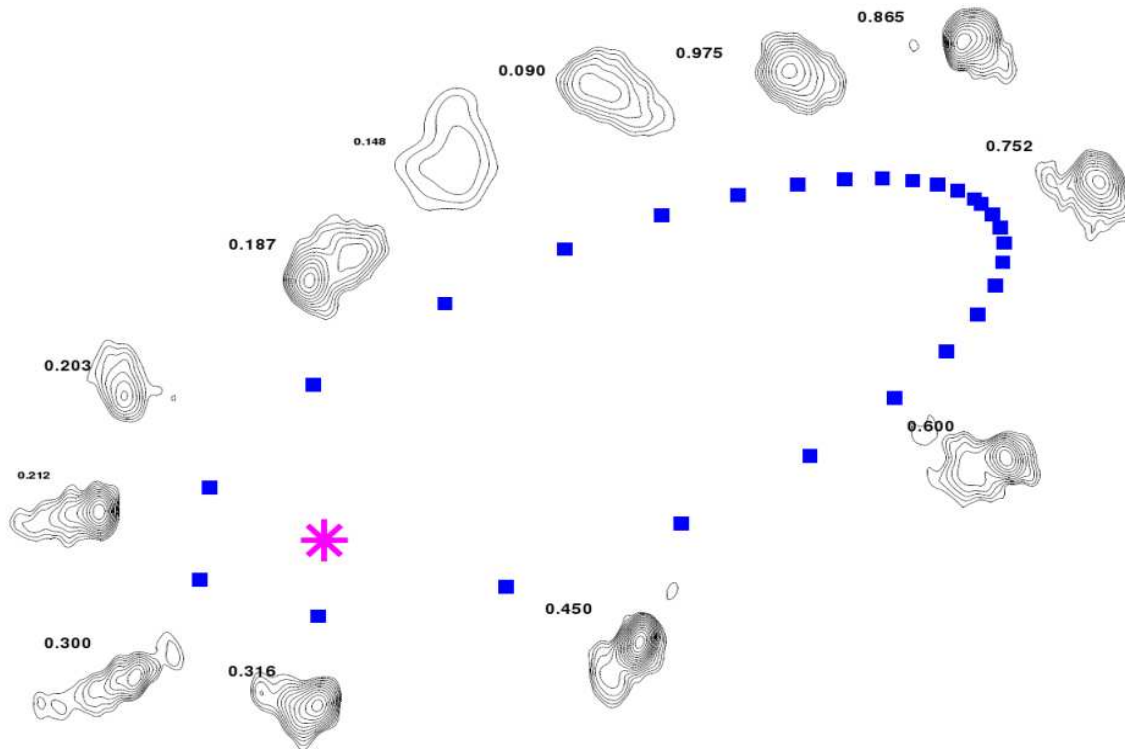


Figure 8.3: Milli-arcsecond scale radio imaging of LS I +61 303 during various orbital phases. The contours are interpreted as the appearance of the cometary tail of a pulsar wind as it is being blown in different directions by the Be solar wind. Taken from Dhawan (2006).

near apastron, the stellar wind is less dense, R_s is larger which consequently lowers the B field near the shock. This opens up the inverse-Compton loss channel increasing the TeV emission to observational levels. This model therefore successfully predicts the TeV peak near apastron and the lack of TeV emission near periastron. However, the amplification of synchrotron emission near periastron implies that the synchrotron emission should reach the keV scale, resulting in the hard X-ray peak of the system occurring near periastron. This stands in contradiction to the observed X-ray peak in the system occurring near orbital phases $\phi = 0.5 \rightarrow 0.7$.

The resulting broadband spectrum produced by this model is shown in figure 8.4 for computed spectra for both periastron (dashed lines) and apastron (solid lines). Plotted over this prediction are the same data as in figure 8.2. As can be seen, the predicted spectra agree relatively well with the radio data, closely modelling the appearance of outbursts in this band. The X-ray data are also predicted relatively well for the RXTE and Swift spectra averaged over the orbital cycle. The model also predicts the spectra observed by VERITAS to a reasonable degree of accuracy, unlike the microquasar model which predicts a cutoff after a few TeV. However, as can be seen, this model fails in its ability to predict the MeV flux reported by EGRET, underpredicting the flux by

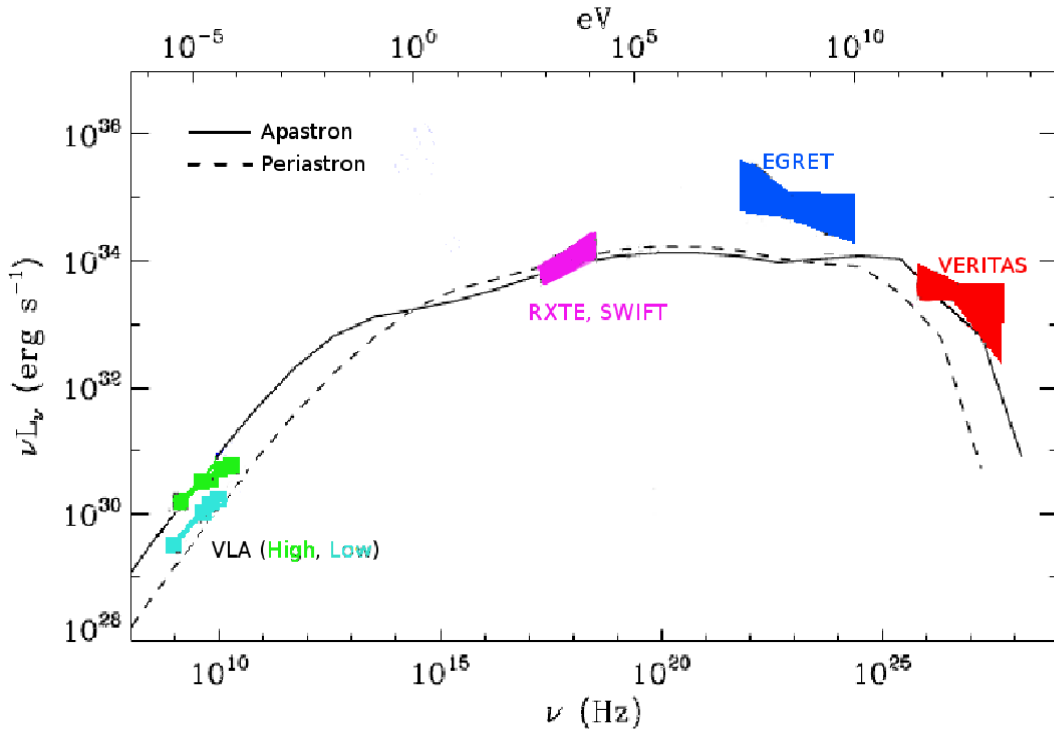


Figure 8.4: The broadband spectra arising from the model of Dubus (2006) compared to the same observational data as in figure 8.2

nearly an order of magnitude. At the same time, however, the EGRET data is notorious for large error boxes in source location and it is not entirely unfeasible that the EGRET flux for this source could be partially due to source confusion.

Where the binary pulsar model runs into trouble is in its fundamental inclusion of a pulsar: no evidence for either X-ray or radio pulsations have ever been detected in this system. This could be due to a suppression of the pulsed signal by interference from the dense Be star wind (Dubus, 2006), although it seems unlikely that total suppression of any pulsed radio signal would occur at all regions of the orbit. It has also been noted (Romero et al., 2007) that it is still an open debate as to whether or not the stellar wind would be strong enough to overcome the pulsar wind, resulting in the “blown-back” appearance of what is assumed to be the cometary tail of the pulsar wind (see figure 8.3). Despite both the relatively good agreement of the predictive models based upon the binary pulsar scenario, as well as the VLBA imaging result of Dhawan (2006), the identification of LS I +61 303 as a binary pulsar is still not decided.

8.3 Conclusion

Although both the microquasar and binary pulsar models satisfy some of the observational constraints, it is clear that in their current form neither completely describes all available observations accurately. On one hand the microquasar model gives a relatively accurate prediction of the rise time of both the X-ray and TeV emission (although the predicted orbital phase is around $\phi = 0.5$ for the model described in this text; one can imagine that by acceptably tweaking the parameters of the model, the prediction could feasibly get close to the peak observed by VERITAS at $\phi \sim 0.65$) and through invoking the likely process of pair production near the Be star manages to explain the lack of TeV emission near periastron passage. This model also gives a physically desirable analogy to AGN which are also detected at TeV energies and display analogous emission properties. This assumption of similarity with AGN (i.e. accretion/ejection based emission) is given credence by the detection of what appears to be bilateral relativistic jets in Merlin/GBI imaging (Massi et al., 2004). However, this model's inability to accurately describe the observed high energy spectrum is a severe shortcoming. This is in addition to the fact that there has never been any observational evidence of accretion occurring in this system (i.e. a thermal X-ray spectrum). Both of these detractions are severe and must be answered before the microquasar model can be lent credibility.

On the binary pulsar side, the ability to predict the high energy spectral behavior is relatively well developed. This is, of course, with the exception of the EGRET GeV data points, which, as mentioned above may not be the most accurate measurements. Despite this, the binary pulsar model's prediction of the TeV spectrum seems quite apt. Adding to this strength is the observations of Dhawan (2006) which can be reasonably interpreted as resulting from a pulsar wind scenario (see figure 8.3). However, it is also possible that the images shown in figure 8.3 could be due to a precessing jet and not a cometary pulsar wind. Such arguments have been raised in conjunction with the objection that it is unlikely that the energetic pulsar wind would be overcome by the slow equatorial wind of the Be star (Romero et al., 2007). As mentioned above, there is also the open issue of the lack of pulsations observed at any band in the system.

What is clear is that if either model accurately describes it, major adjustments must be made to the "standard" picture described by each one. For example (as was mentioned), in the microquasar model it is possible that the standard Bondi-Hoyle accretion model may have to be modified to a more complicated viscous accretion disk model through which the propagation of density waves is responsible for accretion changes and not simply just the infall of material (Romero et al., 2007). If a jet is indeed present in LS I +61 303 and it is responsible for the observed emission

8.3. CONCLUSION

properties, than the precession of such a jet would clearly alter the standard predictions of the emission properties of this system. Such jet precession has been seen in the microquasar SS 433 (Massi, 2005).

If the orbital plane is not exactly aligned with the plane of the stellar disk in LSI, this would also change the predicted behavior in each of these models. For example, in Dubus (2006) the author describes a situation where the orbital plane periodically dips in and out of the stellar wind plane which triggers the variability observed at high energies. If true, this scenario would also incorporate line of sight effects which could help to explain the absence/presence of emission in different bands, such as the presence of the secondary X-ray peak observed in Swift data (currently not explained in either model).

Chapter 9

Conclusions and Outlook

9.1 Overview

When this thesis work was begun, LS I +61 303 was an object of interest to the high energy astrophysics community due to its periodic outbursts in radio, X-ray, and GeV emission. Its properties as a high mass X-ray binary suited theoretical predictions of possible sites of TeV gamma-ray emission long before the initial TeV detection by the MAGIC collaboration (?). One of the fundamental unanswered questions about the system (then and now) was whether the system's high energy emission could be identified with the accretion/ejection processes in microquasars, or with the interaction between the wind of an energetic pulsar and the massive stellar companion. Both scenarios offer a viable configuration for the system that explains some, but not all the observational constraints. Since each scenario offers a slightly different prediction for the behavior in the non-thermal regime (radio, X-ray, gamma-ray) it is extremely useful to observe the system in as many wavelengths as possible at the same time in order to attempt to identify some correlation between emission in different bands. This correlation could then be used to rule out physical scenarios which may be taking place.

In the interest of full disclosure, at the beginning of this thesis work the initial goal was just to detect LS I +61 303 in TeV gamma rays, or alternatively place as strong a constraint as possible on its emission in the very high energy regime and not the full multiwavelength-wavelength approach that is detailed in this work. Working along these lines, the author petitioned for deep observations on LS I +61 303 using the Whipple 10 m telescope. These observations accrued over 50 hours on this target with no signs of TeV emission in either the full integrated data set or the data set binned by orbital phase, resulting in an upper limit on total emission from the system at the 6% Crab Nebula flux level above 540 GeV. The upper limits placed on emission in each individual bin are shown in table 5.1 and are in the 10% to 27% Crab Nebula flux range for the same energy

threshold. This was taken as an indication that the system might not, in fact, be a TeV emitter. However, with the benefit of hindsight it is clear that poor luck and a relatively high energy threshold (due to the large zenith angle of the observations) were at the root of the Whipple 10 m non-detection of the system. Contemporaneously to these observations, the MAGIC collaboration had been observing LS I +61 303 during the same time with their telescope with a lower energy threshold of 200 GeV. This, combined with the fact that the TeV emission in LSI is variable (that year apparently only occurring during orbital phases 0.4→0.7, peaking near orbital phase 0.5) and the Whipple observations did not cover these orbital phases with the depth needed to detect the source mostly due to poor observing conditions during the peak emission periods. On the one hand it is unfortunate that the Whipple observations did not have the sensitivity during peak emission phases to detect the source; but on the other hand without the MAGIC detection the source would have most likely been considered inactive in the TeV regime and not granted observations with the much more sensitive VERITAS array. However, due to the MAGIC detection, the impetus for VERITAS observations was obvious: with the greater sensitivity of VERITAS, our observations could either confirm the detection or be able to refute it with a great deal of confidence. VERITAS observations were therefore carried out from September, 2006 to February, 2007. Fortunately (in the frame of reference of this thesis!), the source was indeed confirmed by VERITAS observations showing strong (15% Crab Nebula flux at times), variable (occurring only during orbital phases 0.5-0.8) TeV emission from this source. It should be noted that this was the first detection of a “new” source by the VERITAS array and its analysis using the (still evolving) standard VERITAS data analysis package, VEGAS, served as a test-bed for the analysis methods which will no doubt be employed extensively over the years to come as VERITAS detects more and more sources.

In the TeV band the source is highly variable apparently showing the strongest emission always near phases $\phi = 0.6 \rightarrow 0.7$. The question of whether or not the peak of emission is located at the same orbital phase is still open. Although the total dataset (binned by 0.05ϕ - see figure 6.10) shows a clear peak at phase 0.67, the sampling of the data is not sufficient to rule out any variation over the timescale of several months in the peak emission location. This is demonstrated by the apparent variation in peak location of each months’ data (see figure 6.10). This could be a sampling effect or real feature of the data. The confirmation (or rejection) of the peak emission location during each cycle is an important observational feature which may help to shed some light on the nature of LS I +61 303 (i.e. microquasar or binary pulsar, see below).

The initial excitement over the detection of LS I +61 303 with VERITAS was such that it warranted the request of target-of-opportunity observations in the X-ray regime with orbiting satellites and this thesis work became a multiwavelength study. Past multiwavelength observations in

the TeV/X-ray band of AGN had yielded interesting results and emission models for LS I +61 303 predicted that there should be some X-ray counterpart to whatever acceleration process was producing the TeV emission. With this in mind, along with Professor Phil Kaaret from the University of Iowa, the author submitted a successful target-of-opportunity request for observations with RXTE (chapter 7) of LS I +61 303 in the 2-10 keV band, every other night for 10 nights in October 2006. These observations covered the (assumed) active phases of LS I +61 303 and an appreciable increase in X-ray activity was detected over the same time scale as the observed TeV emission development detected by VERITAS. In addition to this, observations by the Swift X-ray satellite were being conducted in September and again in November and December 2006. These observations also showed a direct correlation between X-ray flux levels and orbital phase with a peak flux level occurring nearly every cycle during 0.6→0.8, similar to the RXTE results. The Swift data also showed evidence for a secondary X-ray peak near orbital phase 0.0→0.1, a region which RXTE did not observe and our ToO observations therefore could neither confirm nor deny this secondary peak. However, a re-examination of archival X-ray data taken with RXTE and XMM shows evidence for the presence of this secondary peak. By “aligning” the X-ray light curves in section 7.5, it is shown that there is qualitative (albeit statistically weak) evidence that there is indeed a secondary peak in the X-ray data. A correlation test performed on the X-ray data taken in 2006 also shows evidence (again, albeit statistically weak) for periodic behavior. If both of these conjectures are proven by future observations, this would indicate that the X-ray emission in the system is periodic but shifting slightly each orbit. This is obviously an open issue that needs investigation by further observations in the X-ray band.

By comparing the X-ray and TeV lightcurves (see chapter 7) it is seen that there is some evidence for correlation between emission in these two bands. This correlation, however, is not possible to statistically prove at this time due to the sparse and uneven data sampling in the TeV band. The TeV dataset described here does not include data during orbital phases $\phi = 0.0 \rightarrow 0.1$ and therefore can neither confirm nor refute the presence of TeV emission during the same orbital phases as the apparent secondary X-ray peak. This sampling of the later orbital phases is the principal motivation for continued TeV observations.

The models put forth for describing the system as either a microquasar or binary pulsar have been examined and compared to the observational data set. At this time it appears that both the standard pictures arising from the microquasar model of Bosch-Ramon et al. (2006b) as well as from the binary pulsar model of Dubus (2006) both fail in their ability to accurately predict all the emission features present in the system. The microquasar model appears to be able to predict (to within 0.1ϕ or so) the rise time of both X-ray and TeV emission, although the spectral

predictions do not agree with the observations detailed in this work. In the case of the binary pulsar model, the spectral predictions seem to agree relatively well (with the exception of the slightly unreliable EGRET GeV data) with the observations, but the prediction given in the model for X-ray maximum near periastron stands in direct contradiction to the observations. Although the current observations cannot strongly refute or confirm either model, it is clear that if either one is to provide an accurate description of what is occurring in LS I +61 303, they must be appreciably modified in order to take into account more complex phenomena.

9.2 Unresolved Issues

There are several outstanding issues revolving around LS I +61 303 that need resolving before the behavior of the system can be acceptably understood.

- **TeV Flux Maximum Location:** It is important to understand whether or not the TeV flux maximum occurs at the same orbital phase every orbital phase. As was previously stated, although there appears to be a relatively stable location of the peak flux location, there is also an indication that the location of the peak flux may change over timescales of a few months or years. The MAGIC observations in 2005/6 show the peak flux level occurring at $\phi = 0.5 \rightarrow 0.6$ whereas the VERITAS observations clearly show that the averaged peak for 2006/2007 occurred between $\phi = 0.6 \rightarrow 0.7$. The month to month behavior in the TeV band from VERITAS observations also seems to show some evidence for the movement of the peak flux location. However, both of these effects could be entirely due to poor and unevenly sampled TeV data. Further, more detailed observations are needed to examine this issue. It has been proposed to remedy some of the inconsistencies of the binary pulsar model by proposing that the pulsar orbit is inclined with respect to the plane of the stellar wind. If this is the case then it implies that the maximum emission phase should be a definite geometrical location at the same place in every orbit. Observations confirming that the TeV flux peak is changing every orbit, or over the course of a few orbital cycles, would therefore rule out this modification to the binary pulsar model and weaken the overall general ability of the binary pulsar scenario to describe LS I +61 303.
- **Full Orbit TeV Observations:** Due to the similarity of the orbital period of the system and the duration of the lunar cycle, observations of LS I +61 303 with ground based Cherenkov telescopes are limited to a set window of the orbit every year. The upper limit placed on emission between $\phi = 0.2 \rightarrow 0.3$ is not very constraining (13.67% Crab Nebula flux) and this work contains no data between orbital phases 0.9 \rightarrow 0.2. These observations of the later

phases of the orbit are especially important in light of the apparent secondary maximum in X-ray flux shown in the Swift data. If there is indeed a secondary TeV flux located at later orbital phases, this would significantly alter all models for emission from this system.

- **Multiwavelength Correlation:** A more cohesive picture is needed of how non-thermal emission in various bands evolves. Although this thesis work has attempted to provide this, a more in-depth study utilizing contemporaneous X-ray, GeV, TeV, as well as radio observations is desirable. To date, the only broadband spectrum available covering the entire energy range of interest is composed of data in different bands which were taken at different epochs (i.e. the radio data shown in figures 8.2 and 8.4 was taken several years before the other bands, and the GeV spectrum is not considered totally reliable). A coordinated multiwavelength survey in all of the important wavebands would be a very effective tool with which to derive the relative rise times of emission in these non-thermal energy ranges. Providing evidence for correlation (or lack thereof) between high energy emission in different bands is the key to constraining emission models for LS I +61 303.

To attempt to satisfy some of the above issues, further TeV observations on LS I +61 303 have been conducted in 2007 with the full 4 telescope VERITAS array. At the time of writing, a further 14 hours had been taken in October and November 2007 covering orbital phases $0.3 \rightarrow 0.0$, $0.0 \rightarrow 0.1$. In addition to this, Phil Kaaret and the author were successful in obtaining observational time on RXTE for 1 ks pointed observations every other night from September 2007 until February 2008. The overlap between these two observations will provide a similar data set to the current work and increase the range of its observational coverage. For the first time, the orbital phases of $0.9 \rightarrow 0.1$ will be covered simultaneously by TeV and X-ray observations providing a window into the relationship between high energy emission bands in this orbital range.

Additionally, the launch of the GLAST satellite in 2008 will provide an unprecedented window on the GeV range gamma-ray sky. This telescope will provide an ideal platform with which to study the low energy gamma-ray properties of LS I +61 303. This is an important window for this source as the only available observations come from the EGRET dataset which is now considered to be less than totally accurate. The LAT instrument aboard GLAST (see section 1.1.5) will have a sensitivity of roughly an order of magnitude greater than EGRET in the energy range of 20 MeV to 300 GeV. With superior energy resolution to EGRET, GLAST will be able to refine the MeV-GeV spectrum derived by EGRET, nearly connecting it to the TeV spectrum derived from VERITAS observations. In addition,

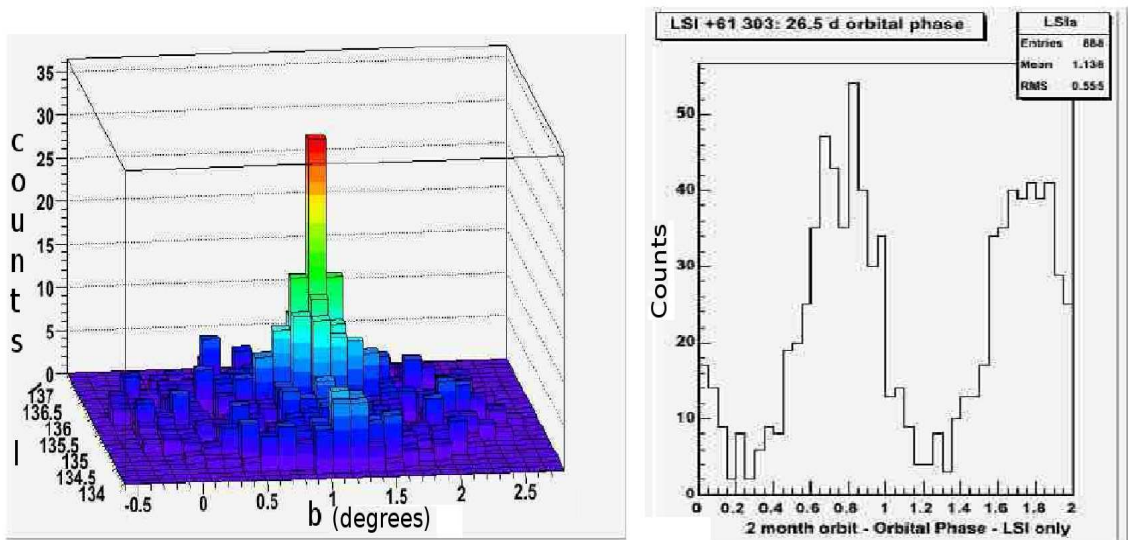


Figure 9.1: The simulated response of the LAT instrument aboard GLAST to 55 hours of exposure on LS I +61 303. The source is readily detected above the background (left) and its gamma-ray periodicity derived accurately to the day timescale. Taken from Dubois (2006).

GLAST will be able to accurately derive the variability in the MeV-GeV emission. Shown in figure 9.1 is a simulation of the LAT instrument's response to LS I +61 303 over 55 days of live LAT observation time. The LAT response was simulated given the observed EGRET spectrum and periodicity. As can be seen the source will be readily isolated against the relatively weak background in the region (Dubois, 2006) and is readily detectable by GLAST. The simulation of the gamma-ray periodicity is shown in the right hand side of figure 9.1. The refined accuracy of the periodicity will be an invaluable tool with which to refine statements of emission correlation between high energy emission bands.

The next decade will see a new multiwavelength window on the universe opening up, shedding new light on the most extreme and violent physical processes in the universe. This window will be provided by experiments probing the non-thermal cosmos at an unprecedented sensitivity; utilizing X-ray monitoring with space-based instruments (such as RXTE or Swift), the unprecedented sensitivity of GLAST, and the ever-improving ground-based TeV observational techniques demonstrated by the VERITAS array. Enigmatic sources such as LS I +61 303, which today provide a great deal of confusion and uncertainty, may in the future be looked upon as prototypical examples of objects that are only understood through the use of these new cutting edge observational tools. The future is indeed bright for high-energy astronomy!

Bibliography

Abdo, A.A. et al., 2007; ApJ Let. 658, L33.

Abdo, A.A. et al., 2007; ApJ 658, L33.

Abraham, J. et al., 2004; Nuc. Inst. and Meth., A523

Aharonian, F. et al., 2002; A&A 393, L37.

Aharonian, F. et al., 2003; A&A, 403, L1.

Aharonian, F. et al., 2004; Nature, 432, 75.

Aharonian, F. et al. 2004; A&A 425, L13.

Aharonian, F. et al. 2004; ApJ, 614, 897.

Aharonian, F. et al., 2005; Apj, 636, 777.

Aharonian, F. et al., 2005; A&A, 435, L17.

Aharonian, F. et al., 2005; A&A, 442, 1.

Aharonian, F. et al., 2005; Science, 309, 746.

Aharonian, F. et al., 2005; A&A, 442, 177.

Aharonian, F. et al., 2006; A&A, 448, 2, L19.

Aharonian, F. et al., 2006; Nature, 439, 695.

Aharonian, F. et al., 2006; A&A, 457, 3, 899.

Aharonian, F. et al., 2006; A&A, 460, 743.

Aharonian, F. et al., 2007; ApJ, 661, 236.

Albert, J. et al, 2006; ApJ, 642, L119.

BIBLIOGRAPHY

- Albert, J. et al, 2006; Science, 312, 1771.
- Albert et al., 2006; ApJ Letters 648, L105 - 108
- Albert, J. et al, 2007; Submitted to Apj, arxiv.org/abs/0705.3244
- Alexander,T., 1997; in *Astronomical Time Series*, eds. D. Maoz, A. Sternberg and E.M. Leibowitz, Kluwer, Dordrecht, p. 163.
- Amenomori, M. et al., 2007; Ap&SS,309, 1-4, 435.
- Arnaud, K.A., 1996 ;Astronomical Data Analysis Software and Systems V, eds. Jacoby G. and Barnes J., p17, ASP Conf. Series volume 101.
- Arqueros, F. et al., 2001; in Proc. of 27th International Cosmic Ray Conference, Hamburg, GE.
- Bacci, C. et al., 2002; Astropart. Phys.,17, 2,151.
- Badran, H.M. and Weekes, T.C., 2004; NIMA, 524, 1, 162.
- Baixeras et al., 2005; in Proc. International Cosmic Ray Conference, Pune, India, 227.
- Barwick, S. et al., 2002; in Proc. of SPIE Conference, Hawaii, 2002.
- Bastieri, D. et al., 2007; in Proc. of 30th International Cosmic Ray Conference, Merida, MX.
- Beilecke, M. et al., 2005; in Proc. of the XXII Texas Symposium on Relativistic Astrophysics.
- Beilecke, M., 2007; VERITAS Collaboration Internal Note
- Belloni, T. et al., 1997; ApJ, 479, L145.
- Berge, D., Funk, S, and Hinton, J. 2006; A&A, 466, 1219.
- Bergstom, L. et al., 1998; Astropart. Phys., 9, 137.
- Bernlohr et al., 2003; Astropart. Phys., 20, 111.
- Bignami, G.F.B. et al., 1981; ApJ, 247, L85;
- Blackett, P.M.S., 1948; Rep. Conf. Gassiot Comm. Phys. Soc., Physical Society, 34.
- Blandford, R.D. and Rees, M.J., 1978; Proc. of Pittsburgh Conference on BL Lac Objects, 328.
- Borione, A. et al., 1992; ApJ, 397, 148.
- Bosch-Ramon, V.. et al., 2005; ApJ, 628, 388.
-

BIBLIOGRAPHY

- Bosch-Ramon, V. et al., 2006; astro-ph/0605489.
- Bosch-Ramon, V. et al., 2006; A&A, 459, L25.
- Bradbury, S., 1999; in Proc. of 26th International Cosmic Ray Conference, Salt Lake City, UT.
- Buckley, J., 1999; in Proc. of 26th International Cosmic Ray Conference, Salt Lake City, UT.
- Carter-Lewis, D.A. ,1990; Exper. Astron., 1, 173.
- Casares, J. et al., 2005; MNRAS, 364, 899.
- Casares, J. et al., 2005; MNRAS, 360, 1105.
- Cassiday, G.L. et al., 1989; Phys. Rev. Lett. 62, 4, 383.
- Catanese, M. and Weekes, T., 1999; Pub. of the Astr. Soc. of the Pacific, 111, 1193.
- Cawley, M.F., 1993; *Towards a Major Atmospheric Cherenkov Detector II*, p176.
- Cherenkov, 1934; C.R. Ac. Sci. U.S.S.R., 8, 451.
- Chadwick, P. et al. 1985; Nature, 318, 642.
- Chernyakova, M. et al., 2006; MNRAS, 372, 1585.
- Chudakov, A.E. et al., 1965; Transl. Consultants Bureau, P.N. Lebedev Phys. Inst., 26, 99.
- Clark, G.W., Garmite, G.P., Kraushaar, W.L. 1968; ApJ, 153, 203.
- Cogan, P., 2006; Ph.D. Dissertation, University College Dublin, Dublin, IE.
- Colin, P. et al., 2007; in Proc. of 30th International Cosmic Ray Conference, Merida, MX.
- Cominsky, L. et al., 1994; ApJ, 427, 978.
- Connors, T.W. et al., 2002; MNRAS, 336, 1201.
- Coppi, P.S., 2000; in ASP Conf. Ser. 161: *High Energy Processes in Accreting Black Holes*, eds. J. Poutanen and R. Svensson
- Cortina, J, 2005; in Proc. International Cosmic Ray Conference, Pune, India, 259.
- Costa, E. et al., 1997; Nature, 387, 783.
- Daniel, M. et al., 2007; in Proc. of 30th International Cosmic Ray Conference, Merida, MX.
-

BIBLIOGRAPHY

- Dar, A. and Laor, A., 1997; A&A, 478, L5.
- Daum, A., 1997; Astropart. Phys., 8, 1.
- Daum, A., 1997; Astroparticle Physics 8, 1.
- Davies, J.M. and Cotton, E.S., 1957; Journal of Solar Energy, Science, and Engineering, 1(2), 16.
- de la Calle Perez, I., 2002; Ph.D. Dissertation, University of Leeds, Leeds, UK.
- Dermer, C. et al., 1992; A&A, 256, L27.
- Dhawan, V. et al., 2006; in Proc. of Microquasars and Beyond: from binaries to galaxies, Como, IT
- Druy, L O'C., 1983; Rep. Prog.Phys., 46, 973.
- Dubois, R., 2006; in Proce. of VI Microquasar Workshop: Microquasars and Beyond, Como IT
- Dubus, G., 2006; A&A, 456, 801 astro-ph/0605287.
- Dwek, E. and Krennrich, F., 2005; ApJ, 618,657.
- Enomoto, R. 2006; ApJ, 638, 397.
- Fazio, G.G. et al., 1968; Canadian Journal of Physics, 46, 451.
- Fegan, S., 2004; Ph.D. Dissertation, University of Arizona, Tucson, AZ.
- Fender, R. et al., 1999; ApJ, 519, L165.
- Fender, R. et al., 2002; MNRAS, 330, 212.
- Fender, R., 2001, To appear in "Relativistic flows in Astrophysics", Springer Verlag Lecture Notes in Physics, Eds A.W. Guthmann, M. Georganopoulos, K. Manolakou and A. Marcowith, astro-ph/0109502
- Fender, R., 2004; in *Compact Stellar X-Ray Sources*, eds. W.H.G. Lewin and M. van der Klis, Cambridge University Press, Cambridge, UK.
- Fichtel, C.E. 1975; ApJ 198, 163.
- Fisher, R.A., 1921; Metron. 1, 4, 1.
- Fortin, P. et al., 2007; in Proc. of 30th International Cosmic Ray Conference, Merida, MX.
-

BIBLIOGRAPHY

- Frank and Tamm, 1937; C.R. Ac. Sci. U.S.S.R., 14, 109.
- Fruin, J.H. et al., 1964; Phys. Lett., 2, 176.
- Gaensler, B. et al. 2006; astro-ph/0601304.
- Galbraith, W. and Jelley, J.V. 1953; Nature, 171, 349.
- Galbraith, W. and Jelley, J.V. 1955; Atmos. Physics, 6, 304.
- Gammell, S. 2004; Ph.D. Dissertation, University College Dublin, Dublin, Ireland
- Gehrels, N. et al., 2004; ApJ, 611, 2, 1005.
- Ghisselini, G., 1999; Astropart. Phys., 11, 11.
- Giacconi, R. et al., 1967; ApJ, 148, L119.
- Giebels, B. et al., 1998; Nuc. Inst. Meth., 412, 329.
- Goldoni, P. and Mereghetti, S., 1995; A&A, 299, 751;
- Gould, R.J. 1965; Phys. Rev. Lett., 15, 577.
- Gregory, P. C. et al. 1972; Nature 239, 114 (1972)
- Gregory, P.C. and Taylor, A.R., 1978; Nature, 272, 704.
- Gregory, P.C., 2002; Apj, 525, 427;
- Greiner, J. and Rau, A., 2001; A&A, 375, 145.
- Grube, J. et al., 2007; in Proc. of 30th International Cosmic Ray Conference, Merida, MX.
- Grube, J., 2007; Ph.D. Dissertation, University of Leeds, Leeds, UK.
- Grove, J.E. et al., 1995; ApJ, 447, L113.
- Gupta, S.K. et al., 2005; Nuc. Inst. Meth. in Phys. Res. A, 540, 311-323.
- Hall, T.A. et al., 2003; ApJ, 583, 853.
- Hanna, D., 2007; in Proc. of 30th International Cosmic Ray Conference, Merida, MX.
- Harrison, F.A. et al., 2000; ApJ, 528, 454.
- Hartmann, R.C., 1979; ApJ 230, 597.

BIBLIOGRAPHY

- Hartman, R.C., 1999; ApJS, 123, 79.
- Helene, O., 1983; Nuc. Inst. and Meth., 212, 319.
- Hermesen, W. et al., 1977; Nature, 269, 494.
- Hill, J. SPIE 5165 217, 2004
- Hillas, A.M., 1985; in NASA Goddard Space Flight Center 19th Intern. Cosmic Ray Conf. Vol. 3, 445.
- Hillas, A.M. et al., 1998; ApJ, 503, 744.
- Holder, J. et al., 2005; in Proc. 29th International Cosmic Ray Conference, Pune, India.
- Holder, J. et al., 2006; Astropart.Phys. 25, 391.
- Holder, J. et al., 2007; in Proc. of 30th International Cosmic Ray Conference, Merida, MX.
- Horan, D. et al., 2007; ApJ, 665, 396.
- Horan, D., 2001; Ph.D. Dissertation, University College Dublin, Ireland.
- Horns, D. et al; Journal of Physics Conference Series; 60, 135-138, 2007
- Horns, D. et al., 2007; to be published in Advances in Space Research, COSPAR meeting Beijing, 2006.
- Humensky, B. et al., 2007; in Proc. of 30th International Cosmic Ray Conference, Merida, MX.
- Humensky, B., 2005; in Proc. 29th International Cosmic Ray Conference, Pune, India.
- Hutchings, J.D. and Crampton, D., 1981; PASP, 93, 486.
- Itoh, C. et al., 2003; ApJ, 584, L65.
- Jahoda, K., 2006; ApJS, 163, 401.
- Jelley, J.V. and Galbraith, W. 1955; Atmos. Physics, 6, 250.
- Jelley, J., 1958; *Cerenkov Radiation And Its Applications* Pergamon Press.
- Johnson, W.N. et al., 1993; ApJ Suppl., 86, 693.
- Johnston, S. et al., 1992; ApJ Lett., 387, L37.
- Johnston, S. et al., 1999; MNRAS, 302, 277.
-

BIBLIOGRAPHY

- Johnston, S. et al., 2005; MNRAS, 358, 1069.
- Kaspi, V.M. et al., 1995; ApJ, 453, 424.
- Kieda, D., 2003; in the Proceedings of the 28th International Cosmic Ray Conference, Tsukuba, Japan.
- Kildea, J., 2007; Astropart. Phys. 282, 2, 182.
- Kirk, J.G. et al., 2007; to be Published in Springer Lecture Notes on *Neutron stars and pulsars, 40 years after the discovery*.
- Kniffen, D.A. et al., 1997; ApJ, 486, 126.
- Koide, S. et al., 2000; ApJ, 536, 668.
- Konopelko, A. et al. 2007; ApJ 658, 1062.
- Kosack, K. et al., 2004; ApJ 608, L97.
- Kosack, K. 2005; Ph.D. Dissertation, Washington University St. Louis, St. Louis, MO.
- Kraushaar, W. et al. 1965; ApJ, 141, 845.
- Lamb, R.C. et al., 1977; ApJ, 212, L63.
- Leahy, D.A. et al., 1997; ApJ, 475, 823.
- LeBohec, S. et al., 2003; in the Proceedings of the 28th International Cosmic Ray Conference, Tsukuba, Japan.
- Lemoine-Goumard, M. et al., 2005; SF2A-2005: Semaine de l’Astrophysique Francaise, Strasbourg, France published in EdP-Sciences Conference Series, p 459.
- Li, T.P. and Ma, Y.Q, 1983; ApJ, 272, 317.
- Liu, Q.Z and van Paradijs, E.P., 2006; A&A, 455, 1165.
- Lloyd-Evans, J. et al., 1983; Nature, 305, 784.
- Longair, M.S., 1994; *High Energy Astrophysics, Volume 2: Stars, the Galaxy, and the Interstellar Medium*, Cambridge University Press, Cambridge, UK.
- Lorimer, D.R., 2001; *Binary and Millisecond Pulsars at the New Millennium*, Living Rev. Relativity 4
-

BIBLIOGRAPHY

- Lynne, A.G. and Graham-Smith, F., 1998; *Pulsar Astronomy* Cambridge University Press, Cambridge, UK.
- Maier, G. 2006, Internal VERITAS collaboration memorandum.
- Maier, G. et al, 2007; In Proc. of 30th International Cosmic Ray Conference, Merida, MX.
- Maier, G. et al., 2007; In Proc. of 30th International Cosmic Ray Conference, Merida, MX.
- Maraschi, L. et al., 1981; ApJ, 248, 1010.
- Maraschi, L. and Treves, A., 1981; MNRAS, 194, 1;
- Maraschi, L. et al., 1992; ApJ, 397, L5.
- Marscher, A.P., 1999; Astropart. Phys, 11, 19.
- Marti, J. and Paredes, J.M., 1995; A&A, 298, 151.
- Massi, M. et al., 2001; A&A, 376, 217.
- Massi, M. et al., 2004; A&A, 414, L1.
- Massi, M., 2004; A&A, 422, 267.
- Massi, M., 2005; Habilitation Thesis, University of Bonn, arXiv:astro-ph/0506731v1.
- Masterson, C., 2001; AIPC Conference Proceedings: High Energy Gamma-Ray Astronomy, 558, 752.
- Mattox, J.R. et al., 1996; Memorie della Societe Astronomica Italia, 67, 607.
- McClintock, J.E. and Remillard, R.A., 2004; *Compact Stellar X-ray Sources* eds. W.H.G. Lewin and M. van der Klis, Cambridge University Press, Cambridge, UK.
- McCullough, M. 2007; Personal Communication.
- Mendelson, H. and Mazeh, T., 1989; MNRAS, 239, 733.
- Mirabel, F., 2006; Science, 312, 5781, 1759.
- Mitsuda, K., 1984; PASJ, 36, 741.
- Mohanty, G., 1998; Astropart. Phys., 9, 15.
- Mori, M., 1997; ApJ 476, 842.
-

BIBLIOGRAPHY

- Motch, C. et al., 1997; A&A 323, 853.
- Murata, K. et al., 2003; Publ.Astron.Soc.Jap. 55, 473
- Nagai, T., 2004; Ph.D. Dissertation, University of Utah.
- Neronov, A. and Chernyakova, M., 2007; submitted to MNRAS, astro-ph/701144
- Nikishov, A., 1962; Journal of Experimental and Theoretical Physics, 14, 393.
- O’Flaherty, K.S. et al., 1990; in Proc. of 21st International Cosmic Ray Conference, Adelaide, AU, 2, 2.
- Omodei, N. et al., 2006; Proc. of the 16th Annual October Astrophysics Conference in Maryland: Gamma Ray Bursts in the Swift Era.
- Ong, R. et al., 1991; in Proc. of the 22nd International Cosmic Ray Conference, Dublin, IE.
- Orellana, M. et al., 2006; accepted for publication in Astrophysics and Space Science, astro-ph/0608707.
- Padovani, P. and Giommi, P, 1995; ApJ, 444, 567.
- Paneque, D. et al., 2004; Nuc. Inst. and Methods in Phys. Res. 518, 619.
- Paredes, J.M. et al., 1997; A&A, 320, L25.
- Paredes, J.M. et al., 1998; A&A, 335, 539.
- Paredes, J.M. et al., 2000; Science, 288, 5475, 2340.
- Paredes, J.M. et al., 2002; A&A, 393, L99.
- Paredes, J.M. et al., 2007; ApJ Lett., 664, 1, 39.
- Parsignault, D.R. et al., 1976; ApJ, 209, L73.
- Pohl, M. and Shlickeiser, R., 2000; A&A, 354, 395.
- Punch, M. et al., 1992; Nature, 358, 477.
- Punsly, B., 1999; ApJ, 519, 336.
- Quinn, J. et al., 1996; ApJ, 456, L83.
- Raue, M. and Mazin,D; astro-ph/0802.0129.
-

BIBLIOGRAPHY

- Reynolds, P.T. et al., 1993; ApJ, 404, 206.
- Roache, E. et al., 2007; in Proc. of 30th International Cosmic Ray Conference, Merida, MX.
- Romero, G.E. et al., 2003; A&A, 410, L1.
- Romero, G.E. et al., 2005; ApJ, 632, 1093.
- Romero, G.E. et al., 2007; A&A, 474, 15.
- Samorsky, M. and Stamm, W., 1983; ApJ, 268, L17.
- Schmidt, F., "CORSIKA Shower Images", <http://www.ast.leeds.ac.uk/fs/showerimages.html>.
- Schoenfelder, V. et al., 1982; In Proc. of 17th International Cosmic Ray Conference, Paris, FR, 9, 295.
- Schroedter, M., 2004; Ph.D. Dissertation, University of Arizona, Tucson, AZ.
- Shakura, N.I. and Sunyaev, R.A., 1973; A&A, 24, 337.
- Shaw, S.E. et al., 2004; A&A, 426, L33.
- Sidoli, L. et al., 2006; A&A, 459, 901.
- Sikora, M. and Madejski, G., 2001; in AIP Conf. Proc: High Energy Gamma-Ray Astronomy.
- Sinnis, G., 2005; AIP Conf. Proc 745: High Energy Gamma-Ray Astronomy, 234.
- Smith, A. et al., 2007; Astrophys.Space Sci., 309, 299.
- Smith, A. et al., 2007; in Proc. of 30th International Cosmic Ray Conference, Merida, MX.
- Stark, M.J. and Saia, M., 2003; ApJ, 57, L101.
- Stecker, F. and deJager, O.C., 1998; A&A, 334, L85.
- Stellingwerf, R.F., 1978; ApJ, 224, 953.
- Stepanian, A.A. et al., 1975; Ap. Space Sci., 38, 267.
- Strickman, M.S., 1998; ApJ, 497, 419.
- Sullivan, G. et al., 2001; in Proc. of 27th International Cosmic Ray Conference, Hamburg, GE.
- Swanenburg, B.N. et al 1981; ApJ, 243, L69.

BIBLIOGRAPHY

- Swank, J.H., 1994; in American Astronomical Society Meeting, 185, 6701.
- Tanaka, Y., 1997; *Accretion Disks-New Aspects* eds. E. Meyer-Hofmeister, H. Spruits, Springer-Verlag Press, New York, 1.
- Tavani, M. et al., 1998; ApJ, 497, L81.
- Tavani, M. et al., 1994; ApJ, 433, L37.
- Tavani, M and Arons, J., 1997; ApJ, 477, 439.
- Taylor, A.R. et al., 1992; ApJ, 395, 268.
- Taylor, A.R. et al., 1996; A&A, 305, 817.
- Taylor, A.R. and Gregory, P.C., 1980; IAU Circ. no 364.
- Taylor, A.R. and Gregory, P.C., 1982; ApJ, 255, 210.
- Taylor, A.R. and Gregory, P.C., 1984; ApJ, 283, 273.
- Teshima, M. et al., 2007; In Proc. of 30th International Cosmic Ray Conference, Merida, MX.
- Thompson, D.J. et al., 1995; ApJS 101, 259.
- Thuczycont, M. et al., 2005; in Proc. 29th International Cosmic Ray Conference, Pune, India, 101.
- Toner, J., 2007; in Proc. of 30th International Cosmic Ray Conference, Merida, MX.
- Tschuchiya, K. et al., 2004; ApJ 606 L115.
- Tudose, V. et al., 2007; MNRAS, 375, 1, L11.
- van der Laan, H., 1966; Nature, 211, 1131.
- van Dijk, R. et al., 1994; in *The Evolution of X-ray Binaries* AIP Press, New York, NY, 324.
- Vassiliev, V., 1999; Astropart. Phys, 12, 17.
- Vassiliev, V., 2003; in the Proceedings of the 28th International Cosmic Ray Conference, Tsukuba, Japan.
- Vincent, P. , 2005; in Proc. 29th International Cosmic Ray Conference, Pune, India, 163.
- Weekes, T.C. and Turver, K.E., 1977; ESA Recent Advan. in Gamma-Ray Astronomy 279.
- Weekes, T.C., 1988; Phys. Rev. Rep., 160, 1.
-

BIBLIOGRAPHY

Weekes, T.C., 1989; ApJ, 342, 379.

Weekes, T.C., 1999; in *GeV-TeV Gamma-Ray Astrophysics Workshop, Towards a Major Atmospheric Cherenkov Detector VI*, eds. Dingus, Salamon, Kieda, 515,3.

Weekes, T.C., 2003; *Very High Energy Gamma-Ray Astronomy*, Institute of Physics, Bristol.

Weekes, T.C., 2006; To be published in the *Proceedings of the International Workshop on "Energy Budget in the High Energy Universe"*, Kashiwa, Japan.

Weinstein, A., 2007; in Proc. of 30th International Cosmic Ray Conference, Merida, MX.

White, R.J., 2007; Ph.D. Dissertation, University of Leeds, Leeds, UK.

Williams, D.A. et al., 2000; Proc. of the Heidelberg Symposium on High-Energy Gamma-Ray Astronomy.

Winkler, C. et al., 2003; A&A, 411, L1.

Zornoza, J.D. et al., 2007; Nuc. Phys. B. Proc. Sup., 165, 196.

Zweeink, J. et al., 1999; in Proc. 26th International Cosmic Ray Conference, 223.